Recent stress history effects in clays and associated improvements to the BRICK model

Alexander Joseph Tuxworth
MENG

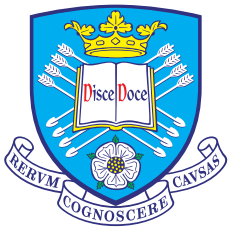

Thesis submitted to

The University of Sheffield
Department of Civil and Structural Engineering

for the degree of Doctor of Philosophy

September 2014

Declaration

I, Alexander Joseph Tuxworth, confirm that the work presented in this thesis is my own. Where information has been derived from other sources, I confirm that this has been indicated in the thesis.

September 2014

Abstract

Recent stress history effects in clays and associated improvements to the BRICK model

It is known that the stiffness of many soils is higher at small strains than at the large strains used in typical triaxial testing. Understanding this initial high stiffness and the factors affecting it is key to accurate displacement predictions.

The recent stress history (RSH) effect describes how the stiffness degradation curve at small strains is affected by the immediately preceding stress path. The effect is usually described in terms of stress path rotation angle between an approach path and the shear probe upon which stiffness degradation is measured.

The principle aim of the work was to investigate the relationship between the RSH effect, approach path length, and time dependent effects in more detail. A combination of physical testing and simulations with the BRICK constitutive model were used to achieve this. This has shown that in multistage testing the residual RSH effect from the first test increased the stiffness exhibited in the second, thus masking the natural behaviour. In addition the stress path rotation from consolidation to testing caused a stiffness reduction in the first test. This effect, newly termed recent consolidation history (RCH), was found to be degraded by the first test and so did not impact on the second. When allowance was made for these effects trends seen in the literature were supported.

Due to the complex stress paths used in the physical testing, a number of improvements were required to the strain rate dependent (SRD) BRICK model to allow accurate simulations to be run. These included implementation of a bisecting iteration within the strain calculations, and a coordinate decent routine to allow creep and creep rupture to be modelled. The model was then used to simulate the physical tests to allow more insight into the interplay between the effects identified in the physical testing, ultimately supporting the conclusions drawn.

Acknowledgements

Firstly, I would like to thank my supervisor Dr Sam Clarke for being a source of constant guidance and advice throughout the period of this research. The quality of the work owes much to his dedication and attention to detail. My thanks also go to Dr Jonathan Black for his guidance regarding the experimental setup and the department's technical staff for their support in the experimental work.

The research project was made possible through an Engineering and Physical Sciences Research Council (EPSRC) DTA award from the Civil and Structural Engineering department at the University of Sheffield.

Contents

List of Tables

List of Figures

List of Abbreviations

AC	Alternating current.
ADVDPC	Advanced pressure / volume controller.
APL	Approach path length.
BEPC	Base earth pressure cell.
CMSE	Constant mean stress extension.
CRS	Constant rate of strain.
CSL	Critical state line.
CT	Creep time.
DC	Direct current.
EOP	End of primary consolidation.
EPC	Earth pressure cell.
IDT	Inductive displacement transducer.
ISE	Incremental strain energy.
KSYS	Kinematic sub yield surface.
LVDT	Linear variable differential transformer.
LVDT	Linear variable differential transformer.
NCL	Normal compression line.
OCR	Over consolidation ratio.
PSRED	Plastic strain reduction.
PWP	Pore water pressure.
RCH	Recent consolidation history.
RMSE	Root mean square error.
RSH	Recent stress history.
SRD	Strain rate dependent.
SRD-B	Strain rate dependent bisecting iteration.
SRDSL	Strain rate dependent string length.
SRS	Stepped rate of strain.
SSE	Sum of squared errors.
TC	Triaxial compression.
TD	Time dependent.
TDSL	Time dependent string length.
TEPC	Top earth pressure cell.
TESRA	Temporary effect of strain rate acceleration.

List of Symbols

α	Slope of linear portion of $ln\dot{\varepsilon}$ vs D relationship from Singh & Mitchell (1968).
α	Viscous constant used by Tatsuoka, Ishihara, Di Benedetto & Kuwano (2002).
β	Viscous constant.
$\|\|\boldsymbol{\Delta\varepsilon}\|\|$	Increment of strain- magnitude of all strain components.
$\|\|\boldsymbol{\Delta\varepsilon_b}\|\|$	Increment of brick strain- magnitude of all strain components.
$\Delta\varepsilon_\theta$	Increment of strain along an axis passing through 0 and a point specified by the vector $\boldsymbol{\Delta\varepsilon}$.
$\boldsymbol{\Delta\varepsilon}$	Increment of strain - vector of all strains components.
$\boldsymbol{\Delta\varepsilon_p}$	Increment of plastic strain- vector of all strains components.
$\boldsymbol{\Delta\varepsilon_b}$	Increment of brick strain- vector of all strain components.
Δg_y	Change in strain component 3 of the BRICK model - shear strain 2.
$\Delta g_{y,b}$	Change in strain of a brick in component 3 of the BRICK model.
Δt	Time increment in SRD BRICK.
Δv	Increment of strain component 1 of the BRICK model- solumetric Strain.
ε_a	Axial strain.
$\dot{\varepsilon}_a$	Axial strain rate.
$\|\|\boldsymbol{\varepsilon_b}\|\|$	Brick strain- magnitude of all strain components.
$\|\|\boldsymbol{\dot{\varepsilon}_b}\|\|$	Magnitude of brick strain rate vector in SRD BRICK.
$\dot{\varepsilon}_{current}$	Strain rate during previous execution of BRICK.
ε_e	Elastic strain used in generic discussion.
$\dot{\varepsilon}_{ir}$	Strain rate of irreversible (in elastic) component of strain used by Tatsuoka et al. (2002).
$\dot{\varepsilon}_{min}$	Time used for the end point of the creep strain rate degradation.
$\dot{\varepsilon}_n$	Neutral strain rate.
ε_p	Plastic strain used in generic discussion.
$\dot{\varepsilon}_{previous}$	Strain rate during previous execution of BRICK.
ε_q	Triaxial shear strain $2/3(\varepsilon_a - \varepsilon_r)$.
$\dot{\varepsilon}_q$	Triaxial shear strain rate.
$\dot{\varepsilon}$	Applied strain rate.
ε_r	Radial strain.
$\dot{\varepsilon}_{ref}$	Reference strain rate.
ε_t	Total strain used in generic discussion.
$\dot{\varepsilon}_{\text{test}}$	Testing strain rate.
ε_v	Volumetric strain $1/3(\varepsilon_a + 2\varepsilon_r)$.
$\dot{\varepsilon}_v$	Volumetric strain rate.
$\boldsymbol{\epsilon}$	Vector of all strain components.
ι	Gradient of the pure elastic behaviour line in log-log space.
κ*	Gradient of the swelling and recompression line in log-log space.
λ	Viscous constant used by Graham, Crooks & Bell (1983).
λ*	Gradient of the normal consolidation line in log-log space.
ν	Poisson's Ratio.
ϕ'	Angle of shearing resistance.
$\dot{\sigma}$	Stress rate magnitude of stress component vector.
σ	Stress used in generic discussion.
$\|\|\boldsymbol{\sigma}\|\|$	Magnitude of all stress components used in the BRICK model.
$\boldsymbol{\sigma}$	Vector of all stress components.

ς_r	Residual standard deviation.
σ'_v	Vertical effective stress.
σ'_{vc}	Maximum vertical effective stress.
θ	Failure angle.
A	Material parameter used by Atkinson (2000).
A	Parameter for log linear creep rate equation strain rate at some arbitrarily chosen time t_1.
A	Constant used for pure TESRA.
B	Skempton pore pressure parameter B.
B	Parameter for log-log creep rate equation strain rate at some arbitrarily chosen time t_1.
c	Integration constant.
C_c	Compression index.
c'	Cohesive strength.
C_r	Recompression index.
C_{sec}	Coefficient of secondary consolidation.
c_v	Coefficient of consolidation.
D	Stress as a percentage of strength used by Singh & Mitchell (1968).
δU	Change in incremental strain energy.
e	Void ratio.
${E_0}'$	Tangent Young's modulus at very small strain.
${E_h}'$	Horizontal Young's modulus.
${E_v}'$	Vertical Young's modulus.
G_s	Specific gravity of soil particles.
G_0	Maximum shear stiffness at very small strain.
G	Tangential shear modulus.
G_Ω	Secant shear stiffness measured to the end of the shear probe.
g_y	Strain component 3 of the BRICK model - Shear strain 2.
K	Tangent Bulk modulus.
k	Permeability of the soil.
K_0	In situ earth pressure coefficient in undisturbed soil.
M'	Gradient of the effective stress path in critical state soil mechanics.
m	Material parameter used by Atkinson (2000).
m	Parameter for log-log creep rate equation negative of the slope of the relationship between the logarithm of strain rate and the logarithm of time.
m	Viscous constant used by Tatsuoka et al. (2002).
m_v	Coefficient of volume compressibility.
N	Specific volume on NCL at a mean normal stress of 1 kPa.
n	Material parameter used by Atkinson (2000).
n'	Ratio of horizontal to vertical Young's modulus.
n	Parameter for log linear creep rate equation negative of the slope of the relationship between strain rate and the logarithm of time.
ν	Specific volume.

$\dot{p'}$	Effective mean normal stress rate.
$\bar{p}$	Average p' during a increment of the BRICK model.
p	Mean normal stress in triaxial testing.
p'	Effective mean normal stress in triaxial testing.
p_α	Reference pressure used by Atkinson (2000) for dimensional consistency.
p_c	Apparent critical pressure used by Bjerrum (1967).
p'_i	Initial effective mean normal stress before application of shear stress.
p'_m	Known maximum effective mean normal stress.
q	Deviator stress in triaxial testing.
q_0	Initial deviator stress normalised by consolidation pressure used by Vaid & Campanella (1977).
q_f	Deviator stress at failure.
$q_{f(ref)}$	Deviator stress at failure for a low reference strain rate.
R_0	Overconsolidation ratio defined using p'.
$\bar{R}^2$	Adjusted coefficient of determination.
R^2	Coefficient of determination.
R_s	Ratio of shear stiffness for θ.
SL	String length.
SL_{app}	String length appropriate to the applied strain rate.
SL_{calc}	String length calculated before damping in SRD BRICK.
SL_{out}	String lengths normalised by the reference string length.
SL_{prev}	String length on previous SRD iteration.
$SL_{previous}$	String length on previous execution of BRICK.
SL_{ref}	Reference string lengths.
SL_{test}	String lengths measured during testing.
S_r	Degree of saturation.
s_u	Undrained shear strength.
T	Distance between brick before strain change and man after strain change used in SRD BRICK.
t	Time.
t_1	A reference time used for creep equations by Singh & Mitchell (1968).
t_c	Current time for time dependency in SRD BRICK.
t_{max}	Time used for the end point of the creep strain rate degradation.
t_p	Previous time for time dependency in SRD BRICK.
t_t	Transition time used in creep rate equation.
t_y	Stress component 3 of the BRICK model - Shear strain 2.
U	Incremental strain energy.
u	Pore water pressure.
Y_1	Yield surface characterising a change from linear elastic to non-linear elastic behaviour Jardine (1992).
Y_2	Yield surface characterising a change from elastic to elasto-plastic behaviour Jardine (1992).

List of BRICK Terms

BRICK	The BRICK constitutive model for soil (Simpson 1992).
`BETA(1)`	Beta-G.
`BETA(2)`	Beta-ϕ.
`GGmax`	Stiffness Reduction Array.
`NB`	Number of Bricks used for BRICK calculations.
`NC`	Number of Components used for BRICK calculations.
`RIOT`	Iota.
`RKAP`	Kappa*.
`RLAM`	Lambda*.
`Zero(2)`	Initial conditions array (1)- Volumetric Strain (2)- Mean Stress.
β	Beta constant.
β_{mod}	Beta modification factor $G_{max,oc}/G_{max,nc}$.
p_0	Initial mean stress in the BRICK model.
v	Strain component 1 of the BRICK model- Volumetric Strain.
v_0	Initial volumetric strain in the BRICK model.

1

Introduction

1.1 Background

As the density and scale of construction in major cities increases, the task of correctly predicting the ground movement caused by construction becomes more important. Modern FE models are capable of predicting the settlements from a range of complex structures but remain only as good as the soil models and properties upon which they are based. A common problem is that the soil stiffness is often much higher at the very small strains associated with retaining wall movement for example, than at the larger strains associated with conventional testing (Atkinson 2000). The observed 'S' shaped stiffness degradation curve at small strains requires both specialised methods for both measurement and modelling.

Measurement in the small strain region requires either dynamic tests such as bender elements or the use of locally mounted transducers in order avoid the errors associated with standard external instrumentation. New methods of modelling small strain behaviour, such as the framework of kinematic sub yield surfaces proposed by Jardine (1992) and the BRICK model from Simpson (1992), have shown significant improvements on the simple linear-elastic / perfectly plastic models. These modelling approaches also predict the phenomenon of recent stress history (RSH) which is observed at small strains.

The RSH effect describes how the small strain stiffness may be affected by the immediately preceding stress path (Atkinson et al. 1990). It is shown that a high rotation of the stress path (e.g. a reversal from extension to compression) will produce a higher stiffness than a low path rotation. This effect is however seen to degrade with increased strain. Further study by Gasparre et al. (2007) has indicated that the RSH effect may be affected by creep and the approach path length, in addition to the stress path rotation angle. The strain rate dependent (SRD) BRICK model (Clarke & Hird 2012) which incorporates viscous effects into the BRICK model allows strain rate effects and creep to be added to models of RSH.

1.2 Aims of the research

The changes in small strain stiffness caused by the RSH effect are becoming increasingly relevant in correctly modelling settlements caused by earthworks and tunnelling in congested urban areas. The research undertaken aims to clarify the little studied interaction between creep, stress path length and RSH effects by using a combination of physical testing and numerical modelling.

The physical testing studies the relationship between the observed RSH effect, creep time and approach path length observed by Gasparre et al. (2007). The three multistage stress path triaxial tests performed in that work led to the conclusion that the RSH effect would be erased by a 7 day creep period for a short ($10\,\mathrm{kPa}$) approach path but not a long ($100\,\mathrm{kPa}$) approach path.

In order to investigate these conclusions an expanded series of tests are performed in a stress path triaxial cell. These show how the stiffness degradation curve of a primary constant p' stress path is affected by a prior approach path. The length and direction of the approach path along with the duration of creep following the approach path and the order of testing was varied. This allowed effects of creep and approach path length on the RSH effect as well as the validity of the multistage testing approach to be investigated.

The soil used in the investigation was a remoulded London clay. London clay was used to allow comparison to previous studies on RSH and because the BRICK model used in the numerical work had been previously fitted for London clay. Production of a remoulded sample was chosen so that the stress history might be fully known for modelling purposes, so that identical homogeneous samples may be produced, and due to limited availability of high quality undisturbed samples.

The numerical work aims to test the capability of the BRICK model in modelling the experimental results, allowing further insight into how stiffness degradation curves are affected by the combined effects of consolidation history, RSH and the multistage testing approach. By doing so a larger range of data points can be investigated and anomalous results associated with physical testing are removed. Modelling used the SRD BRICK model as it incorporated the movable yield surfaces required to simulate RSH effects but made them strain rate dependent and by relating strain rates to time allowed for time-dependent behaviours of stress relaxation and creep. The actaul implention of the model however required improvements to allow modelling of a more generalised set of test circumstances and development of a method to achive the constant stress required for creep.

1.3 Outline of thesis

This thesis contains a total of 7 chapters. The current chapter (Chapter 1) contains an introduction and an overview of the subsequent chapters.

Chapter 2 presents a review of the published literature. This chapter presents background on those aspects of soil behaviour which will both affect the physical testing and require modelling. These include the non-linear soil stiffness in the small strain region, the RSH effect, time related effects of creep and stress relaxation, and strain rate effects. As the work is focused on the small strain region soil behaviour occurring at higher strain and failure are not covered. In addition an outline of the geological history of the London clay deposit provides the basis for the sample consolidation procedure and for modelling of in-situ scenarios. A review of the practical problems of measuring small strains is also provided.

Chapter 3 presents an outline of the planned testing regime. This is then followed by details of the apparatus to be used and a detailed methodology on the various aspects of the testing to be performed. There is then a discussion of how the data has been processed to obtain stiffness curves from noisy stress-strain data.

Chapter 4 presents the results of the testing program. This first covers the classification of the soil used by index properties. The consistency of the sample preparation is then discussed along with parameters indicating soils strength. The tests used to determine approach paths and creep durations in the main testing program are presented. The variation in observed creep strain rates is then discussed before the results of the main RSH effect program are presented.

Chapter 5 first introduces the BRICK model in detail. Then several points around the specific implementation of the SRD string length in the original work of Clarke (2009) are discussed before an improved method for calculating the SRD string length is presented. A coordinate descent method for achieving creep with zero stress change is presented along with the improved creep results observed. Finally in this chapter incremental strain energy (ISE) contours are used to help illustrate the capabilities of the BRICK model and the effects of creep.

Chapter 6 contains the simulation of the physical testing performed in Chapter 4 within the BRICK model. Initially this uses an idealised version of the RSH testing conducted, where only the stress path immediately preceding the test influences the brick positions and therefore the observed stiffness in the measured stage. This is then followed by modelling of the actual tests to show how the multistage testing approach and the effects of the consolidation affect the test results.

Chapter 7 provides a summary of the work and the conclusions that are to be made from it. It also provides suggestions on possible areas for future work.

2

Literature review

2.1 Introduction

In this chapter a review of published literature on the key areas of my research is presented. This first covers the deformation behaviour of saturated clays focussing on small strain stiffness and the effects of RSH. Also introduced are viscous behaviours consisting of strain rate effects and time dependent effects of creep and stress relaxation. The literature presented primarily focuses on London clay as this is the soil for which the BRICK model is fitted and in which previous studies on RSH effcets have focused and is that used by the present work for comparative purposes. The focus is also limited to pre-peak stress strain behaviour as post-peak behaviour as the phenomena studied occur at small strains and the numerical modelling approach used does not incorporate post-peak behaviour.

The SRD BRICK model used for the numerical modelling work is covered in Section 5.1 (p 145) as it required a detailed discussion inappropriate for a literature review. The requirements for a model to predict RSH effects limited the choice to those models which utilised kinematic yield surfaces which enables the stiffness to be impacted changes in stress path direction. Specific model implementations are not discussed in detail as investigating the use of the BRICK model was an initial aim of the research. An overview of the kinematic strain-hardening plasticity frameworks is provided however, as its parameters are discussed in relation to RSH effects.

Returning to practical matters, an overview of the geological history of the London clay deposit is given. This pertains to both the stress history to be modelled, and guides how one may relate London clay from different depths or in different states of weathering for the purpose of comparing physical tests. Finally the published literature on the problem of measuring small strains in triaxial tests is reviewed, which can be seen as background to the development of the methodology.

2.2 Soil behaviour

2.2.1 Non linear soil stiffness

General non-linearity

The stress / strain behaviour of soil is highly non-linear and soil stiffness may decay with strain by orders of magnitude. In characterizing the non-linearity it is necessary to consider stiffness, strength and strain at failure, and the relationships between them. Atkinson (2000) has shown how the understanding of soil stiffness non-linearity has resolved the differences between stiffness measured in lab and field measurements. Figure 2.1 after Atkinson (2000) shows a typical stiffness-strain curve and ranges of strain for different structures and tests. At very small strains the elastic response of the soil gives the maximum stiffness $E_0{}'$ or G_0. A rapid decay of soil stiffness in the small strain region then follows. A relatively low stiffness persists at large strains.

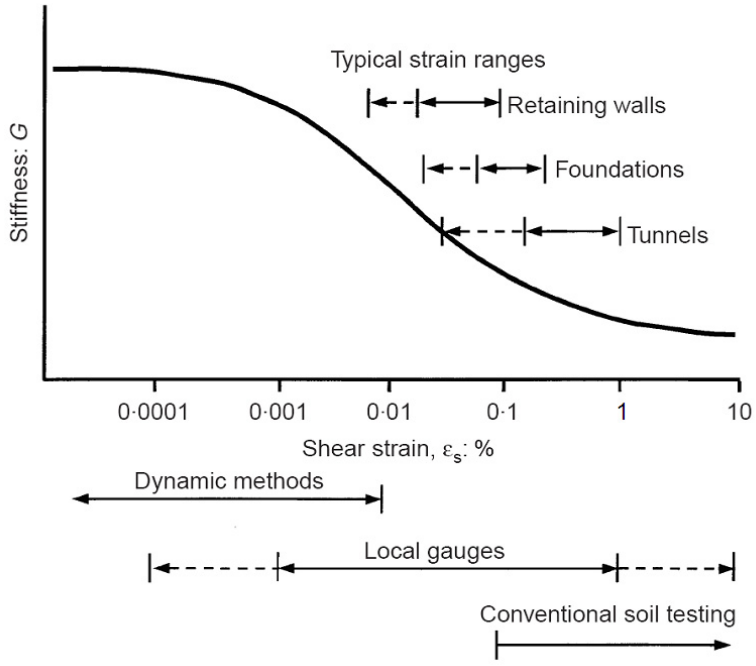

Figure 2.1: Approximate strain limits for reliable measurement, Atkinson (2000)

Clayton & Heymann (2001) shows this non-linear stiffness behaviour for tests performed on London clay, block sampled from tunnels constructed for the Heathrow express rail link. When the stiffness is presented as a undrained tangent Young's modulus in Figure 2.2 the initial elastic response is shown at strains up to $0.002\,\%$ before the stiffness decays.

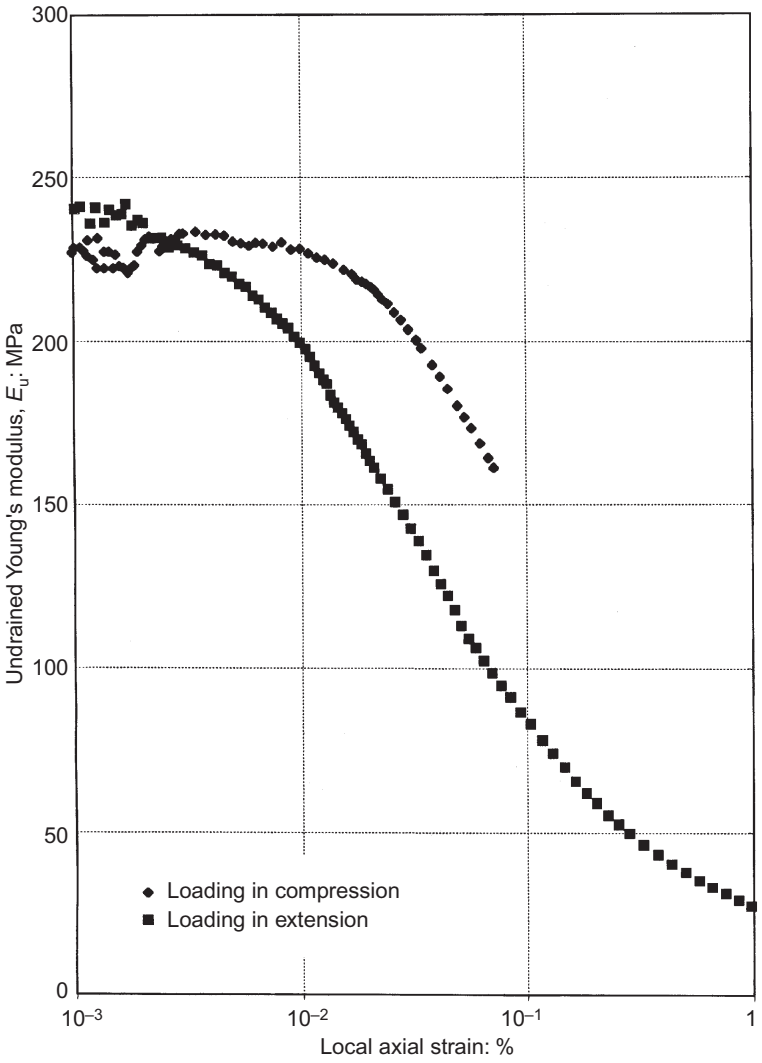

Figure 2.2: Stiffness degradation of London clay , Clayton & Heymann (2001)

Variation of very small strain stiffness with state

The soil state of an isotropic soil can be described by its current effective stress and specific volume with respect of a reference line. The reference line may be the critical state line (CSL) or the normal compression line (NCL). The state is described by the perpendicular distance from the reference line and the soil state is therefore equivalent for any line parallel to the reference line. The relationship between stiffness, stress, specific volume and over consolidation ratio takes the general form shown in Equation 2.1 (Atkinson 2000).

$$G_0 = Af(\nu)p'^n R_0^m \tag{2.1}$$

Where $f(\nu)$ is a function of the specific volume, p' is current effective stress and R_0 is the over consolidation ratio (OCR), A, n and m are material parameters. If R_0 is defined relative to the NCL the equation reduces to Equation 2.2 (Atkinson 2000).

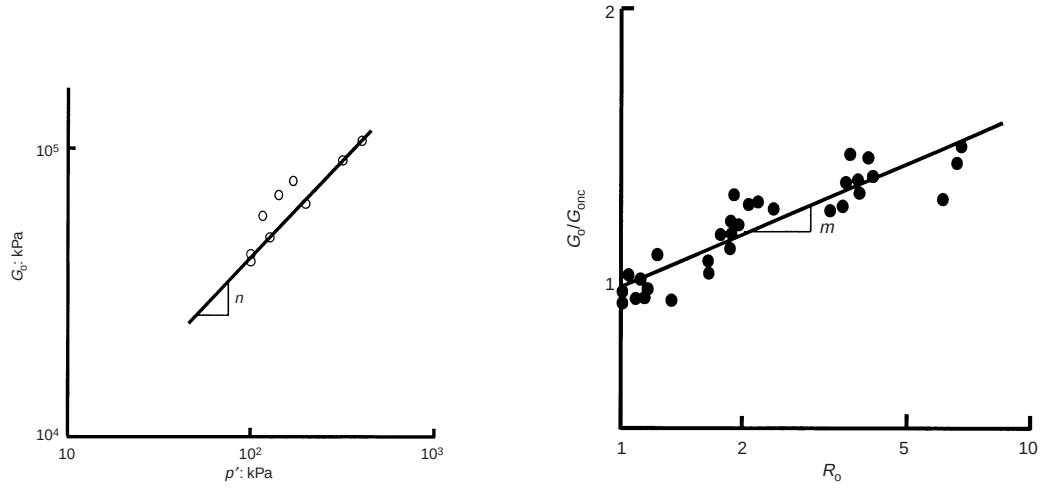

(a) Normally consolidated (b) Overconsolidated

Figure 2.3: Variation of G_0 with state for reconstituted kaolin clay, Viggiani & Atkinson (1995)

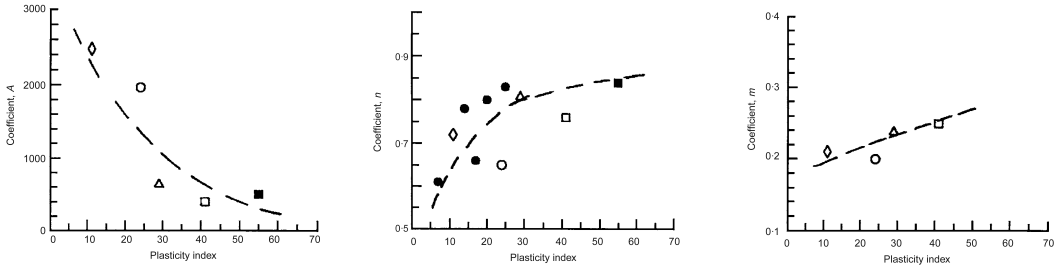

(a) A vs. plasticity index (b) n vs. plasticity index (c) m vs. plasticity index

Figure 2.4: Material parameters for G_0,Atkinson (2000) after Viggiani & Atkinson (1995)

$$G_0/p_\alpha = A(\rho'/\rho_a)^n R_0^m \tag{2.2}$$

Where p_α is a reference pressure, normally $1\,\mathrm{kPa}$. The material parameters A, n and m vary with the nature of the soil. Figure 2.3 shows how the soil parameters n and m are derived from physical tests. Figure 2.4 shows the results of bender element testing by Viggiani & Atkinson (1995) which relates these parameters to plasticity index.

Atkinson (2000) concluded that the value of the small strain shear stiffness G_0 for a particular soil varies with current state in a simple and consistent manner. For soils which are not strongly bonded or highly structured, these parameters depend principally on the nature of the grains and vary consistently with plasticity index, as shown in Figure 2.4.

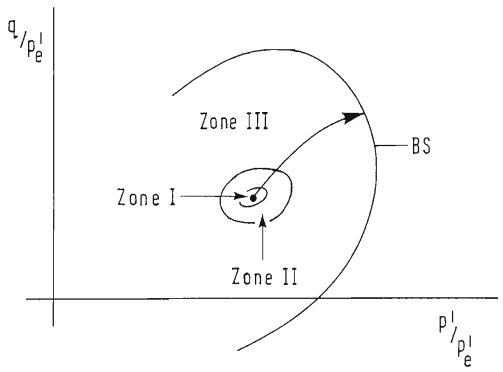

Figure 2.5: Arrangement of sub-yield zones, Jardine (1992)

2.2.2 Kinematic strain-hardening plasticity framework

Described by Jardine (1992) the Kinematic strain-hardening plasticity framework defines soil behaviour in normalised stress-space. The behaviour is defined by an outer bounding surface and three zones of characteristic behaviours within this. The kinematic sub yield surfaces (KSYSs) are kinematic zones that may be repositioned by moving the current stress point.
The scheme set out imagines an element of soil in full equilibrium at a stable point in triaxial space while experiencing negligible creep. A monotonic loading path taken from this point has been experimentally shown to exhibit four phases of behaviour represented by the zones outlined in Figure 2.5.

Zone 1:

Within Y_1 perfect linear elastic behaviour is seen. This zone is most extensive in strongly cemented soils, for example Figure 2.6 shows triaxial test on local instrumented samples performed by Jardine et al. (1985). Intact chalk (sample A) shows a linear elastic behaviour. The other less cemented saturated samples however show a small linear elastic region occupying at a strain magnitude that is often unresolvable.

Zone 2:

Between Y_1 and Y_2 behaviour is non linear but recovers after complete load unload cycles. Stress-strain loops usually involve hysteresis although non-linear elastic behaviour is possible. The energy dissipated in the hysteretic stress-strain loops is thought to be the result of local yielding and fretting at the inter particle contacts (Jardine 1992). Figure 2.7 shows the transition to irrecoverable behaviour for a locally instrumented undrained triaxial test on K_0 Magnus till performed by Jardine (1992). Non-recoverable strains are seen to begin on the second loop.

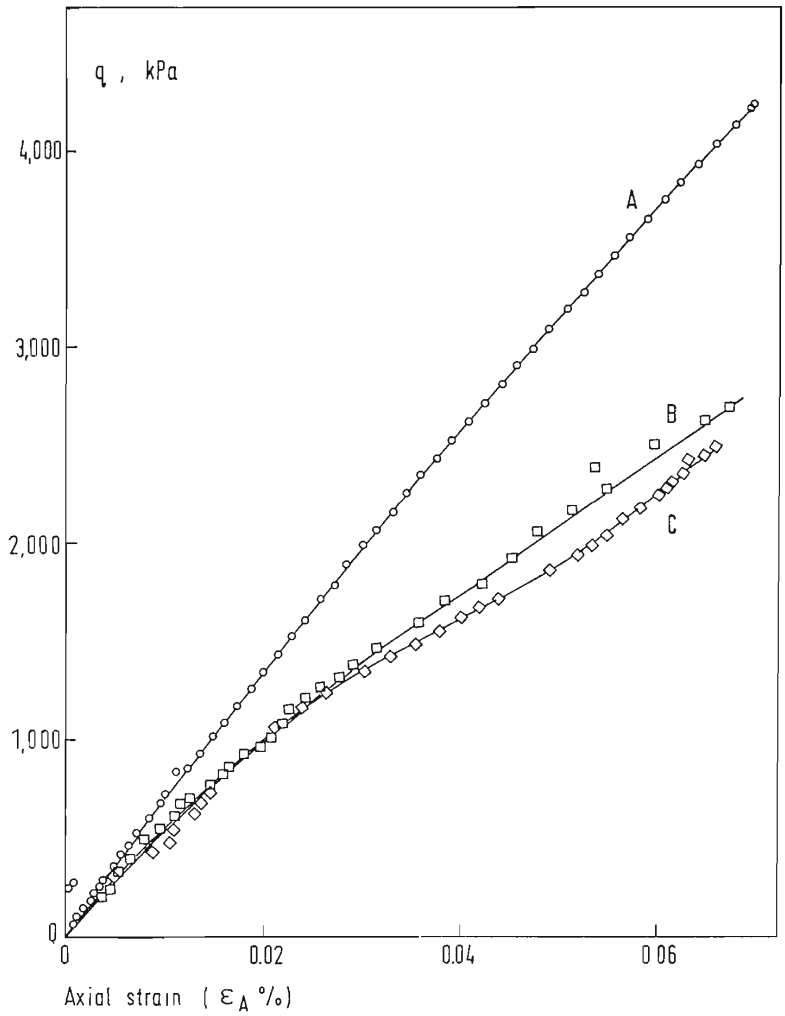

Figure 2.6: Demonstration of linear elastic behaviour, Jardine (1992) after Jardine et al. (1985)

Zone 3:

Outside Y_2 large plastic irrecoverable strains develop. These become more prominent as the local bounding surface is approached, representing an increasing portion of the total strain. When the bounding surface is reached all strain change is plastic and the particles are thought to be sliding relative to each other.

Bounding surface:

The initial bounding surface represents the start of large scale changes in particle packing, either dilation or contraction. This is accompanied (unless the stress path direction is altered) by a low or negative stiffness value.

Kinematic nature of yield surfaces:

As shown in Figure 2.8 each of the KSYSs move when the sub yield surface it contains intercepts its boundary. This allows RSH effects, as while both surfaces may be engaged and plastic strain generated in one direction a stress path reversal causes

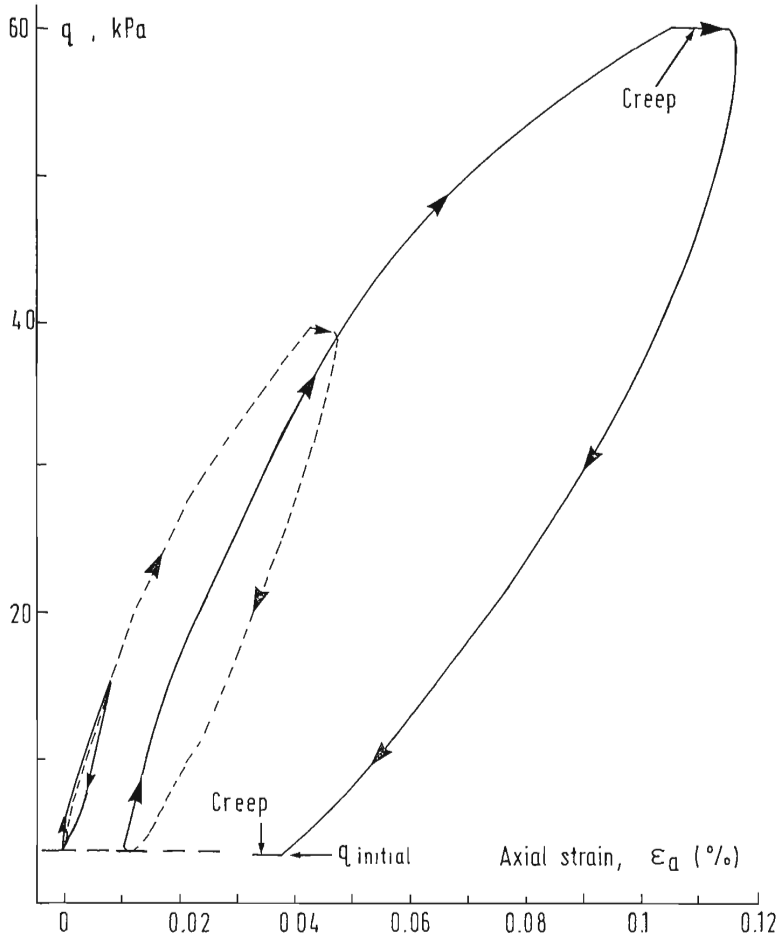

Figure 2.7: Small strain load-unload test on Magnus till Jardine (1992)

the stress point to travel though the elastic zone again, increasing the stiffness.

2.2.3 Recent stress history

The soil stiffness observed is influenced by the soil characteristics, current stress state and stress history. The stress path followed also has influence. Current soil models such as Cam-clay define stress strain behaviour by current state and OCR. This however only defines the total stress history and effects of the more recent stress history are ignored. The concept of RSH is first discussed by Atkinson et al. (1990) who define it as "The most recent loading either extended period of rest or change in stress path direction". The change in stress path direction is quantified by the concept of stress path rotation shown in Figure 2.9a. The stress paths CO and DO have rotated through a different angle before shearing along path OA. The effect of these different approach paths upon the stress-strain behaviour along the path OA is shown in Figure 2.9b.

In order to quantify this effect Atkinson et al. (1990) performed triaxial tests following constant p' and constant q stress paths. It is necessary to use a constant p'

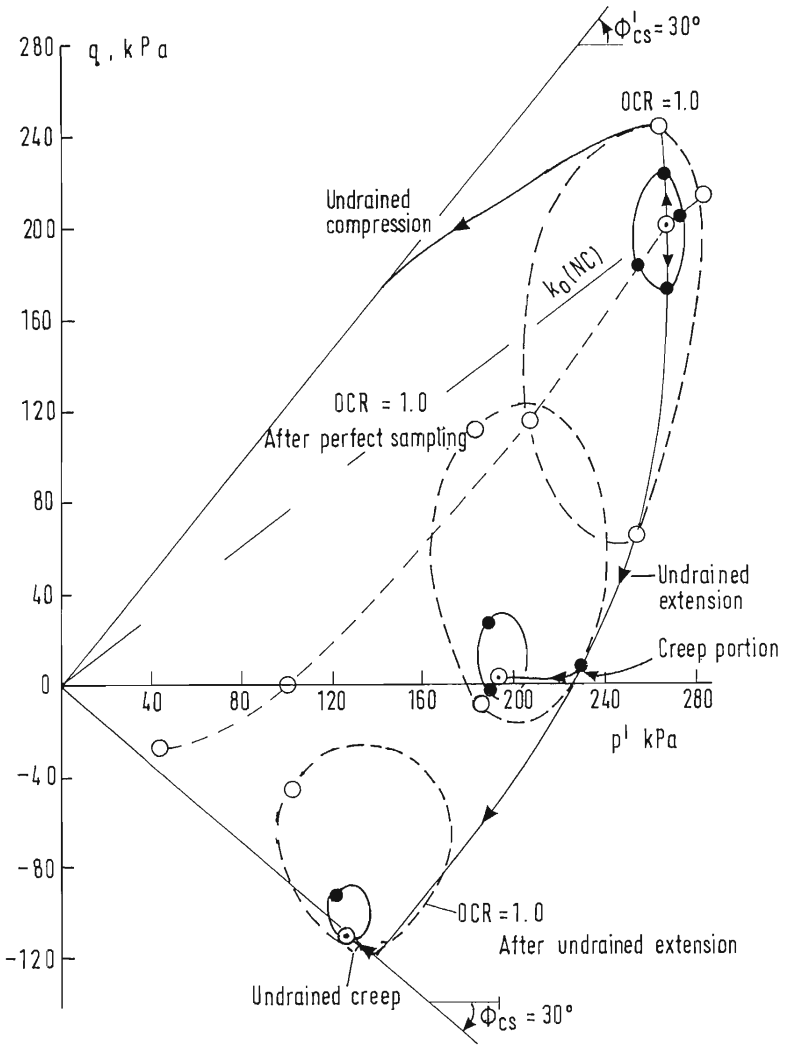

Figure 2.8: Arrangement of sub-yield zones Jardine (1992)

or constant q test in order to obtain stiffness parameters. These cannot be obtained from conventional tests due to cross linking of constitutive equations. By keeping p' or q constant, the cross linking is eliminated and Equation 2.3 and Equation 2.4 can be used for constant p' or q tests respectively.

$$dq'/d\varepsilon_s = 3G' \tag{2.3}$$

$$dp'/d\varepsilon_s = K' \tag{2.4}$$

The tests were performed on reconstituted London clay samples of $38\,\mathrm{mm}$ diameter and $76\,\mathrm{mm}$ length. The samples were first isotropically compressed to a preconsolidation pressure p'_m = $400\,\mathrm{kPa}$ and swelled to initial stress of p'_i = $200\,\mathrm{kPa}$ at a stress rate of $\dot{p'}$ = $5\,\mathrm{kPa\,h^{-1}}$. The pore pressure throughout was u = $150\,\mathrm{kPa}$ whilst the R_0 = 2 and the specific volume at the start of the testing was ν = 1.766. Drained loading would be run either with constant p' where test path OA was approached from point P or Q (Figure 2.10a), or in constant q where test path OB

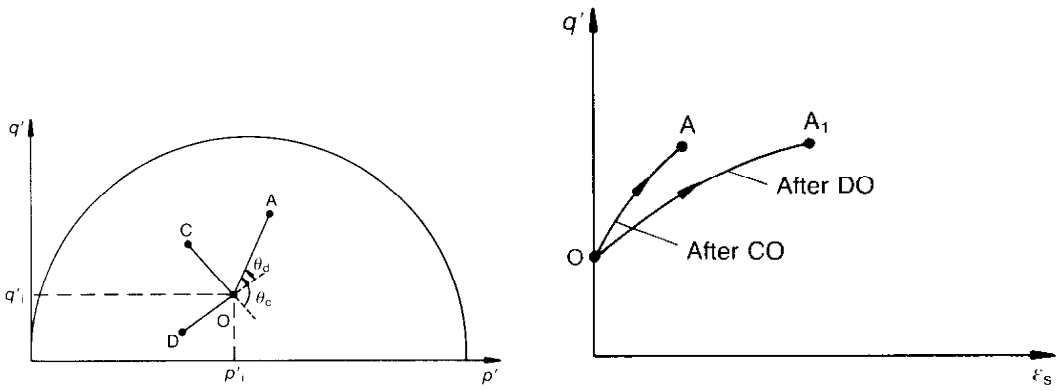

(a) (b)

Figure 2.9: Effect of recent stress history on current stiffness, Atkinson et al. (1990)

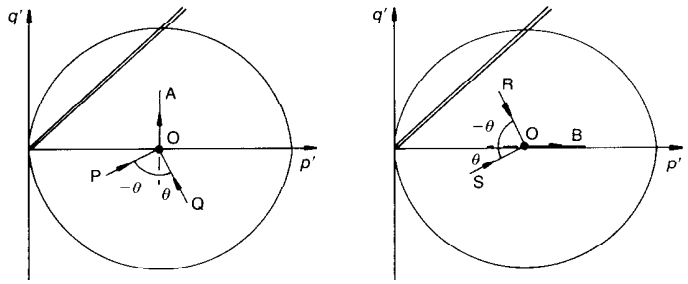

(a) constant p' (b) constant q

Figure 2.10: Tests paths followed, Atkinson et al. (1990)

was approached from point R or s (Figure 2.10b). The stress rate along the approach path was $5\,\mathrm{kPa\,h^{-1}}$ with an approximate path length of $90\,\mathrm{kPa}$ measured along the stress path. To reduce creep effects, the samples were held at constant stress of $0\,\mathrm{kPa}$ for $3\,\mathrm{hours}$ before loading, The creep strain rate was too small to be measured by Atkinson's instrumentation.

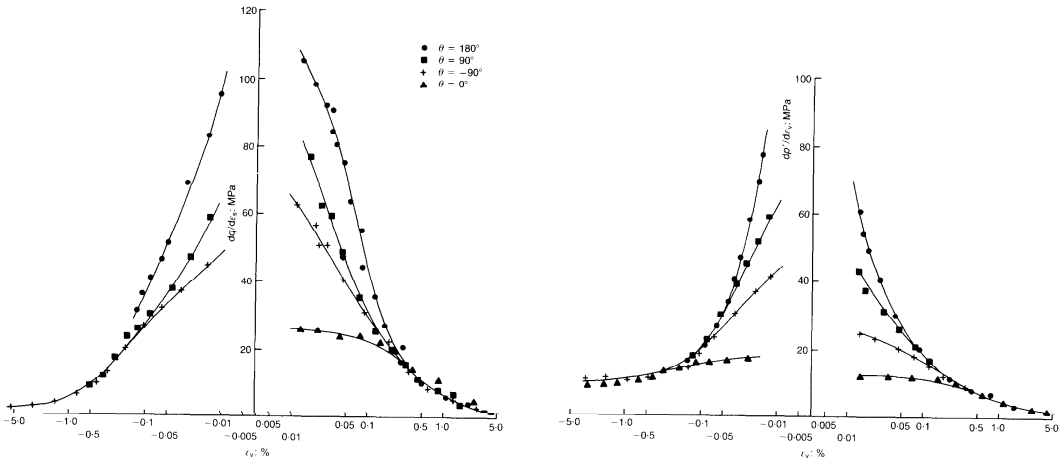

(a) constant p' (b) constant q

Figure 2.11: Stiffness of reconstituted London clay tests, Atkinson et al. (1990)

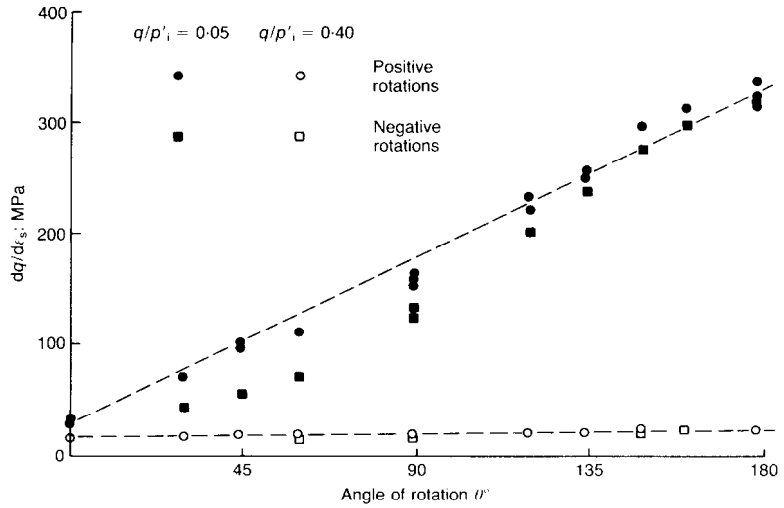

Figure 2.12: Variation of shear stiffness with stress path rotation measured in constant p' laboratory tests on reconstituted London clay, Atkinson et al. (1990)

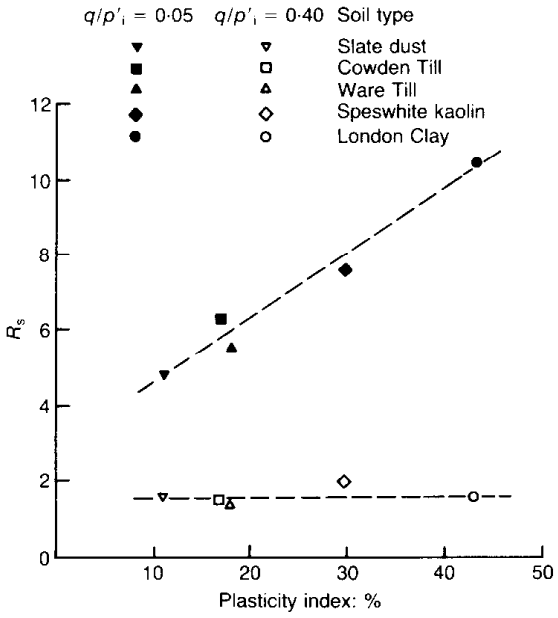

Figure 2.13: Variation of shear stiffness with plasticity, Atkinson et al. (1990)

It can be seen in Figure 2.11 that the initial stiffness is increased by an order of magnitude due to the increased rotation angle in the stress path for both the constant q and constant p' tests. The effect of rotation angle on stiffness however deteriorates with increased strain until it has minimal effect. This can be demonstrated by plotting the stiffness versus rotation angle at a high and low deviator stress. This was expressed as the normalised stress q/p'_i as $p'_i = 200\,\mathrm{kPa}$ the value at $q = 10\,\mathrm{kPa}$ and $80\,\mathrm{kPa}$ was expressed as $q/p'_i = 0.05$ and 0.4 respectively. A linear relationship between stiffness value dq/de and rotation can be seen in Figure 2.12 for small stress increases but effects drops considerably by $q/p'_i = 0.4$.

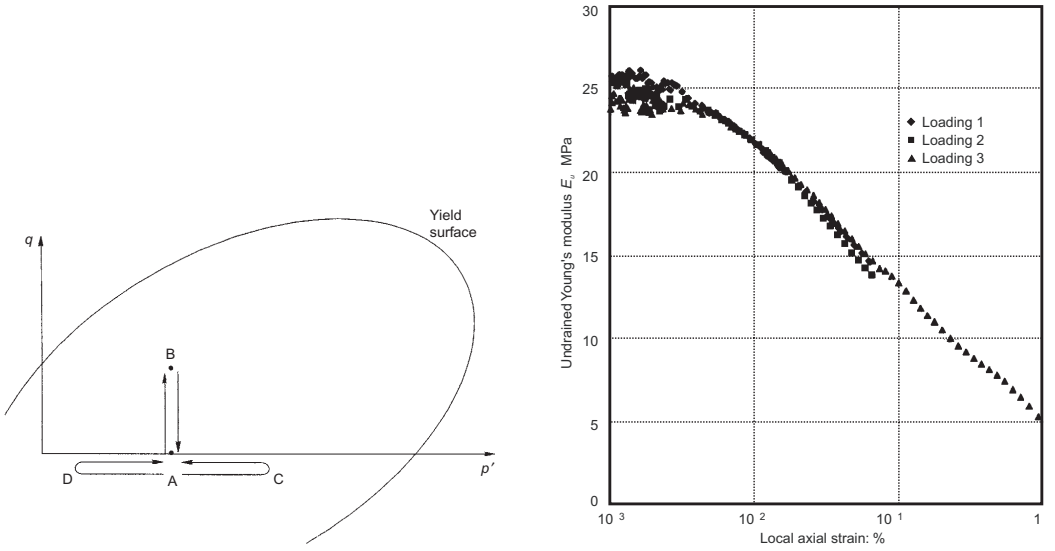

(a) Stress paths

(b) Stiffness degradation curves

Figure 2.14: Bothkennar clay subjected to three identical loading paths following different approach paths, Clayton & Heymann (2001)

Tests shown in Figure 2.13 show that the ratio of stiffness at $180°$ rotation to that at $0°$ rotation R_s increases linearly with plasticity. Clayton & Heymann (2001) postulated that effects of RSH observed by Atkinson et al. (1990) might result from creep strains contributed by previous loading path. These where observed to be of similar magnitude to those of current loading at small strains. Therefore to avoid creep influencing the results, rest periods of 6 to $12\,\mathrm{days}$ were allowed between each loading until creep rates were less than $0.01\,\%/\mathrm{d}$. Tests were performed on $100\,\mathrm{mm}$ samples of Bothkennar clay as shown in Figure 2.14a in which three constant p' probes along path AB after approach paths BA, CA and DA respectively. The approach path length was $10\,\mathrm{kPa}$ and the first 2 outgoing stress paths were of length $9\,\mathrm{kPa}$. These produced axial strains of more than $0.06\,\%$ and thus induced plastic strains in the material (Smith, Jardine & Hight 1992). The final stress path (AB) was taken to failure. The results in Figure 2.14b show no perceptible difference in the value of maximum small strain stiffness or the rate of stiffness degradation between the different loadings.

To address the contradictory results and the differences in experimental method, Gasparre et al. (2007) conducted a series of probing tests on clays. These consisted of undrained compression or extension starting from a near isotropic initial stress. The tests investigated the effect of recent stress history after being approached by constant p' drained paths $10\,\mathrm{kPa}$ or $100\,\mathrm{kPa}$ in length. It was desirable to perform drained shear probes but this was not possible due to the low shearing rates required. Undrained shear probes at a rate of $5\,\mathrm{kPa\,h^{-1}}$ were used instead. Tests were conducted on 2 samples taken from London clay at a depth of $11.5\,\mathrm{m}$ below the surface.

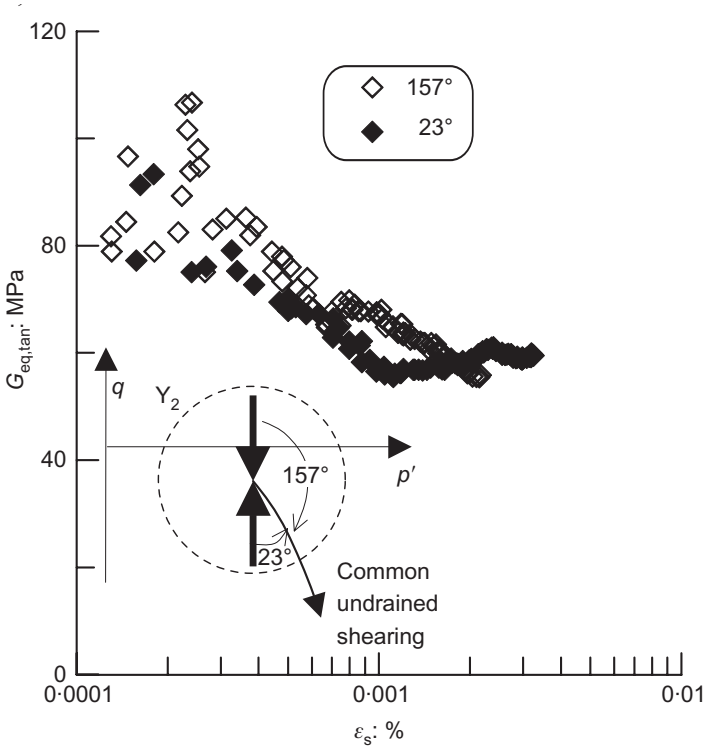

Figure 2.15: Tangent stiffness degradation curves for probes with approach paths within the Y2 region creep allowed, Gasparre et al. (2007)

These samples were probed repeatedly in 3 tests types as follows:

- Short approach paths of $10\,\mathrm{kPa}$ within Y_2 region (see Section 2.2.2) followed by a $7\,\mathrm{days}$ creep period so the creep rate before testing was negligible, less than $1 \times 10^{-4}\,\%\,\mathrm{h}^{-1}$. Figure 2.15 shows that the RSH appeared to have no influence on results as found by Clayton & Heymann (2001).
- Short approach paths of $10\,\mathrm{kPa}$ within the Y_2 followed by a $3\,\mathrm{hours}$ creep period so the creep rate before testing was $0.001\,\%\,\mathrm{h}^{-1}$. The result shown in Figure 2.16 indicated a clear stress history effect. This showed an increase in initial stiffness with stress path rotation. The shape of the response showed an unexpected peak stiffness and early scatter in the $105°$ result.
- Long approach paths of $100\,\mathrm{kPa}$ where used which engaged and relocated the Y_2 surface. A rest period of $10\,\mathrm{days}$ was allowed until creep became negligible. The result showed a strong effect of recent stress history on the initial undrained stiffness but with scatter shown at small strains as shown in Figure 2.17.

The conclusions of the study were that where the approach paths did not engage the Y_2 surface, creep could erase RSH effects. If creep was not allowed, the RSH effects persist within Y_2, and when approach paths went outside the Y_2 surface, creep was unable to eliminate RSH effects.

Another study of RSH effects is given by Finno & Cho (2011) using samples of

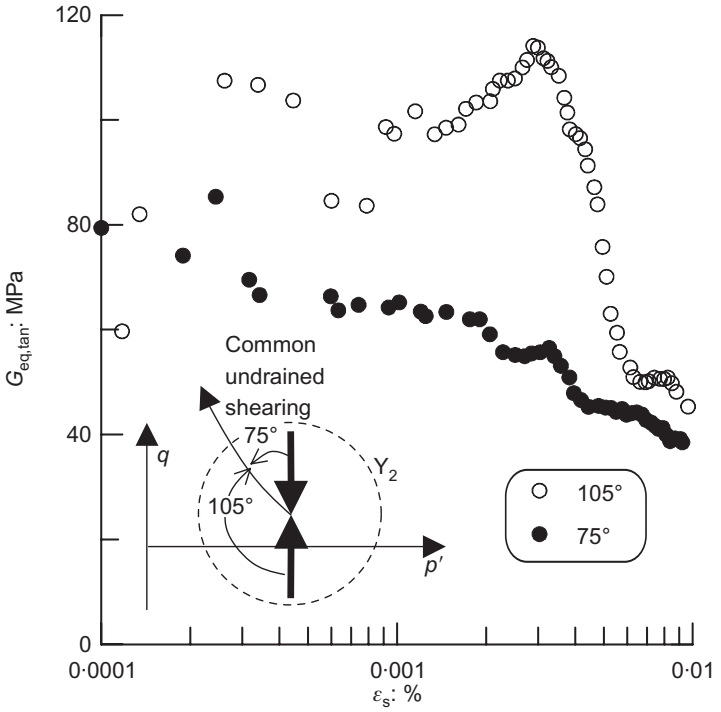

Figure 2.16: Tangent stiffness degradation curves for probes with approach paths within the Y_2 region creep not allowed, Gasparre et al. (2007)

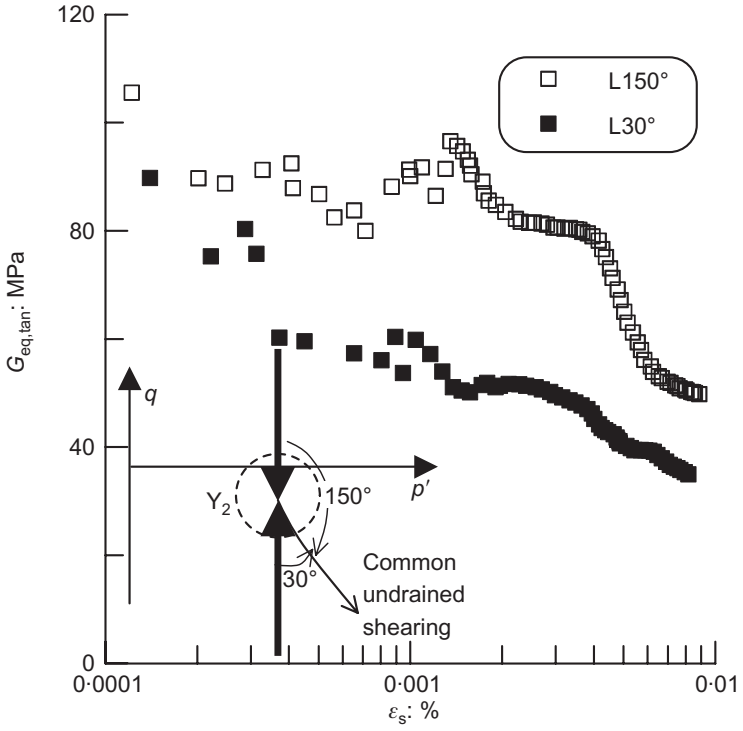

Figure 2.17: Tangent stiffness degradation curves for probes with approach paths above the Y_2 region creep allowed, Gasparre et al. (2007)

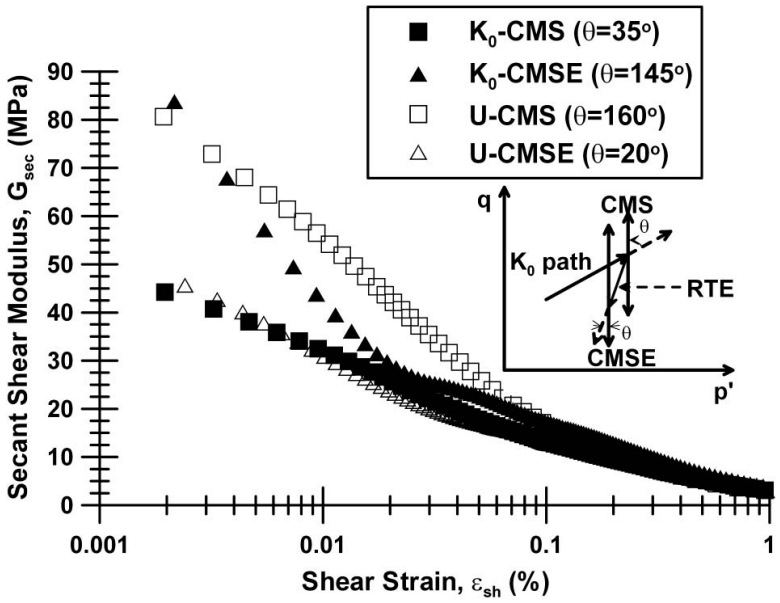

Figure 2.18: Secant shear modulus degradation for different stress path rotation in Chicago clay, Finno & Cho (2011)

Chicago glacial clay. The samples were equipped with local transducers and a series of shear probes were performed on different samples from one of two starting points:

- K_0 consolidation to a vertical effective stress of $137\,\mathrm{kPa}$ approximately (p' = $100\,\mathrm{kPa}$, q = $60\,\mathrm{kPa}$).
- Post unloading where the K_0 consolidation path was followed by swelling until p' was halved (p' = $90\,\mathrm{kPa}$, q = $30\,\mathrm{kPa}$).

Creep periods of approximately $36\,\mathrm{hours}$ were imposed after consolidation and unloading resulted in a axial creep rate of $8.3 \times 10^{-4}\,\%\,\mathrm{h}^{-1}$, which is slightly slower than rate observed after 3 hours by Gasparre et al. (2007). Axial stress rates of $2.4\,\mathrm{kPa\,min}^{-1}$ for the first $10\,\mathrm{kPa}$ and $1.2\,\mathrm{kPa\,min}^{-1}$ thereafter where used. The results of the testing showed the presence of RSH effects, as illustrated by the increased stiffness for the paths showing grater rotation in Figure 2.18.

Finno & Cho (2011) went on to investigate the effects of creep time upon the results by performing a test with an extended creep period. As shown in Figure 2.19 this $7\,\mathrm{day}$ creep period does increase the stiffness at small strain for the low rotation triaxial compression (TC) path, but not nearly to the extent of the high rotation constant mean stress extension (CMSE) path. As the approach paths were greater than the Y_2 sub yield surface, this is in accordance with the findings of Gasparre et al. (2007). The influence of creep however does reduce the overall difference in stiffness at small strain.

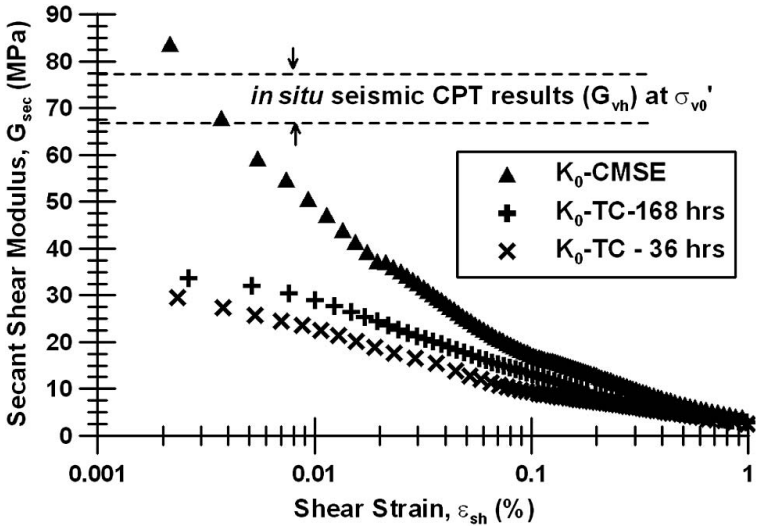

Figure 2.19: Secant shear modulus degradation showing effect of creep duration on RSH effect in Chicago clay, Finno & Cho (2011)

2.3 Time related behaviour

2.3.1 Introduction

Time related behaviour is considered to be the behaviour that is purely a result of time and is separate from strain rate behaviour in which a strain is imposed on the soil.

2.3.2 Creep and stress relaxation

Creep refers to the process whereby strain continues at a constant stress level. Here the term creep strain is the strain that occurs while under constant stress creep conditions while creep strain rate is the rate of strain occurring in the soil while under creep conditions. The creep curves of strain versus time exhibited by different materials vary significantly across the different soil types, as shown in Figure 2.20 (Mitchell & Campamella 1964).

The creep behaviour of a soil is dependent on the creep stress it is under. Singh & Mitchell (1968) quantify the behaviour using the value D. D is defined as the deviator stress expressed as a percentage of the strength. When D <30 % a small creep strain is produced for a limited time. For D which is between 30 % and 60 to 90 % the creep may continue indefinitely. At large stresses where $D > 60$ to 90 % the creep strain rate may accelerate until failure; a process referred to as "creep rupture" as seen in Figure 2.21.

It was suggested by Finnie & Heller (1959) that after a transient period of decreasing

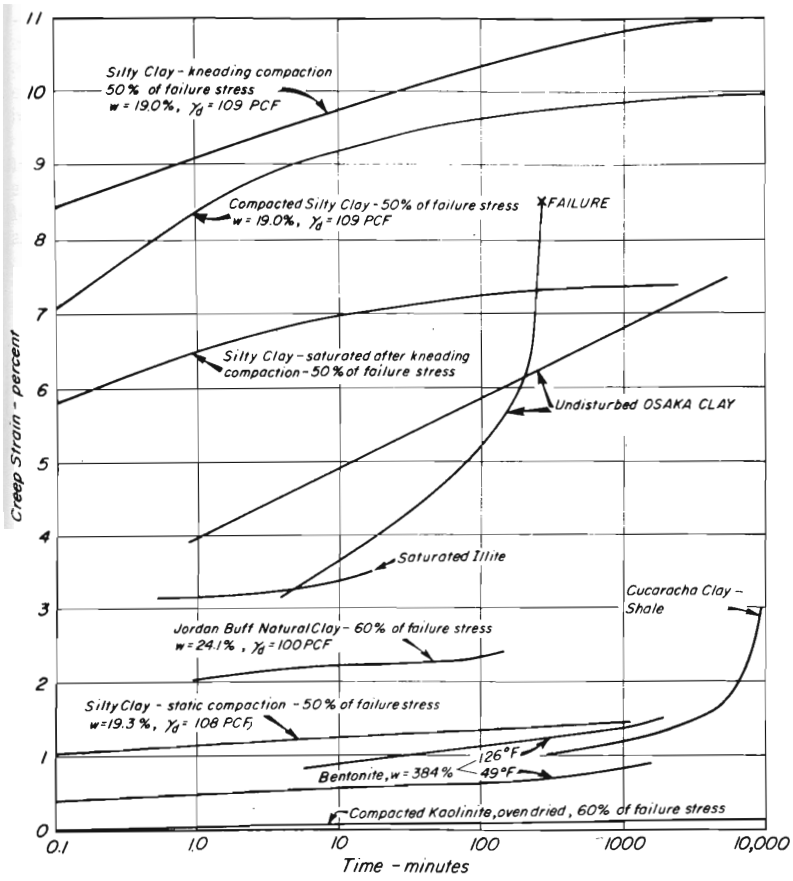

Figure 2.20: Sustained stress-creep curves illustrating different forms of behaviour, Singh & Mitchell (1968) after Mitchell & Campamella (1964)

creep strain rate, a constant creep strain rate would persist for some period of time. While the theory of steady state behaviour fails to describe the complete creep behaviour (Singh & Mitchell 1968) it provides an approximation for engineering time scales and loads.

A characteristic relationship between time and creep rate has been shown to exist for clays within engineering stress ranges of 30 to $90\,\%$ of the failure strength. This is shown in Figure 2.22 (Singh & Mitchell (1968) based on results from Bishop (1966)). Similar relations have been observed by other authors. The relationship shows that the logarithm of strain rate decreases linearly with the logarithm of time, and that creep stress serves only to shift the line vertically, not change its slope.

The influence of creep stress intensity is also shown to have a linear relationship with log strain rate at mid rage stress intensities. This relationship is valid at any point in time,as shown diagrammatically in Figure 2.23 (Singh & Mitchell 1968), and in tests on a sample of remoulded Illite by Campanella (1965) in Figure 2.24.

Singh & Mitchell (1968) express the two observed logarithmic relationships in algebraic form for the effect of time, this is given by Equation 2.5.

$$\ln \dot{\varepsilon} = \dot{\varepsilon}_{(t_1 D)} - m \ln \left(\frac{t}{t_1} \right) \tag{2.5}$$

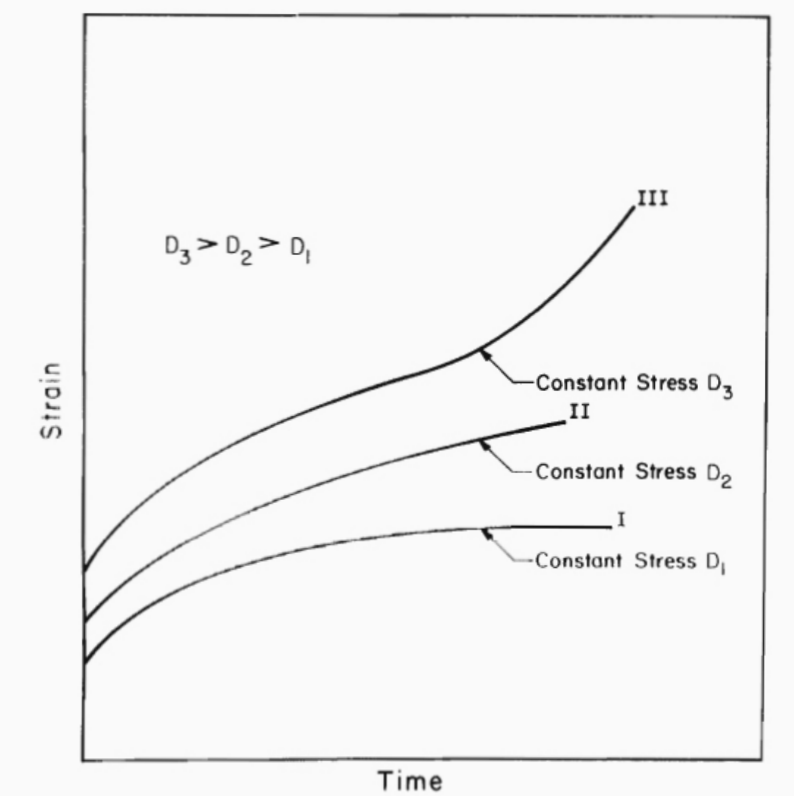

Figure 2.21: Typical creep behaviour of soils under constant stress, Singh & Mitchell (1968)

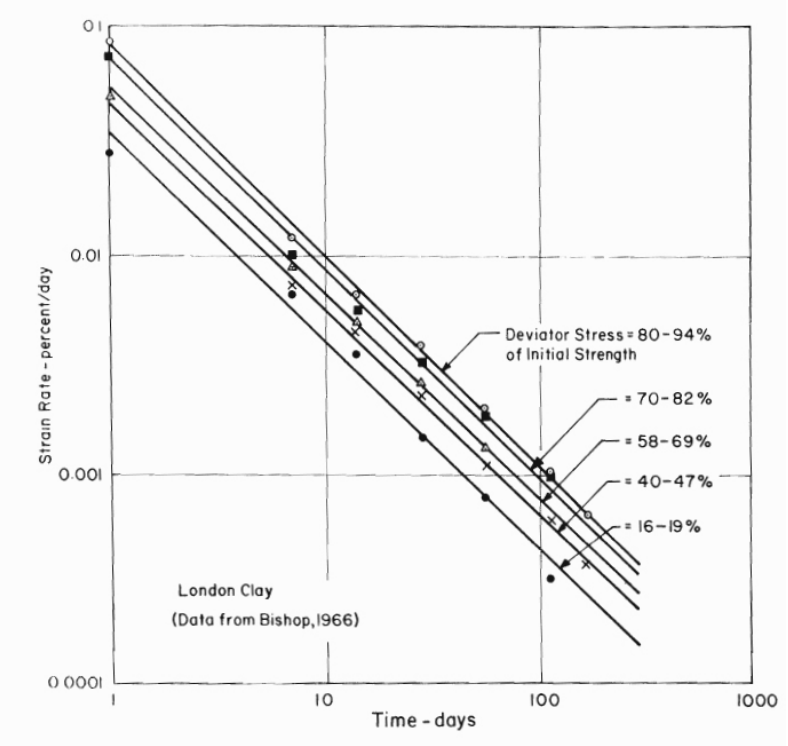

Figure 2.22: Strain rate verses time relationship during drained creep of London clay, Singh & Mitchell (1968)

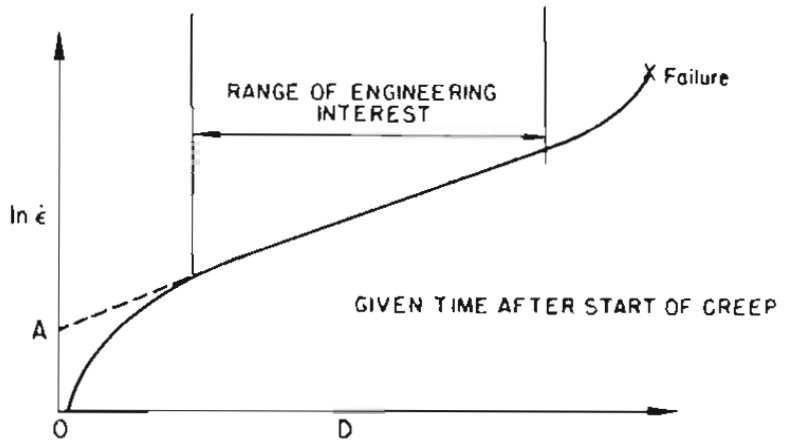

Figure 2.23: Influence of creep stress intensity of creep rate, Singh & Mitchell (1968)

Where $\dot{\varepsilon}$ is the strain rate, t_1 is a reference time (e.g $1\,\mathrm{min}$) D is a stress intensity and m is the absolute value of the slope of the straight line. Therefore $\dot{\varepsilon}_{(t_1 D)}$ is a strain rate that lies at t_1 on a specified stress intensity D. The value of the slope m is found to be between 0.75 and 1.0 (Singh & Mitchell 1968). The relationship between strain rate and stress intensity is shown in Figure 2.23, and can be expressed for its linear section by Equation 2.6.

$$\ln \dot{\varepsilon} = \ln \dot{\varepsilon}_{(tD_0)} + \alpha D \tag{2.6}$$

Where $\dot{\varepsilon}_{(tD_0)}$ is the fictitious strain rate where the linear trend intercepts the D= 0 (point A in Figure 2.23). α is a value for the slope of the linear portion of the trend. The whole relationship between the three parameters of strain rate, time and creep stress may be expressed by Equation 2.7 in which $\dot{\varepsilon}_{(t_1 D_0)}$ is the fictitious strain rate, where time is at the unit time t_1, and D =0.

$$\dot{\varepsilon} = \dot{\varepsilon}_{(t_1 D_0)} e^{\alpha D} \left(\frac{t_1}{t} \right)^m \tag{2.7}$$

Integration of Equation 2.7 gives the strain as a function of time creep stress and some reference strain point using determined creep constants. There are two formulations for $m \neq 1$ and $m = 1$ given in Equation 2.8 and 2.9 respectively:

$$\varepsilon = \alpha + \frac{a}{1-m} e^{\alpha D} (t)^{1-m} \tag{2.8}$$

$$\varepsilon = \varepsilon_1 + A e^{\alpha D} \ln t \tag{2.9}$$

Where: $A = \dot{\varepsilon}_{(t_1 D_0)}$ and a=$\varepsilon_0 - \frac{A}{1} - m e^{\alpha D}$, the comparison between the theoretical and observed creep is shown to be reasonable, as shown in Figure 2.25.

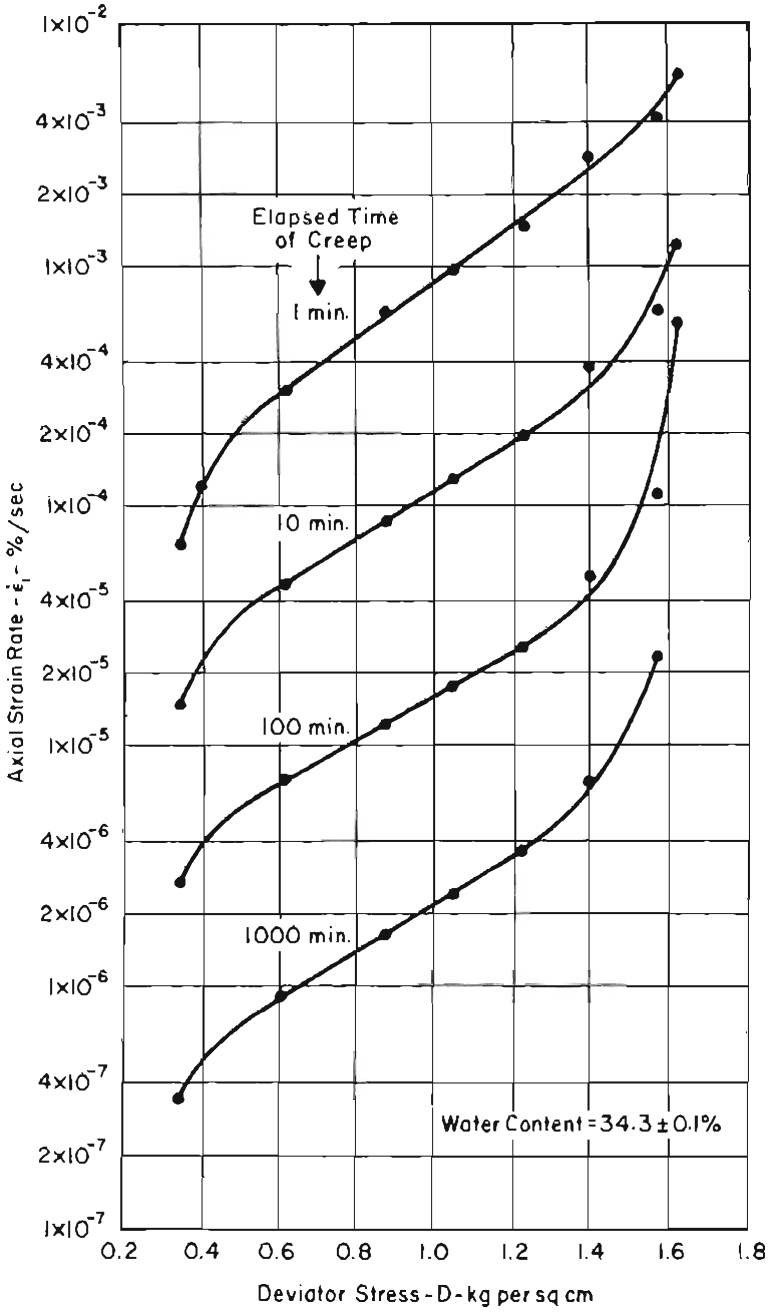

Figure 2.24: Variation of strain rate with deviator stress for undrained creep of remoulded illite, Singh & Mitchell (1968) after Campanella (1965)

In samples that are allowed to creep at a higher load the sample will experience creep rupture. This process involves a sudden increase in the strain rate, as shown by Vaid & Campanella (1977) in Figure 2.26.

Figure 2.27 shows the relationship between the rupture life (time until creep rupture is observed) and the deviator stress normalised with respect to the isotropic consolidation stress q_0. There is a unique relationship independent of consolidation stress showing degradation of rupture load with time. There is also a suggestion of the relationship being asymptotic to an upper yield point lying somewhere around q_0 =

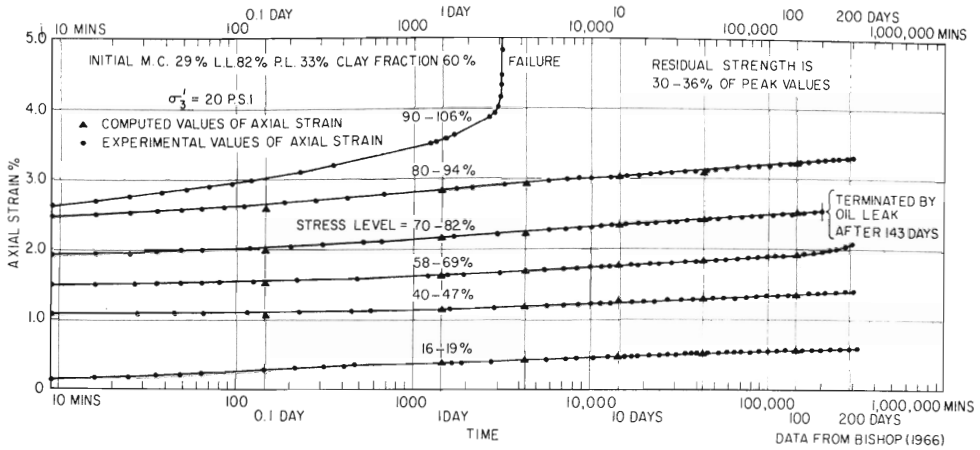

Figure 2.25: Comparison between theoretical and observed creep of London clay, Singh & Mitchell (1968)

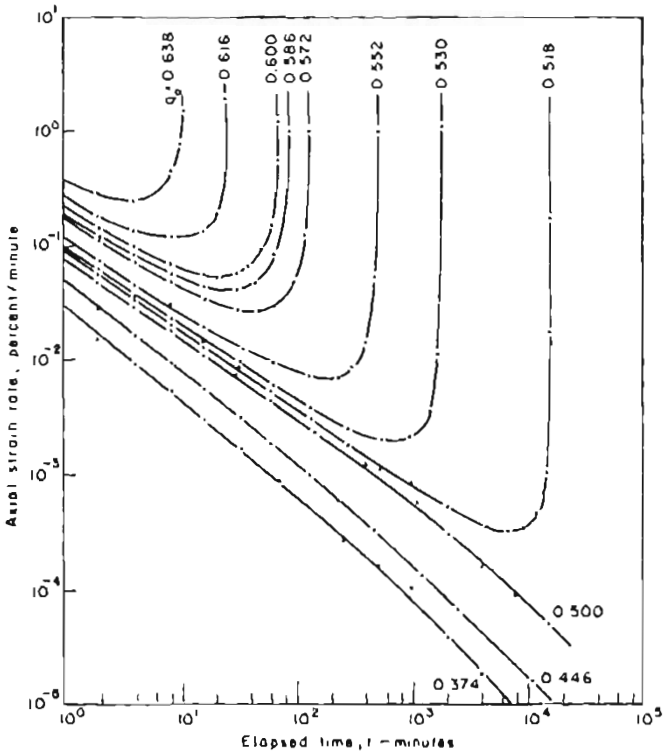

Figure 2.26: Variation of creep rate with time in constant stress creep, Vaid & Campanella (1977)

0.5, below which rupture will not occur.

Vaid & Campanella (1977) also performed tests using constant load creep where the increase in sample area results in decreasing stress. The behaviour was essentially the same as for constant stress creep, but with a slower rate and less deformation as a direct result of the creep stress lowering with time. While samples with q_0 above 0.54 did proceed to rupture, there was no catastrophic collapse of the samples as any acceleration of the creep rate was countered by a decrease in the creep stress.

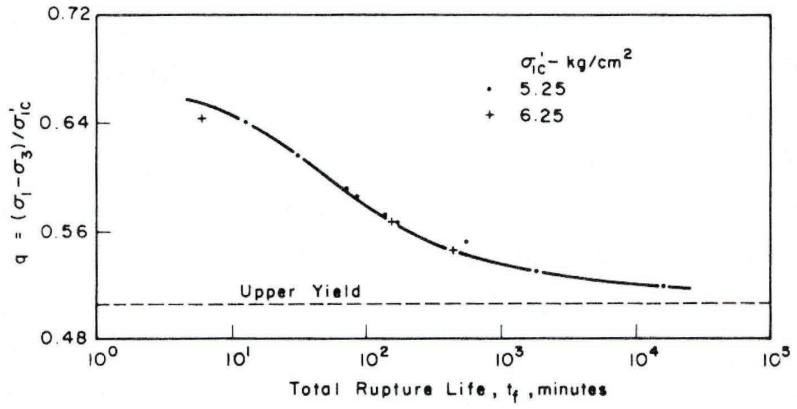

Figure 2.27: Time dependence of undrained strength in constant stress creep, Vaid & Campanella (1977)

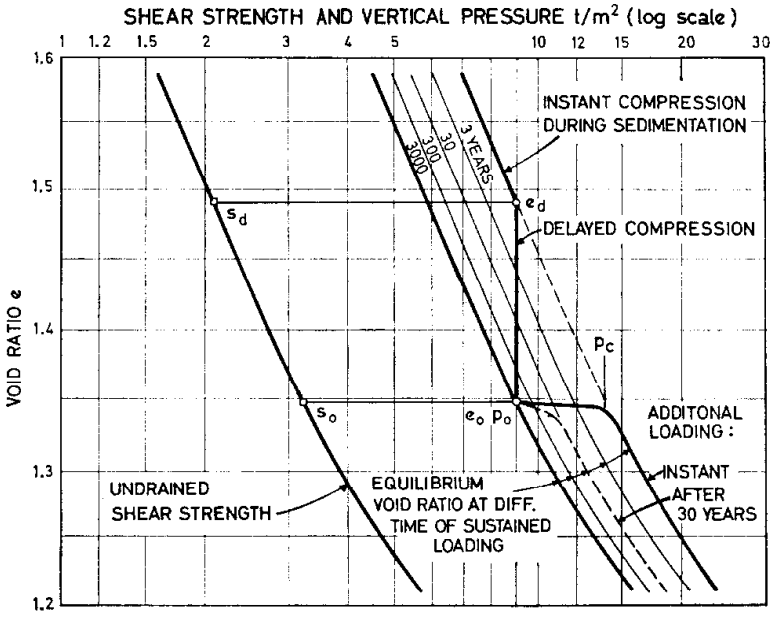

Figure 2.28: Isochrones used for the delayed consolidation model, Bjerrum (1967)

Creep also occurs in the drained conditions of natural samples usually referred to as secondary consolidation, to indicate the consolidation occurring once excess pore water pressure has dissipated. Work on normal consolidated clays by Bjerrum (1967) illustrates the effects of creep termed delayed consolidation on the consolidation behaviour by a series of lines or isochrones in the e-log p' space, as shown in Figure 2.28. The lines have been shown by consolidation tests to be approximately parallel (Taylor 1942), (Crawford 1965). This indicates that the rate of delayed consolidation is about the same throughout a homogeneous deposit or (as the lines are actually slightly curved) decreases slightly with increasing overburden pressure. The system of isochrones thus is assumed to represent a unique void ratio effective stress time relationship. The definition of instant and delayed compression used by Bjerrum (1967) differs from the definition of primary and secondary compression

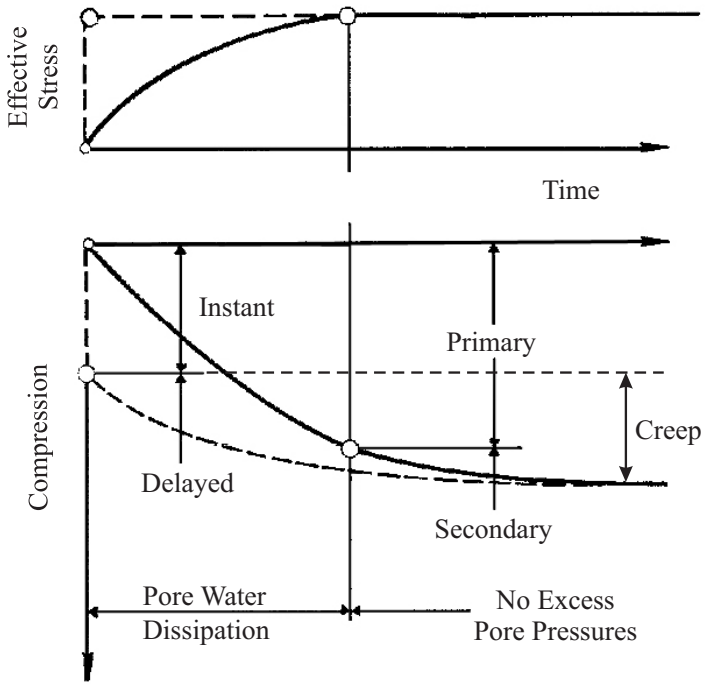

Figure 2.29: Illustration of concept of instant and delayed consolidation, Bjerrum (1967)

normally used. While the conventional definitions divide the consolidation before and after the excess poor pressures have dissipated, the instant and delayed compression are defined as follows:

1. An 'instant compression' which occurred simultaneously with the increase in effective pressure and caused a reduction in void ratio until an equilibrium value was reached, at which the structure effectively supported the overburden pressure.
2. A 'delayed compression' representing the reduction in volume at unchanged effective stresses.

Figure 2.29 shows the two definitions while the dotted line represents the response expected if pore water dissipated immediately and the applied pressure was transferred immediately to the clay structure. This implies that the delayed compression begins when loading occurs and runs in parallel with the instant compression which is retarded by the slow dispersal of excess pore pressures.

Figure 2.28 shows an additional curve representing the undrained shear strength. It was Bjerrum's working hypothesis that by combining this line with the isochrones, the undrained shear strength at any pressure and time after load application can be found. This also allows calculation of the increase in shear strength resulting from the decrease in void ratio due to delayed consolidation.

Due to the reduction in water content during delayed consolidation, the number

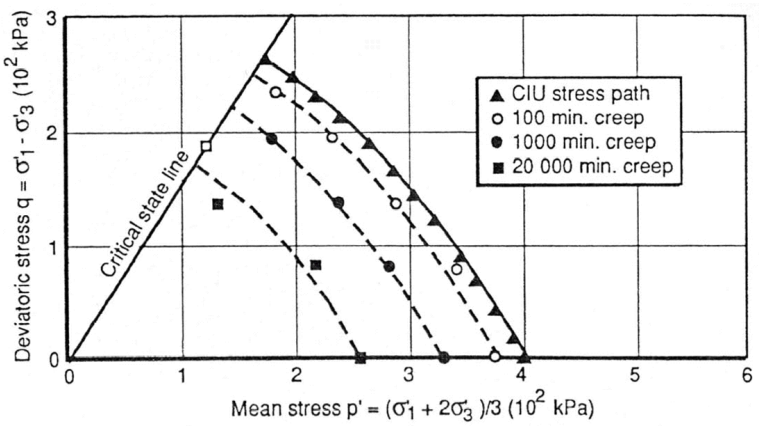

Figure 2.30: Influence of creep time on the yield envelope in triaxial stress space in tests on San Francisco bay mud, Leroueil & Marques (1996) data from, Arulanandan et al. (1971)

of contact points within the clay will increase resulting in an increase in strength. The result is that the clay can support additional load without significant volume change. This gives rise to an apparent critical pressure p_c under which the clay only undergoes minor elastic settlements. For pressures exceeding p_c only the proportion of the load above the critical pressure causes large instant settlements. This reserve resistance increases with time after loading and as the curves are parallel, the critical pressure developed increases linearly with effective overburden pressure.

Results from undrained triaxial creep tests on San Francisco bay mud at different stress levels by Arulanandan et al. (1971) are reported by Leroueil & Marques (1996). This show that the isochrone concept proposed by Bjerrum (1967) in one-dimensional compression could be extended to the entire yield surface in triaxial stress space (Figure 2.30). It can be seen that the entire yield envelope in stress space progressively moves towards smaller stresses with time while maintaining the same shape. To enable the correct interpretation of the time-dependent settlements of soil layers, the effects of creep must be accounted for. To do this it is important to know whether the increased time taken for settlement of thick soil layers causes the strain at the end of primary consolidation (EOP) to increase over that obtained from thin soil sample. There are two hypotheses to explain the relationship between creep and primary consolidation, shown in Figure 2.31:

- Hypotheses A: The effects of creep do not start until after the primary consolidation is complete. Therefore the EOP strain independent of time.
- Hypotheses B: Creep takes effect alongside primary consolidation and so EOP strain is increasing with time.

The isotach concept detailed in 2.4.1 (p 29) implies that hypothesis B is correct. This is supported by Degago et al. (2011) who re-evaluates studies by Aboshi, Mat-

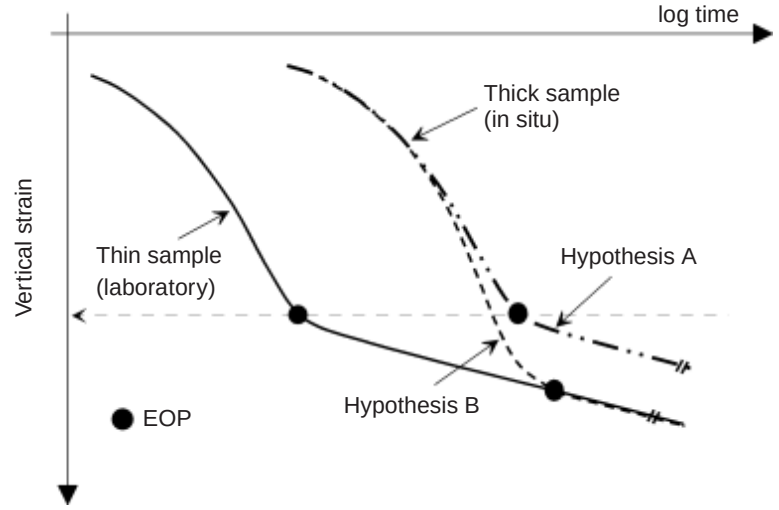

Figure 2.31: Effects of sample thickness according to creep hypotheses A and B, Degago et al. (2011) after Ladd et al. (1977)

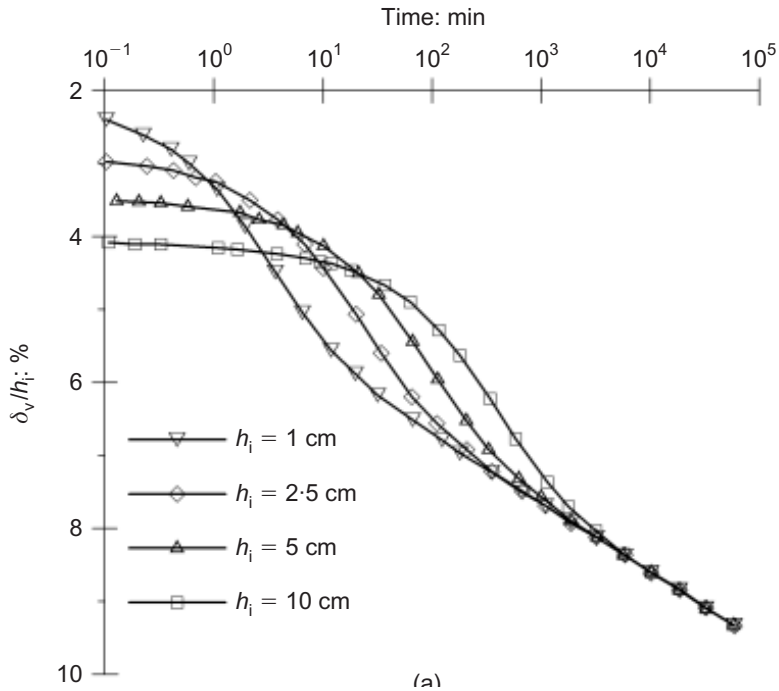

Figure 2.32: Consolidation curves for load increment from 230 to 430 kPa from Konovalov & Bezvolev (2005), expressed as in overall nominal strain by Degago et al. (2011)

suda & Okuda (1973), Imai & Tang (1992) and Konovalov & Bezvolev (2005). When one accounts for the different void ratio- stress history of the samples as they pass through p_c, hypothesis B is shown in all cases. This is achieved by reporting the results in terms of absolute strain change instead of incremental strain change. This is shown in Figure 2.32 for test date from Konovalov & Bezvolev (2005).

The phenomenon of stress relaxation where stress decreases at constant strain may

be considered another form of creep. It is first necessary to define the change in stress as the elastic strain multiplied by the maximum stiffness (Equation 2.10), and the change in total strain as the sum of the change in elastic and plastic strains (Equation 2.11).

$$E_{max} = \frac{\Delta\sigma}{\Delta\varepsilon_e} \tag{2.10}$$

$$\Delta\varepsilon_t = \Delta\varepsilon_e \times \Delta\varepsilon_p \tag{2.11}$$

In a creep test the stress is constant, thus $\Delta\varepsilon_e$ = 0 and $\Delta\varepsilon_t$ = $\Delta\varepsilon_p$. In a stress relaxation test the total strain is constant and it follows that since $\Delta\varepsilon_t$ = 0, $\Delta\varepsilon_e$= -$\Delta\varepsilon_p$. Therefore if continuing plastic strain $\Delta\varepsilon_p$ results in a negative elastic strain $-\Delta\varepsilon_e$, hence σ reduces. It can be deduced that the rate of reduction in stress during stress relaxation is directly linked to the creep potential of the sample at the same state.

2.4 Strain rate dependent behaviour

It is generally accepted that the behaviour of a soil is dependent upon the rate at which it is strained. The dependence of stress-strain behaviour on strain rate is generally measured by shearing different samples at different constant rate of strain (CRS). To eliminate the effects of sample variability, Richardson & Whitman (1963) proposed a method whereby during a single test stepped rate of strain (SRS) is performed in order to investigate the immediate strain rate effects. Curves for a given strain rate could be obtained by interpolation between portions of curves. A comparison of the CRS and SRS methods is shown Figure 2.33. When SRS tests are used several forms of viscous behaviour may be observed, as illustrated in Figure 2.34.

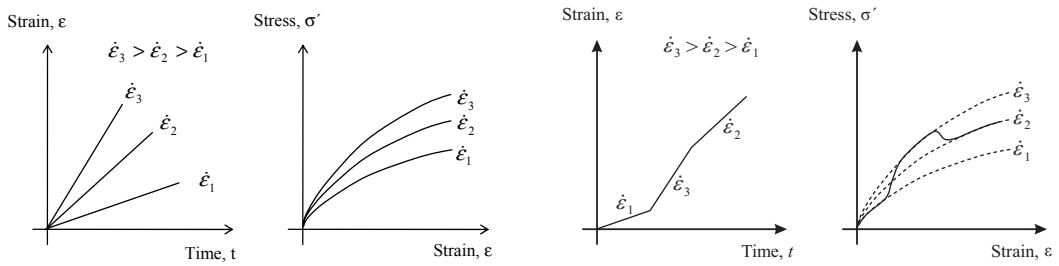

(a) Constant rate of shearing CRS (b) Step-changed rate of shearing SRS

Figure 2.33: Comparison of CRS and SRS tests in triaxial compression, after Sorensen (2006)

2.4.1 Isotach behaviour

The isotach concept describes behaviour where the stress state during both creep and shearing is uniquely defined by the current strain and its strain rate (Leroueil et al. 1985) (Vaid & Campanella 1977). The isotach concept must be valid for the use of SRS test in the manner described above to be applicable. If the concept is not valid, effects of strain rate history, strain level or strain rate acceleration will cause the SRS curves to diverge from CRS curves. There exists a wealth of experimental data to confirm the presence of isotach behaviour. A review of literature by Sorensen (2006) found evidence for isotach behaviour in soft clays (both undisturbed and reconstituted), undisturbed natural stiff clays and soft rocks. As the experimental work is on reconstituted London clay strain rate effects in this type of material are those reviewed.

The rate-dependence of the one-dimensional compression behaviour of Batiscan clay is shown in Figure 2.35 with data from both CRS and SRS tests (Leroueil et al. 1985). It can be seen that the strain rate influences both the normal compression curve and the yield pressure (apparent pre-consolidation pressure), and there appears to be a unique normal compression curve for a given strain rate independent of strain history.

The effects of strain rate behaviour can also be observed in several other test types, such as triaxial compressions and creep. Vaid & Campanella (1977) showed in Figure 2.36 how the increasing strain rate influenced the stress strain response as well as the undrained shear stress. It is noted however that the strain at peak strength does not appear to change.

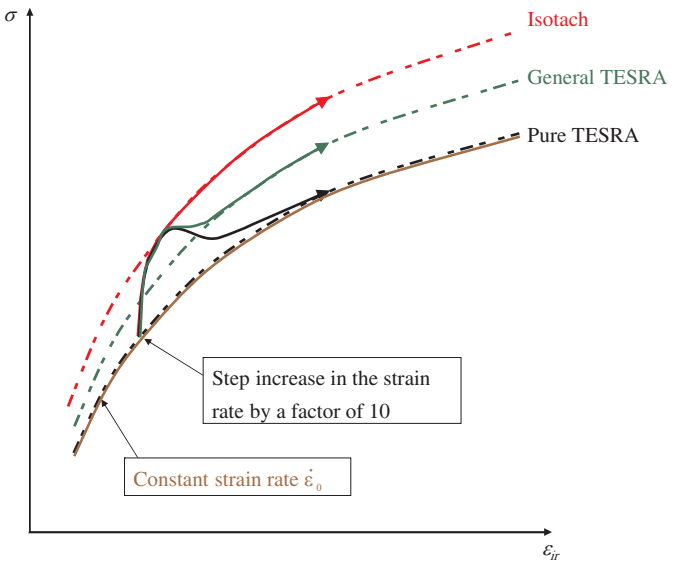

Figure 2.34: Illustration of different viscous effects after Tatsuoka (2007)

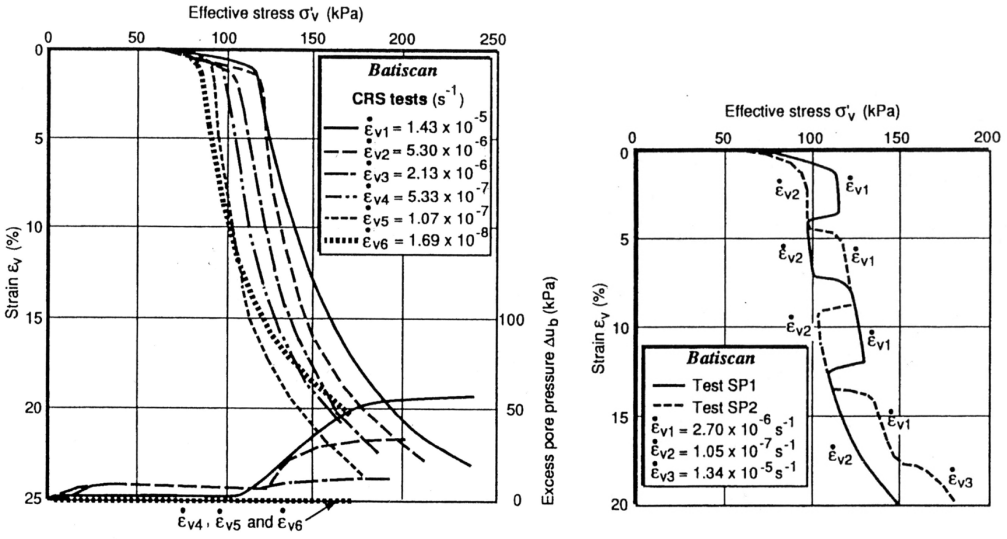

Figure 2.35: Typical CRS and SRS oedometer tests on Batiscan clay, Leroueil et al. (1985)

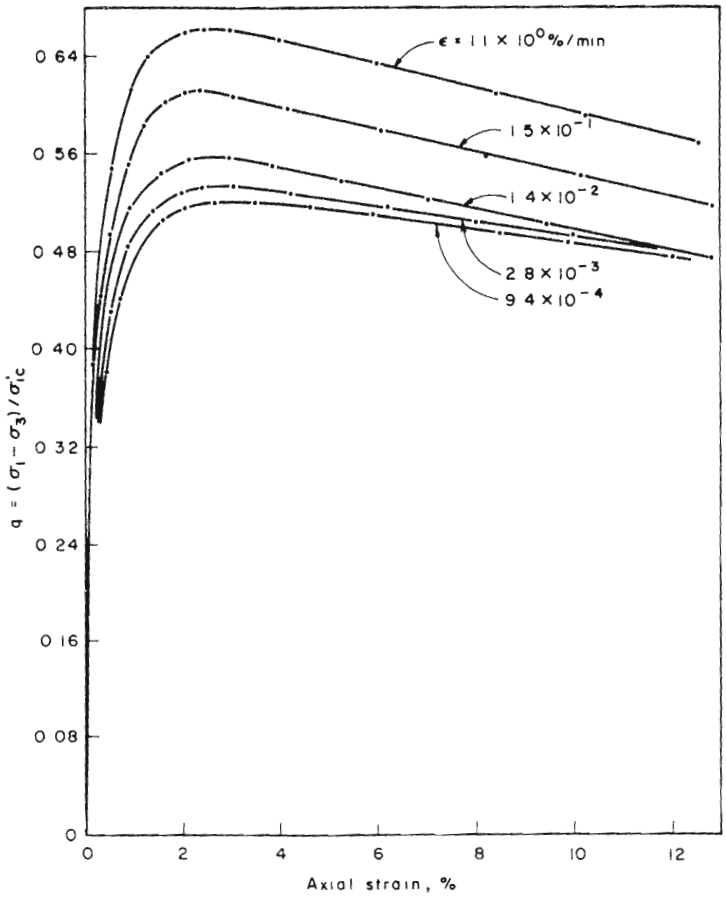

Figure 2.36: Influence of rate of strain on undrained stress-strain behaviour in CRS tests, Vaid & Campanella (1977)

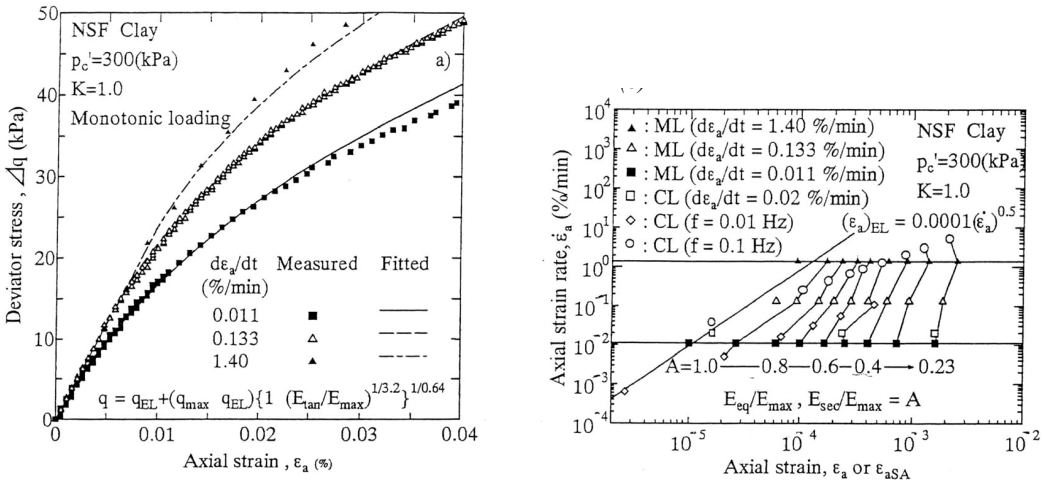

(a) (b)

Figure 2.37: Effect of strain rate on stress-strain relationship in undrained TC tests on NSF-clay, Shibuya et al. (1996)

It is generally accepted that the very small strain stiffness or elastic stiffness is independent of strain rate and only dependent on soil state (Lo Presti, Jamoilkowski, Pallara & Cavallaro (1996); Shibuya et al. (1996); Tatsuoka, Santucci de Magistris, Hayano, Koseki & Momoya (2000)). Results from Shibuya et al. (1996) shown in Figure 2.37 show that the very small strain ($\varepsilon <\approx 0.004\%$) elastic shear stiffness is independent of strain rate over the range $0.01\,\%\,\mathrm{min}^{-1}$ to $1.4\,\%\,\mathrm{min}^{-1}$ equal to $0.7\,\%\,\mathrm{h}^{-1}$ to $84\,\%\,\mathrm{h}^{-1}$. The elastic limit strain at which the elastic stiffness is observed until is however shown to increase with strain rate.

2.4.2 TESRA behaviour

The temporary effect of strain rate acceleration (TESRA) model is relevant to soils which exhibit a temporary effect of change in strain rate which decays with further strain, Tatsuoka et al. (2002). The pure form of this behaviour is observed in granular material such as the two sand studied by Tatsuoka et al. (2002). In these cases the strain rate effects are temporary across the whole strain range. A more generalised version of this behaviour is one where the strain rate effects transitions between an isotach behaviour at low strains and TESRA behaviour at higher strains. This type of behaviour was observed for reconstituted clays by Sorenson et al. (2007) and is shown for reconstituted London clay in Figure 2.38. It was also shown by Tatsuoka et al. (2002) that this general TESRA behaviour was observed in the work of others in several reconstituted clays but not in undisturbed clays.

General TESRA behaviour has been briefly mentioned here as it was at the early stages considered a potentially relevant behaviour for the reconstituted London clay used. TESRA behaviour was thus implemented into the BRICK model as detailed in

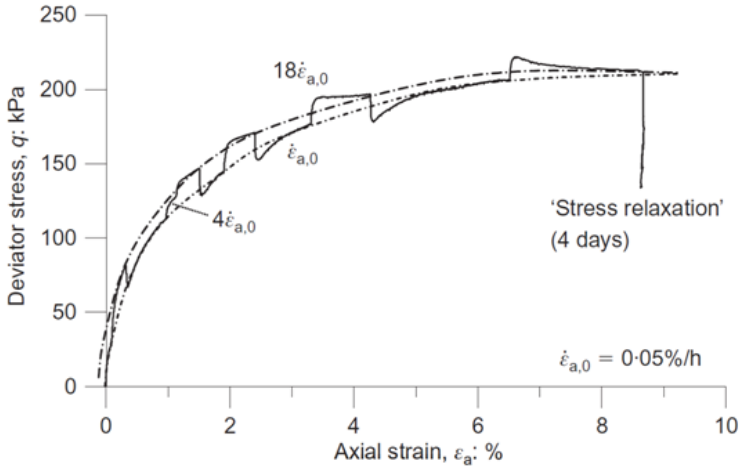

Figure 2.38: An example of general TESRA behaviour in normal consolidated reconstituted London clay, Sorenson et al. (2007)

Section 5.1.7 page 156. On further clarification of the numerical modelling however it was found not to be relevant to required models.

2.5 Geological history of London clay

In this section an overview by Pantelidou & Simpson (2007) of the deposition of London Clay and the removal of overburden is summarised. This allows the long term stress history of the clay deposit to be estimated. This information was used to inform the design of the experimental program. It was also required for the numerical modelling as the BRICK model used required the whole stress history to be simulated to adjust parameters for over consolidation. It should be clarified that this stress history is not considered RSH due to the effects of creep and ageing occurring subsequent to the removal of overburden. An overview of the effects of weathering is also included as a weathered London clay sample was used and the impacts of this needed to be discussed.

2.5.1 Deposition of London clay

London clay is often treated as a uniform material however it contains significant variations in strength, stiffness and consolidation characteristics. These are the result of a variable depositional history when the clay was laid down as a marine formation in the Early Eocene age 44-56 million years ago. The Hampshire and London Basins were formed as a single depositional area at the time. The thickness of the clay is always measured from its base as deposition occurred from the base upwards, as erosion, re-deposition and other geological events have continuously changed the top of the Formation and hence its thickness.

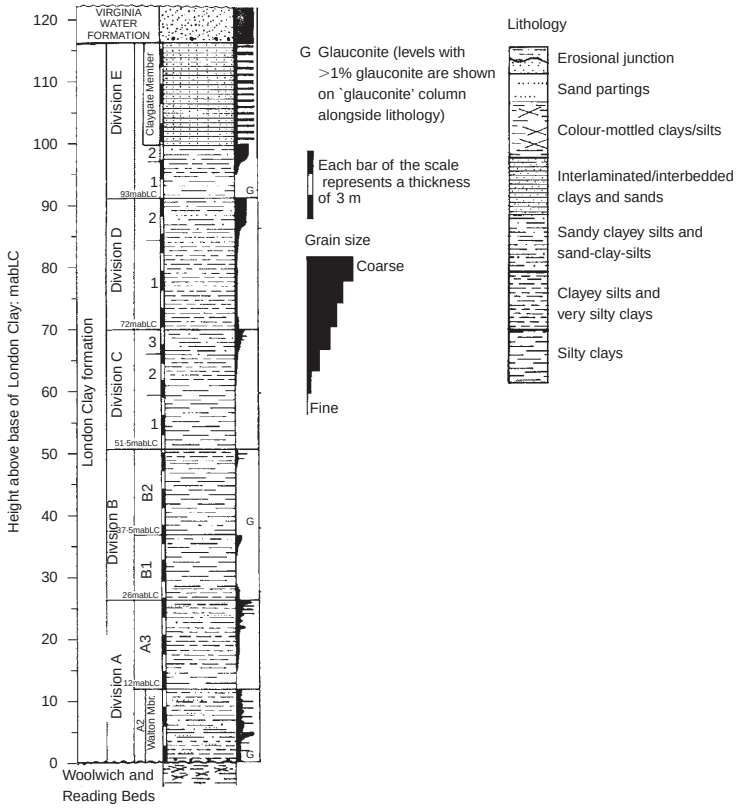

Figure 2.39: Stratigraphic sequence for central London, Pantelidou & Simpson (2007) after King (1981)

The definitive study on the geology of the London clay deposit is considered to be that of King (1981). Five sedimentary cycles (Divisions A to E) are recognised within the London clay; these consist of an initial marine transgression before a shallowing of the sea. This leads to abrupt changes in the coarse-grained content and mineralogy at the boundaries. Typically a cycle starts with a bed containing scattered glauconitic grains and in some cases rounded flint pebbles. A sequence of clays which become progressively more silty and sandy upwards follows. The stratigraphic diagram for central London, Figure 2.39 (King 1981), shows the subdivisions of the clay as well as the general coarsening caused by the swallowing of the sea.

2.5.2 Removal of overburden

In central London much of the London clay deposit has been eroded with its full thickness only present at Hampstead heath. Another succession close to the maximum thickness is seen at Crystal Palace where the Claygate Member caps the hill. For most of central London however subdivisions C, D and E are absent. According to King (1981) the total thickness of the London clay in central London was about $130\,\mathrm{m}$. There existed however a tertiary stratum above the London clay for which

estimation of thickness is more problematic. Table 2.1 gives several of these estimates and $170\,\mathrm{m}$ of overburden is considered to be a reasonable estimate. Using this estimate and the stratigraphy indicated in Figure 2.39 gives a estimate that $250\,\mathrm{m}$ of material has been eroded from the B2 division that exist at foundation depth in central London.

Reference	Location	Thickness of tertiary strata, removed by erosion (m)
Burland, Simpson & St. John (1979)	Central London	170
Skempton & Henkel (1957)	Central London	152-213
Bishop, Webb & Lewin (1965)	Ashford Common: $20\,\mathrm{km}$ west of London	365-400
Smith (1978)	Regents Park	190-396
Skempton (1961)	Bradwell Essex: $80\,\mathrm{km}$ north-east of London	150
Henkel (1957)	North London	150-210

Table 2.1: Estimates of eroded overburden of London clay, (Pantelidou & Simpson 2007)

2.5.3 Weathering

Weathering affects the surface of the London clay deposit. The most readily observed effect is the colour change from blue to brown. This is a result of oxygenated groundwater converting ferrous [Iron (II)] to ferric [Iron(III)] oxide (Gasparre 2005). There is also a removal of pyrite and dissolution of any calcium carbonate cement. The chemical change is accompanied by physical weathering such as desiccation (causing rough sub vertical discontinuities) at shallow depths and ground freezing at large depths. Strong weathering where soil has a granulated fragmented texture is observed to depths of $1.5\,\mathrm{m}$. Below 3 to $4\,\mathrm{m}$ however there is little evidence of weathering aside from the colour change (Hight, McMillan, Powell, Jardine & Allenou 2003).

Chandler & Apted (1988) performed a detailed study on the effects of weathering on London clay from a site in South Ockendon, Essex. At that site unweathered clay was found below $5\,\mathrm{m}$ (Zone I) overlaid by and increasingly weathered clay (Zones II to IV). Studies on the chemical changes in Table 2.2 show only one significant change in the leaching of carbonate from the more weathered areas. There was no

Weathering zone	CO_3^{2-} (%)	Fe (%)	Ca (%)	Mg (%)	Si (%)	Al (%)	Ti (ppm)
IV	0.1	4.0	1.0	1.9	36	13	5500
III	0.2	3.9	1.4	2.2	35	15	6100
II	0.6	5.2	1.2	3.1	38	18	6400
I	1.0	3.2	1.2	2.4	32	14	5100

Table 2.2: Chemical composition of the London clay at South Ockendon (Chandler & Apted 1988)

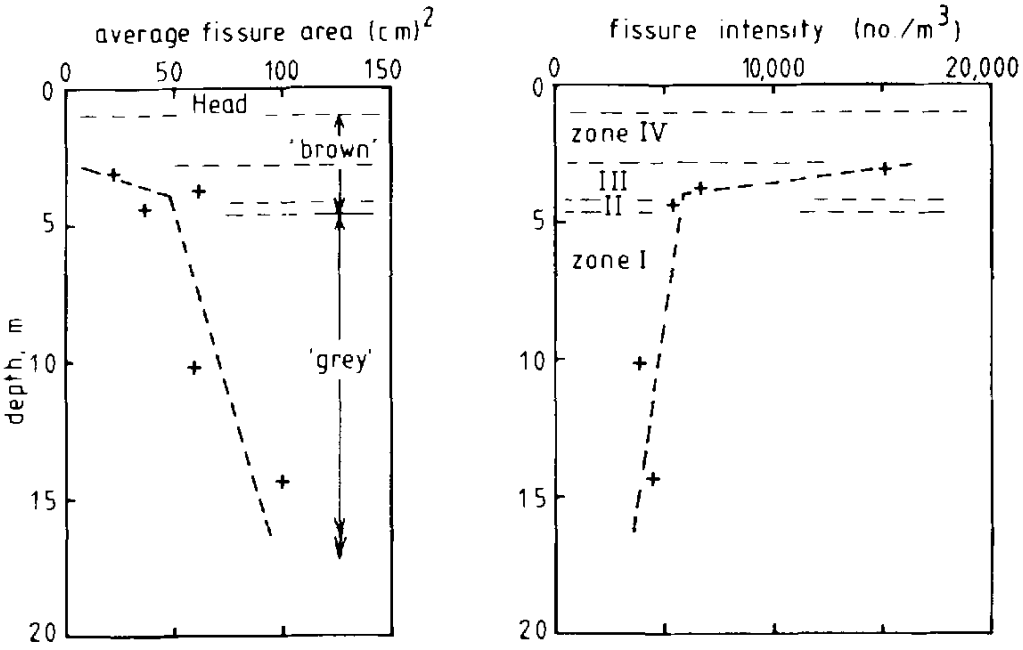

Figure 2.40: Fissuring in the London clay, South Ockendon (Chandler & Apted 1988)

significant change in the clay mineralogy or index properties.

The physical effect of weathering resulted in a dramatically increased fissuring in the weathered clay, as shown in Figure 2.40. Results of undrained triaxial tests on undisturbed $100\,\mathrm{mm}$ samples shown in Figure 2.41 have shown that, with an assumed ϕ' = 20° Zone 1 samples show a cohesion c'=28 kPa while the heavily weathered samples have c' = 18 kPa. It is also suggested that weathering results in a $4\,\%$ increase in water content, resulting in a reduction of the apparent OCR from 38 to 22. It is apparent that the physical effects of weathering are more pronounced than the chemical and mineralogical changes and are therefore likely to account for the majority of the observed behaviour difference.

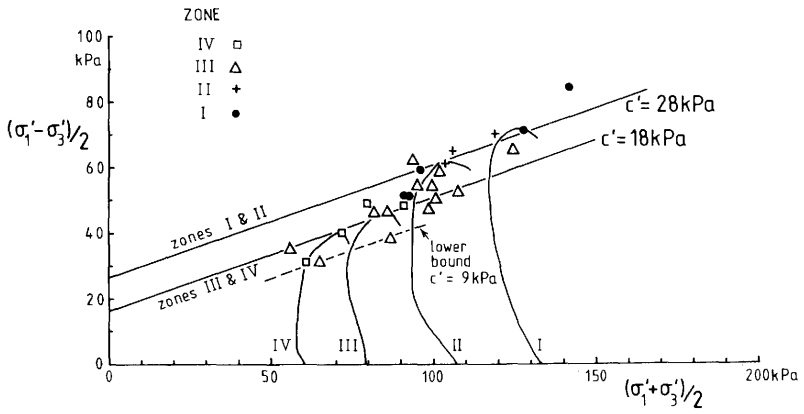

Figure 2.41: Undrained triaxial compression tests, London Clay, South Ockendon (Chandler & Apted 1988)

2.6 Measuring small strains

2.6.1 Error caused by standard external measurement

The use of external measurements for small strains is considered unreliable due to a number of factors that can cause an error between the measured and actual strain. Some of the common sources of error were examined by Baldi et al. (1988) given in Table 2.42 and illustrated in Figure 2.42.

Seating errors caused by gaps closing between:	Ram or internal load cell and top platen Platers and porous stones
Alignment errors resulting from equipment and specimen non-conformity specifically:	Porous stones of non-uniform thickness Nonverticality and eccentricity of loading ram Nonhorizontality of platen surfaces Tilt of specimen
Bedding errors caused by surface irregularity and poor fit at the interfaces between the specimen and porous stone	
Compliance errors which may occur because:	The tie bars extend and cause relative displacements of the top of the cell with respect to the piston The internal load cell deflects The lubricant is compressed in systems using lubricated ends The porous paper is compressed

Table 2.3: Sources of errors in conventional deformation measurement, (Baldi et al. 1988)

A study by Lo Presti et al. (1993) used sensors positioned at different points in

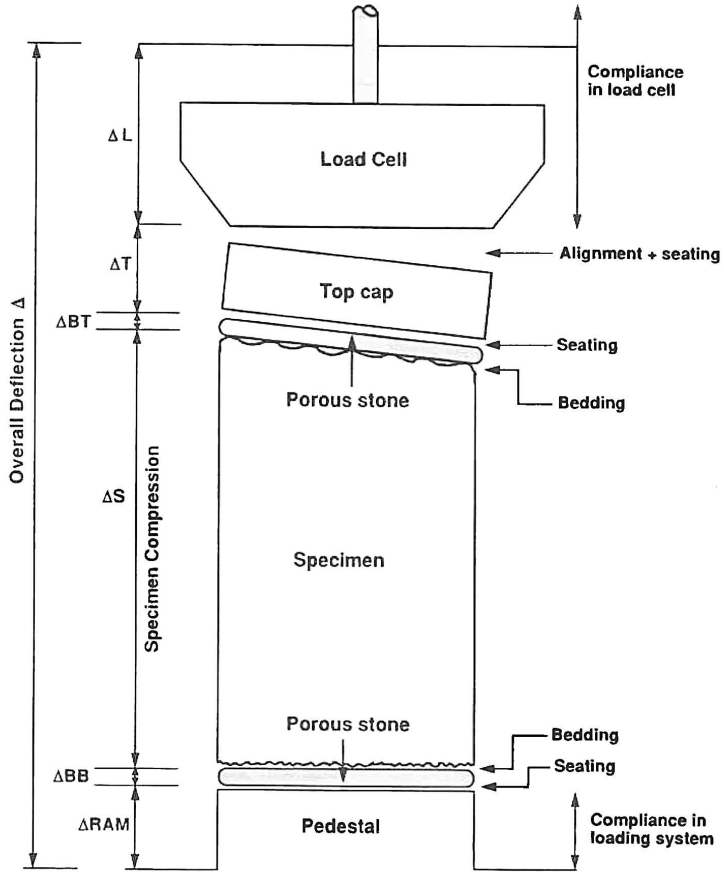

Figure 2.42: Sources of error in external strain measurement, Scholey et al. (1995) after Baldi et al. (1988)

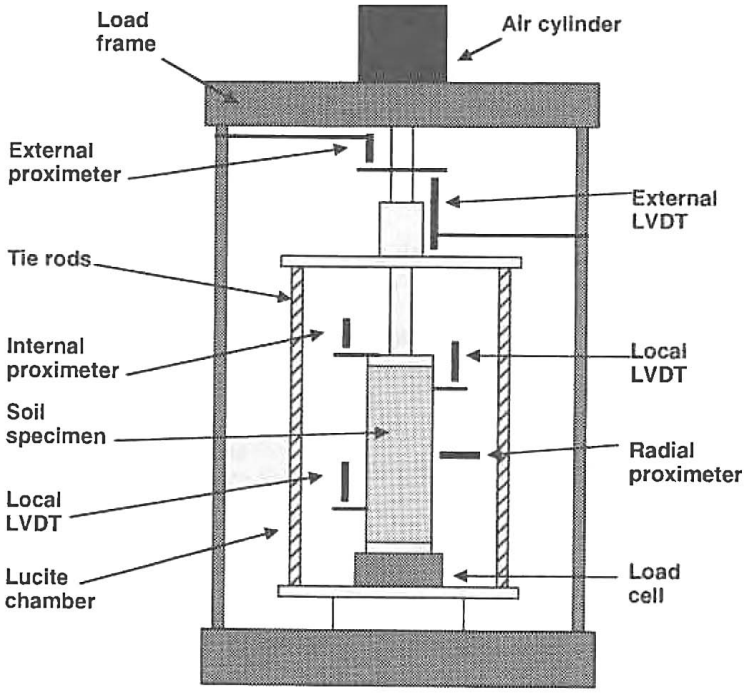

Figure 2.43: Location of strain measurement systems to quantify errors in external measurement, Scholey et al. (1995) after Lo Presti et al. (1993)

the triaxial system (as shown in Figure 2.43) to quantify the significance of the different sources of error by comparison between local and external measurement. The sensors used were:

- Local strain linear variable differential transformers (LVDTs) attached to sample, unaffected by errors.
- High resolution non-contacting proximity transducer measured between pedestal and top cap, affected by bedding and seating errors.
- Non-contacting proximity transducer and conventional inductive displacement transducers (IDTs) mounted externally, affected by all error sources.

The results of the study gave the following quantifications on the potential errors in conventional external strain measurement:

- Strains between top cap and pedestal 10 to $15\,\%$ larger than local LVDTs and conventional external strains 20 to $30\,\%$ larger.
- The conventional IDT was unreliable at strains less than $0.1\,\%$ because of resolution. External LVDTs were unable to resolve strains less than 0.005 to $0.01\,\%$.
- System compliance, bedding and seating errors were present for a strain range of 0.001 to $0.01\,\%$. Within this range they were seen to increase with increasing stress.
- Bedding and seating errors increase with grain size so will be less for clays.

It was also noted that due to the effects of end restraint, the local measured radial strain would differ from that interpreted from local axial strain and sample volume measurement.

2.6.2 Requirements for small-strain measuring equipment

The axial and radial strain must be measured locally to avoid the errors associated with external strain measurement. This is normally achieved by a combination of diametrically opposed axial strain measurements of the central third of the sample, and a diametric measurement at the centre. A good quality local sensor has the following features:

- Accuracy of at least $1 \times 10^{-3}\,\%$ or about $0.7\,\mu\mathrm{m}$ for axial strain measurement of the central third of a $100\,\mathrm{mm}$ diameter sample.
- Coupled axial and radial deformations without loss of accuracy.
- No interference with soil behaviour
- Capable of operating under different stress paths
- Capable of submersion and operating under typical cell pressures.
- For cyclic tests, must have low hysteresis and rapid response.

Several types of transducers were considered for measuring the strain of the sample. Inclinometer level based systems and local deformation transducers based on bending of phosphor bronze strips where discounted as they did not provide a radial strain measurement. Proximity transducers where considered to require too large a mounting to perform axial measurements.
Both hall effect transducers and LVDTs where found to stratify all the practical considerations. The linear variable differential transformers (LVDTs) had a resolution of ± 0.0001-$0.001\,\%$ compared to $\pm 0.002\,\%$ for hall effect transducers (Scholey et al. 1995). This, accompanied by improved linearity and reduced electrical noise, led to the selection of LVDTs for strain measurement.

2.7 Summary

This chapter has presented a review of the literature as it pertains to work presented in the rest of the thesis. The main topic of interest is that of RSH. This phenomenon is related to the widely demonstrated concept of non-linear soil stiffness at small strain. Here the soil shear stiffness varies against the logarithm of shear strain to form a s-shaped stiffness curve from the linear elastic behaviour described by G_0 at very small strain to a low stiffness after typical testing strains. It is in this small strain region where some authors have observed RSH effects where shear stiffness increases with the angle of a rotation in the stress path.
The literature is divided on existence of the RSH effect. The short approach path long creep period test of Clayton & Heymann (2001) did not see a RSH effect while the long approach path short creep period test of Atkinson et al. (1990) did. This difference is explained by Gasparre et al. (2007) who concluded that an extended creep period could erase RSH effects for tests with short approach paths but not for longer approach paths. While the general premise of trends proposed are accepted the limited data set means there is need for further study on the effects of creep and approach path length on the RSH effect. The suggestion by Gasparre et al. (2007) that the crossing of the Y_2 yield surface is key to the influence of approach path length is also questioned as a smooth trend is expected not a sharp change in behaviour.
The kinematic strain hardening plasticity framework was presented to illustrate the concept of kinematic yield surfaces and explain their definitions when used. Models of this type produce RSH effects but were discounted in favour of the BRICK model which more accurately models the small strain stiffness degradation.
For the purposes of test setup the geological history of London clay was studied. Several sources where consulted to provide an estimate of the previous overburden stress. The effects of weathering on London clay were found to be severe near the

surface. In this area physical effects of weathering were present. At greater depth only a colour change was observed. Despite there being no direct comparative study, it was however possible to conclude that reconstituted weathered London clay where the physical effects of weathering are not present would behave like unweathered London clay.

When reviewing literature on the technical aspects of achieving a small strain measurement the need for using locally mounted strain measurement was widely supported as a method to eliminate the errors associated with external instruments. As all errors associated with external measurements were eliminated by local transducers it was not considered necessary to consult widely to fix their exact magnitude. The literature on transducer selection is presented as a single comparative snapshot of the benefits and limitations of the transducers. This illustrates how LVDTs were selected for use in the experimental work.

3

Experimental methodology and data analysis

3.1 Introduction

The experimental work performed as part of this research project was required for two purposes. Firstly it was a self-contained investigation into the effects of approach path length and creep on RSH effects in London clay. Secondly the data was required to provide parameters for use in the BRICK model, and a series of fully quantified stress paths to compare to brick predictions. .

The test programme was developed in order to meet the flowing criteria required to show the effects of creep and approach path on the RSH effect:

- The non-linearity of the stiffness response needed to be captured.
- Small strains needed to be captured.
- Stress paths needed to be performed in compression and extension.
- A repeatable starting stress state and consistent stress history was required for samples.
- Creep needed to be performed under isotropic stress conditions.

To ensure the repeatability of specimens and provide a quantifiable stress history for BRICK modelling, samples where consolidated one dimensionally from a clay slurry. This produced $100\,\mathrm{mm}$ diameter samples that only required end trimming to be used in a stress path triaxial apparatus. Small strain accuracy was accomplished by using locally mounted strain transducers. Although the samples were produced for cross-comparison, the time required to produce samples necessitated that the maximum amount of data be gathered from each sample. As such a multi-stage testing approach was developed with repeats used to test the efficacy of the multi-stage approach.

In this chapter the sample preparation and testing methods are described, along with the computer controlled one dimensional consolidation, and stress path triaxial apparatus used respectively. Detail is given on the data acquisition, transducers used

and calibration. Where appropriate problems with the apparatus and their solutions will be discussed.

3.2 Testing methodology

3.2.1 Scope of experimental work

The scope of this work encompasses two areas, quantification of soil parameters for the BRICK model and soil characterisation, and an investigation into what affects the magnitude of the recent stress history effect. The purpose of characterising the soil is to allow for comparative work and numerical modelling however the purpose of the RSH investigation requires some discussion. As discussed in Section 2.2.3 research by Atkinson et al. (1990) and Clayton & Heymann (2001) on the RSH effect in London clay gave differing results. Work by Gasparre et al. (2007) explains the differing outcomes as the result of differing creep durations and approach path lengths allowed in each test. From the results of three tests the following conclusions are reached:

1. Creep can erase RSH effect if the approach path remains within the original Y_2 yield surface.
2. A RSH effect exists at all levels of creep when the approach path crosses the Y_2 surface.

The limited data set used to make these conclusions provides the scope for further study. Figure 3.1 combines the conclusions into a surface that predicts the RSH effect for any combination of approach length and the duration of creep allowed between the approach and shear probe. The axis of RSH effect indicates the difference in small strain stiffness between paths following a $180°$ or $0°$ stress path rotation. The lower end of the axis indicates identical stiffness degradation curves while higher values indicate stiffness after $180°$ rotation is more than that after $0°$. When the approach path remains within the Y_2 yield surface the relationship between creep time and RSH effect (shown as a thick dashed line in Figure 3.1) is based on only two data points, leaving room for further investigation. More problematic is the assertion on the effect of approach path length (shown as a thick dotted line in Figure 3.1). The observation of a RSH effect with a path crossing Y_2 and none when it does not provides no actual indication of the trend. More data points are required on the approach path axis to draw conclusions as to the effect if any of the Y_2 yield surface. The other point of investigation is on the implied point of no creep and a long approach path. If creep has no effect with an approach path crossing Y_2 the RSH effect here would be the same as that with creep. If however creep continues to have an effect for paths above Y_2 the no creep result should show

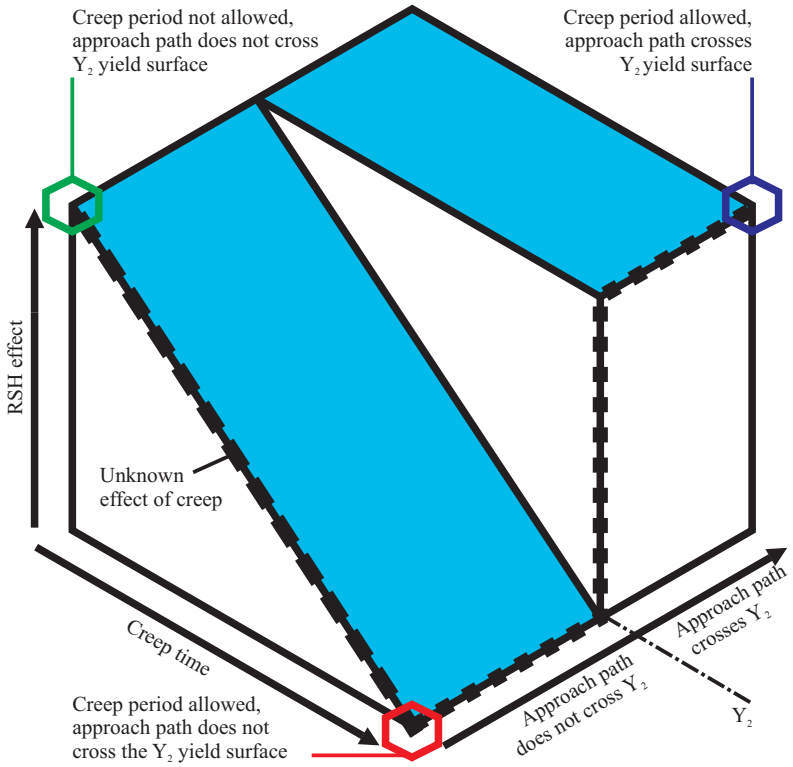

Figure 3.1: Relationship between RSH effect, creep and approach path length by extrapolation from conclusions of Gasparre et al. (2007)

a greater RSH effect: this is therefore another key point to investigate.

3.2.2 Testing strategy

Classification tests

The following set of routine soil tests were performed to give a description of the soil being tested:

- LL and PL tests
- Particle size analyses
- Three consolidated undrained tests on full size specimens to establish failure criteria for the consolidated soil sample
- Undrained triaxial tests on 3 vertical and 2 horizontal $38\,\mathrm{mm}$ sub samples from a $100\,\mathrm{mm}$ sample to investigate the undrained strength and the anisotropy of the one dimensionally consolidated sample
- Oedometer tests on 7 sub samples to establish:
  - Coefficient of consolidation c_v
  - Volume compressibility coefficient m_v
  - Permeability coefficient k
  - C_c,N, and C_r from ν versus ln σ'_v plots to describe consolidation and

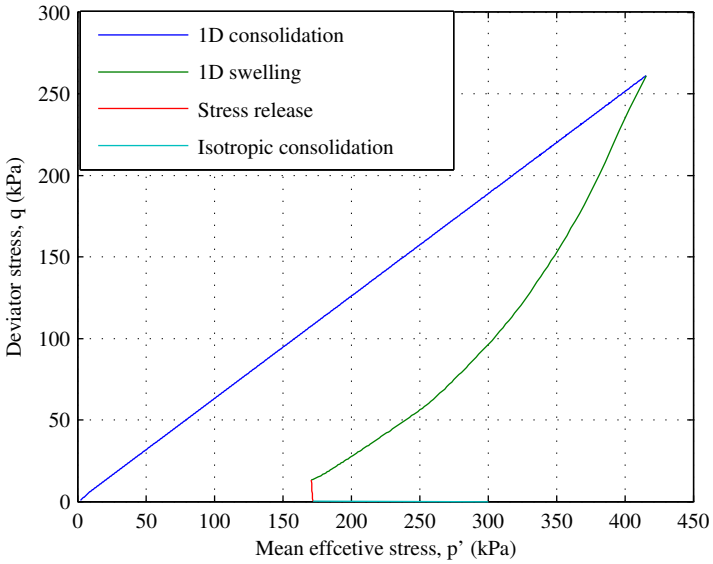

Figure 3.2: Illustration of consolidation path used

swelling behaviour and provide key inputs for the Brick routine.

– The actual preconsolidation stress in the samples for comparison against the maximum applied preconsolidation pressure. This was done as the low permeability of the clay prevented the full distribution of excess pore pressure evenly during the sample preparation.

Recent stress history tests

The method of assessing the effects of RSH was derived from that followed by Atkinson et al. (1990) but expanded the number of creep durations and approach path lengths studied in the previous work. The samples used were produced by one dimensional consolidateion under an applied vertical stress σ_v = 2800 kPa by the method described in Section 3.4.1 (page 66).

The precise effective stress path taken prior to isotropic consolidation is unknown as neither the total radial stress or pore water pressure could be accurately measured. Figure 3.2 gives a indication of the consolidation stress path based on a BRICK simulation (details Section 6.3 page 208) of the 1D consolidation using the maximum effective stress p'_m obtained by the odometer test (Section 4.5.1 Page 118) and p' at the end of 1D consolidation is taken as the mean initial effective stress measured at the start of the triaxial test (see Section 4.2.2 Page 98).

When placed in the triaxial cell the testing method, illustrated in Figure 3.3, was to consolidate the sample isotropically to a confining stress of 300 kPa with no deviator stress. This isotropic consolidation stress level was chosen so long deviatoric stress paths could be performed without approaching failure. This was dictated by the 700 kPa pressure limit of the triaxial cell and the need to maintain a 400 kPa

back pressure to keep any air in the pore fluid in solution. Following the conclusion of consolidation, the sample was kept at a constant p' value to avoid the cross linking of the shear and bulk modules. The test consists of several stages as follows:

1. An approach path will increase the deviator stress to some predefined limit before returning to $0\,\mathrm{kPa}$.
2. A creep period at $q = 0\,\mathrm{kPa}$ for a predefined amount of time.
3. A shear probe to take the deviator stress to a higher level than the approach path.
4. A reset stage to return the deviator stress to $0\,\mathrm{kPa}$.
5. A period of creep (5 days) to minimise the effects of multi-stage testing.
6. An approach path to the same stress as the first but in the opposite direction.
7. A creep period at $q = 0\,\mathrm{kPa}$ for a predefined amount of time.
8. A shear probe to take the deviator stress to a higher level than the approach path.

The recent stress history effect is evaluated by comparing the stiffness of the two shear probes (4 and 8), which have opposing high and low stress path rotation angles. The approach paths themselves are not intended to provide stiffness degradation curves. Consequently no effort has been made to achieve interesting comparisons and the process of docking and data acquisition was optimised for speed rather than the quality of small strain measurements required to obtain a stiffness degradation curve. The investigations into the effects of creep and approach path length on the RSH effect consisted of performing a series of these RSH tests at different approach path lengths and creep durations, as illustrated in Figure 3.4. The precise values to use for approach path length and creep period were selected following a series of tests to establish the soil behaviour.

Tests S1 and S2, shear in compression and extension respectively, established an approach path length of $60\,\mathrm{kPa}$, limited by a yield in extension and a shear probe of $80\,\mathrm{kPa}$ limited by yield in compression (details in Section 4.6.1). The effect of creep was shown by tests C1 and C2, constant strain rate stress paths to q=$60\,\mathrm{kPa}$ and back followed by extended period of creep. The results of these tests (detailed in Section 4.6.2) gave a range of creep between $3\,\mathrm{h}$ and $5\,\mathrm{d}$ for the investigation of creep on short approach paths. As the effect of approach path was to be studied at a creep level that showed no RSH effect for short paths, the RC (RSH Investigations on effect of creep) series of tests on the effect of creep was run first with the results informing the creep duration to use for the RA (RSH Investigations on effect of approach path length) series on the effect of approach path. A flowchart explaining how each set of test results fed into the next is shown in Figure 3.5.

The multi-stage testing employed has the disadvantage of inducing a greater degree of sample disturbance and stress history complexity to the second shear probe than

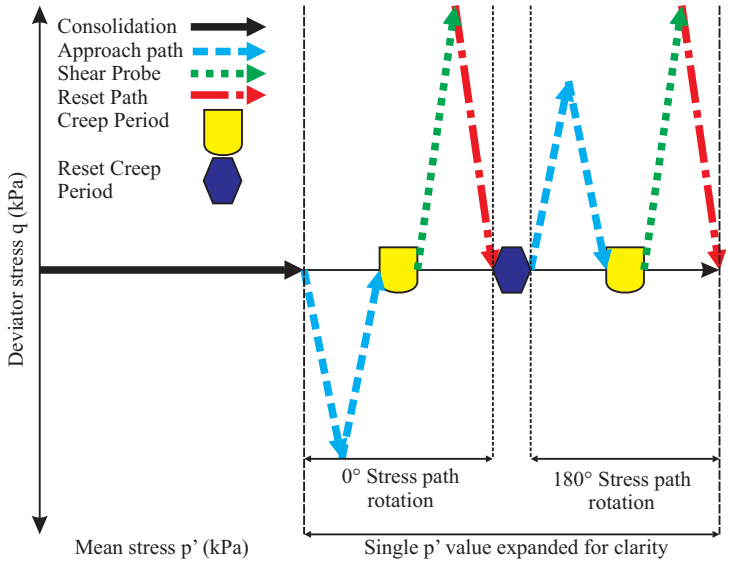

Figure 3.3: Recent stress history effect test 0° rotation first

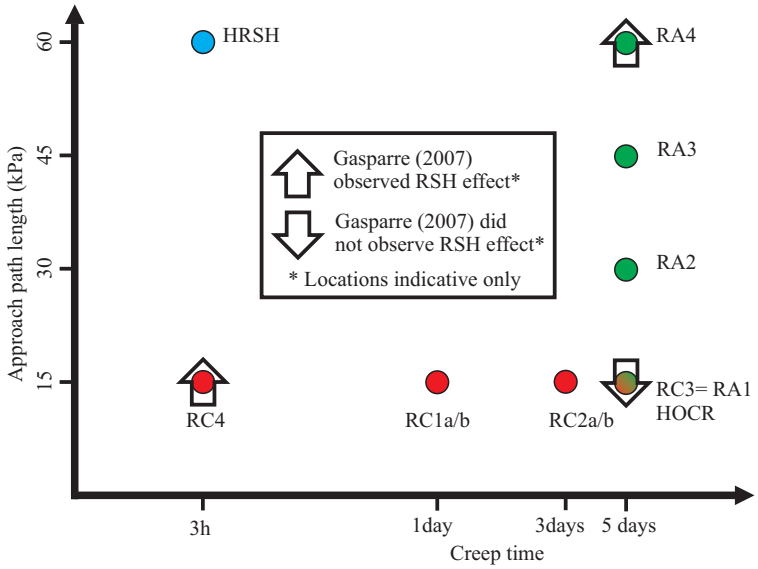

Figure 3.4: Points RSH effects are investigated by comparison of small strain stiffness curves

the first. Ideally comparison would be made between identical samples comparing the effect of 0° and 180° stress path rotations the first shear probe. The use of multi-stage testing however eliminates repetition of the long (6 week) sample creation process and effects of sample variability. As a compromise tests were performed in two different orders. Tests were performed on one sample with a 0° rotation followed by an 180° rotation and on another by a 180° followed by 0° rotation. This allows a comparison of both the RSH effect on the virgin soil and the comparison of RSH effect on the same sample. The comparison opportunities available are detailed in Table 3.1 and show how the validity of multi stage testing may be

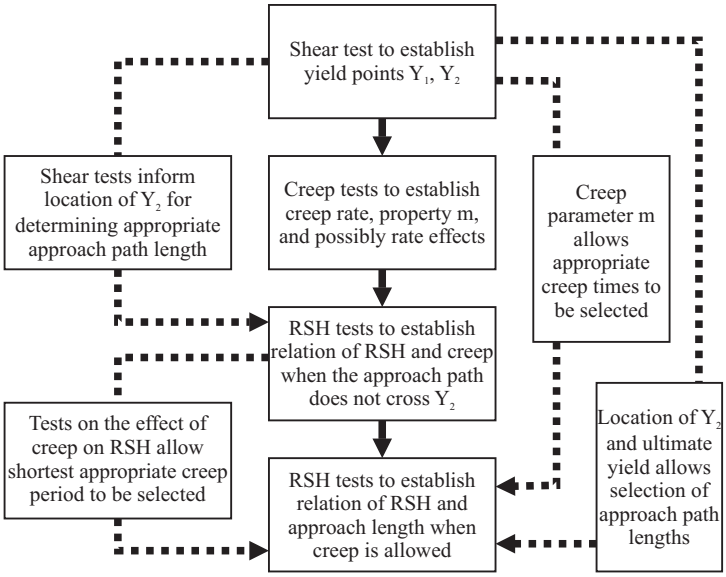

Figure 3.5: Testing flow chart

	Path 2 θ = 180°	Path 1 θ = 180°	Path 2 θ = 0°
Path 1 θ = 0°	RSH effect multi stage with 0° first	RSH effect comparison of virgin soils	Effect of previous test stage on 0° rotation path.
Path 2 θ = 180°		Effect of previous test stage on 180° rotation path.	RSH effect comparison second stage soils
Path 1 θ = 180°			RSH effect multi stage with 180° first

Table 3.1: Multi stage comparisons

assessed.

3.2.3 Testing program

The preliminary tests required for the RSH parameters where performed as detailed in Table 3.2. The preliminary results informed the location of the tests in the main test program which is detailed in Table 3.3 and illustrated in Figure 3.4. Test RC3 in the effect of creep series is also considered test RA1 in the effect of approach path length series. Test HOCR is a repeat of test RC3 performed with a higher OCR. Running concurrently to the main test program was a series of oedometer tests (Table 3.4) and quick undrained triaxial tests (Table 3.5).

Test / sample name	Test Description
S1	Shear in constant p undrained compression from standard start point
S2	Shear in constant p undrained extension from standard start point
C1	Creep at q = 0 kPa p' =300 kPa following a constant p,
C2	constant strain rate stress path from q=60 kPa

Table 3.2: RSH preliminary tests

	First approach path length (APL) (kPa)[a]	Creep period
RC1a	-15	1.5 days
RC1b	15	1.5 days
RC2a	15	3 days
RC2b	-15	3 days
RA1/ RC3	15	5 days
RC4	15	3 hours
RA2	30	5 days
RA3	45	5 days
RA4	60	5 days
HOCR	15	5 days
HRSH	60	3 hours

Table 3.3: Recent stress history tests

[a]Positive values result in a 180° rotation first. Negative values result in a 0° rotation first.

Test	Sample	Sample location	Comment
O1T	O1	Top	Low stress sample to establish soil consolidation characteristics
O1B		Base	
O2B	O2	Base	Used to establish the spacial distribution of the consolidation
O2M		Middle	
O2T		Top	
S1B	S1	Base	Performed on excess trimmed from the end of the sample
S1T		Top	

Table 3.4: Oedometer tests

Test	Sub sample location	Confining pressure (kPa)
V1	38 mm vertical sub-samples from lower half	400
V2		400
V3		500
H1	38 mm sample from top half.	400
H2	Sample at right angles to H1.	400

Table 3.5: Quick undrained triaxial tests on sample O2

3.3 Apparatus

3.3.1 Sample consolidation apparatus

One dimensional consolidation of a clay slurry was performed using the apparatus shown in Figure 3.6 and schematically in Figure 3.7. A $200\,\mathrm{mm}$ diameter pneumatic ram with a $600\,\mathrm{mm}$ stroke regulated by a VJ Tech VJT2270 Automatic Pressure Controller was used to provide a $2800\,\mathrm{kPa}$ axial pressure to a $100\,\mathrm{mm}$ sample consolidation cylinder. The cylinder barrel was formed from a $600\,\mathrm{mm}$ high $100\,\mathrm{mm}$ $+0.054\,\mathrm{mm}$ diameter tube with a polished finish. The high quality of the finish allowed for sample creation with a dimensional tolerance greater than the standard U100 sampling tubes, used to recover undisturbed samples from bore holes which are only nominally $100\,\mathrm{mm}$ in diameter. The quality of the cylinder barrel allows an o-ring restrained under the cylinder barrel and two placed on the $99\,\mathrm{mm}$ diameter piston to resist the full fluid pressure in the tube. This ensures all drainage goes though the sintered bronze disks to the drainage channels, shown for the moving piston at the top of Figure 3.7. Measurement of the total pressure at each end of the sample was provided by PC18 thick film ceramic pressure gauges manufactured by TMS Ltd with a $50\,\mathrm{bar}$ rating. These were secured with epoxy resin into mountings placed at the centre of the base and piston to from a plane surface with the porous disks. In later tests pore pressure was measured at $110\,\mathrm{mm}$ above the porous disk (the mid height of the average completed sample) by SICK PBT pressure transducers with a $100\,\mathrm{bar}$ pressure capacity. Measurement of the vertical displacement was achieved using draw wire transducers.

3.3.2 Calibration of sample consolidation apparatus

The consolidation of the sample was monitored in three ways: the displacement, the pore pressure, and an earth pressure measurement. It was also possible to approximate the load applied to the sample through the air pressure applied to the piston.

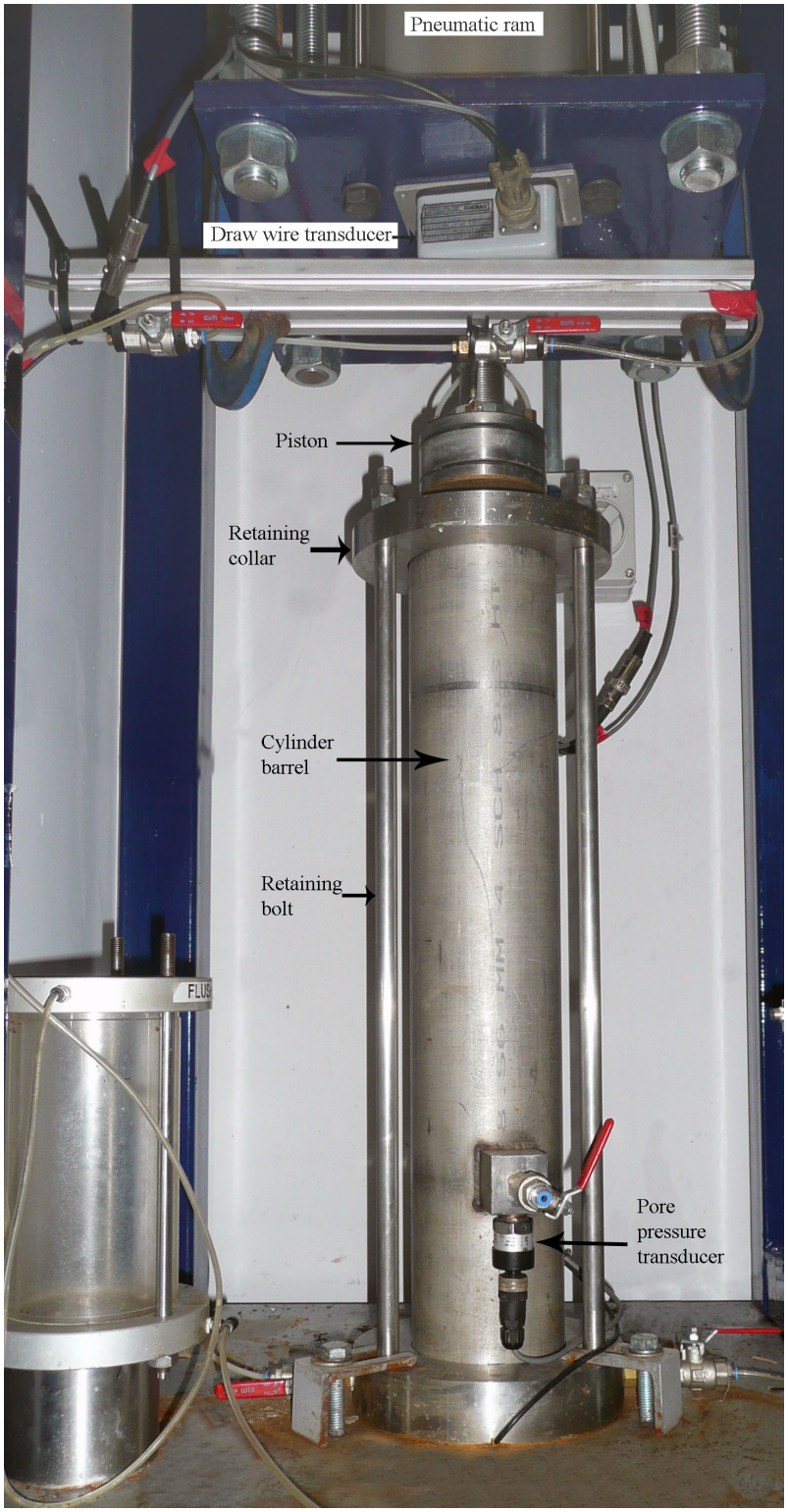

Figure 3.6: Consolidation apparatus

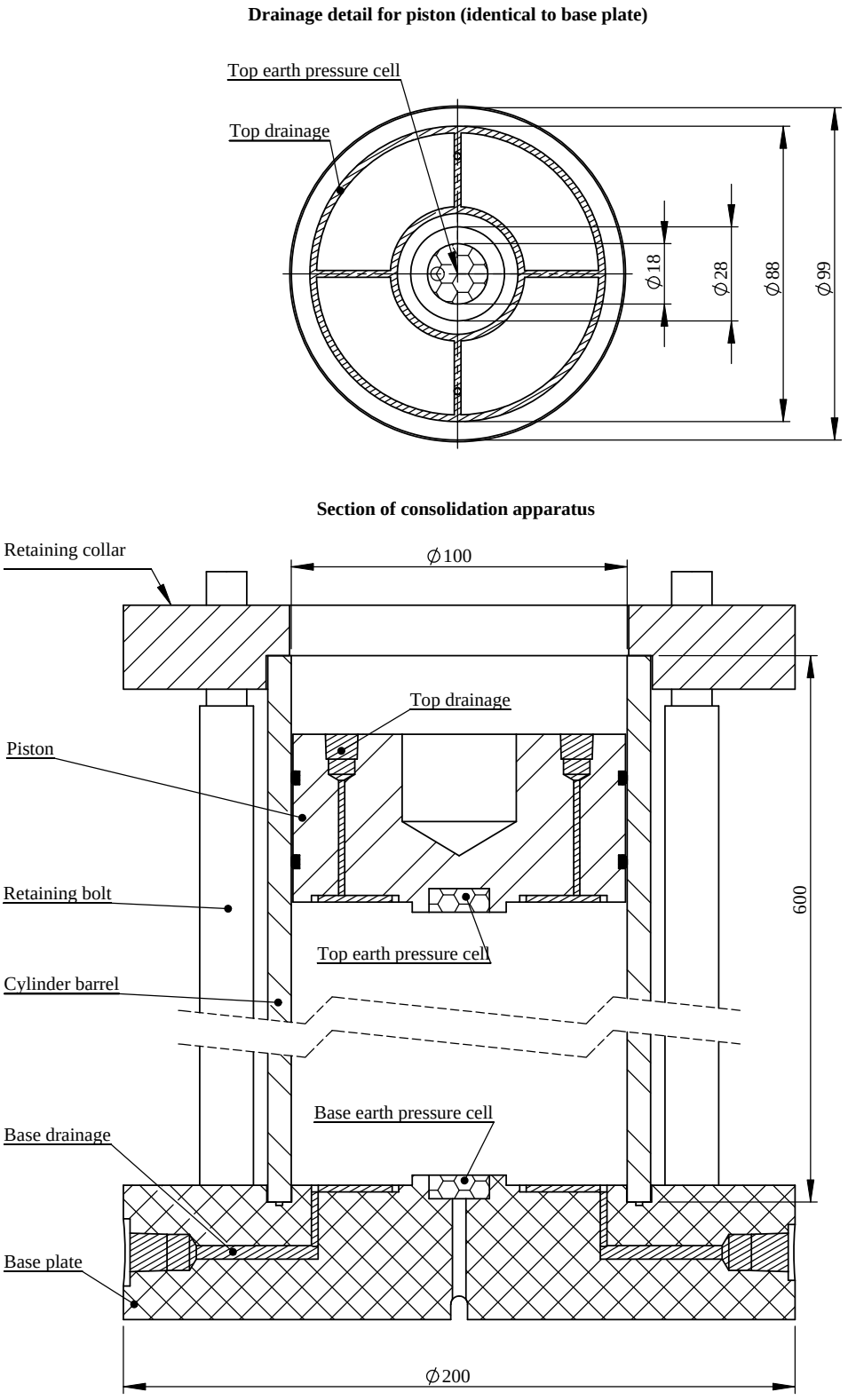

Figure 3.7: Diagram of consolidation apparatus

Calibration problems and management strategy used

Calibration of the pressure and displacement transducers used on the consolidation rig used a two point calibration, where a linear trend was calculated from readings made at the ends of the transducer range. This was a limitation of the software along with output in the form of a unit-less quantity of divisions rather than actual voltage. This prevented the normal approach of fitting a calibration curve to a multipoint, multi-run data set. The calibrations used also failed to be properly applied by the software therefore the calibrations were considered unreliable for the pressure transducers. A pressure test with water after each test was used to provide a correction to the observed values.

Displacement

The displacement transducer was calibrated at the two extremes of the $600\,\mathrm{mm}$ stroke of the pneumatic ram.

Load measurement

The measurement of load applied by the piston was calibrated experimentally from the air pressure applied to the piston. Three cycles of pressure 0 to $600\,\mathrm{kPa}$ and back where applied by the piston to a load cell mounted vertically under the piston. The ratio of applied air pressure to observed force could then be calculated and converted into the ratio of applied air pressure to pressure on the sample. This calibration (Table A.1) occurred outside the sample tube therefore the side friction of the sample piston is not accounted for.

Pore water pressure

The pore water pressure (PWP) transducers were calibrated against a Budenberg hydraulic dead weight pressure reference at pressures from 0 to $5000\,\mathrm{kPa}$. A initial two point calibration allowed the production of a best fit between the actual and measured pressure over three load-unload loops. This was then used to amend the initial two point calibration (Table A.2). Pressure tests after each sample production compared the pore pressure in the tube to the theoretical pressure based on the applied load. The change in pressure was recorded accurately but the correction to the absolute value had a mean value of $-28\,\mathrm{kPa}$ with a standard deviation of $55\,\mathrm{kPa}$. A negative correction here meant the pore pressure measurement had to be lowered to give the actual pressure in the tube. This is the opposite of what would be expected if the actual pressure was lower than the applied pressure calculation due to piston side friction.

Earth pressure

The earth pressure cells where calibrated in position against a fluid pressure in the consolidation tube calculated from the applied pressure. A zero point was set against atmospheric pressure and a second point was set between $2000\,\mathrm{kPa}$ and $3000\,\mathrm{kPa}$. In all cases the upper calibration point was linearly extrapolated to be equivalent a $3000\,\mathrm{kPa}$ pressure. Pressure tests performed subsequently showed that the initial calibrations (Table A.3) were accurate for incremental pressure change however corrections to the zero point were between -71 and $95\,\mathrm{kPa}$ for the base earth pressure cell (BEPC) and between -40 and $53\,\mathrm{kPa}$ for the top earth pressure cell (TEPC).

3.3.3 Stress path apparatus

The experimental investigation into the RSH effect in London clay was performed using computer controlled triaxial stress path testing apparatus. Two almost identical Bishop & Wesley (1975) type stress path cells for $100\,\mathrm{mm}$ specimens were used. One was developed by Hajj (1990) while a second was commissioned to the same design by Pierpoint (1996). A view of the apparatus is shown in Figure 3.8 or schematically in Figure 3.9. The pressure supply was provided to the lower chamber cell, and back pressure by a GDS advanced pressure / volume controller (ADVDPC). These provided pressure up to $2\,\mathrm{MPa}$ by use of a microprocessor-controlled screw pump and had a volumetric capacity of $1000\,\mathrm{cm}^3$ for cell pressure and lower chamber, while a $200\,\mathrm{cm}^3$ volume was provided on the back pressure. The resolution of the ADVDPCs measurement was $2\,\mathrm{kPa}$ for pressure and $0.5\,\mathrm{mm}^3$ for volume. The accuracy of the measurement was <0.1% of the full range for pressure and <0.25% for volume. Measurements of load and displacement were made by a load cell and external LVDT respectively. An auxiliary pressure transducer was also used to measure the cell pressure. To achieve high accuracy strain measurement and avoid bedding and seating errors, the standard instruments were supplemented with high resolution submersible LVDTs mounted directly to the sample.

3.3.4 Control and acquisition systems

The control of the tests was coordinated though GDSLAB, a proprietary software provided by GDS to enable the control of the ADVDPCs. The software was designed for performing standard triaxial tests at a normal strain rate, hence several workarounds were required in order to allow low stress docking and low strain rate. Data acquisition was provided by a GDS 8 channel 16-bit serial data acquisition pad with a $1\,\mathrm{Hz}$ data acquisition rate. The data-acquisition limits the resolution to

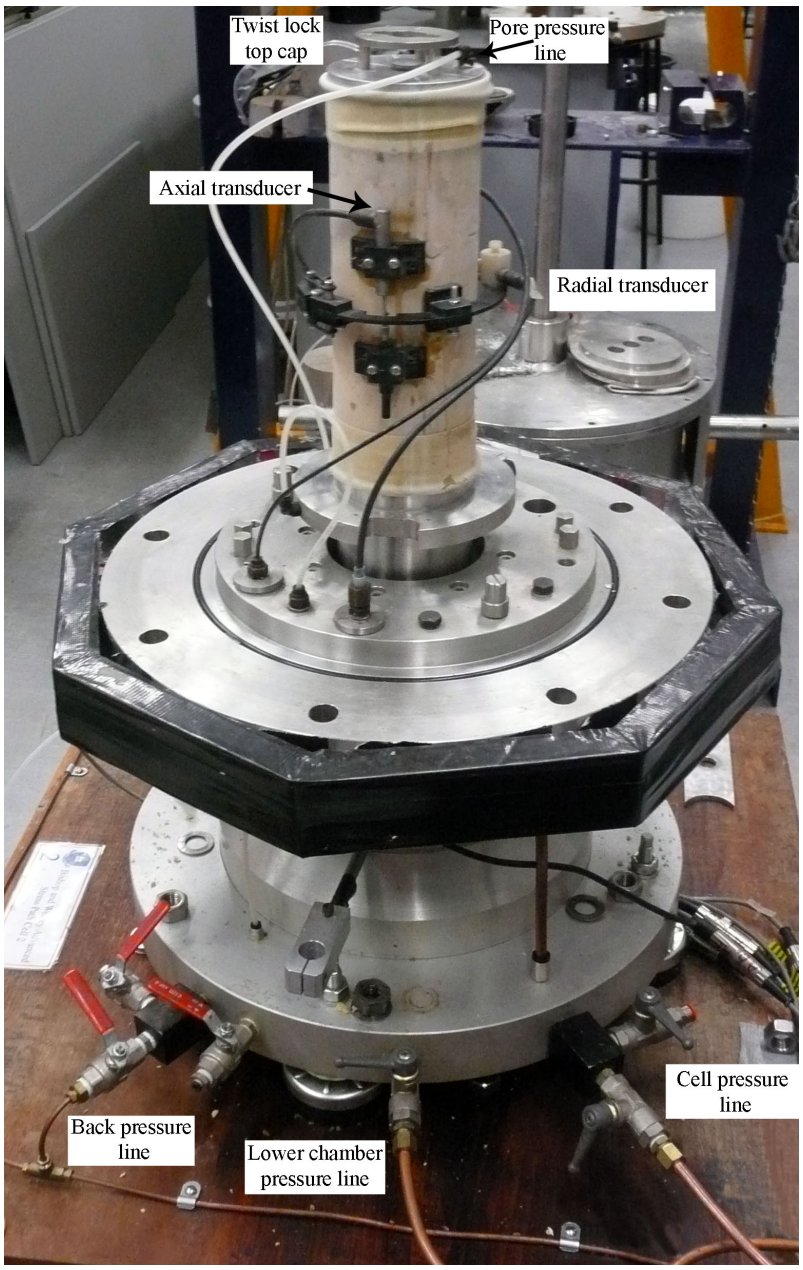

Figure 3.8: Stress path cell

$0.0015\,\%$ of the range of the transducer. The resolution worsens if the voltage range of the transducer does not match one of the set of discrete input voltage ranges accepted by the data acquisition. In addition a limited range of engineering units and logging to only 4 decimal places can also limit the resolution, for example displacement can only be logged to $0.1\,\mu\mathrm{m}$ as displacement can only be logged in mm.

3.3.5 General calibration procedure

The general calibration procedure used was to apply three cycles of load and unload to the transducer. The transducers where allowed to warm up and moved through their full range three times prior to the calibration. All transducers were sufficiently

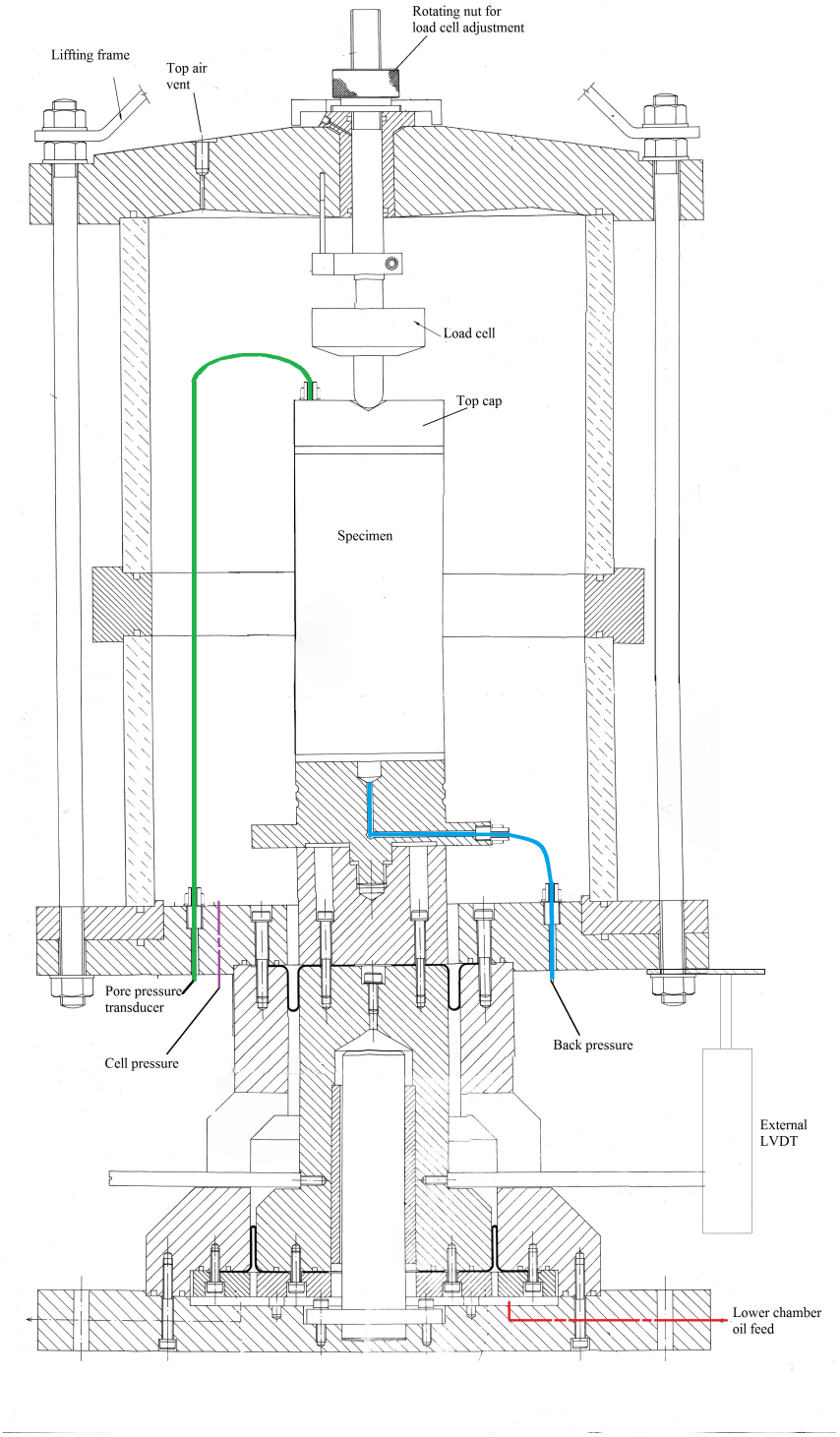

Figure 3.9: Stress path cell schematic

linear to allow the best fit straight line trend to form the calibration. The error of the calibration was assessed by the residual standard deviation, ς_r (also known as standard error of calibration) defined in Equation 3.1. Where y_i is the observed value of y for a given value of x_i, $\hat{y}_i$ is the value of y predicted by the calibration line for a given value of x_i , and n is the number of calibration points.

$$\varsigma_r = \sqrt{\frac{\sum_{i=1}^{n}(y_i - \hat{y}_i)^2}{n-2}} \tag{3.1}$$

If the transducer was found to be inaccurate this would be addressed by repeat calibration or replacing the transducer if still found to be inaccurate. An overview of the apparatus used and the calibration procedure used is given in the following sections while details are given in Appendix A.

3.3.6 Displacement transducers

Description and electrical connection

The measurement of local strains used three LVDTs two axial and one radial. These work by utilising a magnetically permeable core that causes a coupling between a primary coil excited by an alternating current (AC) current and 2 secondary receiving coils. This arrangement means that when the output of the receiving coils is rectified by a signal conditioning unit, the output voltage varies linearly with displacement and has a distinct zero point at mid range. The resolution and accuracy are usually a result of the electronics used and the displacement range of the transducer. A typical system has a noise of $\pm 5\,\mathrm{mV}$ or $\pm 2.5\,\mu\mathrm{m}$ however high quality signal condition can yield noise of $\pm 0.15\,\mathrm{mV}$ or $\pm 0.075\,\mu\mathrm{m}$ (Da Re, Santagata & Germaine 2001). The noise and drift of LVDTs are however lower than other transducers (as shown in Figure 3.10) and they are less susceptible to temperature variation than resistive type transducers being temperature stable between -45 to $93\,^{\circ}\mathrm{C}$ (Cuccovillo & Coop 1997).

The transducers used were RPD D5/200W transducers with linear and radial cable exits for radial and axial measurements respectively. These provide a +- $5\,\mathrm{mm}$ displacement range and the manufacture gives the linearity as $10\,\mu\mathrm{m}$.As the LVDTs required an AC power supply not provided by the GDS data acquisition unit a RDP 621 LVDT amplifier was used. This provides a $1.1\,\mathrm{V}$ AC excitation at $5\,\mathrm{kHz}$ to power the transducer and then rectifies and amplifies the output to +-$10\,\mathrm{V}$ direct current (DC). The amplification process however imparts a +-$5\,\mathrm{mV}$ noise to the output signal.

In order to achieve higher accuracies it is prudent to amplify the central range to focus on the linear range of the transducers as shown by Cuccovillo & Coop (1997).

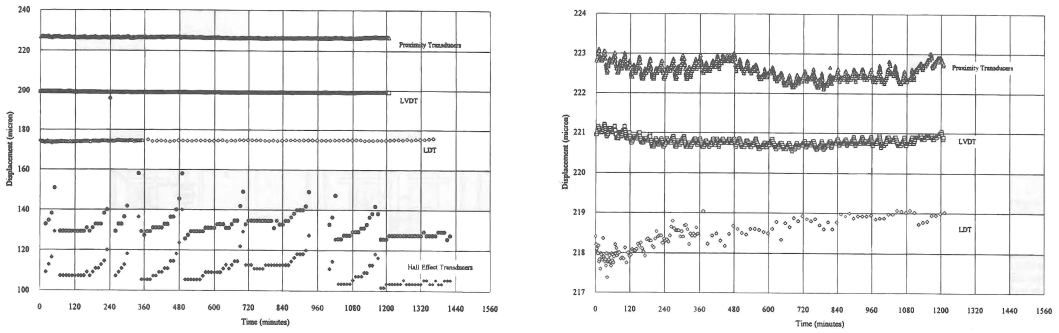

(a) Noise (b) Drift

Figure 3.10: Stability of selected internal strain measurement systems, Scholey et al. (1995)

In addition the effect of the amplifier noise is mitigated by amplifying a tighter range. If a +-5 mm range is amplified to +-10 V a +-5 mV noise is equivalent to signal noise of +-2.5 µm, while using a +-2 mm range reduces the error to +-1 µm. The use of a smaller range is acceptable given the small movements observed. Smaller transducers where not used in order to prevent transducer damage with excessive strain and expand the linear range.

Mountings

The mounting of the local transducers was achieved by gluing specially designed mounting blocks to the sample. This is possible as Burland & Symes (1982) demonstrated compatible displacement of the membrane and soil until after failure. The axial transducers were mounted diametrically opposed across a 70 mm span at the centre of the sample. The radial transducer uses a strain belt to allow a measurement of the sample diameter; this was lightly sprung belt to maintain contact while minimising any disturbance caused by the spring force. The design of the axial and radial mounts is illustrated in Figure 3.11. The axial mount used a freely balanced armature without any firm fixity at the lower end. A sharply angled cone was placed at the end of the armature which rested in a shallow cone at the top of the support. The lower cone was set up to be coaxial with the LVDT body at the beginning of the test. This set up was used as it was found that using a fixed support for the armature would lead to sticking at small amounts of misalignment. Using this method the armature was free to rotate at the base, allowing barrelling to be accommodated without damage to the transducer.

The radial transducer was positioned approximately twice as far from the pivot as the displacement measurement point. The effects of the geometry were addressed in the calibration procedure. Early on in the testing it was found that the play between the sample mountings and the strain belt was permitting the sample to move while

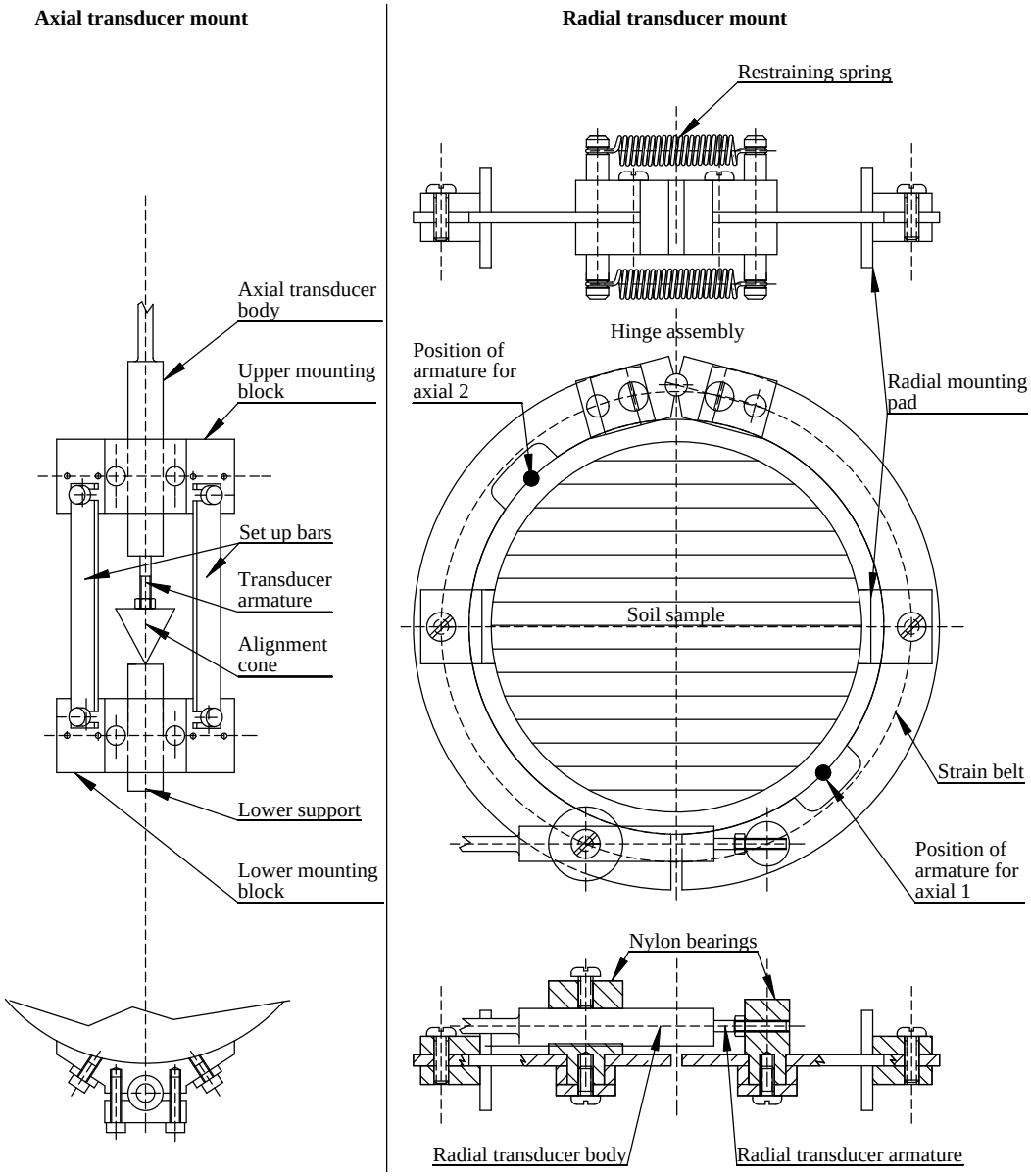

Figure 3.11: Mountings for on sample LVDTs

the belt remained in position. Along with swelling of the nylon bearings which prevented rotation of the LVDT, this prevented the measurement of small radial strains. To prevent these problems the bearings where fixed and a spring was added to hold the sample mount to the rear most extent of the play in the pivot.

Calibration

Achieving strain measurement accurate to 0.001% required a displacement measurement accurate to $0.7\,\mu\mathrm{m}$ across the $70\,\mathrm{mm}$ measurement span and $1\,\mu\mathrm{m}$ for the diameter. Allowing for +-3% axial strain the axial transducers were calibrated over +-$2\,\mathrm{mm}$; in an undrained test radial strain was expected to be +-1.5% so +-$3\,\mathrm{mm}$ range was used for the radial transducer. The resolution of the data was expected to be limited to $0.1\,\mu\mathrm{m}$ by the 4 decimal place data storage, while the +-$5\,\mathrm{mV}$ noise of

Figure 3.12: Micrometer calibration

the amplifier would cause variation of $1\,\mu m$ axial and $0.75\,\mu m$ radial.

Calibration was performed using a micrometer with a $0.5\,\mu m$ resolution mounted vertically, as shown in Figure 3.12. This prevented a $15\,\mu m$ discrepancy between increasing and decreasing calibrations that had been observed when mounted horizontally, which was believed to be caused by slop in the micrometer screw threads. As a fixed armature caused sticking problems it was found that restraining the armature coaxially with the LVDT body free to rotate provided the best result. This limited rotation to $0.166°$: a consistent $0.21\,\mu m$ error compared to a variable error between $7.19\,\mu m$ and $2.86\,\mu m$ found if no lateral restraint was provided.

As amplifier adjustments would affect the calibration, amplifiers and transducers where paired as a single system and not adjusted after initial set-up. Care was taken to ensure that the LVDTs were as close as possible to their physical zero point before the electrical zero was adjusted, to provide a reading of exactly zero on the data acquisition. The gain on the amplification was adjusted to output $9000\,mV$ at the maximum range of calibration before calibration was performed using 21 points across the range.

Measurements of the radial strain belt provided a ratio of diameter change to transducer change of 0.5198 on cell 1 and 0.5323 on cell 2, which were used to convert the radial transducer calibration to diameter change.

A linear calibration was used but to allow for a polynomial correction to be applied later, zeroing the LVDTs was done by the soft software zero and the offset used was recorded. The linear calibration is given in Table 3.6; the standard error of

calibration describes the non-linearity of the transducer of the whole range. The error after the non-linearity is expressed as the mean of the standard deviation of the signal recorded at each calibration point converted into displacement by the linear calibration. The error between readings was larger than expected as the micrometer could not be returned to the same point accurately on successive runs . An indication of errors induced by electrical noise was assessed by a second calibration, logging the transducer readings every 3 seconds for a minute.

Cell	1	1	1	2	2	2
Transducer	Axial 1	Axial 2	Radial	Axial 1	Axial 2	Radial
Serial Number	149968	149970	50954	149967	149969	50953
Sensitivity $\mu m\,mV^{-1}$)	-0.223	-0.223	-0.174	-0.222	-0.222	-0.178
Offset (µm at $0\,mV$)	-2.49	2.15	-1.68	6.98	-5.18	0.296
ς_r (µm)	1.8517	2.5081	3.5229	1.2419	1.7992	1.1241
Error between readings. (mean of SD at point) (µm)	1.1398	0.675	0.5384	0.8731	1.2303	0.4672
Error over time (Mean of SD at point) (µm)	0.0518	0.0374	0.0303	0.0366	0.0595	0.0292

Table 3.6: LVDT calibration summary

3.3.7 External displacement measurement

Calibration of external transducer

The external displacement transducer was mounted on an arm connected to the lower chamber and acted against a plate secured by the bolts holding the triaxial cell in place. The transducer used was a sprung return $50\,mm$ span DC LVDT produced by LSC Transducer. An improved resolution of $1.3\,\mu m$ was achieved by calibrating over a $42\,mm$ range.

Limitations of external transducers and use of displacement derived from lower chamber volume change

In the default setup, the GDSLAB control software used the external displacement measurement to determine whether an applied change in lower chamber volume had resulted in the correct displacement. Due to the $0.1\,\mu m$ per minute testing and $1.3\,\mu m$ resolution rate it would take up to $13\,min$ for the external displacement reading to change. During this time the control software observes no change in displacement and so applies an increased volume change. The increased volume change will

result in an increased displacement. When this is registered by the external transducer it will be too high and the sample will be lowered. This process resulted in an oscillating movement of the sample which was reflected in the deviator stress and triaxial strain, making them unsuitable for the tests.

The external axial transducer was renamed so the software was configured without axial displacement measurement. The axial displacement was then calculated by the fluid flow into lower chamber, the geometry of which was programmed into the software. This set-up had a $0.047\,\mu\mathrm{m}$ displacement resolution but as this was the limit on both applied and measured displacement, oscillations were minimised. The external axial transducer provided a check on the actual displacement occurring which may differ for following reasons:

- Incorrect calibration of the lower chamber geometry.
- Air in the lower chamber compressing when the lower chamber pressure increases (particularly if the lower chamber is initially supported and a large pressure change occurs to balance with the cell pressure)
- Temperature variations

Despite these problems, with careful management a smooth displacement rate was achieved from the lower chamber displacement calculation, and actual strain rates were calculated from the external or local transducers.

3.3.8 Pressure transducers

Pressure transducers where provided to measure the pore pressure and for an auxiliary measurement of the cell pressure. These where calibrated against a Babenberg hydraulic dead weight pressure reference at pressures between 0 and $700\,\mathrm{kPa}$. The details of the transducers and the results of the calibrations are given in Table A.5.

3.3.9 Load cell

Load cell calibration

The load on the sample was measured by $15\,\mathrm{kN}$ submersible pressure compensated load cells. These were mounted on a screw adjustable sealed stem at the top of the triaxial cell. These where calibrated over the range 0 to $15\,\mathrm{kN}$ by using the Budenberg hydraulic dead weight pressure reference and a lubricated rotating piston to provide a force reference. The calibration of the load cell is detailed in Table A.6. Calibration for negative stress was assumed to continue from the calibration at positive stress.

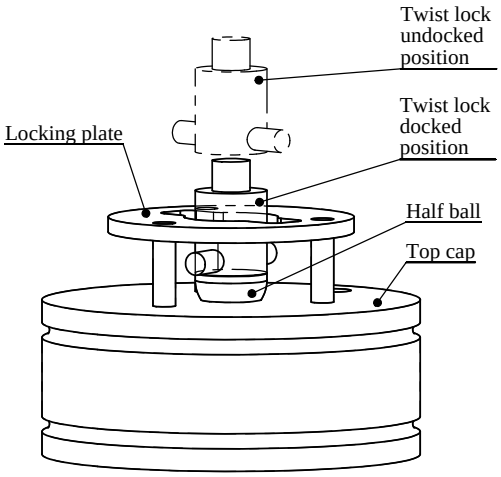

Figure 3.13: Twist top cap

Docking mechanisms

It was not possible to hold q to better than $\pm$ 1 kpa therefore creep was achieved at an isotropic condition by disconnecting the sample from the load cell. A mechanism was therefore required to dock the sample to the load cell when applying deviator stress in compression or extension. It was found that a suction top cap would not allow a smooth docking, as seating the top cap in place and applying suction would induce loads and strains in the sample. A twist lock top cap was developed (Figure 3.13) so the load cell could be lowered into place and twisted to provide docking in extension using the 2 prongs. Docking in compression was achieved through a free half ball docking system. This system prevented the docking imposing rotation or translation in compression and prevented the imposition of translation in extension. Some early tests used a fixed half ball for docking in compression but this was changed after this imposed a translation to the top cap if not aligned correctly. The floating thread that moved the load cell was found to move when the direction of the applied stress changed. This movement was significant at the slow test rate used so a locking solution was used to prevent this.

3.3.10 Temperature issues

When measuring small strain changes the effects of a variable temperature begin to be significant to the results. Temperature change has been shown to cause errors by expansion of the cell fluid and the cell equipment, such as inducing a variation in the volume of the drainage system as shown in 3.14 (Cekerevac et al. 2005). The submersible stress and strain transducers have also been shown to have both zero points and sensitivities affected by temperature (Cekerevac et al. 2005). An example of the effect on the sensitivity of a load cell is given in Figure 3.15.

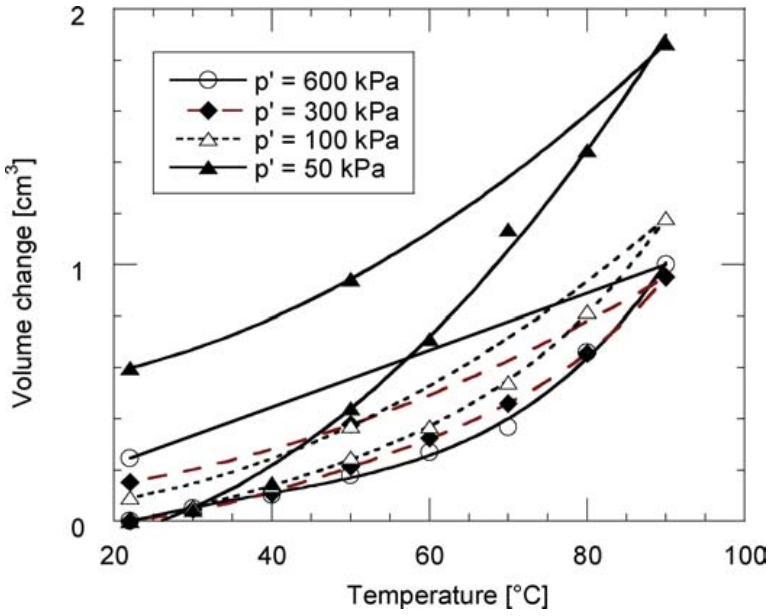

Figure 3.14: Volume change of drainage system during a heating and cooling cycle from $22\,°\mathrm{C}$ to $90\,°\mathrm{C}$ to $20\,°\mathrm{C}$ under $100\,\mathrm{kPa}$ back pressure, Cekerevac et al. (2005)

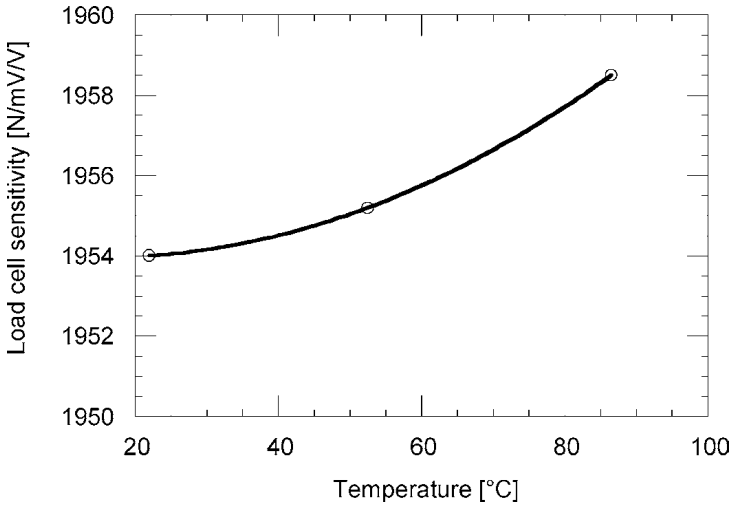

Figure 3.15: Sensitivity of a load cell with respect to temperature, Cekerevac et al. (2005)

The effect of temperature variation which was observed in my data in the initial lab tests showed a cyclic variation in deviator stress, with a period of approximately $1\,\mathrm{h}$ and an amplitude of $0.5\,\mathrm{kPa}$. An underlying diurnal variation in stress and strain was also observed. Temperature logs of the lab temperature showed a $0.5\,°\mathrm{C}$ variation in the lab temperature oscillating on a $1\,\mathrm{h}$ period, most likely the result of the feedback system controlling the lab temperature. When the lab temperature was measured over a $24\,\mathrm{h}$ period a $\pm 1\,°\mathrm{C}$ temperature variation was observed: this matched that observed by Kuwano et al. (2000). Assuming a similar construction

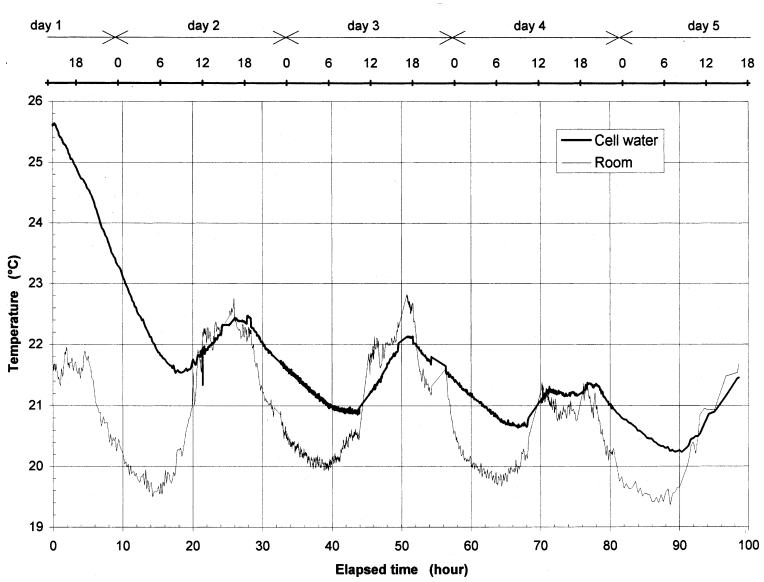

Figure 3.16: Temperature variation of triaxial cell fluid, Kuwano et al. (2000)

the temperature variation within my triaxial cell should be similar to the $\pm 0.5\,^{\circ}\mathrm{C}$ variation observed by Kuwano et al. (2000), as shown in Figure 3.16.

The use of an active temperature control system to eliminate the temperature variation was ruled out, as common systems are unable to regulate temperature better than $\pm 0.25\,^{\circ}\mathrm{C}$ due to lag in the feedback loop controlling the temperature (Cekerevac et al. 2005). Insulation had been shown by Gasparre & Coop (2006) to reduced the maximum temperature change of the cell fluid from $\pm 0.7\,^{\circ}\mathrm{C}$ to $\pm 0.1\,^{\circ}\mathrm{C}$. The theoretical effects of insulation where studied by approximating my triaxial cell as a cylindrical $400\,\mathrm{mm}$ high and $170\,\mathrm{mm}$ in radius with Perspex walls and aluminium ends, using the thermal properties in Table 3.7. The effect of a $\pm 1\,^{\circ}\mathrm{C}$ diurnal variation on a lab with a mean temperature of $21\,^{\circ}\mathrm{C}$ was calculated using basic heat conductions and specific energy equations. The result was a $\pm 0.31\,^{\circ}\mathrm{C}$ variation for the uninsulated case and $\pm 0.01\,^{\circ}\mathrm{C}$ for this idealised case. The lagging of the cell temperature variation behind the room temperature variation was consistent with both Kuwano et al. (2000) and the observed lag of the load cell variation behind the lab temperature variation. When the modelled insulation was installed over the triaxial cell the load cell variation dropped to +-$0.4\,\mathrm{N}$ compared to +-$1.5\,\mathrm{N}$ for an uninsulated cell, and the shorter term temperature effects had been much reduced. It was not possible to fully eliminate temperature variations through insulation due to access requirements for the triaxial cell so some effect of diurnal temperature variation is still observed in the later tests.

Material	Thickness (mm)	Thermal conductivity ($W\,m^{-1}\,K^{-1}$)	Specific heat capacity ($kJ\,kg^{-1}\,K^{-1}$)
Aluminium	20	180.00	0.9
Perspex	60	0.2	1.45
Hollow fill fibre insulation	100	0.04	
Water			4.18

Table 3.7: Parameters used in thermal calculation

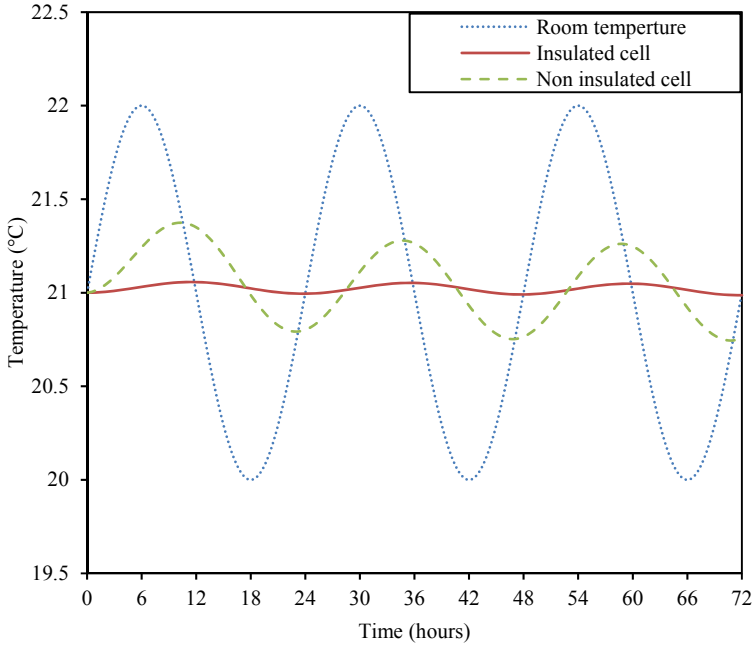

Figure 3.17: The effect of insulation on cell temperature variance

3.4 Methodology

3.4.1 Specimen preparation

Preparation of clay slurry

Samples of a weathered London clay where obtained from Mayfair, London. The samples were extracted as part of an underpinning operation carried out by Kier at a depth of approximately $2\,m$. The initial water content upon arrival was between 27.0% and 32.5% for samples taken from the outside and inside of the clay lumps respectively. The sample was manually divided into $10\,mm$ pieces; large inclusions ranging from $2\,mm$ to $40\,mm$ in diameter and accounting for 2 % of the starting dry mass were removed. The soil was then oven dried at $105\,°C$ for $24\,h$ and mechanically crushed in a reciprocating jaw crusher. After crushing a significant portion

Normal pressure		Low pressure	
Load (kPa)	Duration (h)	Load (kPa)	Duration (h)
100	48	50	18
200	48	100	36
2800	336	200	36
	864 for test HOCR	400	36
800	48	600	36
400	48	200	20
100	48	100	20
29(=0 air pressure)	42	50	24
		29(=0 air pressure)	24

Table 3.8: Sample preparation loading patterns

of the clay did not pass a $425\,\mu\mathrm{m}$ sieve, therefore an extended wetting period of $10\,\mathrm{days}$ at 100% moisture content was used. The clay had wetted significantly but showed a distinct change from plastic at the base to a light suspension at the top of the tubs. This was rectified by $3\,\mathrm{h}$ mixing in a large mixer which homogenised the clay into a uniform clay slurry.

Preparation of 100 mm triaxial samples

The preparation of London clay samples in the 1D consolidation apparatus was governed by the fill height of the slurry placed in the tube and the loading regime (Table 3.8). The large loading steep between $200\,\mathrm{kPa}$ and $2800\,\mathrm{kPa}$ was employed to ensure a large excess PWP to drive consolidation as well as to simplify the consolidation process to be primarily in a single stage. The small initial stages were used to prevent loss of slurry while it was in the slurry state The low pressure loading regime was used for the short sample O1 which had a $168\,\mathrm{mm}$ fill height. The remaining test used the normal pressure loading regime however test HOCR extended the $2800\,\mathrm{kPa}$ stage from 336 to $864\,\mathrm{h}$ to achieve a higher OCR. The nominal fill height used was $544\,\mathrm{mm}$; the precise heights are detailed in Table A.7.

The set-up of the apparatus was to flush the porous discs to ensure good drainage and apply silicone grease to the tube to aid sample release and minimise side friction. With the drainage system saturated, a filter paper was placed on each of the porous disks and $30\,\mathrm{mm}$ of water added to the tube to prevent air entrainment. The slurry was manually homogenised and then carefully added to the required height. Samples for moisture content determination were taken at 4 points during the filling.

The consolidation tube was then positioned under the piston and a small air pressure was manually applied to overcome the resistance of the o-rings, and place the piston

Figure 3.18: Horizontal extruder

in contact with the slurry. Measurements of the draw wire reading at this point and the top of the tube confirm the fill height and provide the datum for the start of consolidation. The drainage was closed for the first $30\,\mathrm{min}$ of the the computer controlled loading pattern to ensure a uniform stress distribution. The consolidation was then allowed to run automatically, monitored periodically for slurry passing the filters and to ensure the overflow reservoir was neither overflowing nor empty.

To remove the sample a -$10\,\mathrm{kPa}$ net pressure was applied for $2\,\mathrm{h}$, resisted by the sample suctions and side friction of the piston. This allowed a small swelling before the drainage lines were emptied and the upward pressure was increased at about $16\,\mathrm{kPa\,min^{-1}}$ until the sample released.

The sample tube was then transferred to the horizontal extruder shown in Figure 3.18 and the sample carefully extruded onto a lubricated half tube. The sample which had a typical height between $250\,\mathrm{mm}$ and $260\,\mathrm{mm}$ was placed symmetrically into a $200\,\mathrm{mm}$ high cylindrical split mould and trimmed carefully to ensure both ends were level. Measurements were made of the sample height, weight and diameter both before and after trimming, along with assessment of the water content from the trimmings.

3.4.2 Setting up the stress path cell apparatus

Cell preparation

The procedure used to set up the triaxial cell is based on that set out in Head (1998) and aims to minimise the air in the system to allow accurate volume measurement. De-aired and deionised water was prepared in Nold deaerators and stored under vacuum until required. Before the test the de-aired water in the cell and back pressure ADVDPCs was replaced, and the pipe work flushed along with the pore pressure transducer. The cell pressure cylinder was left at the lowest limit of its range to allow for the increased volume change required to drive excess air in the cell into solution. The back pressure cylinder was positioned centrally to allow water to flow

both into and out of the sample. The top cap was positioned inverted with its top level at the sample mid height. The back pressure cylinder was emptied to form a thin film of de-aired water on the inverted top cap the zero of the back pressure and pore pressure transducers was then set. The remaining areas for volume loss were air inclusions in the porous disk and filter papers, along with the possibility of the membrane taking up water. These were therefore soaked for $24\,\mathrm{h}$ in the de-aired deionised water while in a desiccator under vacuum, to ensure full saturation.

Sample mounting

The mounting of the sample on the pedestal occurred as soon as possible after the trimming of the sample to minimise sample desiccation. The base pedestal was covered with a film of de-aired water and the porous disk slid in place without trapping any air. A filter paper disk was then placed on the porous disk and the sample mounted in place avoiding air bubbles in both cases. A double layer filter paper side drain was used, as this was shown by Sivakumar, Mackinnon, Zaini & Cairns (2010) to reduce consolidation time (t90) to 6% of the time taken with no filter and 35% of the time with a single filter. The wet double filter papers were applied simultaneously to the sample, positioned to minimise the possibility of short-circuiting. A second filter paper and disk were placed at the top of the sample along with the top cap. The membrane was placed over the sample and sealed with o-rings at the base, any excess air was removed from between the membrane and the sample and the membrane was sealed with o-rings to the top cap. At this point the sample was sealed and would be ready for testing in a conventional test. Negative pore pressure would then build up in the sample as it swelled due to the release of the confining stress of the consolidation tube. This was measured by the back pressure and pore pressure readings which had their zero point set before being sealed.

Local transducer set-up

The axial mounts were attached to the sample symmetrically about the sample mid height, diametrical opposed, and with the cable spiralling half way around the sample to minimise resistance to vertical movement. To ease set-up, temporary support bars connected the halves of the mount. The lower support was set in position such that when the transducer was at zero, the lower support and LVDT body would be equidistant from the centre line. The axial transducer mounts were secured in place using a silicone rubber compound applied to the mounting pads; temporary supports and rubber bands were used to hold the mount for $1\,\mathrm{h}$ while the adhesive dried. While the adhesive was wet the armatures and LVDTs were positioned and

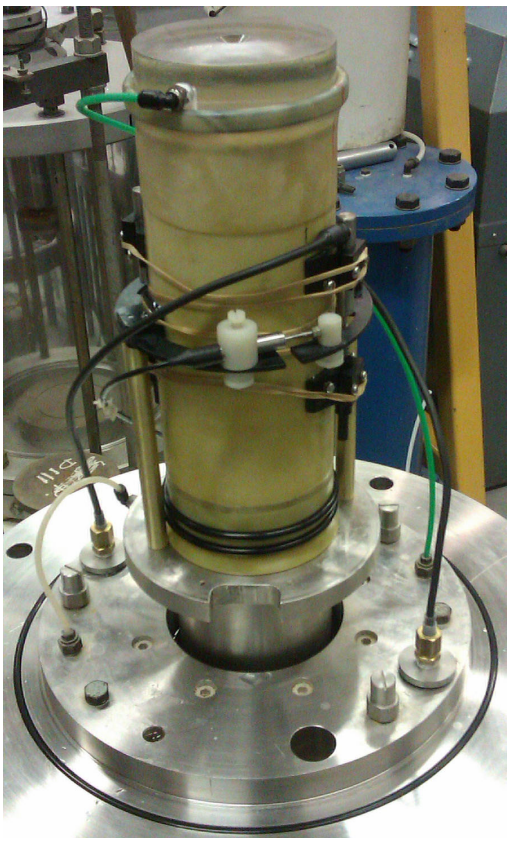

Figure 3.19: Local transducer mounting

adjustment made so the armature was vertical and centred in the lower support, and the transducer read approximately zero. When the adhesive had dried the axial support bars were removed and the radial transducer was mounted. The set up at this stage is shown in Figure 3.19. All transducer support and bands were removed and the position of the LVDT body was adjusted until the transducer reading was within $0.01\,\mathrm{mm}$ of zero. The test set-up was then checked, the twist lock docking stem aligned correctly with the top cap, and the half ball positioned. The cell was then secured and filled. When full (but still open to atmosphere) the load cell, cell pressure and lower chamber where set to read zero stress and volume.

3.4.3 Application of confining pressure

The application of a confining pressure was carried out immediately after the triaxial cell was full. The back pressure line to the pressure controller was left open but the stepper motor driven controller was capable of holding a constant volume so as to prevent damage to the sample. To ensure no movement of the back pressure a B-check type test was programmed into the GDSLAB software. The cell pressure was increased in stages until the pore pressure reading was a stable value greater than $50\,\mathrm{kPa}$. By this method an estimate of the initial effective stress of the sample could be obtained (Burland & Maswoswe 1982).

Soil stiffness	$S_r = 100\%$	$S_r = 99.5\%$	$S_r = 99\%$
Soft	0.9998	0.992	0.986
Medium stiff	0.9988	0.963	0.93
Stiff	0.9877	0.69	0.51
Very stiff	0.913	0.20	0.10

Table 3.9: Relationship between degree of saturation, S_r, and the observed B value for a range of soil stiffnesses (Black & Lee 1973)

3.4.4 Saturation and initial consolidation

An automatic saturation routine was used to raise the back pressure and cell pressure simultaneously and prevent detrimental cyclic effects associated with a stepped approach. In all cases a $4\,\mathrm{days}$ period was used to raise the back pressure to $400\,\mathrm{kPa}$ and the cell pressure to $400\,\mathrm{kPa}$ above the initial effective stress, thus minimising the volume change of the sample. A B-check was then performed to check the degree of saturation of the sample by applying an increase in cell pressure while maintaining the sample volume. The parameter B is defined by Equation 3.2 where Δu_w and $\Delta\sigma_3$ are the changes in pore water pressure and cell pressure respectively.

$$B = \frac{\Delta u_w}{\Delta \sigma_3} \tag{3.2}$$

A B value of 1 indicates a perfectly saturated soil while lower values relate to lower degrees of saturation. It was shown by Black & Lee (1973) that relatively small changes in saturation, S_r, could cause a large change in B value. In clays the relationship between the B value and the degree of saturation is outlined in Table 3.9. The stiff clay used was always found to have a high degree of saturation at this point so consolidation proceeded.

The cell pressure was increased to $700\,\mathrm{kPa}$ to give p'=$300\,\mathrm{kPa}$ to match that used by Atkinson et al. (1990) and be within the stress range of the equipment. The consolidation was run for $6\,\mathrm{days}$ at which point the back volume rate which indicated flow into the sample had stopped, and the excess pore pressure had dropped to less than 5% of the original value.

3.4.5 Sample docking

The docking process described here was designed to ensure that docking occurred with the minimum possible disturbance to the sample. Firstly the load cell was reset to zero just prior to each docking to minimise the cumulative effects of a downward drift on the load cell, which could have caused a $5\,\mathrm{kPa}$ error if left unchecked. Rectifying the problems caused by the drift and the reset procedure used is discussed

in section 3.5.3.
Docking was achieved by using constant p' stress paths set at constant strain rates of 1, 0.1 and $0.001\,\mathrm{mm\,min^{-1}}$. The $1\,\mathrm{mm\,min^{-1}}$ stage was used for approximate positioning, the $0.1\,\mathrm{mm\,min^{-1}}$ stage for a fine visual position until no gap could be resolved, and the $0.001\,\mathrm{mm\,min^{-1}}$ stage was run until an change in deviator stress was observed. This point is the nominal docking point at which the stress path stage would be started, as discussed in section 3.5.4 it may not be the actual docking point. When the docking stages were started, GDSLAB switched to a docked state at which point the sample height and diameter calculated from local transducer measurements were input as the sample height and diameter. This 'software docking' state was necessitated by limitations in the control software, however as the sample was actually undocked this caused complications in the interpretation of the data as discussed in section 3.5.2.

3.4.6 Stress path stages

The implementation of stress path stages in the testing were all automated by the GDSLAB software. The paths were set up with a target q value appropriate to the test being performed, while the mean stress p was maintained at $700\,\mathrm{kPa}$. The approach paths were run drained and had a back pressure of $400\,\mathrm{kPa}$ maintained. The longer shear probes where run undrained due to the long durations required for drainage in the low permeability clay and therefore did not require a back pressure to be specified.
A displacement rate of $0.0001\,\mathrm{mm/\,min}$ was used for the displacement stages. This is equivalent to $3 \times 10^{-3}\,\%\,\mathrm{h^{-1}}$. This low strain rate was selected to allow the low rate data acquisition to obtain strain data at strains less than $1 \times 10^{-4}\,\%$.
Due to the long durations involved and the need for small strain data a two stage approach was taken. Each stress path e.g. q 0 to $80\,\mathrm{kPa}$ was split into two parts; the first obtained data every $1\,\mathrm{s}$, the second every $10\,\mathrm{s}$. The termination of each path was determined by the GDSLAB software. This unfortunately had a $3\,\mathrm{kPa}$ buffer around the target value therefore while a termination might be set at $80\,\mathrm{kPa}$ for example the data may only run up to $77\,\mathrm{kPa}$.

3.4.7 Creep stages

Creep at a constant stress state would ideally be possible at any stress state, however poor control of the interaction between the lower chamber and cell pressure led to a variation of +-$0.5\,\mathrm{kPa}$ in p' and +-$0.25\,\mathrm{kPa}$ in q. This prevented creep conditions and so creep could only be achieved under isotropic stress conditions. Creep was performed drained with a $400\,\mathrm{kPa}$ back pressure and a $700\,\mathrm{kPa}$ cell pressure

using two different methods. Creep stages followed approach paths and were run as a continuation of the returning stress path. The stress path would be allowed to continue until it became undocked and then on for the required creep time. The precise undocking point was determined by the change in the load cell rate back to the load cell drift rate. Reset creep stages followed the return from shear probes and were performed as consolidation stages, with p'= $300\,\mathrm{kPa}$ following a automated undocking of the sample. The automated undocking only worked when undocking from shear in compression and would undock up to $3\,\mathrm{kPa}$ early. The premature undocking had a strain rate in excess of the testing rate and no data acquisition. As such it was unsuitable for assessing the effect of testing rate on initial creep strain rate, hence it was only used on the stages where this data was not required.

3.4.8 CU tests

Consolidated undrained tests were performed without LVDTs which would have been damaged by the 15% strain applied to the sample, but otherwise used the set-up and saturation procedure described above. Consolidation stages were performed with a back pressure of $400\,\mathrm{kPa}$ to p'=200, 300 and $400\,\mathrm{kPa}$ for test CU3, CU1 and CU2 respectively. To utilise the full strain range of the apparatus, a manual docking was used to lower the load cell to the sample rather than raising the sample to the load cell. These tests did not require precise measurement of the initial stiffness and no stage in extension was performed. The problems of inducing an initial deviator stress and movement of load cell retaining nut normally associated with manual docking, were therefore negated for these tests.
The strain rate for testing was derived by establishing the time to failure for a CU test. Head (1998) gives the time to failure as $1.8 \times t_{100}$, t_{100} was calculated from the consolidation stage of CU1 as $1180\,\mathrm{min}$ giving a time to failure of $35\,\mathrm{h}$. A strain rate of $0.005\,\mathrm{mm\,min^{-1}}$ or $0.15\,\%\,\mathrm{h^{-1}}$ was selected to give a margin of error to the consolidation time so ensuring the same rate could be used for all tests.

3.4.9 Oedometer tests

A set of $75\,\mathrm{mm}$ diameter $19\,\mathrm{mm}$ deep oedometer samples were trimmed from $25\,\mathrm{mm}$ slices of the $100\,\mathrm{mm}$ sample as detailed in Table 3.4. These were tested using Wykeham Farrance model 24251 load frames and brass oedometer cells up to a pressure of $2800\,\mathrm{kPa}$. The loading increments used are given in Table 3.10; the durations used are approximate as initial stages were terminated early if swelling was observed and all stages would be extended if consolidation was incomplete.
The procedure used was as described in Head (1998) except that an automated data logger was used. This consisted of using a spring loaded LVDT with a $10\,\mathrm{mm}$ span

Load increment (kPa)	Duration (h)
0-50	24
50-100	24
100-200	24
200-400	24
400-800	24
800-1600	24
1600-2800	24
2800-1600	24
1600-800	24
800-200	24
200-50	24

Table 3.10: Loading increments for oedometer tests

which was placed at mid span atop the load stem. Displacement readings where acquired at $1\,\mathrm{s}$ intervals during the fist minute then every minute thereafter.

3.4.10 QU tests

The set of $38\,\mathrm{mm}$ quick undrained (QU) tests detailed in Table 3.5 were also performed. Five $38\,\mathrm{mm}$ sample tubes were extracted from the $100\,\mathrm{mm}$ sample. Three vertical samples of $90\,\mathrm{mm}$ height were obtained from the lower half of the sample and two perpendicular horizontal samples from the top half. The sample tubes were capped to minimise desiccation and $76\,\mathrm{mm}$ high samples extruded and trimmed when required.

The samples were placed without drainage on the triaxial pedestal and sealed with a latex membrane before the confining pressure (indicated in Table 3.5) was applied. The sample was loaded at $1.5\,\mathrm{mm\,min^{-1}}$ or approximately $2\,\%\,\mathrm{min^{-1}}$ until the strain reached 20%. The stress readings were taken manually every $0.25\,\mathrm{mm}$ for the first $2\,\mathrm{mm}$ of displacement and every $0.5\,\mathrm{mm}$ thereafter.

3.5 Data processing

3.5.1 Introduction

In order to make comparisons of stiffness degradation curves and between multiple stages the raw data needed to be processed before use. The data processing was divided into 3 broad categories:

1. Modification: Adjustments applied to the data to ensure a consistent data set

reflecting the actual state of the sample is produced. For example, ensuring that if the back pressure cylinder was emptied or filled, due to running out of travel, this was not recorded as a change in sample volume.

2. Refinement: Processing of the data to remove the effects of electrical noise and allow rate calculation.
3. Smoothing: A further layer of processing that allows for stiffness calculation and comparison between tests.

3.5.2 Creating a consistent data set

Removing data resets

In order to run the docking procedure described in Section 3.4.5, the GDSLAB software running the equipment had to be set as docked despite the sample being free from the load cell. When the sample became docked in the software the following actions would occur automatically:

- The back volume would be reset to zero
- The internal measure of axial displacement would be reset to zero
- The lower chamber volume would be reset to the volume at the start of the tests
- The axial displacement would be set to zero
- The sample height and diameter would be calculated based on isotropic strain that had occurred during the nominally undocked stage

On the software becoming undocked:

- The back volume would be reset to zero
- The lower chamber volume would be reset to the volume at the start of the tests.
- Sample height and diameter recalculated.

In addition to the automated resetting of volume measurements, the load cell was reset prior to docking to minimise the effects of drift on the tests. In order to provide a consistent data set (for example to track the sample volume through the test) the resets where removed and a zero datum set at the start of the first approach path. This reverted the load cell to the reading that would have been made if it had not been reset.

Correcting sample dimensions

The sample dimensions (and consequently the stresses) were calculated by the GDSLAB software using Equation 3.3 . When the software was in a docked state ΔH was the observed axial displacement and when undocked ΔH was calculated

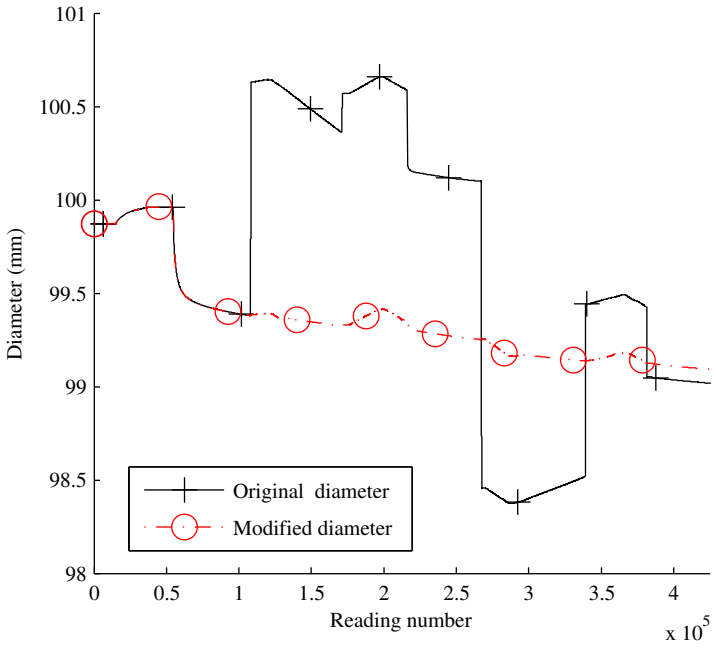

Figure 3.20: Correction to sample diameter calculation

by Equation 3.4 assuming isotropic strain.

$$A = \frac{V_0 + \Delta V}{H_0 - \Delta H} \tag{3.3}$$

$$\Delta H = H_0 - \left(H_0 \left(\frac{V_0 + \Delta V}{V_0} \right)^{1/3} \right) \tag{3.4}$$

All datum values where taken at the point where the sample changed docking state and the change is measured from that point. As the software was set docked before the actual docking, a substantial axial displacement could occur between being docked in software and reality. This resulted in an incorrect calculation of sample height, sample diameter and sample stress. The problem was rectified by repeating the calculation using the corrected docking point which much improved the calculation of sample diameter, as shown in Figure 3.20.

3.5.3 Load cell drift correction

The load cell was reset prior to each docking to manage the drift in the transducer, shown as original data in the example in Figure 3.21. The removal of the load cell resets results in the reset corrected data. A linear trend can be plotted through the undocked portions of the data where the load cell should read 0. This trend allows the comparison of the drift rate shown in Figure 3.22, which shows a rate of $-3\,\mathrm{Pa\,h^{-1}}$ observed in cell 1 while a higher rate of about $-10\,\mathrm{Pa\,h^{-1}}$ observed in cell 2. Both of the cells however have significant variation in the drift rate. The

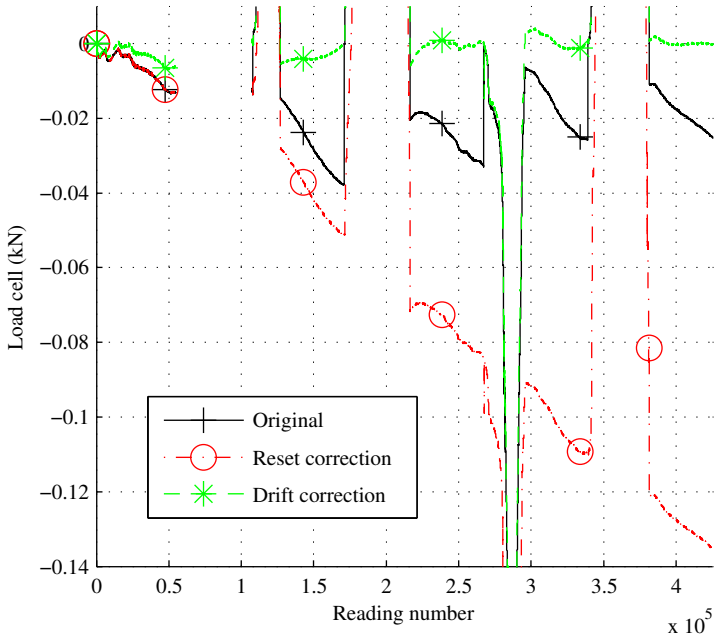

Figure 3.21: Load cell drift demonstration

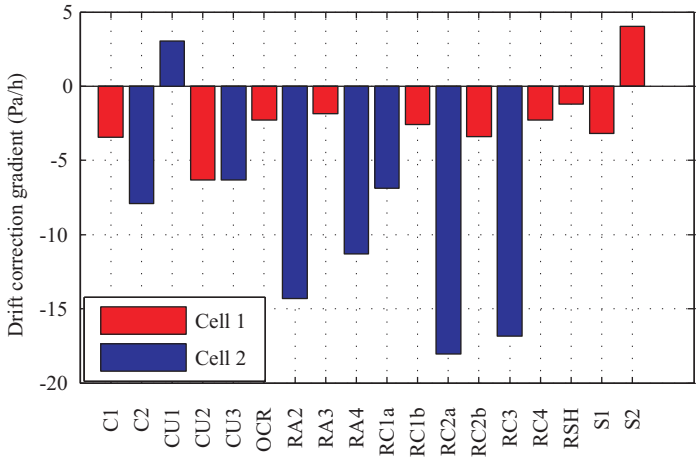

Figure 3.22: Drift of load cell

drift is not constant and so using a single linear trend will distort the zero position such that the known zeroes at resets points are no longer at zero stress. To avoid this problem a piecewise linear spline with nodes at the reset points was used. This maintains the start zeroes and corrects for the drift occurring over the stress paths, as shown in Figure 3.23. The drift, while significant, never exceeded $1\,\%$ of the load cell range. The drift was considered to be related to the age of the transducer and associated data acquisition equipment but no conclusive cause was found.

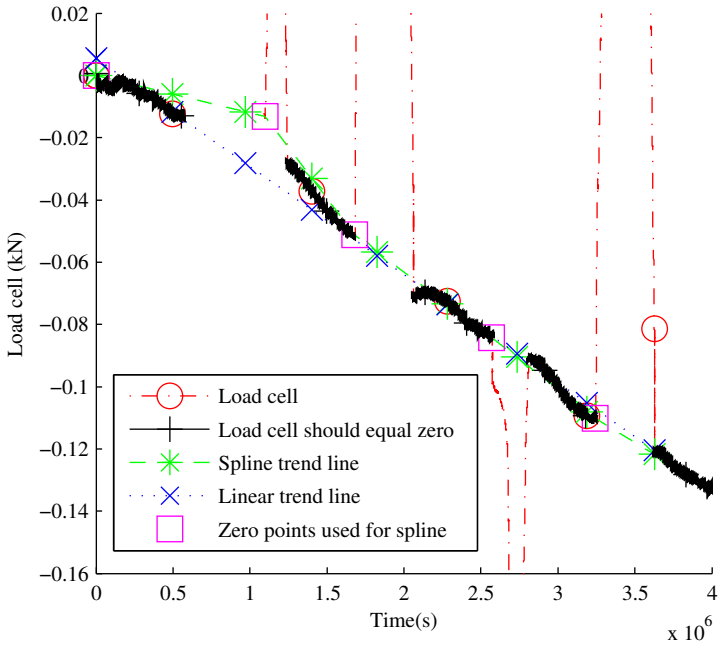

Figure 3.23: Drift correction

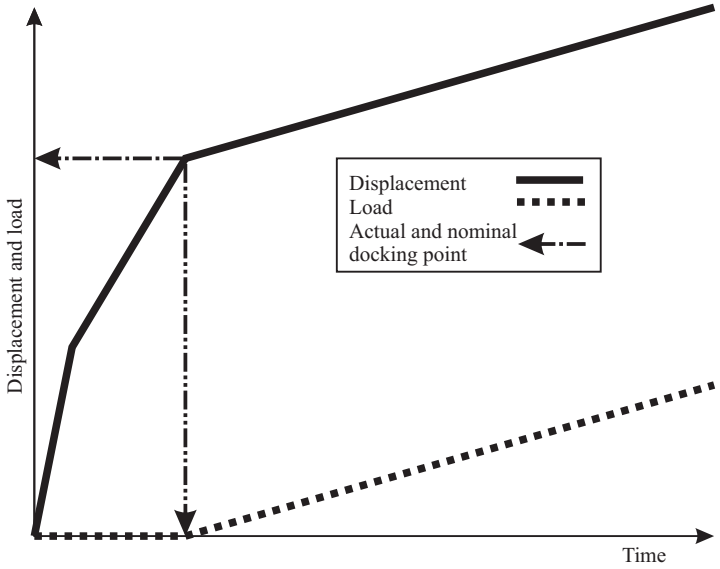

Figure 3.24: Idealised docking behaviour

3.5.4 Docking point selection

The idealised behaviour of a stepped displacement rate docking procedure is shown in Figure 3.24, where the sample becomes docked and at the precise instant the strain rate is dropped to the test rate and the stress begins to increase. This is however difficult to achieve; firstly there is no reliable indication of precise displacement to allow the judgement of when contact has been made, secondly the distances are too small to be resolved visually. The common solution is to permit

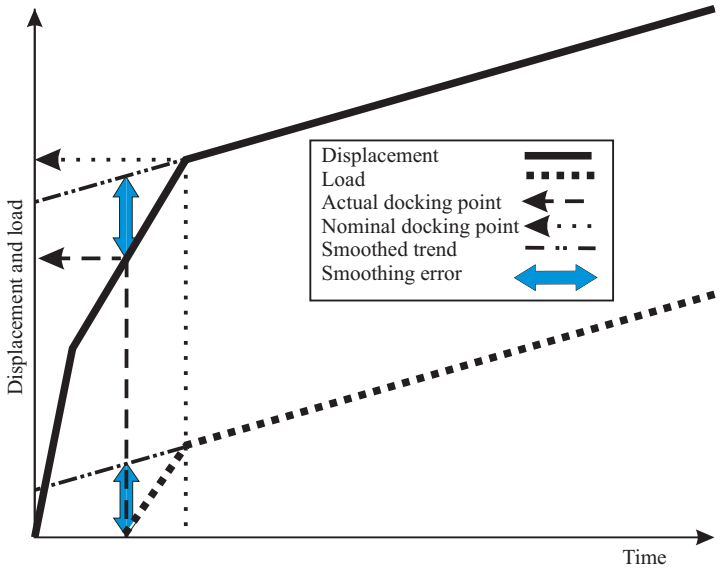

Figure 3.25: Over-docking: the test is dropped to the test rate too late

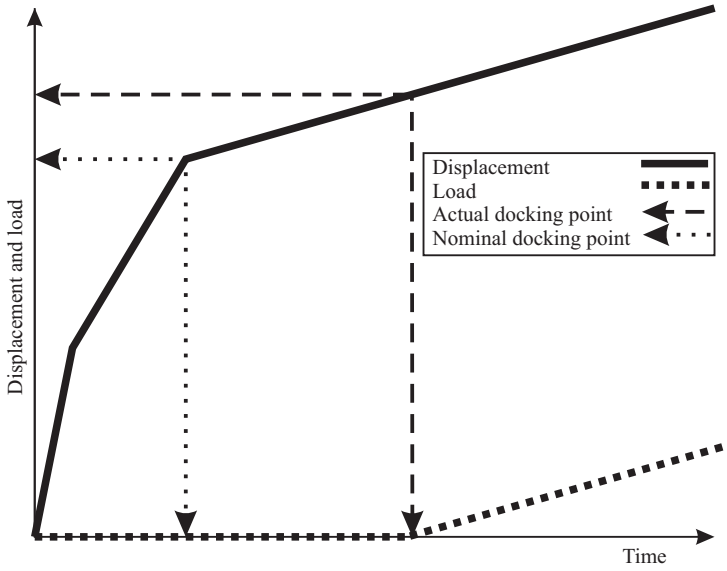

Figure 3.26: Under-docking: the test is dropped down to the test rate too soon

a limited amount of over docking as shown in Figure 3.25. This is where the load cell is monitored for change and the test rate is activated when a change in stress is observed. The problems with over-docking are that the rate is higher at the beginning than for the rest of the test, giving a possibility of rate effects on the stiffness. Additionally the smoothing used to remove the noise is not good at allowing a 10 fold change in rate so often is inaccurate at predicting the initial values. This can shift entire stress strain curves quite dramatically.

The opposite problem to over-docking is under-docking shown in Figure 3.26. This often occurs due to the apparent observation of docking, such as in test RA4 AP1 which had apparently been over-docked by the planned docking procedure to $0.2\,\mathrm{kPa}$.

This stress then dissipated and the sample had not shown a strong sign of docking in $24\,\mathrm{h}$ so an increased displacement was applied. With low displacement rates of $0.0001\,\mathrm{mm\,min^{-1}}$ very small under-docking can take a long time to become docked at the test rate. The persistent drift observed can be especially problematic in under-docking cases as a reliable indication of zero stresses is soon lost due to drift.
Manual docking was used primarily for the CU tests where an initial stiffness is not required. Manual docking is more likely to lead to over-docking as it applies larger increments of strain. Due to these complications the nominal docking point observed during the testing was not a reliable indicator of when the sample began to strain. The point at which to start a stress path stage can be determined in several ways:

1. When the stress changes in the appropriate direction.
2. When the triaxial strain changes in the appropriate direction.
3. When the average axial strain changes in the appropriate direction.
4. When both axial transducers are changing in the appropriate direction.

The stress change as observed by the load cell reading was used only for the CU series of tests which did not have local transducers attached. In the other slower tests, the noise and drift on the load cell reading, along with the possible bedding stress when the load cell comes into contact, rule out stress change as a docking criterion. Triaxial strain change is not used due to the unreliable radial transducer belt which prevents triaxial strain from local transducers being a constant criterion. The start of the axial strain on the central third of the sample is used as a criterion for the start of the test. Using the average axial strain allows for the sample to be tilting with one axial transducer moving and not the other. By waiting until both axial transducers are moving the sample tilt has been much reduced and the strain rate is typically matched indicating the start. Due to the noise a bespoke algorithm was used to determine when the displacement began to increase. This takes advantage of the fact that the displacement measurements have a fixed $0.1\,\mu\mathrm{m}$ resolution. The noise in the data is observed to be around $0.05\,\mu\mathrm{m}$. The observed reading for any fixed displacement could therefore deviate by +- $0.1\,\mu\mathrm{m}$ from the true value. This behaviour is shown in Figure 3.27, as the direction of expected improvement is known, a routine can be used to draw boxes around regions which oscillate over the same range. The routine works like this:

- Box bounds are first assigned at the minimum value and 1 resolution above it.
- The box continues until either the upper or lower bound is changed.
- The upper bound is increased at the point the data exceeds the current upper bound.
- The lower bound is increased at the point where no further values exist at the

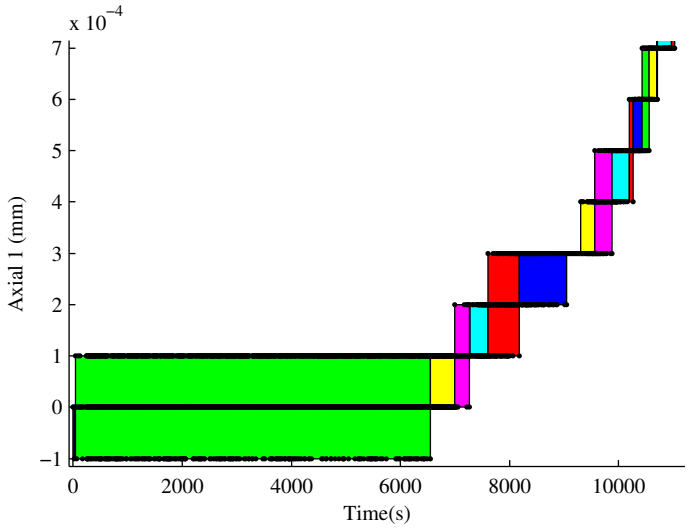

Figure 3.27: Axial displacement variation

lower bound and increase to the next lowest value.

The increase in the axial displacement is taken as the start of the box which has a mean displacement at least 1 resolution above the mean of the first box. In the current example this is the third box with a mean of $0.05\,\mu\mathrm{m}$. Further information on the Matlab code used can be found in section B.1.1.

3.5.5 Selecting appropriate data for strain calculation

With the addition of the local transducers several measurements are duplicated between those measured directly and those inferred from volume change and external displacement. While the ideal scenario would have all the measurements compatible the assumptions made do not allow this. Also due to the unreliable local radial measurement, using local transducers exclusively is also a problem. Selecting how key measurements are calculated is important, for example there are over 900 possible combinations for calculating triaxial strain. The selection of the data from which to calculate strain to use is approached by introducing a rank to the precedence in which the transducers are selected. The rank is based on both the resolution of the data and the errors, and is shown in Table 3.11.

An evaluation of the experimental results reveals that combinations of strain data available on each test can be categorised into 4 categories as follows:

1. Local; all local transducers are working.
2. External radial; the local radial transducer is not working and has to be inferred from the local axial transducers and the sample volume change.
3. External; no local transducers work, strain is calculated from external axial displacement and sample volume change.
4. Internal; the external axial transducer goes out of range (CU test only), strain

Rank	Measurement	Resolution	Errors
1	Local displacement transducers	$0.1\,\mu m$	Direct measurement of sample displacement
2=	Sample volume measure (back pressure cylinder volume change)	$1\,mm^3$	Affected by leaks and air in system
2=	External axial displacement transducer	$1.3\,\mu m$	Subject to knocks and bounce of long support as well as bedding strains
3	Inferred displacement from lower chamber volume change	$0.047\,\mu m$	Does not measure the actual movement so is affected by the geometry and pressure in the lower chamber
4	Cell volume change	$1\,mm^3$	Air in the chamber causes significant volume change

Table 3.11: Rank of strain data sources

is calculated from inferred axial displacement and sample volume change. The external radial approach can be used for shear probe stages on all RSH tests and is used as a common data set for comparison. The local data set is used when it is available for fine detail and the internal data set is used for CU tests going out of range of the external data set. In all occurrences the reference datum values, such as sample height and diameter at the start of a stage, are calculated from the same data as the incremental displacement. For example when using the local data set the sample height and diameter are calculated based on the cumulative movement of the local transducers, and the deviator stress based on the area measured by the local radial transducer.

3.5.6 Refinement to remove noise

Selection of broad methodology

The electrical noise on the transducers causes a rapid increase and decrease in the stress and strain. This problem causes the rate calculation to vary rapidly between large positive and negative values. To eliminate the noise in the data and provide a smooth rate output, a refinement routine was developed to conform to the following criteria:

- Not impose a form on the data.
- Provide a smooth rate plot.
- Remain close to the original data set throughout.
- Avoid control parameters chosen based on visual assessment of the output.

- Accounts for all data.

Table 3.12 list some of the multiple methods of data refinement tested along with how well they match the criteria required for the refinement. Of the methods tested, the best performing strategy was a smoothing spline; this is the method used to refine the data and eliminate noise.

Implementation of a smoothing spline based refinement of data

The best method found to remove the effects of noise from the data was to fit a smoothing spline curve to each input variable when evaluated against time. The evaluation against the time axis was desirable as time was monotonically increasing, not the case if evaluating against another measurement due to the noise. Additionally fitting a spline curve against time gave the advantage of calculating the rate by differentiation of the spline equation. The smoothing spline was fitted using *spapsNew.m*, a version of Matlab's smoothing spline routine *spaps.m* modified for lower memory usage. The changes which have no effect on the output are described in section B.2.1. The function finds the smoothest cubic spline function that satisfies a supplied error tolerance. Smoothness is found by minimising the integral of the square of the second derivative of the fitted spline function f. The error tolerance is found by Equation 3.5. This equation describes the error criteria as a weighted sum of squares for the error. Here a set of data points are described in cartesian coordinates by the vectors x and y. For each index j the value calculated by the spline function f at position $x(j)$ is compared to the data point at that index $y(j)$ to calculate the error of the fit. This error is than squared and multiplied by the value of the weighting function $w(j)$ (Equation 3.6) before being summed for all data points. The value dx in Equation 3.6 is a vector containing the differences between adjacent elements of the vector x.

$$E(f) = \sum_{j=1}^{n} w(j)|(y(j) - f(x(j)))|^2 \tag{3.5}$$

$$w = ([dx; 0] + [0; dx])/2; \tag{3.6}$$

The effect of the default weighting is to increase the relative importance of errors with the spacing between the points. In the context of curve fitting this means more error is allowed for each point of the denser data. This is however balanced by the increased number of points so the fit stays uniform when data rate changes.
This is key as the requirements of the testing took a sample every second during the initial hour to capture small strain behaviour, before dropping to every $10\,\mathrm{s}$ to keep a manageable amount of data over the long duration test. All the tests contained different proportions of data at the two sampling intervals and a different number of

Refinement method description	Criteria matched	Criteria broken
Parametric fits (e.g. high order polynomial)	Uses all data. Provides a smooth rate plot.	Imposes a form on the data. Arbitrary selection of equation. Does not necessarily stay close to the data.
Methods based on averages of subsamples of the data	Uses all data. Does not impose form.	Subsample size is arbitrary. Does not necessarily stay close to the data. Output not necessarily smooth.
Linear interpretation between a subsample of points	Does not impose form.	Subsample size is arbitrary. Does not necessarily stay close to the data. Output not necessarily smooth. Does not use all data.
Moving averages	Uses all data. Provides a smooth rate plot. Does not impose form.	Arbitrary number of data points used. Moving average shift result from data.
Lowpass filters	Uses all data. Stays close to data Does not impose form.	The cut off frequency was arbitrarily defined. Output not necessarily smooth.
Smoothing Spline	Uses all data. Stays close to data. Does not impose form. Provides a smooth rate plot. Smoothing criteria can be related to transducer resolution.	

Table 3.12: Refinement methods tested

Transducer(s)	Resolution	Comments
Local transducers	$0.1\,\mu m$	Resolution limited by 4dp input.
External Axial transducer	$1.2\,\mu m$	Resolution observed from results.
Load	$0.2\,N$	Resolution observed from results.
Back volume	$1\,mm^3$	Resolution limit of volume measure.
Internal Axial transducer	$0.1\,\mu m$	Resolution limited by 4dp input.
Deviator stress q	$25.5\,Pa$	Calculated based on load cell resolution and $100\,mm$ sample.

Table 3.13: Transducer resolutions used for data refinement

data points. This made using the weighted sum of errors squared term inconsistent between tests. Instead the tolerance of the spline Tol was calculated by Equation 3.7 from the weighting matrix w calculated by Equation 3.6 and a user input tolerance $TolIn$.

$$Tol = sum(w * (TolIn^2)); \tag{3.7}$$

The input $TolIn$ functions as a limit to the weighted RMS error of the fit, although with no control over the RMS error directly. To provide a standard reference for the tolerance value a normalised tolerance $TolNorm$ is used, as defined by Equation 3.8. Where Res is the resolution used for each type of transducer, as given in Table 3.13.

$$TolIn = TolNorm * Res \tag{3.8}$$

A parametric study was performed to ascertain the best value of $TolNorm$. The error expressed as the mean error over the whole data span increases linearly with tolerance as expected (as shown in Figure 3.28) so minimising error will be achieved by the lowest normalised tolerance. The smoothness of the fit was assessed by comparing both the maximum first and second derivatives of the fitted trend, as shown in Figures 3.29 and 3.30 respectively. These both show a sharp increase when $TolNorm$ is lower than 0.6. For this reason a $TolNorm$ = 0.6 is used as a tolerance for the refinement. The comparison of fits in Figure 3.31 shows how a $TolNorm$ = 0.6 (b) balances minimising the allowed error and smoothness shown at 0.4 and 0.8 in (a) and (c) respectively.

Refinement of strain measurements

Ideally the refinement would only occur on the raw transducer readings that are affected by the electrical noise. When strain is calculated for the refined data however it is found not to match that calculated from the raw data. Strains are calculated relative to the first data point and so noise on the raw reading can lead to the calculation

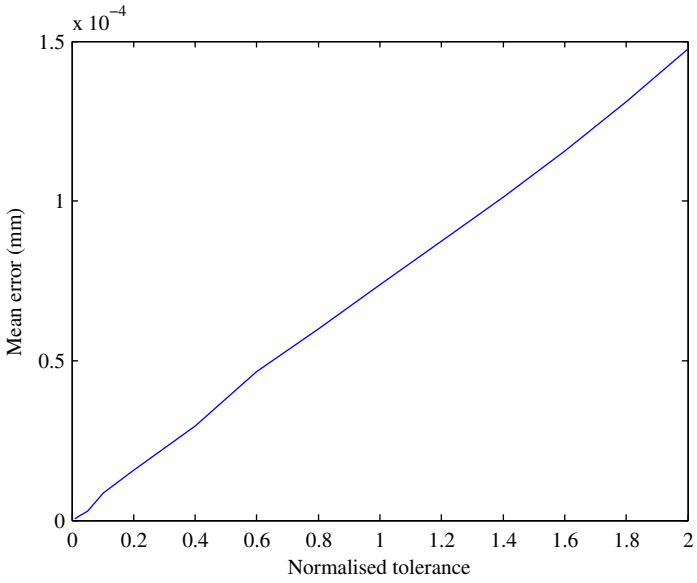

Figure 3.28: Effect of tolerance on error

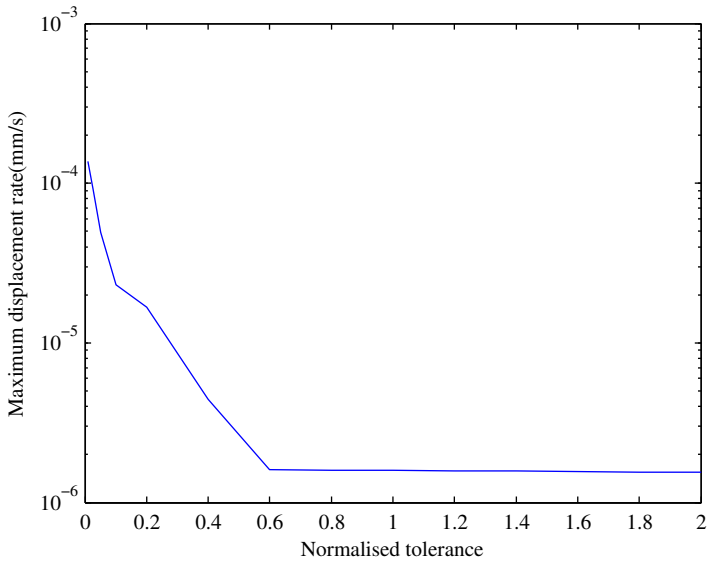

Figure 3.29: Effect of tolerance on maximum rate.

of negative strains. When the raw data is refined the initial result is produced at the minimum displacement value and so the calculated refined strain starts at zero. As is shown in Figure 3.32, this causes the refined strain data to be lifted relative to the raw strain data and so the refined strain does not fit the raw strain.

When calculating composite strains from multiple transducers the errors are cumulative. The refinement of strains is therefore done on the strain readings independently of the transducer refinement. This requires calculating a resolution for the strain. In the case of a simple local transducers this is accomplished by:

Strain resolution= (transducer resolution / initial transducer span)*100;

Composite strains made up of multiple transducer readings are also refined directly.

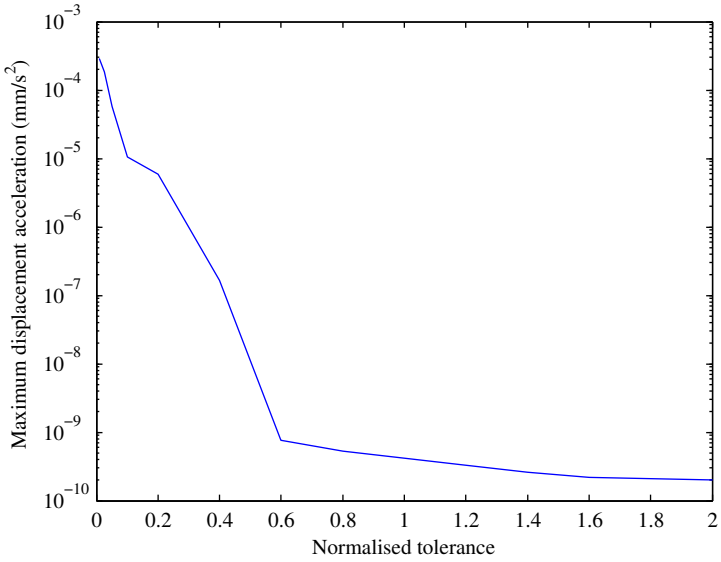

Figure 3.30: Effect of tolerance on maximum second derivative

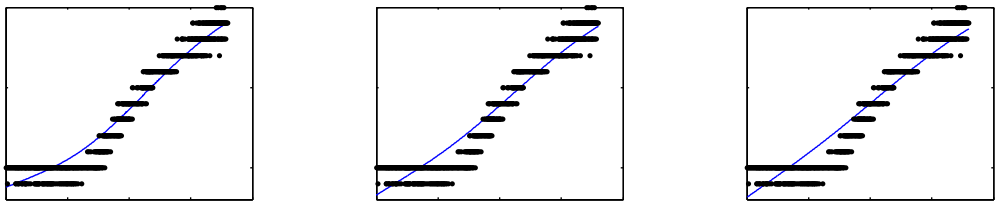

(a) 0.4 (b) 0.6 (c) 0.8

Figure 3.31: Effect of tolerance on fit

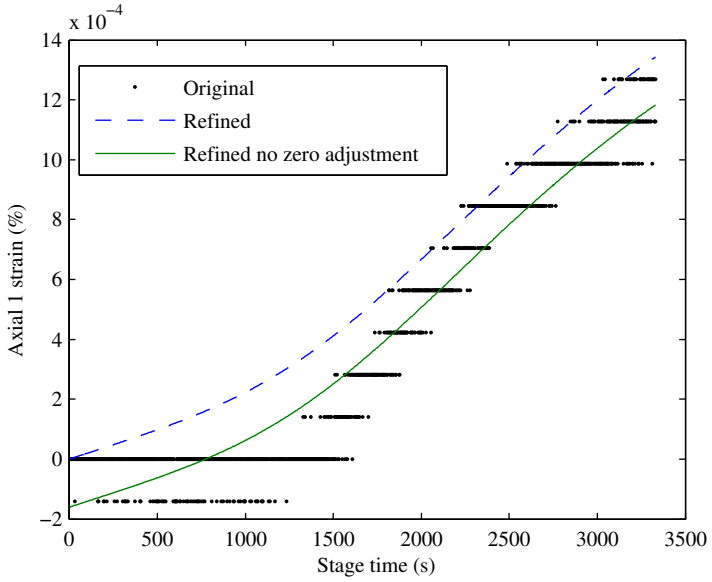

Figure 3.32: The effect of calculating refined strain

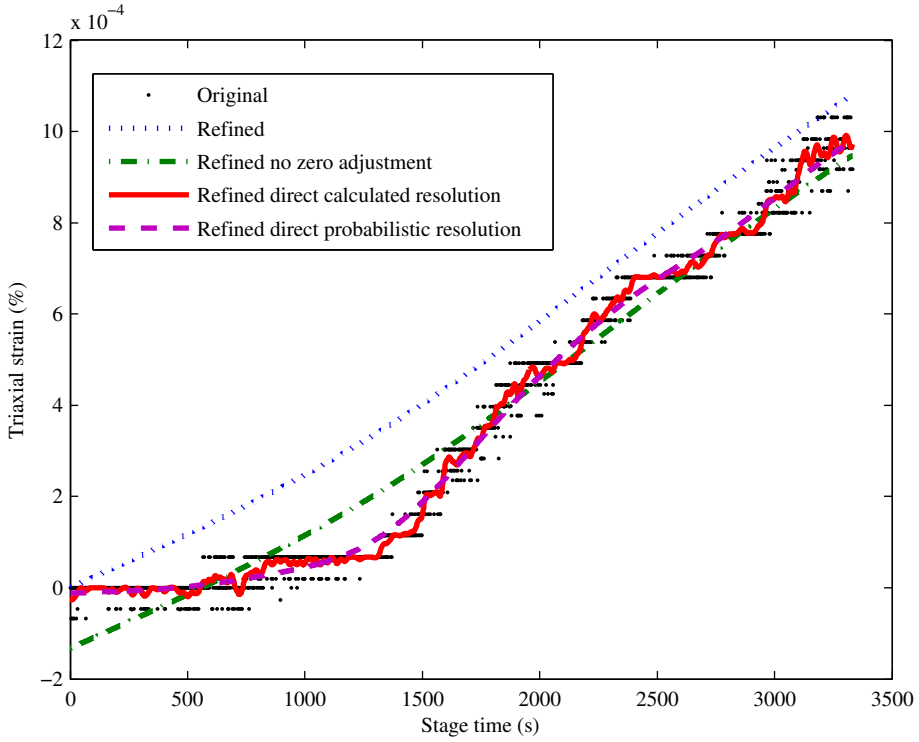

Figure 3.33: Direct refinement of triaxial strain

Transducer resolution (%)	
Axial displacement	$0.1\,\mu\mathrm{m}$
Radial displacement	$0.1\,\mu\mathrm{m}$
Axial strain, assuming $66\,\mathrm{mm}$ span	1.515×10^{-4}
Radial strain, assuming $100\,\mathrm{mm}$ diameter	1×10^{-4}
Triaxial strain= $2/3\varepsilon_a - \varepsilon_r$, assuming $66\,\mathrm{mm}$ span	3.43×10^{-5}

Table 3.14: Simple calculation of triaxial strain resolution

This is done because adding multiple sets of refined data to calculate a higher level refined strain accumulates the errors in the original refinements. This is shown in Figure 3.33, where the fit calculated from the individual refined transducers does not represent the actual trend of the data.

The difficulty with refining the composite strains directly is selecting which resolution is appropriate to use. Table 3.14 shows how the triaxial strain resolution is calculated for an example test with a $66\,\mathrm{mm}$ axial span on the local transducers and a $100\,\mathrm{mm}$ sample diameter. Using the $3.43 \times 10^{-5}\,\%$ strain resolution however results in a fit that is to tight too the data, as shown in Figure 3.33.

The calculation of the strain resolution, based on the same logic as the calculation of strain, fails to account for the fact that the triaxial strain is made from 3 transducers that can all change up, down, or not at all between adjacent data sites. Table 3.15 gives the possible changes in triaxial strain if the axial span is $66\,\mathrm{mm}$ and the

ε_{a1}	ε_{a2}	ε_r	Resolution of ε_q (%)	Probability of occurring	Probability for non-zero strain change
1	0	0	5.05e-5	4/27	4/24
1	0	1	1.617e-5	4/27	4/24
1	0	-1	1.17e-4	4/27	4/24
1	1	0	1.01e-4	2/27	2/24
1	1	1	3.43e-5	2/27	2/24
1	1	-1	1.677e-4	2/27	2/24
0 or 1	0 or -1	1 or -1	6.667e-5	6/27	6/24
0 or 1	0 or -1	0	0	3/27	N/A
Probable resolution (%)				6.4470e-5	7.2556e-5

Table 3.15: Probabilistic calculation of triaxial strain resolution grouped by output resolution and not showing equal results

diameter is $100\,\mathrm{mm}$, and both axial strains are assumed to have the same resolution. It is shown that the resolution calculated above is only relevant if all transducers change at once and does not represent the normal noise on the data. Assuming that each transducer has an equal probability of increasing, decreasing, or remaining the same, the probability of each combination of transducers movements can be calculated. Given the large datasets being used it is possible to apply the probabilistic model to get an average resolution of $6.4470 \times 10^{-5}\,\%$ assuming a $66\,\mathrm{mm}$ span. The inclusion of the probability of zero change in the resolution calculation is problematic. The resolution has been defined as the smallest none zero change possible. If the possibility of zero strain change is eliminated from the results the triaxial strain resolution becomes $7.2556 \times 10^{-5}\,\%$ for a $66\,\mathrm{mm}$ span, it is this calculation which is used for the triaxial strain resolution. As shown in Figure 3.33 this is far superior to the simple calculation of the resolution. The actual calculation uses the average axial strain resolution, as slight differences in the actual resolution caused by different transducer spans vastly increases the number of resolution permutations while changing the output very little.

The actual change between successive points was measured for an example data set of triaxial strain readings. Slight differences in span for the axial transducers prevented the calculation of the exact theoretical resolution so changes were grouped to the nearest theoretical resolution.

Excluding the $48\,\%$ of results undergoing little or no change, the actual probabilities of obtaining a change in triaxial strain at each level are calculated and summarised in Table 3.16. The highest likelihood occurs at $4.72 \times 10^{-5}\,\%$, the value of change occurring when one of the axial strains changes. This difference from the outlined theoretical framework is likely the result of the directional change imposed

Resolution, based on actual spans (%)	Actual probability (%)	Theoretical probability (%)
1.98e-5	5.2	16.7
2.74e-5	0.6	8.3
4.72e-5	63.9	16.7
6.70e-5	16.3	25.0
9.44e-5	7.2	8.3
1.14e-4	5.7	16.7
1.61e-4	1.1	8.3
Probable resolution	5.73e-5	7.05e-5

Table 3.16: Actual triaxial strain change

on the transducers, such that increase is more likely than decrease for axial transducers. The differing axial resolutions and possibility transducers moving by more than one resolution step makes obtaining a distribution of the triaxial strain resolution for real data problematic to automate. The simplified probabilistic approach without the possibility of zero strain change is therefore utilised as an appropriate approximation.

Limitations of the smoothing spline methodology

The use of smoothing splines to refine the noise out of the data is largely successful, there are however limitations to the approach. Firstly the refinement is not accurate when there are segments of the data oscillating with amplitude more than the resolution. In these cases as the error term is actually based on the sum errors, error can be reduced by more in absolute terms at the sections with higher oscillation amplitude. The error reduction is however minimal when taken as a proportion of the large oscillation so the plot remains peaky. In segments with normal noise the error allowed is lowered, as the error has been allocated to the higher amplitude oscillation so these areas are also less smooth. Second in some stages such as C1 stage 3 the change at the beginning of the stage is rapid, therefore the refined spline does not curve enough and gets the start position of the curve wrong. This is shown in Figure 3.34, if strains were calculated from the refined displacement readings the whole plot would be shifted. By using a refinement on the strain however the error is confined to inaccurate strain at the start of the test stage.

Stiffness calculation

The secant shear stiffness can be calculated simply by Equation 3.9 and can be calculated from both the original and refined data.

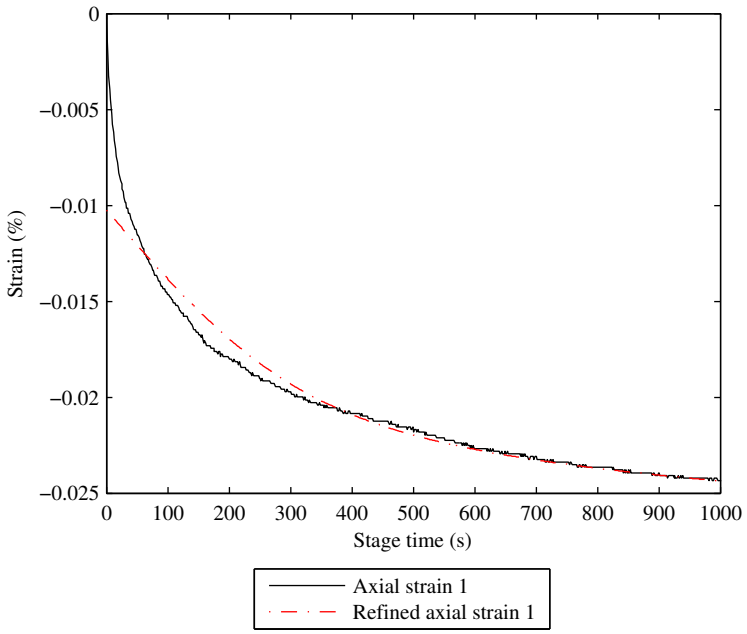

Figure 3.34: Fitting at start problem

$$G_s = \frac{\frac{\Delta q}{\Delta \gamma}}{3} \tag{3.9}$$

The tangent shear stiffness however is only calculated for the refined data. This is because the unrefined data varies so much that a tangent stiffness is meaningless. The refined spline curve can by differentiated to calculate the triaxial shear strain rate (Equation 3.10) and the deviator stress rate (Equation 3.11). It is then possible to calculate the tangent shear stiffness directly from the stress and strain rates, as shown in Equation 3.12.

$$\dot{\gamma} = \frac{d\gamma}{dt} \tag{3.10}$$

$$\dot{q} = \frac{dq}{dt} \tag{3.11}$$

$$G = \frac{\frac{dq}{d\gamma}}{3} = \frac{\left(\frac{dq}{dt}\frac{dt}{d\gamma}\right)}{3} = \frac{\left(\frac{\dot{q}}{\dot{\gamma}}\right)}{3} \tag{3.12}$$

3.5.7 Smoothing to obtain stiffness curves

The refinement eliminates the noise in the transducers and allows a output of a tangent shear stiffness plot. The resulting trend however still contains multiple changes in stress and strain rate that prevent the stiffness output being useful for comparison. This is shown as the refined local deviator stress curve in Figure 3.35 for stress versus strain, and the refined local G line in the stiffness strain plot Figure 3.36.

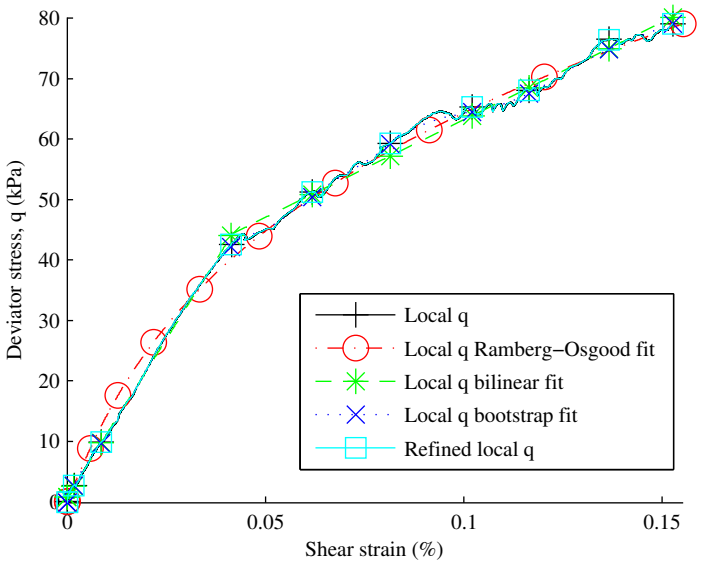

Figure 3.35: Example stress strain plot showing smoothing options

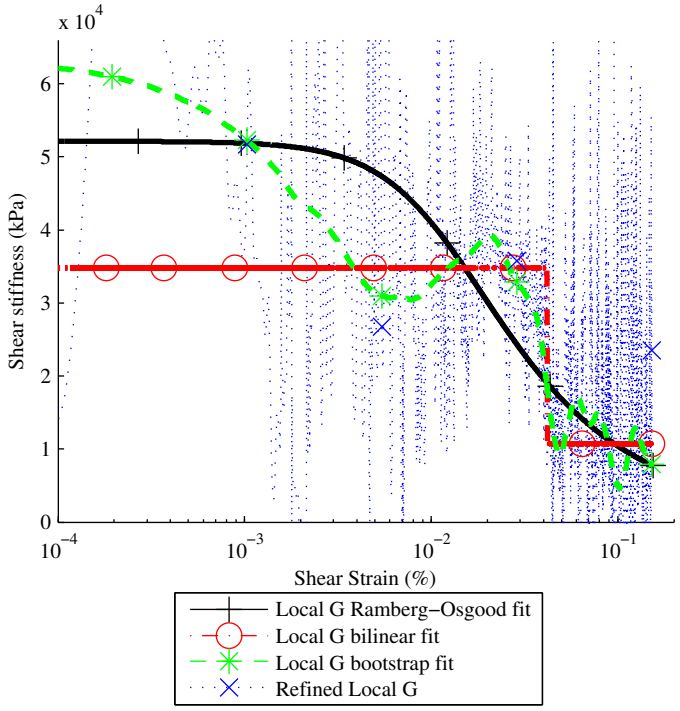

Figure 3.36: Example stiffness plot showing smoothing options

In order to allow the comparison of the stiffness on a log strain scale several smoothing strategies are implemented. The term smoothing is used to differentiate from refinement as the smoothing is a looser fit to the data that allows a greater degree of error from the original data and can impose a new form on the data. Three possible methods of data smoothing are presented here which have varying levels of fit quality and smoothness.

Bilinear fit

The test results were observed to have a distinct change in stiffness, either side of which a linear fit would provide reasonable fit. To accomplish this simple brute force routine is used to test dividing the data set into 2 data sets. A linear equation is fitted to each half of the data in a least squares fashion using Matlab's polyfit with degree 1. The 2 equations produced are then merged at their intersect (not necessarily the same as the split point) to form a single trend line of 2 linear segments. The error between the trend line and the original data is calculated and an overall sum of squared errors (SSE) term is calculated. The split point that minimises the SSE measure is then used as the best fit to the data; the code used can be found in Section B.3.1. The fit to the stress strain plot is reasonable as shown in Figure 3.35, the stiffness plot is however unrealistic and not good for detecting the high stiffness at very small strains, as shown in Figure 3.36. This calculation method is included as it provides a very simple approximation of the transition to a lower stiffness and is useful as an indicative measure of when an stiffness increase effect might end.

Ramberg-Osgood parametric fit

Parametric fitting was performed using a modified Ramberg-Osgood equation to fit stress strain curves near the yield point (Equation 3.13). This fit was used to fit soil stiffness by Pierpoint (1996) but was derived by El-Rimawi (1996) for steel at elevated temperatures.

$$\varepsilon = \frac{\sigma}{A} + B\left(\frac{\sigma}{C}\right)^n \tag{3.13}$$

Where ε is the strain ,σ is the stress and A, B, C, and n are constants to be determined. Theses constants can be fitted using a custom equation and the fitting functions in Matlab to determine the constants by a non linear least squares fit, the code for which is given in section B.3.2 . The fit is only produced on the outbound approach paths and shear paths due to its enforced form. The advantage of this equation is its stiffness curve is by definition an S-shaped trend when plotted on a log strain scale and the stiffness can be calculated arithmetically by Equation 3.14.

$$\frac{d\sigma}{d\varepsilon} = \frac{1}{\frac{1}{A} + \frac{nB}{C}\left(\frac{\sigma}{C}\right)^{n-1}} \tag{3.14}$$

The fit of the function to the data appears reasonable as shown in Figure 3.35. The stiffness trend in Figure 3.36 mirrors the refined stiffness to a greater extent than the bilinear calculation, while retaining a smooth form. The use of this fit is again to facilitate a comparison between stiffness trends while not necessarily representing the true form of the data.

Limited points bootstrap fitting

The limited points bootstrap method attempts to find a stress strain plot that produces a good stiffness output while not applying any prescribed form to the data. This is achieved by the Matlab routine in section B.3.3. The function of this code is as follows:

- The data was divided into sections of approximately $5\,\mathrm{kPa}$ in stress.
- A random point in each of the stress sections was selected.
- The start and end points were also selected.
- A cubic spline curve was plotted through points.
- The process was repeated 1000 times so that 1000 possible fits where produced.
- By taking the median stress at any point a typical result could be found. The median was used to prevent the effects of extreme outliers that would shift the mean.
- Additional curves for confidence bounds where added at the 10 and 90 percentiles.
- The stiffness was gathered from the differentiation of each of the test curves.
- The stiffness of the median stress path is mathematically the same as the median of the individual stress paths stiffness.

The result shown in Figure 3.36 follows the stiffness change of the data more precisely than the bilinear or Ramberg-Osgood fit, but is significantly more readable than the stiffness from the refined data. This method of smoothing has a smoothness controlled by the stress spacing however the repeated fitting eliminates the problems of selecting a limited number of data points.

3.5.8 Parametric fitting for creep strain rate

The long term degradation of the strain rate of a soil undergoing creep can be modelled by Equation 3.15, a simplified version of that proposed by Singh & Mitchell (1968) which was used in the SRD brick model (Clarke 2009).

$$\dot{\varepsilon} = B \left(\frac{t_1}{t} \right)^m \tag{3.15}$$

B = strain rate at some arbitrarily chosen time t_1.
m= negative of the slope of the relationship between the logarithm of strain rate and the logarithm of time.
t = time.
It was found from observation of the creep rates of the test performed that initially the degradation of the strain rate obeyed the log linear Equation 3.16.

$$\dot{\varepsilon} = A - n \log\left(\frac{t}{t_1}\right) \tag{3.16}$$

A = strain rate at some arbitrarily chosen time t_1.
n = negative of the slope of the relationship between strain rate and the logarithm of time.
A parametric solution that transferred from Equation 3.16 to Equation 3.15 at a transition time t_t was defined. Ensuring that both the strain rate and the strain rate gradient were identical at point t_t and defining $t_1 = 1$ parameters m and B could be calculated by Equation 3.17 and Equation 3.18 respectively.

$$m = -\frac{n}{A - n \log(t_t)} \times \frac{1}{\ln(10)} \tag{3.17}$$

$$B = \frac{A - n \log(t_t)}{\left(\frac{1}{t_t}\right)^m} \tag{3.18}$$

It has been shown that the smoothing spline refinement does not produce a good fit to creep strains (Figure 3.34). It is therefore appropriate to fit the parametric equation to the creep strain directly. This is achieved by the integration of Equation 3.15 and Equation 3.16 with respect to time. Integration of the initial part of the fit (Equation 3.16) results in Equation 3.19 with an integration constant $c = 0$ as $\varepsilon = 0$ at $t = 0$.

$$\varepsilon = A \times t - n\left(\frac{t \times \ln(t) - t}{\ln(10)}\right) \tag{3.19}$$

Integration of the second half of the fit (Equation 3.15) is more complicated, when $m \neq 1$ the strain can be expressed by Equation 3.20. The integration constant c is given by Equation 3.21 based on the calculable strain at t_t. When m=1 the strain is expressed by Equation 3.22 with integration constant c expressed by Equation 3.23.

$$\varepsilon = \frac{B\left(\frac{1}{t}\right)^{m-1}}{1-m} + c \tag{3.20}$$

$$c = At_t - n\left(\frac{t_t \times \ln(t_t) - t_t}{ln(10)}\right) - \frac{B\left(\frac{1}{t_t}\right)^{m-1}}{1-m} \tag{3.21}$$

$$\varepsilon = B \log(t) + c \tag{3.22}$$

$$c = At_t - n\left(\frac{t_t \times \ln(t_t) - t_t}{ln(10)}\right) - B\log(t_t) \tag{3.23}$$

The fitting of the parametric fit to the strain vs. time plots obtained for creep stages was performed by a combination of brute force and the curve fitting algorithms

available in Matlab. When the whole equation and all three parameters were evaluated as a customised equation within Matlab curve fitting tool box the solution failed to converge. Instead a brute force method was used to evaluate a finite number of values for t_t. At each value Equation 3.19 was fitted to a maximum of 1000 points extracted from before t_t. The fitted values A and n were then used to calculate the remainder of the fit and compute the fit parameters sum of squared errors (SSE), R^2, $\bar{R}^2$ and root mean square error (RMSE). The value of t_t that produced the best fit was evaluated based on these parameters. By using a reasonable sized data set for the curve fitting and taking advantage of the embarrassingly parallel set-up a solution could be reached in about 5 minutes.

4

Experimental results

4.1 Base soil properties

Samples of weathered London clay were obtained from an underpinning operation carried out by Kier at a depth of approximately $2\,\mathrm{m}$ in Mayfair, London. The moisture content was found to vary between $27.0\,\%$ and $32.5\,\%$ between the outside and inside of the clay masses delivered. Inclusions ranging from 2 to $40\,\mathrm{mm}$ in diameter accounting for $2\,\%$ on the initial dry mass were removed. These inclusions where mainly external to the clay masses and believed to have been included as a result of the foundation construction or removal for underpinning.

Tests to determine Atterberg limits, particle size distribution and density of the clay were carried out. This was manually ground for the purpose of testing so as to pass dry through a $425\,\mu\mathrm{m}$ sieve which was not achieved by the mechanical crushing. Atterberg limits and the specific gravity of the soil grains were measured using the standard techniques described in Head (1998); LL by cone penetrometer and specific gravity by density bottle.

The particle size analyses were performed using a Malvern Mastersizer/E laser diffraction particle size analyser. The test was performed both with and without a sodium hexametaphosphate dispersant and produced the grading shown in Figure 4.1. The clay fraction $<2\,\mu\mathrm{m}$ ($13.1\,\%$ without dispersant and $18.6\,\%$ with) is significantly lower than the $49\,\%$ to $57\,\%$ found at Heathrow (Gasparre 2005). This is because the laser diffraction and pipette method both assume spherical particles and the platy shape of clay particles affects both differently. Work by Konert & Vandenberghe (1997) suggest using the $<8\,\mu\mathrm{m}$ fraction of a laser diffraction to approximate the $<2\,\mu\mathrm{m}$ boundary of a pipette method test. When this is done the clay fraction is $57.0\,\%$ without dispersant and $58.4\,\%$ with. The adjusted value with dispersant is taken as the clay fraction of the soil, although correlation between laser diffraction and pipette method particle size is only an approximation. As was discussed by Eshel, Levy, Mingelgrin & Singer (2004) neither the laser diffraction nor pipette method provide a fully accurate measure of particle size distributions as

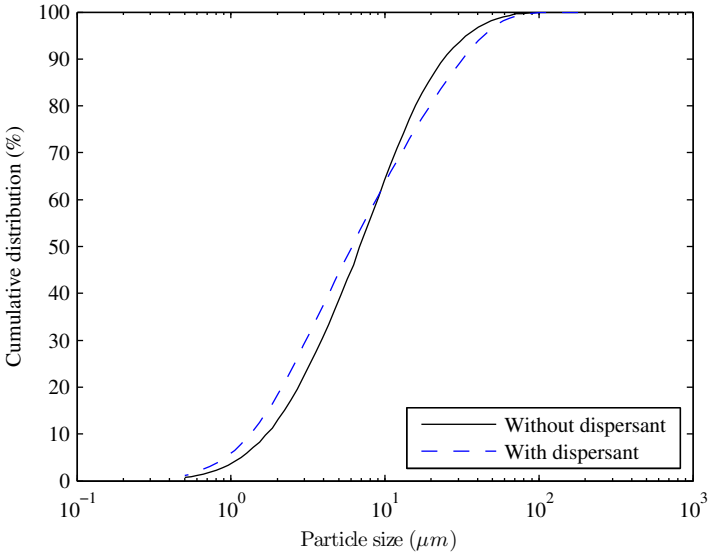

Figure 4.1: Cumulative particle size analyses

	Present Study	Ashford common (Bishop et al. 1965)	Heathrow T5 (Gasparre 2005)
LL (%)	72.26	59 - 75	60 - 71
PL (%)	31.88	21 - 32	24 - 29
PI (%)	40.38	33 - 48	36 - 43
Clay fraction (%)	58.4 [a]	49 - 57	42 - 60
Activity	0.69	0.67 - 0.77	0.67 - 0.86
Specific Gravity	2.69	2.66 - 2.27	2.72 - 2.77

Table 4.1: Soil index properties

[a] Used PSA obtained with dispersant and considers clay to be $<8\,\mu m$

both make assumptions about particle shape. The adjustment is made to reflect the pipette method in this case so comparison may be made to historical results. The index properties and specific gravity are given in Table 4.1. The range of results from tests on London clay in west London from Bishop et al. (1965) and Gasparre (2005) are included for comparison.

4.2 Sample preparation

4.2.1 Consistency of preparation method

The consistency of the sample preparation method can be assessed by the height of the soil placed into the consolidation tube and the moisture content of the clay slurry. The fill heights (Table A.7) were nominally $544\,mm$. Sample O1 was intentionally

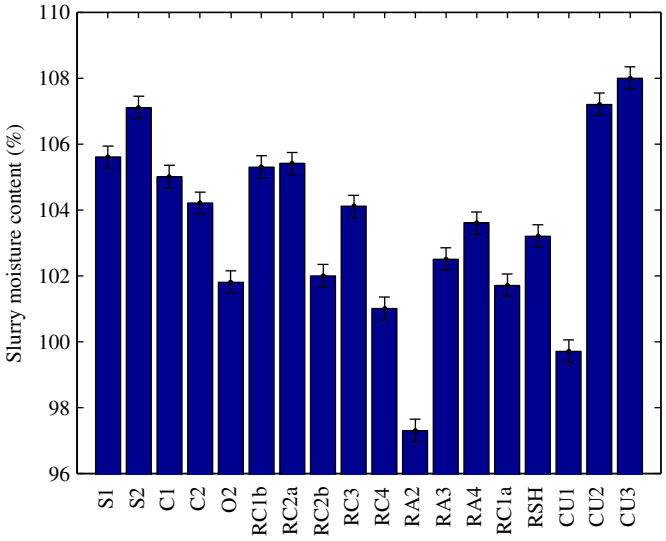

Figure 4.2: Variation of slurry water content

short at $168\,\mathrm{mm}$, while sample S1 was conservatively high at $599\,\mathrm{mm}$, sample C2 and RC1b at $530\,\mathrm{mm}$ were produced slightly short. With these exceptions, due to the refinement of the method the standard deviation of the remaining samples was $3\,\mathrm{mm}$, a result of the error inherent in filling the tube. There was no correlation between starting height and the final sample density, nor between starting height and the final sample height as other factors have a greater impact.

The water content of the clay slurry is shown in Figure 4.2. On average the slurry moisture content is $104\,\%$ with a standard deviation of $3\,\%$. The measurement error for the water content was +-$0.34\,\%$ which is shown as error bars. This variation had no collation with the void ratio of the consolidated sample. The clay slurry had been prepared in a single batch and stored in six tubs until required, a slight drying occurred when each tub was opened for use.

4.2.2 Consistency of resulting samples

The sample water content shown in Figure 4.3 had a mean value of $28.22\,\%$ with a standard deviation across the tests of $1.08\,\%$. The measurement accuracy was established to be $\pm 1\,\%$ as shown by the error bars. The slight upward trend observed has a very weak correlation.

The void ratio was assessed based on the measured density of the trimmed sample and a specific gravity G_s= 2.69. For a $100\,\mathrm{mm}$ sample with a mass of $3\,\mathrm{kg}$ and $28\,\%$ moisture content the measurement accuracy of the specific volume was given as $\pm$0.037465. When assessed as a whole e = 0.8044 $\pm$0.0337 and an upward trend is seen with progressive tests although this is weakly correlated. An increase in the specific volume could not be correlated with the change in sample height or slurry

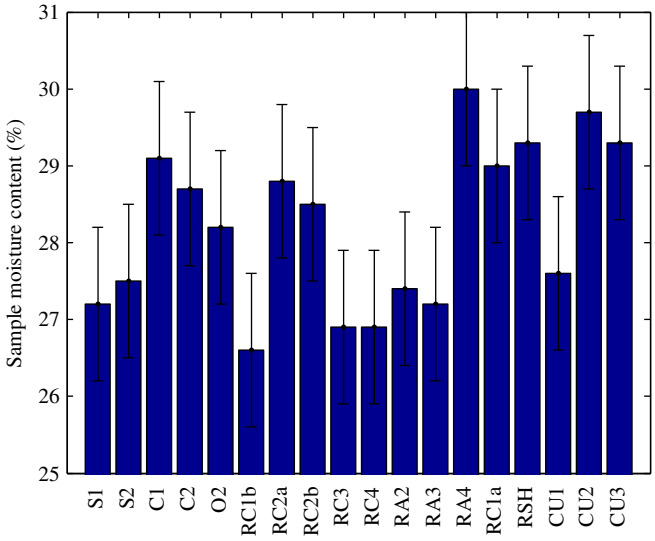

Figure 4.3: Variation of sample water content

water content. The saturation ratio measured after one dimensional consolidation was $94 \pm 2\,\%$. However, this was not considered reliable as it was highly sensitive to the inaccuracies found in sample water content measurement.

Clogging of the porous disks would cause a reduced drainage that would accumulate over successive tests and result in less dense samples towards the end of the sample preparation. As the samples were created in two tubes the effects had to be assessed on each tube individually. As shown in Figure 4.4, tube 1 shows a very weak correlation between specific volume and test number. Tube 2 however shows a steeper trend indicating a more rapid clogging of the disks with a strong correlation.

Measurements of the initial effective stress were made (by the method detailed in Section 3.4.3, p 69) for all triaxial tests except S1. The result for test RA3 was made invalid as a membrane leak prevented the measurement. The high OCR test (HOCR) had an effective stress of $438.7\,\mathrm{kPa}$ while the remaining samples had a mean initial effective stress of $159\,\mathrm{kPa}$. When arranged by the test tube (as shown in Figure 4.5) a decrease in initial effective stress is observed with consecutive tests. Tube 1 shows a small decrease with a moderate correlation that is the result of tests CU1 and CU2. Tube 2 shows a large decrease with a strong correlation. These trends mirror those observed with void ratio. There is a strong correlation between initial effective stress and void ratio as shown in Figure 4.6. On this plot the trend line ignores test RA3 where the initial effective stress was affected by a leaking membrane and is not accurate.

The acceptable range of values was taken as within two standard deviations of the mean of tube 1. This assumes tube 1 was unaffected by clogging and represents

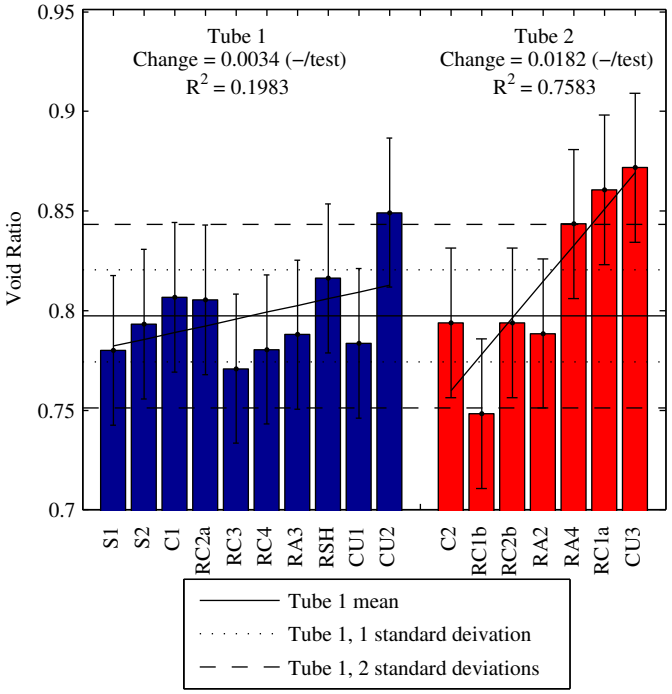

Figure 4.4: Sample void ratio

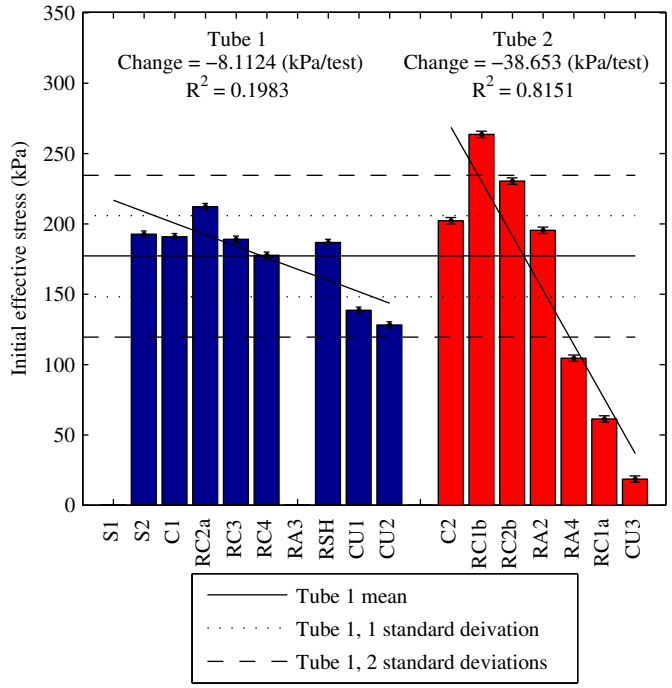

A initial effective stress test was not performed on sample S1 and a membrane leak prevented a meaningful result on sample RA3

Figure 4.5: Sample initial effective stress

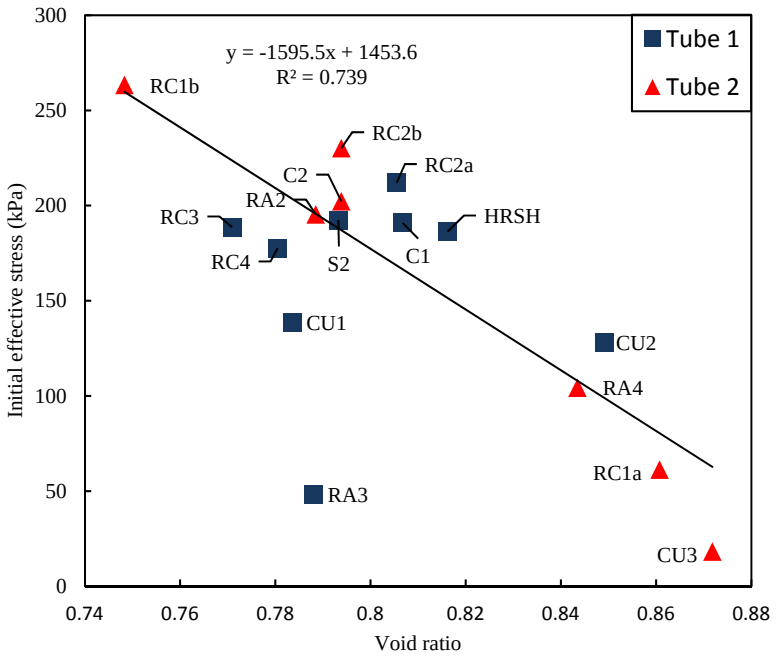

Figure 4.6: Void ratio after 1D consolidation vs. initial effective stress at the start of triaxial test

a normal distribution of results. Under this assumption if all samples had been produced in tube 1 95 % would be considered acceptable. The range of e and initial effective stress allowed is therefore large due to the variance in tube 1. It is expected that the lower consolidation indicated by higher e will result in lower stiffness and strength of the sample. The ranges are shown on Figure 4.4 and Figure 4.5 for void ratio and initial effective stress respectively. Tests RC1b, RA4, RC1a, and CU3 are to be considered erroneous as they are outside this range on both void ratio and initial effective stress. Test CU2 is considered questionable based on the void ratio. It is shown that test RA3 was produced within an acceptable range of void ratio but a leaking membrane limited its use for actual results.

4.3 Factors influencing the effective stress history of the 1D consolidation.

The effective stress history of the one dimensionally consolidated samples will differ from the applied stress history due to the effects of pore water pressure and side friction in the sample tube. The effective stress history of the test is evaluated through the monitoring of the sample and oedometer tests performed on selected samples.

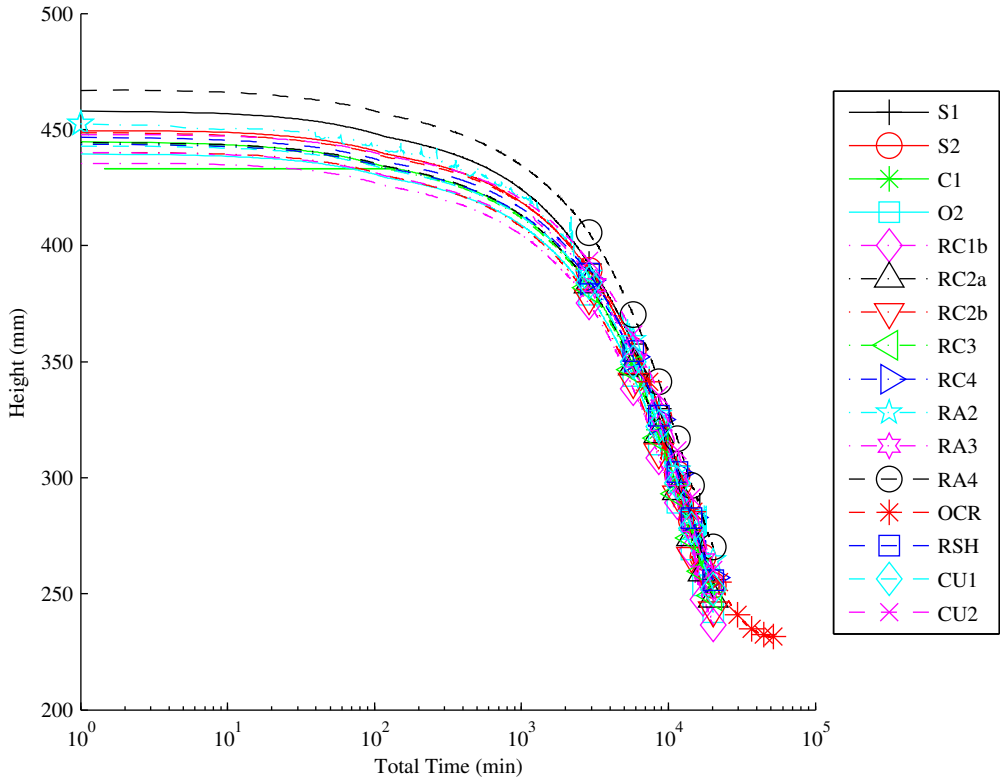

Figure 4.7: Sample hight vs log time for $2800\,\mathrm{kPa}$ applied stress consolidation stage

4.3.1 Incomplete 1D consolidation

The shape of the settlement trace of the 1D consolidation indicated an incomplete consolidation, therefore properties c_v, m_v and k could not be obtained for most consolidation stages using either the square root or log method. The few exceptions to this are detailed in Table 4.2. Test HOCR represented an extended test and therefore produced an extended height vs time plot allowing curve fitting by the log method, as shown in Figure 4.7. Test O1 was a shorter sample so consolidated quicker and test C2 was anomalous in that it consolidated by approximately half the typical amount. A clear end to consolidation can be observed on samples O1 and C2 using both graphical interpretations, c_v is however high for a clay and potentially indicates an anomalous result where displacement was halted before consolidation was complete.

An estimate of the degree of consolidation for those tests that did not consolidate sufficiently can be made using the deformation of the long duration sample HOCR. Curve fitting with a square root method indicated $93\,\%$ consolidation while the log method indicated $102\,\%$ consolidation i.e. some creep occurring. When corrected for piston friction (by the method described in Section 4.3.2) the stress change in this stage was $2554\,\mathrm{kPa}$. Using strains calculated at theoretical $100\,\%$ consolidation,

Test	Pressure increment (kPa)	$m_v(\mathrm{m^2\,MN^{-1}})$	$c_v\ (\mathrm{m^2\,yr^{-1}})$	$k\ (\mathrm{nm\,s^{-1}})$
O1	50-100	1.5023	20.53 +-1.760	9.56 +- 0.92
C2	0-100	0.4654	26.78 +- 0.9477	3.86 +-0.137
HOCR	200-2800	0.1861	0.4179 +-2.464e-4	0.0241 +- 1.42e-5

Table 4.2: Consolidation properties from 1D consolidation

the stiffness $E_0{}'$ was given between $4904\,\mathrm{kPa}$ and $5396\,\mathrm{kPa}$. Using this as the stiffness of the clay for this load increment and assuming this remained applicable to the similar increments in the other tests, the degree of consolidation could be estimated. The difference in assumed $E_0{}'$ caused a difference of $8\,\%$ between the Sqrt and log methods of calculation. The mean degree of consolidation was $85\,\%$ and $93\,\%$ using Sqrt and log methods respectively, the standard deviation between tests using the same method was $3\,\%$.

4.3.2 Piston friction

The assessment of the piston friction was made by two methods. The first was to assess the difference between the TEPC, and the applied pressure calculated from the calibration of the loading piston and the applied air pressure. The piston friction calculated by this method is shown in Figure 4.8 for the duration of the 1D consolidation. The friction observed varied widely with maximum magnitudes between $123\,\mathrm{kPa}$ and $589\,\mathrm{kPa}$ loss in applied pressure. An increase in friction as the test progressed was also notable.

The high magnitude friction values and their increase over the course of the test could be the result of consolidation of the slurry occurring between the tube and the piston below the first o-ring; the residue of which was observed on several tests. A higher piston friction would result in a lower total stress on the sample and hence a higher void ratio and a lower initial effective stress. This result was observed on results from tube 2 with a strong correlation, while results from tube 1 or all the data were not correlated (Figures 4.9 and 4.10). In addition the piston friction was seen to correlate with the test number in the same manner as void ratio and initial effective stress. Any effect of drift on the transducer is negated by the post-test calibration check and adjustment. There is however no plausible mechanism for the piston friction to increase with successive tests as the tube and o-rings were cleaned each time. The reduction in the TEPC reading over time could be a bridging effect as the soil stiffness increases. A reduction between successive tests could be the result of increased stiffness in the clogged porous disks. The TEPC results are therefore not considered a reliable measure of the total pressure in the sample.

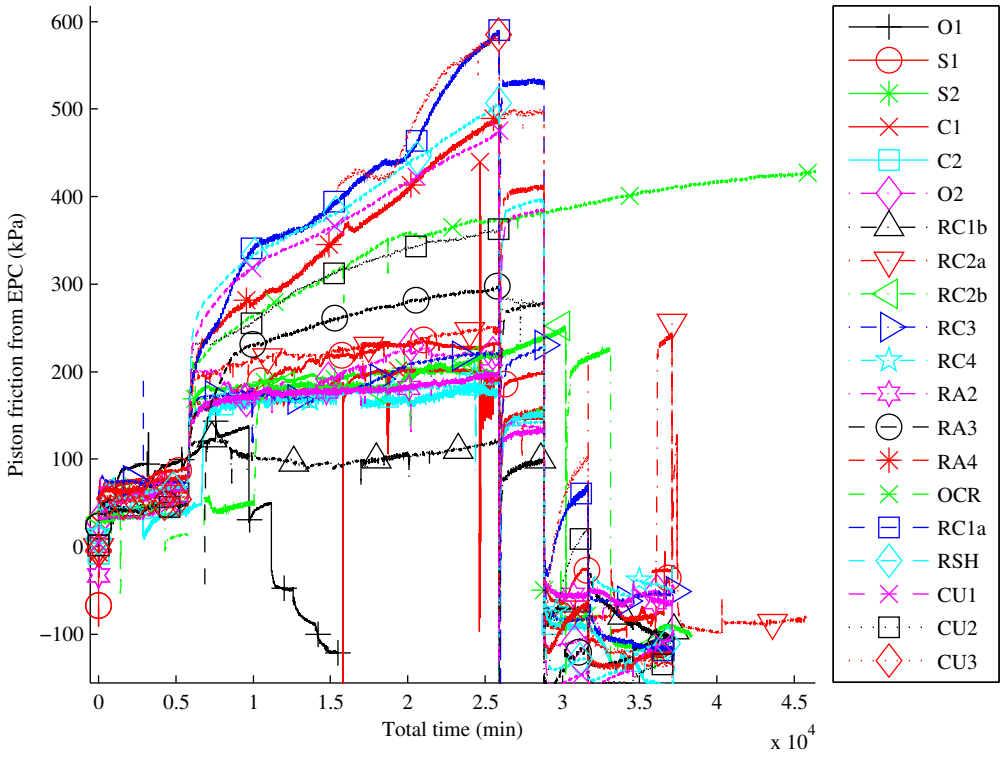

Figure 4.8: Apparent piston friction = applied pressure - TEPC (kPa)

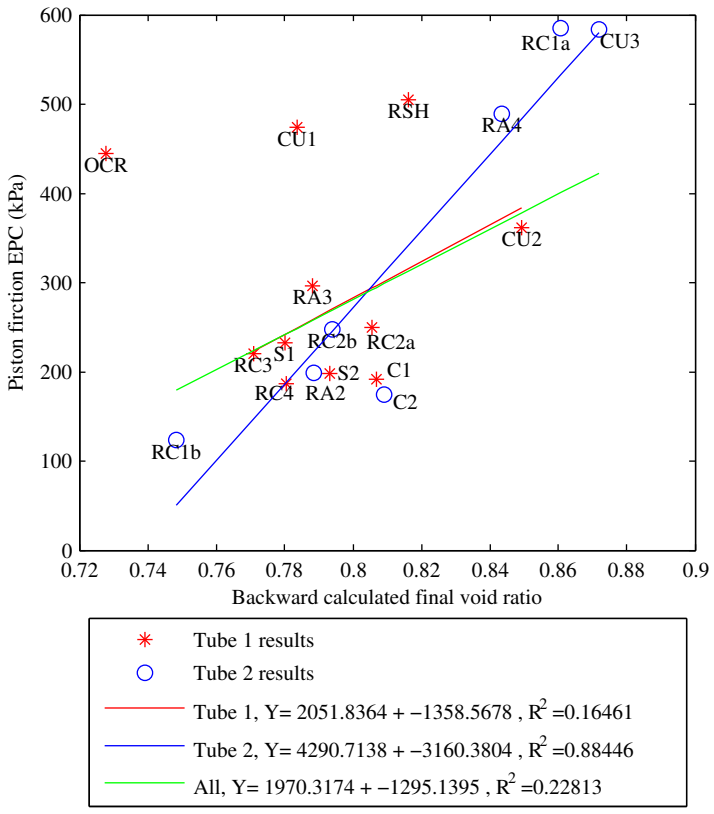

Figure 4.9: Apparent piston friction vs. final void ratio (kPa)

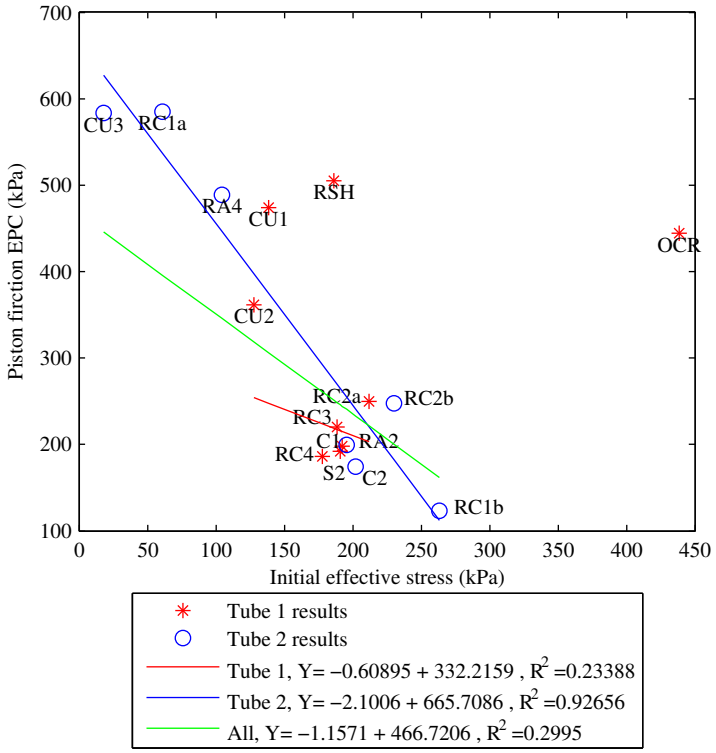

Figure 4.10: Apparent piston friction vs. initial effective stress (kPa)

Friction was also assessed during the water filled pressure tests that were performed to check the transducer calibration. The applied pressure was raised to 2800 kPa over 20 minutes and then lowered back to 0 kPa. The PWP transducer, BEPC and TEPC transducers were logged during this stage along with the applied pressure and piston movement. Figure 4.11 shows the applied pressure against the measured pore pressure for the calibration check after test CU3. It is clear that the increasing and decreasing tests produce different results. The difference is a result of friction opposing the applied pressure when it is increasing but acting with it when decreasing. Consequently the actual applied pressure can be assessed as the average of the increasing and decreasing paths. The effective direction does not change immediately on a reversal in applied pressure direction but transitions over a small stress range. To account for this, a subset of results is taken at the upper end of the PWP range for increasing pressure and the lower end for decreasing pressure.

A linear regression through the selected data range is used to generate a simple model for increasing and decreasing applied pressure vs. PWP. The friction at any PWP can then be calculated as half the difference in applied pressure between the two model lines. In addition to the friction there is also the possible mis-calibration of the PWP transducer. If calibrated correctly the average between the increasing and decreasing path would be coincident with the equality line where PWP = ap-

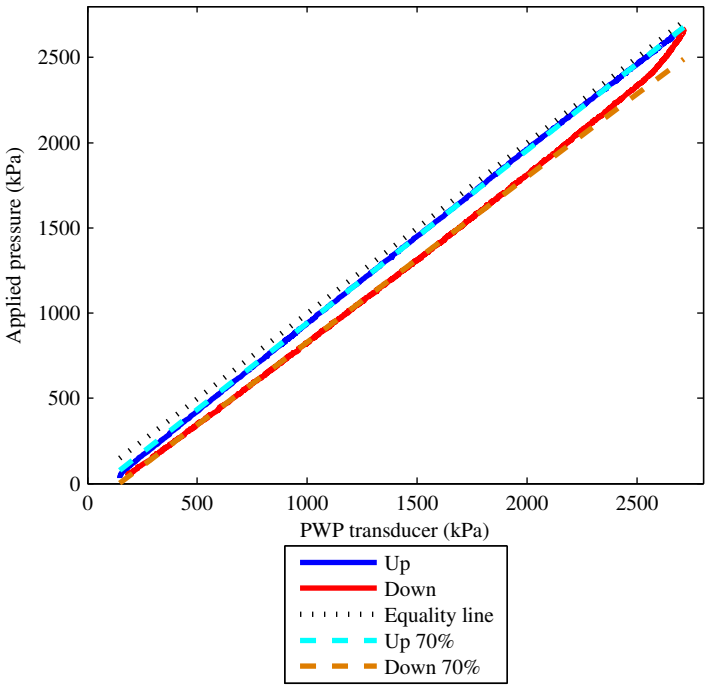

Figure 4.11: Example post test calibration (kPa)

plied pressure. Figure 4.11 shows a particular large distortion to the calibration. The calibration correction is calculated so that the average between the model increase and decrease path is transformed to the equality. The BEPC and TEPC are then calibrated to this modified PWP transducer. The data range selected influences the calculation of both friction and the adjustment to PWP, BEPC and TEPC calibration. A data range of 70 % of the PWP range of the test was selected based on the shape of the decreasing path to eliminate the curve of the transition but retain a representative dataset.

Parameters to relate piston friction to applied pressure are given in Table 4.3. This shows a lower friction with a smaller range than that from the TEPC reading. The observed variation in friction could be as a result of misalignment of the apparatus and changing o-rings after damage. The friction correction used was that obtained from the pressure test following the consolidation.

	Intercept (kPa)	Gradient	Calculated at 2800 kPa (kPa))
Mean	34.7367	0.0176	84.0527
Standard Deviation	8.4493	0.0090	21.3613
Min	12.7002	-0.0041	29.7505
Max	49.6362	0.0343	132.4088

Table 4.3: Piston friction calculations from post consolidation calibration check

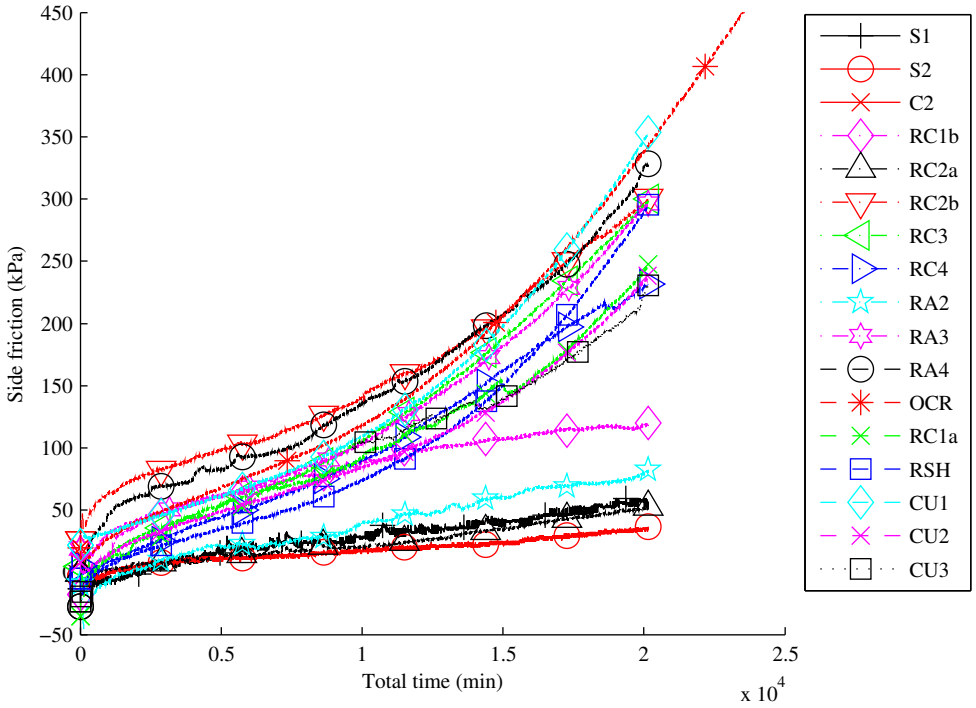

Figure 4.12: Side friction = TEPC - BEPC during 2800 kPa consolidation stage

4.3.3 Side friction

The side friction is taken as the difference between the two earth pressure cell (EPC) measurements. As shown in Figure 4.12 this increases with time through the course of the test as expected. There is however a wide range of friction magnitudes such that after 336 hours at 2800 kPa applied pressure, the standard deviation of the side friction is 126 kPa, around a 186 kPa mean. It is not possible to comment conclusively on the side friction along the sample due to the potential inaccuracies of the EPC stress measurement. There is also no correlation between the side friction and either the output void ratio or initial effective stress as would be expected if it were an actual measurement.

For the purpose of completeness the BEPC and TEPC and data obtained during the 1D consolidation is presented in Figure 4.13 and 4.14 respectively. These trends show how the EPCs responded to the loading steps and provided an indication of applied pressure but also the gradual lowering of the measured stress thought to result from bridging as the soil stiffens. The range of the readings observed also indicates the data quality problems that prevent the readings providing any useful additional insights.

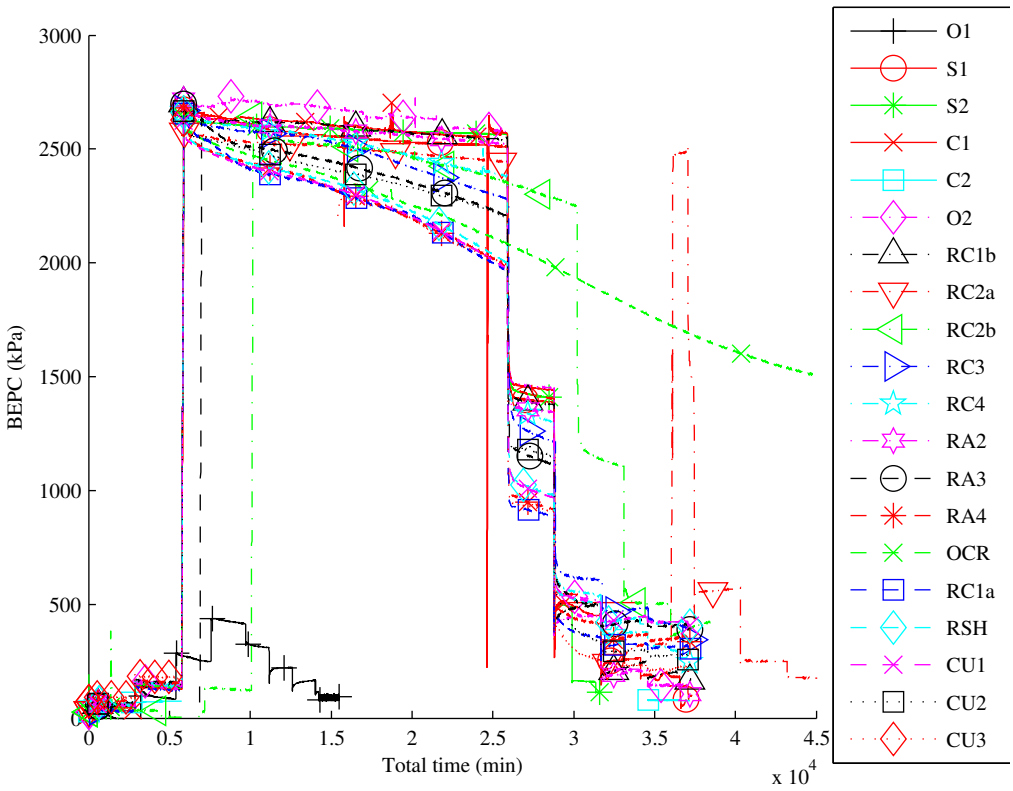

Figure 4.13: BEPC data during 1D consolidation

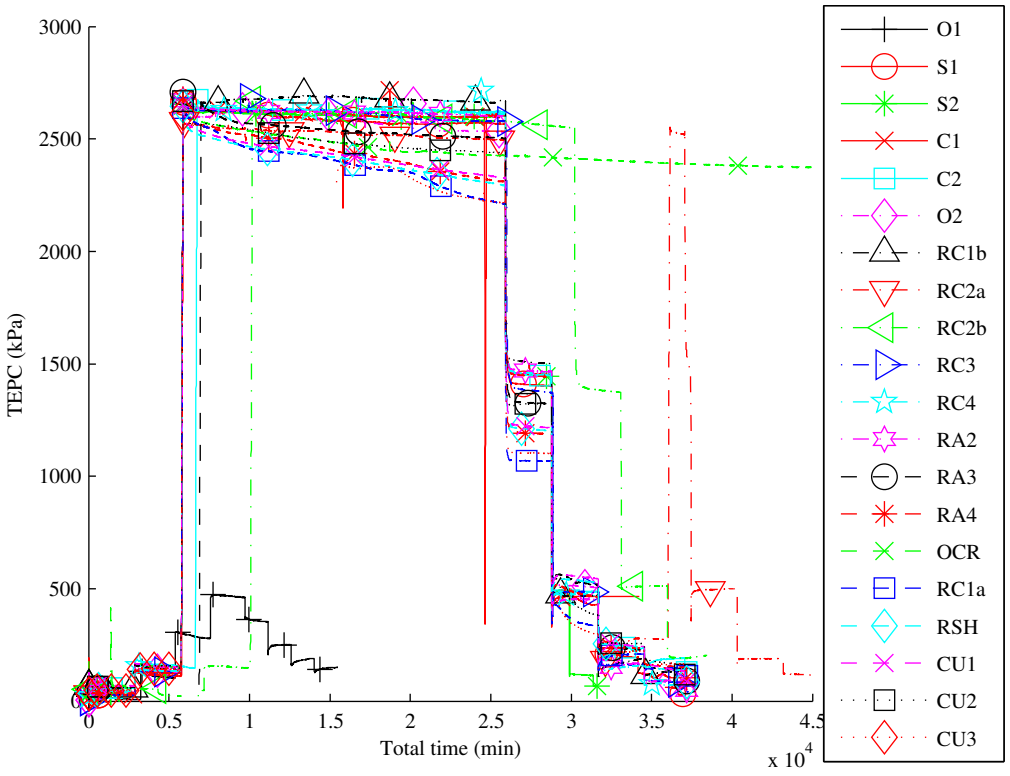

Figure 4.14: TEPC data during 1D consolidation

4.3.4 Effective stress

The effective stress measurement is derived from the pore pressure transducer located $110\,\mathrm{mm}$ from the base. The pore water measurement was erratic on tests RC3, RC2b and the first $10\,\mathrm{days}$ of HOCR, which have been removed from Figure 4.15 showing the development of effective stress. Test RA4 was also removed as it showed a very rapid decrease in pore pressure that indicated a leak around the pore pressure transducer and did not match the trend observed in the rest of the data.
The long duration consolidation (HOCR) showed a more reliable PWP reading at the end of the stage and reached an effective stress of $2640\,\mathrm{kPa}$ at the end of the stage. As PWP had dropped to $72\,\mathrm{kPa}$ from $2647\,\mathrm{kPa}$, $97\,\%$ of the excess PWP had dissipated. Attempts were made to fit the parabolic isochrones solution for one dimensional consolidation to the HOCR data set in order to obtain a full PWP profile from PWP at the measurement point. The large stress range and a large change in void ratio of the test stage however allowed significant changes in permeability and stiffness though the tests. It was therefore not possible to correctly model the settlement and so no inference on the PWP distribution in the sample could be made.

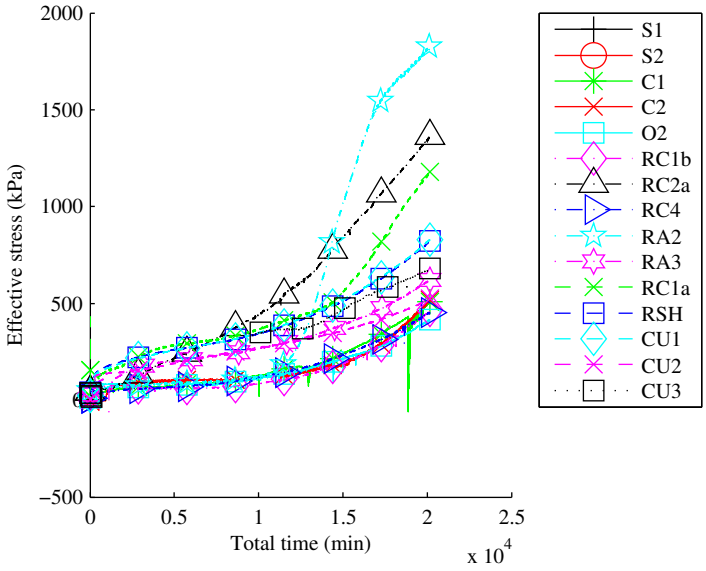

Figure 4.15: Effective stress = applied pressure - PWP measurement, during $2800\,\mathrm{kPa}$ consolidation stage

Given that the relative height of the PWP transducer at a point in time would be similar in each test due to the fixed position and similar settlement plots, the range of PWP measurement is excessive. Two weeks into the $2800\,\mathrm{kPa}$ consolidation stage, the effective stress of those tests not excluded varied from $417\,\mathrm{kPa}$ to $1827\,\mathrm{kPa}$ with an $838\,\mathrm{kPa}$ mean and $456\,\mathrm{kPa}$ standard deviation. This variation does not correlate with the output void ratio, initial effective stress or the order of the testing. The

transducer readings must therefore be considered unreliable and the effective stress applied to the sample cannot be determined from the pore water measurement.

4.4 Saturation and consolidation

As described in Section 3.4.3 and 3.4.4, the one dimensionally consolidated samples were isotropically confined to determine the initial effective stress before an automated saturation and consolidation to $p' = 300\,\mathrm{kPa}$. The initial effective stress has already been discussed in Section 4.2.2 as its magnitude relates to the 1D consolidation process, not to the saturation or consolidation. The quality of the saturation and consolidation are discussed after an explanation of some problematic results.

4.4.1 Experimental problems

Discrepancy between pore and back pressure

In order to correctly assess the effective stress of the sample the pore pressure and back pressure must be set to read zero when open to atmosphere. This was meant to be achieved by setting a soft zero of the back pressure and pore pressure before the test. It transpired however that on several occasions the pore pressure had not been zeroed (as the back pressure was zeroed after filling the ADVDPC it was considered harder to miss, hence the problem was assumed to be pore pressure). On these occasions the $0.7\,\mathrm{m}$ height between the top of the sample and the location of the pore pressure would, along with other factors, increase the pressure reading without an adjustment and would read higher than the back pressure. To resolve this the difference between PWP and back pressure was calculated and a horizontal line was fitted to the point representing the base line. An example of this for a single test is shown in Figure 4.16 with the adjustments used for all tests given in Table 4.4.

Pauses in consolidation stage

The consolidation stage was meant to run for 5 to $6\,\mathrm{days}$ for each test. This was often complicated however by a termination of the test when the back pressure cylinder became full, a situation that occurred due to the $200\,\mathrm{mL}$ back pressure cylinder being close to the end of its travel at the start of consolidation or on those stages later identified as having leaked. As the samples were unable to drain when the test was stopped data acquisition was also paused. The test time has been adjusted for the purposes of this discussion to not increase while there is no drainage on the consolidation stage. As the cell volume was not actively held when the test had ter-

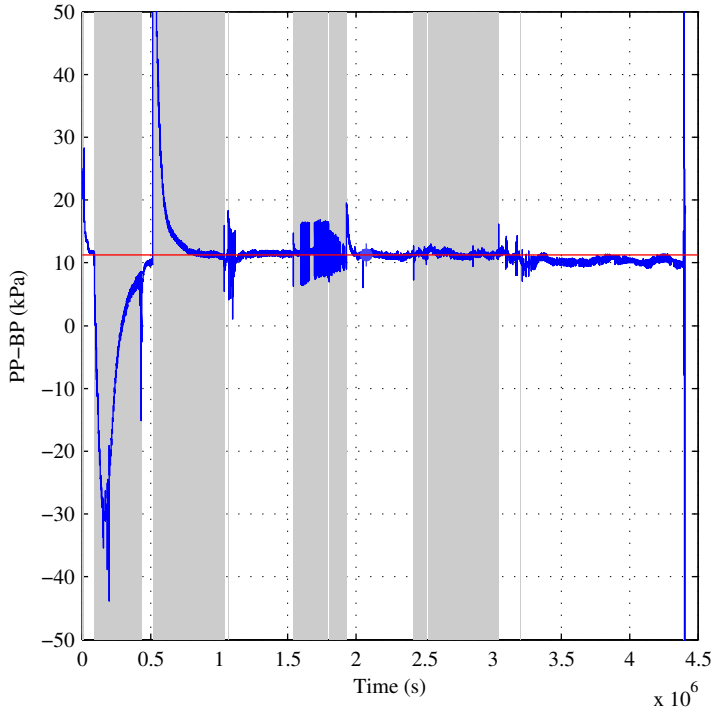

Figure 4.16: Example of pore pressure base line

minated, there is some movement of local strain transducers that appears as a sharp change in strain.

Leaks in sample membrane

It was found on two occasions that the sample membrane had leaked allowing a fluid flow from the cell into the sample. The first of these leaks occurred during test RA3 and was noted during the course of the testing as an excess of pore fluid left the sample, equivalent to $81\,\%$ of the original sample volume. This level of

Name	Base line offset (kPa)	Name	Base line offset (kPa)
S1	9.32	RA2	0.17
S2	6.85	RA3	6.11
C1	10.80	RA4	-0.19
C2	-0.68	HOCR	3.77
RC1b	9.81	RC1a	1.67
RC2a	-27.84	HRSH	8.09
RC2b	10.17	CU1	0.93
RC3	11.30	CU2	12.04
RC4	-0.19	CU3	-9.94

Table 4.4: Pore pressure baseline

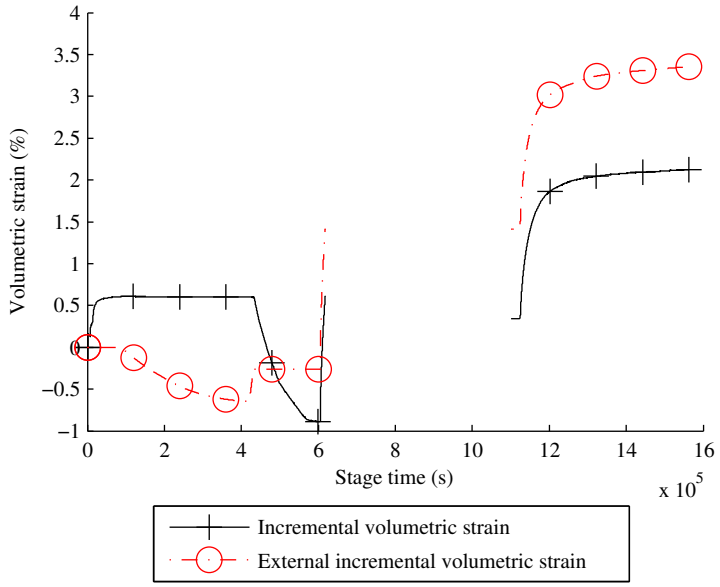

Figure 4.17: Evidence for a leak in test RC4

flow negates its use as a reliable test. A second leak in the membrane was observed on test RC4 during the saturation stage of the test. As shown in Figure 4.17 the external volumetric strain reverses direction at the end of the saturation stage. The flow of fluid out of the sample is stopped by the B-check stage. Consequently the back and pore pressures increase toward the cell pressure, giving a B value of 2.58 and allowing the sample to swell as the effective stress reduces. It appears however that the leak self-clogged during the consolidation stage, the volumetric strain from consolidation to the end of the test is $0.5\,\%$ from the movement of pore fluid and $0.3\,\%$ from the observed local strains. This discrepancy is within the range commonly observed as a result of barrelling and problems with the radial transducer.

Measurement of sample dimensions

The measurement of the sample dimensions was complicated by the failure of the local radial transducer on some of the tests. Without a local diameter measurement it was impossible to accurately track the sample volume through the stages before complete saturation was achieved and back volume would provide a reliable volume change indicator. A volume change could not be obtained from the cell volume measurement as the effect of dissolution of air into the cell fluid, and the movement of the lower chamber could not be calibrated reliably. It was also found that the sample was responding anisotropically so the local axial strain could not provide an accurate volume measurement.

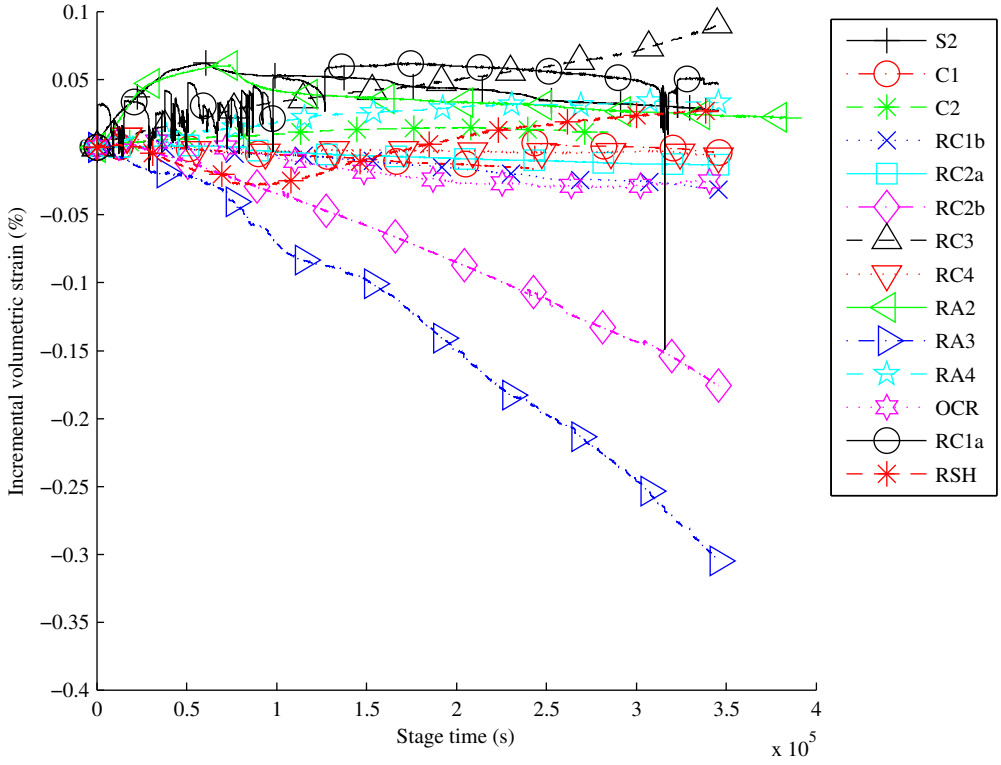

Figure 4.18: Volumetric strain during saturation

4.4.2 Saturation

Holding of constant effective stress

The saturation stage was set up to hold p' constant at level of the initial effective stress, while increasing the back pressure to $400\,\mathrm{kPa}$. This was intended to minimise any volume change during the saturation stage. The volumetric strain of the samples during the saturation stage is shown in Figure 4.18. It can be seen that test RC2b and RA3 show a larger than typical amount of swelling. The swelling of RA3 is a result of the membrane leak while RC2b had a $-36\,\mathrm{kPa}$ effective stress change due to a programming error. This was in excess of the typical -1.3 to $8.1\,\mathrm{kPa}$ change across the saturation stage.

Degree of saturation

Due to the problems associated with gaining an accurate measurement of the sample volume, it was not possible to accurately gauge the volume of air which went into solution during the saturation stage. This was compounded by the potential inaccuracy in the initial measurement of void ratio and saturation. The degree of saturation was therefore assessed by the use of a B-check with $50\,\mathrm{kPa}$ cell pressure change occurring after the saturation. The results of this check are shown in Table 4.5 as maximum and final values for both the pore pressure and back pressure

change.

	From back pressure		From pore pressure	
	Max	End	Max	End
S2	0.96	0.92	1.02	0.99
C1	0.96	0.92	1.04	1.03
C2	0.97	0.93	1.04	1.03
RC1b	0.96	0.95	1.02	1.01
RC2a [a]	0.96	0.58	1.29	0.86
RC2b	0.92	0.85	1.02	0.99
RC3	1.04	1.00	1.06	1.05
RC4 [b]	2.56	2.43	2.58	2.57
RA2	1.03	1.03	1.08	1.08
RA3 [c]	0.96	0.94	1.01	1.00
RA4	0.98	0.97	1.04	1.03
HOCR	0.86	0.69	1.20	1.19
RC1a	1.01	1.01	1.01	1.01
HRSH	0.95	0.88	1.00	0.89
CU1	1.05	1.05	1.01	1.01
CU2	0.96	0.89	0.94	0.91
CU3	1.03	1.01	1.01	1.00

[a] Unreliable pore pressure transducer
[b] Membrane leak, became self clogged
[c] Membrane leak, not yet evident

Table 4.5: B values after saturation

The results show a generally high B value (>0.9) consistent with at least $99\,\%$ saturation for a medium to stiff clay. There are however some anomalies: the B-values greater than unity are an indication that the internal fluid pressure increased more than the confining pressure. This occurs most frequently on the pore pressure measurement where the pore pressure has not equalled the back pressure at the end of the saturation stage. Another complication is the decay in the back and/or pore pressure away from the maximum value, shown as a reduction in B-value. This is thought to be the result of an uneven pressure distribution within the sample. If both pore pressure and back pressure decrease from a maximum during a B-check (such as with test HRSH shown in Figure 4.19) this indicates a flow towards the centre of the sample. If there is a decrease in back pressure accompanied by an increase in pore pressure this indicates a flow to the pore pressure transducer, such as for test HOCR shown in Figure 4.20. These flows indicate an incomplete saturation of the sample and as such the flow of water out of the sample during consolidation will be less than the observed volume change. The lack of an accurate volume measurement

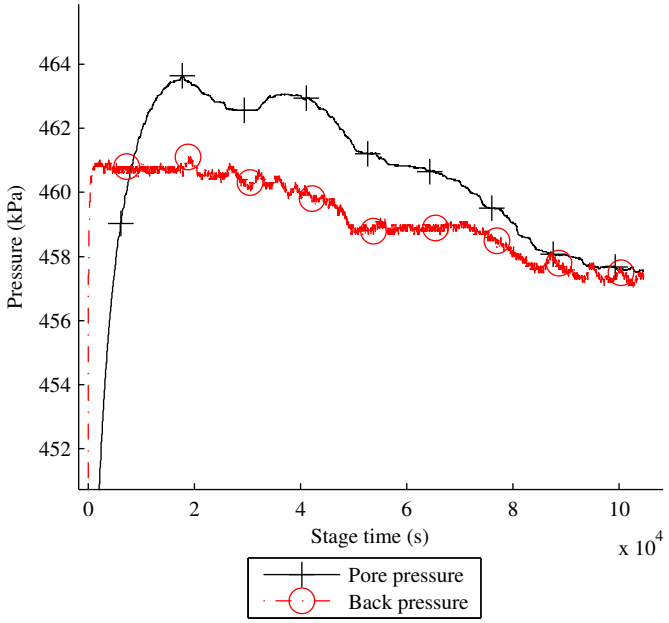

Figure 4.19: Pore pressure change during test HRSH flow to centre

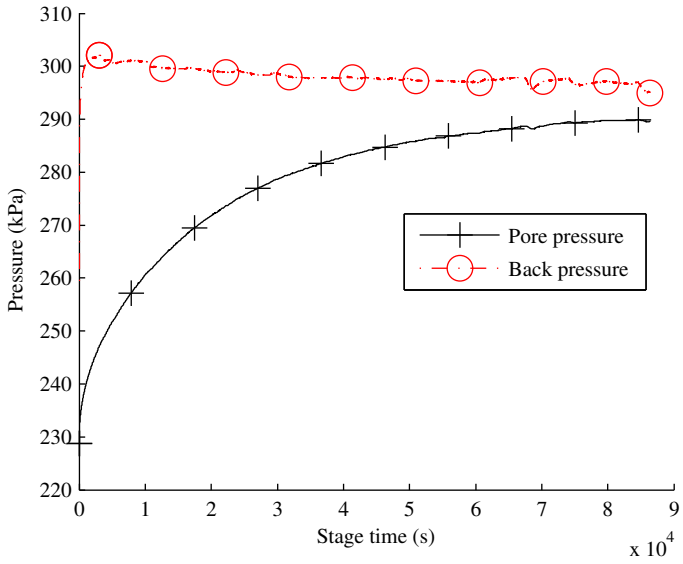

Figure 4.20: Pore pressure change during test HOCR flow to end

prevents this from being reliably observed however.

4.4.3 Consolidation

All of the samples for the main RSH testing program were consolidated to p'=300 kPa. The completion of the consolidation was assessed based on the dissipation of the excess pore water pressure, the observed local strain rate, and the observed flow rate of pore fluid.

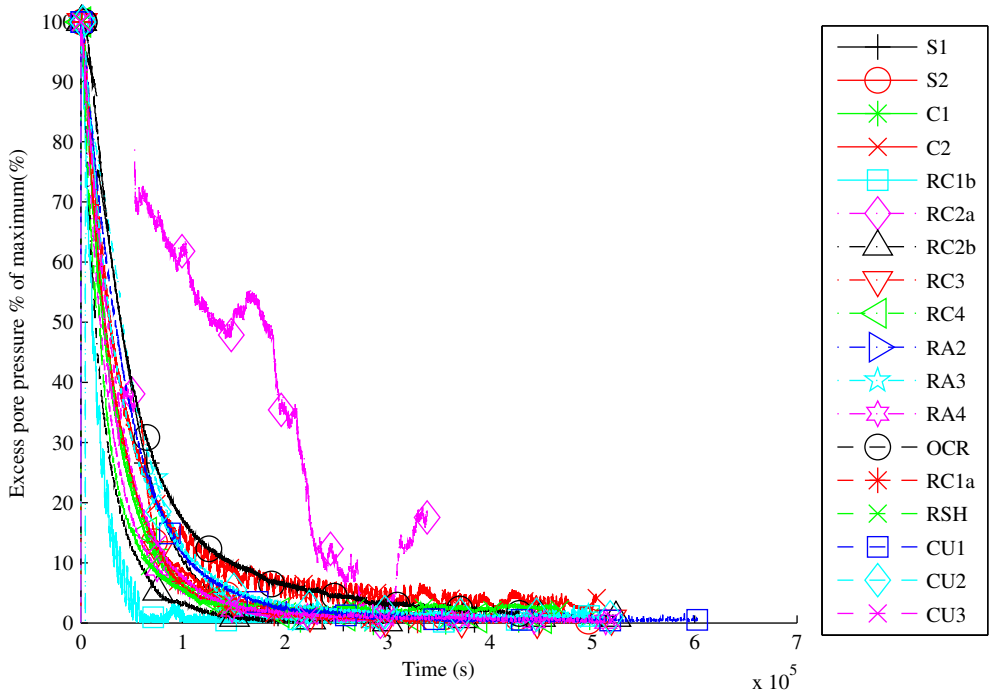

Figure 4.21: Excess pore pressure dissipation during isotropic consolidation

Dissipation of excess pore pressure

The dissipation of excess pore water pressure as measured by the pore pressure transducer was shown to be on average 99% complete. This excludes the leaking test RA3, RA2 which had no data logging due to an electrical fault, and RC2a which had a fault on the PWP transducer evidenced by the atypical degradation plot shown in Figure 4.21.

Residual strain rates

Residual strain rates, expressed in terms of the volumetric strain on the sample occurring per hour, were calculated from both local strain measurement and externally measured sample volume change. The results are shown in Figure 4.22 and 4.23 for local and external measurements respectively. These both show how the strain rate dips to below $0.003\,\%\,\mathrm{h}^{-1}$ for all tests; a point at which the rate is determined by the noise in the transducers.

Resulting void ratio at the end of consolidation

At the end of the consolidation stage, the void ratio of the samples was compared to ascertain the impact of the saturation and consolidation procedure on the sample consistency. Problems with the reliability of the radial strain transducers complicated the process of a reliable void ratio measurement. To provide an estimate, the

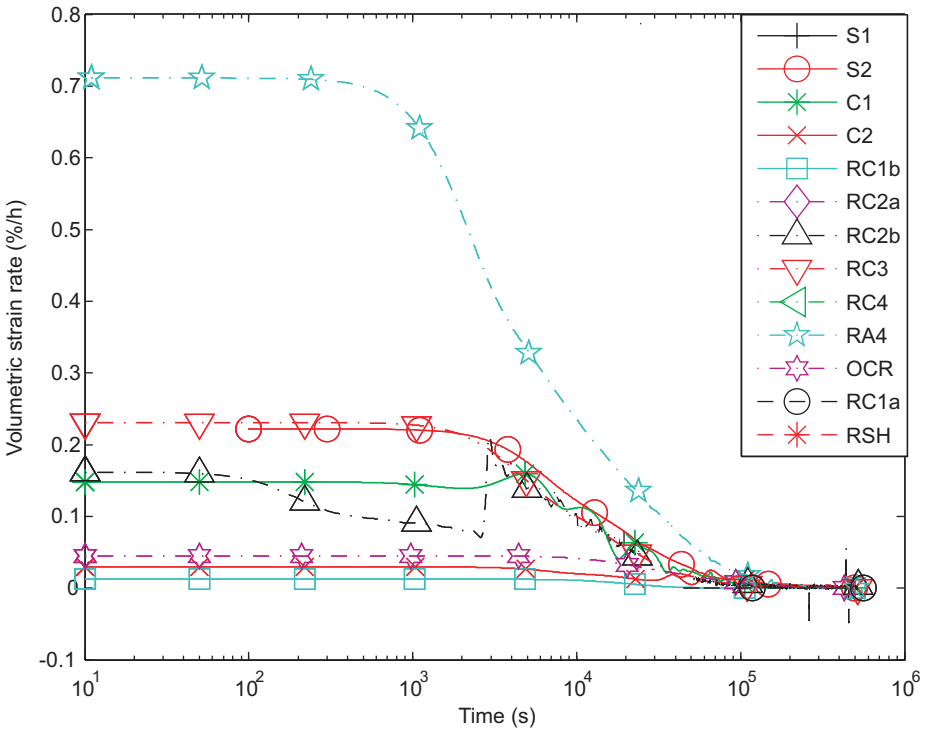

Figure 4.22: Locally measured volumetric strain rate

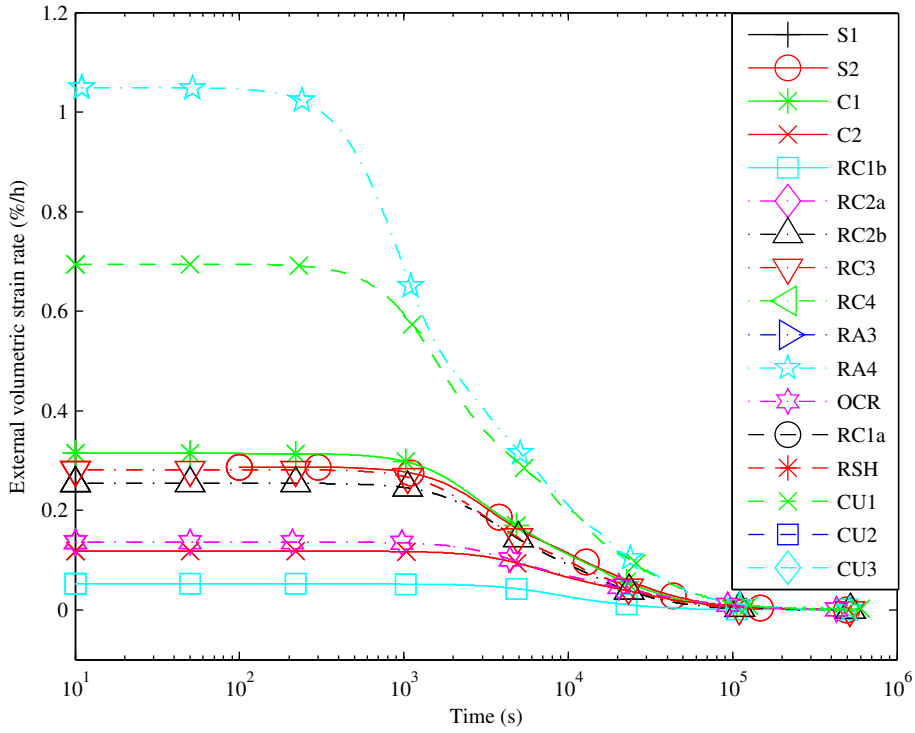

Figure 4.23: Back volume derived volumetric strain rate

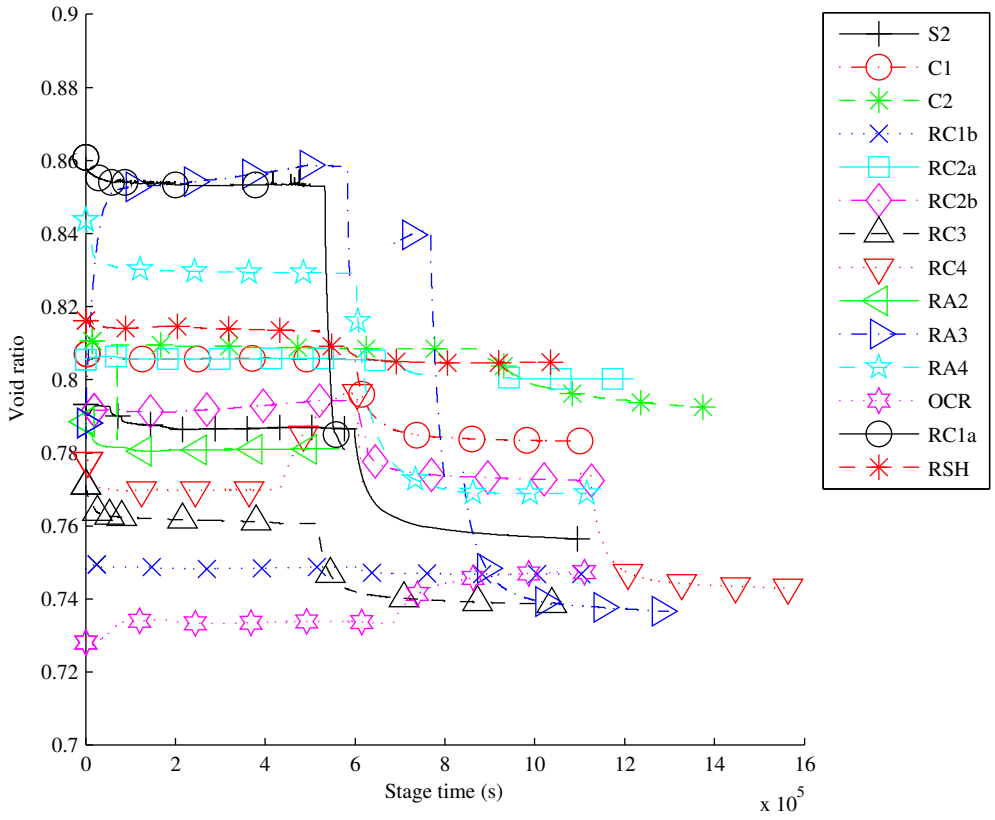

Figure 4.24: Void ratio change during saturation and consolidation stages

sample was assumed to act isotropically so the radial strain was taken equal to the local axial strain. The void ratio through the saturation and consolidation process is shown in Figure 4.24. As indicated in Table 4.6 the consolidation process has reduced both the mean void ratio of the samples and the range of values taken.

Name	Start	End
Mean	0.796	0.781
Range	0.131	0.057
Standard deviation	0.034	0.016

Table 4.6: Void ratio change during consolidation

4.5 Characterisation of strength and stress history

4.5.1 Oedometer results

The oedometers tests performed allow an estimate to be made of the pre consolidation pressure σ'_{vc} and the value of the constants C_c and C_r. Table 4.7 gives these results: σ'_{vc} was derived by the Casagrande graphical construction of e vs. log σ'_v

plots, the mean is assessed over test O2 and S1 only as test O1 had a lower applied pressure (Detailed results for m_v, c_v and k in Appendix C in Tables C.1 to C.5). As expected there is a clear negative correlation between σ'_v and initial void ratio e when comparing between the samples consolidated from slurry under either $600\,\mathrm{or}$ $2800\,\mathrm{kPa}$ applied vertical stress. When examining results consolidated under the same applied stress however there is no correlation due to the uncertainty in e and σ'_v.

A rough comparison between the measured maximum vertical effective stress and that deduced from the oedometer test is available on sample O2M where σ'_{vc} = $525\,\mathrm{kPa}$ and the maximum vertical effective stress estimated from the piston friction corrected applied pressure and mid height PWP measurement is $673\,\mathrm{kPa}$, this occurred during the $1600\,\mathrm{kPa}$ swelling stage.

An estimate of the mean effective stress p'_m reached during the 1D consolidation is made by approximating $K_0 = 1 - \sin(\phi')$ where ϕ' =20.9° this gives p'_m = $414 \pm 21\,\mathrm{kPa}$. Thus when at the standard isotropic stress state of p' = $300\,\mathrm{kPa}$ used for trixaial testing the samples are lightly over consolidated.

The oedometer test also noted some degree of swelling during the 50, 100 and $200\,\mathrm{kPa}$ stages on test on samples S1 and O2. The 50 and $100\,\mathrm{kPa}$ stages showed significant swelling and so the next increment was applied after a short time (<2 h) the $200\,\mathrm{kPa}$ did not swell in the first few hours and so was left overnight for a stage duration of between 16 and $24\,\mathrm{hours}$. While no formalised assessment was made a swelling pressure between 200 and $400\,\mathrm{kPa}$ can be estimated from the observed deformation.

			Reconsolidation		Swelling		
Test	C_c	v_1	C_r	v_1	C_r	v_1	σ'_{vc} (kPa)
O1B [a]	0.164	2.790	0.054	2.164	0.059	1.940	239
O1T [a]	0.162	2.783	0.049	1.114	0.055	1.920	287
O2B	0.137	2.617	0.047	0.979	0.057	1.968	531
O2M	0.129	2.554	0.018	0.917	0.041	1.846	525
O2T	0.134	2.550	0.034	0.888	0.044	1.834	544
S1 B	0.120	2.455	0.026	0.840	0.050	1.891	592
S1 T	0.120	2.435	0.035	0.873	0.053	1.881	526
Mean	0.138	2.598	0.038		0.051		544
Standard deviation	0.018	0.143	0.013		0.007		28

Table 4.7: General consolidation properties from oedometer tests

[a] Used the low pressure consolidation test to a $600\,\mathrm{kPa}$ applied vertical stress instead of the usual $2800\,\mathrm{kPa}$

4.5.2 Vertical anisotropy

The oedometer test O2 provided an opportunity to examine the anisotropy of the sample on the vertical axis. Table 4.8 shows how the degree of consolidation varies through the sample. The total load on the sample is highest at the top and is reduced by side friction towards the base. The pore water pressure also increases towards the sample centre. This is highlighted by the effective preconsolidation stress which shows a decrease between the top and the base due to side friction and a minimum at the centrer due to PWP distribution. The same trend is observed with the sample unit weight and the inverse with the sample void ratio. As sample strains are assessed over the central third of a sample taken from the centre of the produced sample it is assumed that there will be minimal effects of vertical anisotropy over the measured span.

	Preconsolidation pressure (kPa)	Unit weight ($\mathrm{kN\,m^{-3}}$)	Starting void ratio	Water content
O2T	544	19.76	0.715	28.85%
O2M	525	19.12	0.812	31.70%
O2B	531	19.42	0.728	27.55%

Table 4.8: Parameters indicating vertical anisotropy from test O2

4.5.3 Assessment of anisotropy during isotropic consolidation

The sample was consolidated one dimensionally to σ'_{vc} = $544\,\mathrm{kPa}$ or p'_m = $414\,\mathrm{kPa}$ (based on the oedometer results) which would induce some cross anisotropy. The subsequent release of confining pressure and isotropic consolidation to p'= $300\,\mathrm{kPa}$ is unlikely to be sufficient to completely remove this anisotropy. Due to problems with the local radial transducer, the only good quality local strain data for the consolidation stage is for test RC3 where the ratio n'= ${E_v}'/{E_h}'$ = 1.40. Taking all tests that had a working radial transducer and no leaks (S1, S2, C1,C2, RC2b, RC3 and RA4) a range of n'=$1.34\ \pm 0.44$ is found.

4.5.4 Undrained shear strength

CU triaxial tests

A series of CU tests described in Section 3.4.8 were performed to establish the large scale shearing properties of the clay. These are detailed in Table 4.9. Of the samples tested, test CU2 and CU3 shearing from p'=$400\,\mathrm{kPa}$ and p'=$200\,\mathrm{kPa}$ respectively

resulted in the formation of a distinct shear plane. Calculating from the measured vertical displacement at the end of the test, the slip plane formed at ε_a = 14.2 to 14.8 % on test CU2 and ε_a = 10.7 to 12.7 % on test CU3. The difficulty in precisely measuring the vertical deformation on the slip plane would result in a potentially erroneous distortion to the results if any corrections were made based on the slip plane movement. Hence the only correction made was the automated recalculation of the sample area as the test progressed.

Test name	Consolidation pressure (kPa)	Peak deviator stress q (kPa)	Mean effective stress p' at peak (kPa)	Axial strain ε_a at peak (%)	Axial strain ε_a at slip (%)
CU3	200	140	144	8.3	10.7 to 12.7
CU1	300	197	253	6.8	
CU2	400	224	280	10.0	14.2 to 14.8

Table 4.9: Test results CU triaxial tests

The stress displacement plots for the 3 test performed shown in Figure 4.25 shows no clear sign of a peak which would have been characteristic for a over consolidated clay. There is however a drop off after the formation of the slip plane. When plotted in terms of effective stress ratio M' (Figure 4.26) test CU1 and CU2 converge at M' =0.81 while test CU3 shows a peak stress ratio M'=0.96. Assuming a zero cohesion solution M' is related to ϕ' by equation 4.1 giving ϕ'=20.9° for CU1 and CU2 but ϕ'=24.4° from CU3.

$$M' = \frac{6 \sin \phi'}{3 - \sin \phi'} \tag{4.1}$$

Similar remoulded samples of London clay at Heathrow Terminal 5 (Gasparre 2005) and Ashford common (Bishop et al. 1965) have ϕ'=21.3° and ϕ'=20.1° respectively. The effective stress path plot in Figure 4.27 shows how CU3 does not fit the trend from CU1 and CU2. From the angle of the shear plane to the horizontal of θ=56° and θ=52° for CU2 and CU3 respectively and given that θ = 45° + ϕ' /2, it is calculated that ϕ'=22° and ϕ' = 14° respectively. This is a simplistic analysis based on drained data and does not make any account of dilation. This shows how the approximation of ϕ' is appropriate to observed failure.

QU triaxial tests

The results of the set of quick undrained tests on 38 mm samples described in section 3.4.10 are given in Table 4.10. The undrained shear strength from the vertical test is s_u = 208 kPa. The horizontally obtained samples gave too wide a range of result to be confident in assigning a undrained shear strength based on the limited

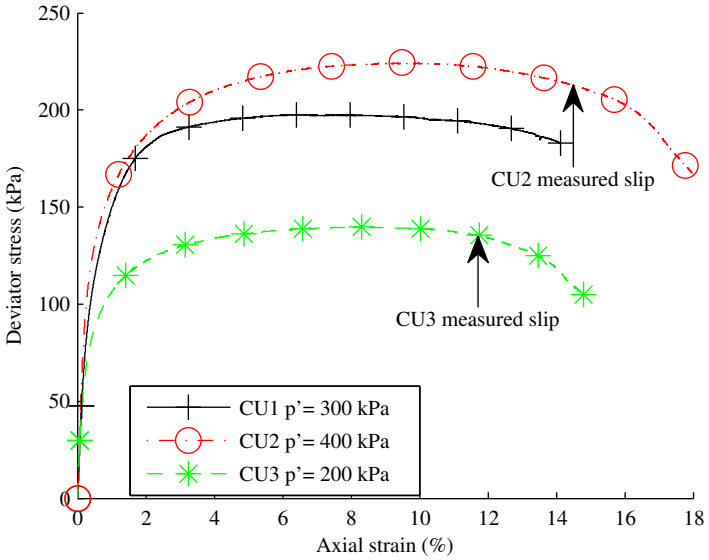

Figure 4.25: Deviator stress versus axial strain CU tests

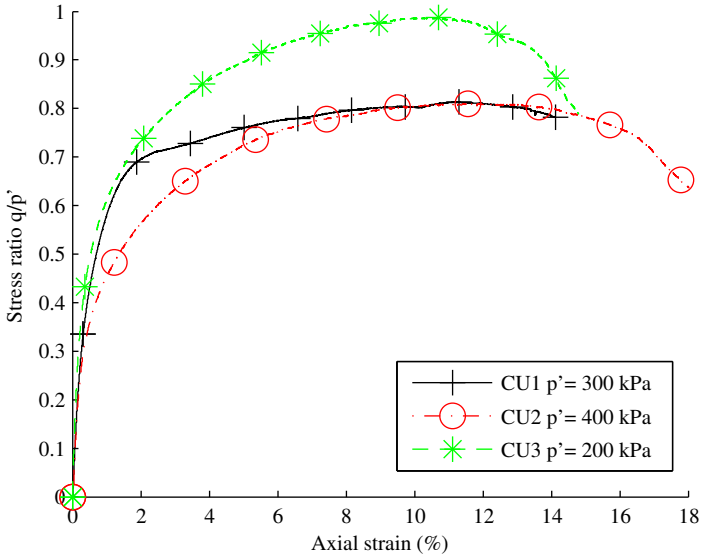

Figure 4.26: Effective stress ratio versus axial strain CU tests

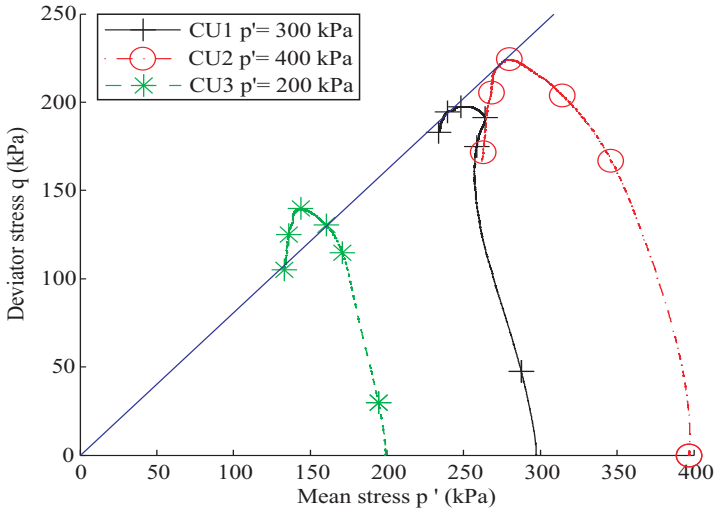

Figure 4.27: Effective stress paths CU test

results. It is also therefore not possible to asses the any effect of anisotropy on strength. The form of the failure did however indicate the presence of anisotropy as those samples obtained horizontally failed by slip while this obtained vertically bulged.

Sample	Confining pressure (kPa)	Deviator stress peek (kPa)	Failure mechanism
V1	400	198.2	Bulging at base
V2	400	220.2	Bulging at top
V3	500	205.5	Bulging at top
H1	400	221.7	Slip at top
H2	400	321.9	Slip at base

Table 4.10: Results of QU tiaxial tests

4.6 Ascertaining range for RSH test program

This section describes the tests performed prior to the main testing program to establish the appropriate approach path length and creep time range to use in the RSH tests.

4.6.1 Initial shear tests

Test outline

In order to define a safe working region undrained shear tests were performed in compression and extension, S1 and S2 respectively. The samples were saturated and consolidated isotropically to p'=300 kPa by the procedure described in section 3.4. Schematic representations of the constant p stress path followed are given in Figure 4.28 and Figure 4.29 for tests S1 and S2 respectively. Two sets of stress paths were followed in each test. The first was conducted at the $0.0001\,\mathrm{mm\,min^{-1}}$ displacement rate used in the future RSH tests and applied $0.2\,\%$ axial strain. The second set at a rate of $0.001\,\mathrm{mm\,min^{-1}}$ was used to investigate higher strains impractical at the slower rate.

Limits on usable stress region

The primary goal of the two tests was to determine the appropriate level of deviator stress for the RSH tests. The tests at $0.0001\,\mathrm{mm\,min^{-1}}$ reached deviator stress of $63.5\,\mathrm{kPa}$ and -$28.6\,\mathrm{kPa}$ in compression and extension respectively without any clear indication of yielding. The test at $0.001\,\mathrm{mm\,min^{-1}}$ (shown in Figure 4.30) reached $q = -112\,\mathrm{kPa}$ and $186.5\,\mathrm{kPa}$ in extension and compression respectively. There was

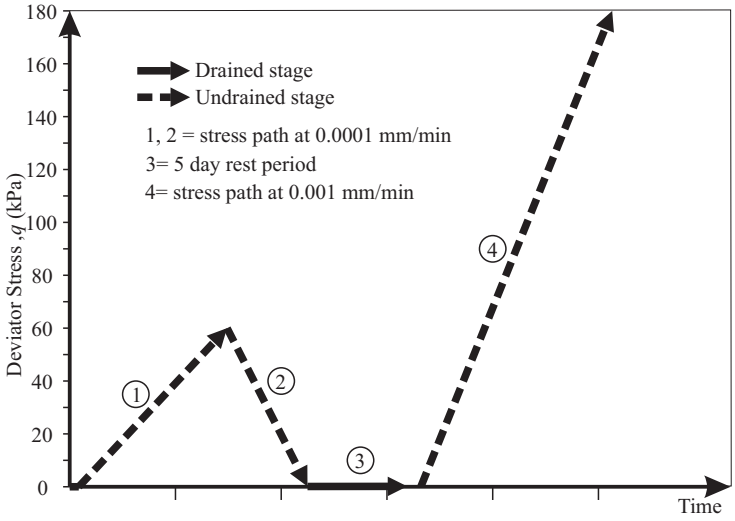

Figure 4.28: Schematic of test S1

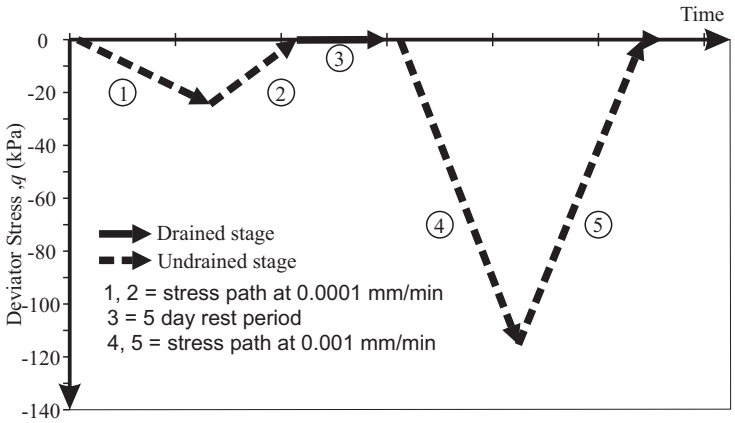

Figure 4.29: Schematic of test S2

again no indication of failure consistent with the failure predicted for ϕ'=20.9° at q=243 kPa in compression and q=191 kPa in extension.

The limiting factors determining the range of approach paths to use are the minimisation of plastic strain and the time taken. These are both controlled by the reduction in shear stiffness. This was observed from Figure 4.30 as the point where the stress strain plot diverged from a linear trend. A limit of 60 kPa in extension and 80 kPa in compression was therefore imposed on the length of the shear probes.

Approximating the location of Y_1 and Y_2 yield points

The locations of the kinematic Y_1 and Y_2 sub yield surfaces as defined by Jardine (1992) where obtained from the initial shear (S) and creep (C) test series. A manual evaluation was made of Y_1 as the end of constant shear stiffness. Y_2 was assessed manually as the point of change in effective stress path direction for undrained paths, or point of deviation from a linear trend on ε_q vs. ε_v for drained stress paths.

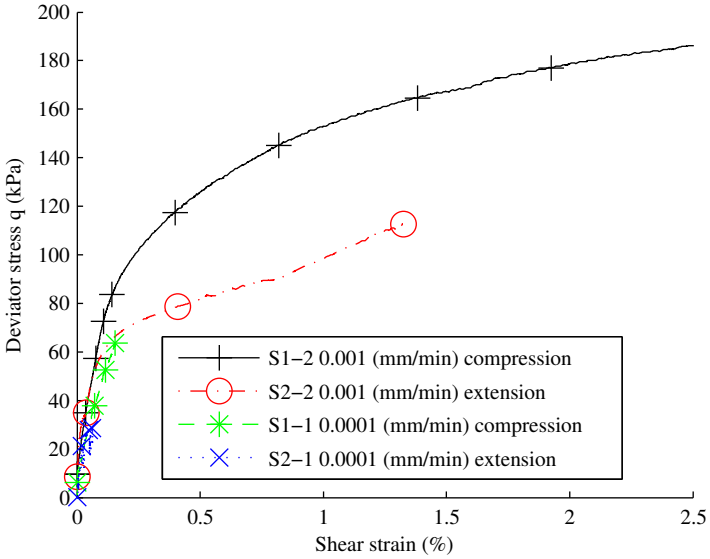

Figure 4.30: S1 and S2 stress strain paths

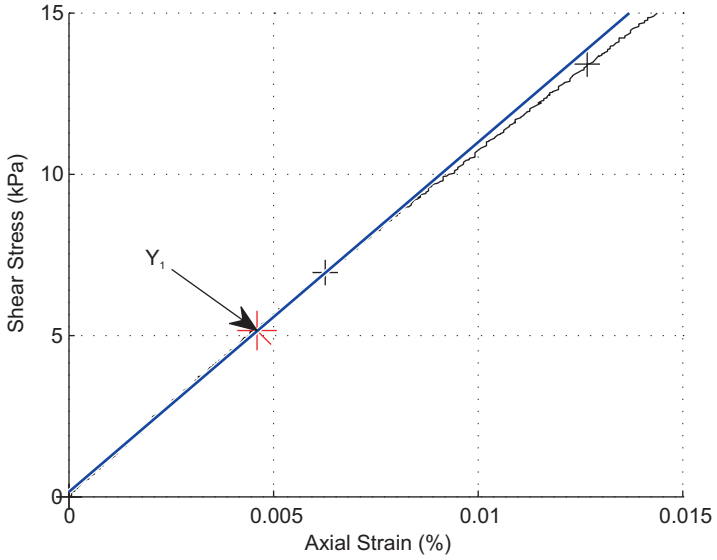

Figure 4.31: Example Y_1 fitting test C2 shear 3

An example of the derivation is shown for test C2 shear 3 in Figure 4.31 and Figure 4.32 for Y_1 and Y_2 respectively. The data was of insufficient quality to draw the full sub yield surface for Y_1 and Y_2 in the p' q space as done by Gasparre et al. (2007). Using the initial results from tests C1 and C2, which did not have the non zero starting stress observed in S1 and S2, it was possible to approximate Y_1 at q= 3.24 kPa $\pm$ 1.61 kPa, and Y_2 at q=23.7 kPa $\pm$ 4.7 kPa. Given this data the approach path was tested at lengths of 15, 30, 45 and 60 kPa so that the effect of approach paths crossing the Y_2 yield surface could be observed.

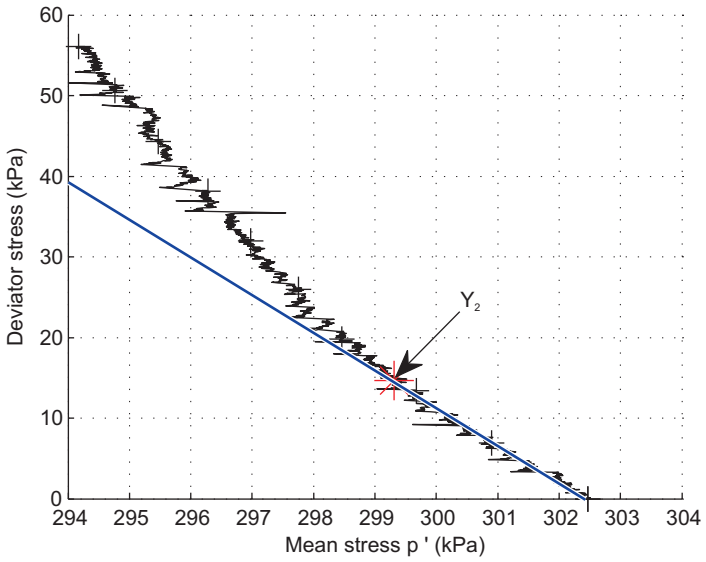

Figure 4.32: Example Y_2 fitting test C2 shear 3

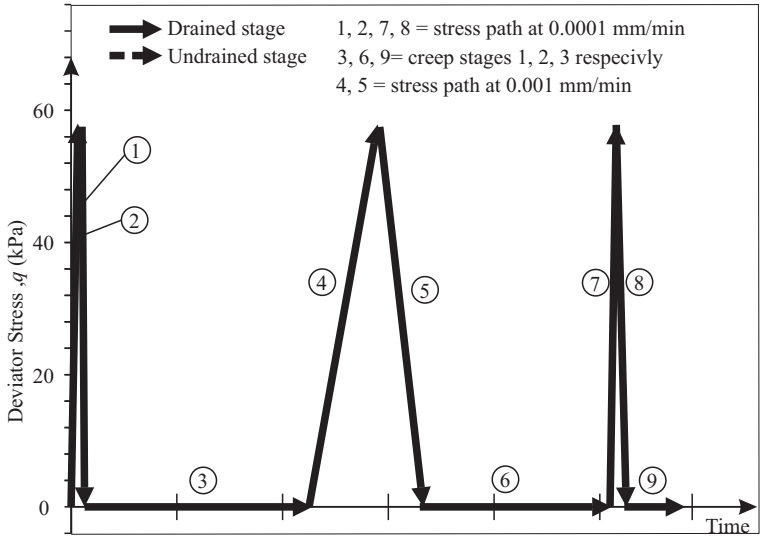

Figure 4.33: Schematic of test C2

4.6.2 Initial creep tests

Test outline

The creep at an isotropic stress state p'=300 kPa following a stress path from 0 to 60 kPa and back was compared in test C1 and C2. C1 began with a $0.0001\ \mathrm{mm\ min^{-1}}$ applied displacement rate and C2 began with a $0.001\ \mathrm{mm\ min^{-1}}$ displacement rate. No usable data was produced by test C1 due to temperature variation so multiple stages were performed on test C2 as shown schematically in Figure 4.33.

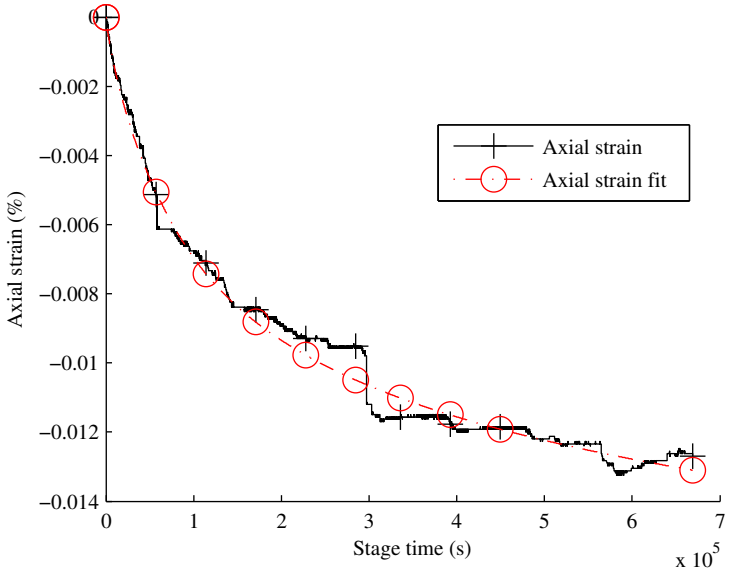

Figure 4.34: Fitting of axial strain during C2 creep stage 2

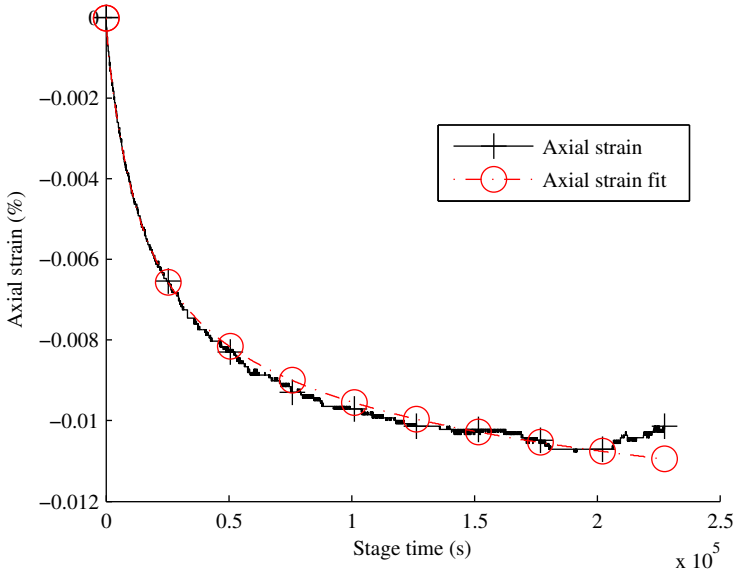

Figure 4.35: Fitting of axial strain during C2 creep stage 3

Creep rate

The axial strain rate degradation of the creep 2 and creep 3 (respectively stages 6 and 9 in the test schematic) was assessed using the method detailed in Section 3.5.8. The fit to the strain plot is shown in Figure 4.34 and Figure 4.35 for creep 2 and 3 respectively. The fit is of a high quality as illustrated by the high R^2 values and low RMSE given in Table 4.11. The parameters of the fit are given in Table 4.12 to be read with reference to Equation 3.15 and 3.16.

The idealised strain rate degradations obtained from stages creep 2 and creep 3 are given in Figure 4.36. In Gasparre et al. (2007) a negligible creep rate is de-

	R^2	Adjusted R^2	RMSE
C2 creep 2 drained post 0.0001	0.98	0.98	4.4E-04
C2 creep 3 drained post 0.001	0.99	0.99	2.1E-04

Table 4.11: Fit quality for initial creep tests

	A	n	t_t	B	m
C2 creep 2 drained post $0.0001\,\mathrm{mm\,min^{-1}}$ ($8.3 \times 10^{-7}\,\%/\mathrm{s}$)	4.29E-7	7.87E-8	113931.9	1.21E-2	1.11
C2 creep 3 drained post $0.001\,\mathrm{mm\,min^{-1}}$ ($8.3 \times 10^{-6}\,\%/\mathrm{s}$)	1.81E-6	3.91E-7	18539.5	1.88E-2	1.20

Table 4.12: Fit coefficients for initial creep tests

fined as $<1 \times 10^{-4}\,\%/\mathrm{h}$, while the creep rate after a limited creep time of $3\,\mathrm{hours}$ was given as $1 \times 10^{-3}\,\%/\mathrm{h}$. As detailed in Table 4.13 the strain rate dips below $1 \times 10^{-4}\,\%/\mathrm{h}$, $35\,\mathrm{hours}$ after the $0.0001\,\mathrm{mm\,min^{-1}}$ path (creep 2) and $20\,\mathrm{hours}$ after the $0.001\,\mathrm{mm\,min^{-1}}$ path (creep 3). For both creep stages however the strain rate after $3\,\mathrm{hours}$ is lower than $1 \times 10^{-3}\,\%/\mathrm{h}$. As creep tests shorter than $3\,\mathrm{hours}$ are impractical the allowed creep time was based on the magnitude of strain rate change. In order to show the effects of a 10 fold decrease in creep strain rate, as used in the work by Gasparre et al. (2007), creep periods of 3, 36, 72 and $120\,\mathrm{hours}$ were used.

Test	C2 creep 2	C2 creep 3
Applied axial strain rate ($\%/\mathrm{h}$)	3.00×10^{-3}	3.00×10^{-2}
Strain rate at 1 second A ($\%/\mathrm{h}$)	1.50×10^{-3}	6.50×10^{-3}
Strain rate after 3 hours ($\%/\mathrm{h}$)	4.00×10^{-4}	8.40×10^{-4}
Strain rate after 36 hours ($\%/\mathrm{h}$)	9.6×10^{-5}	4.90×10^{-5}
Strain rate after 72 hours ($\%/\mathrm{h}$)	4.50×10^{-5}	N/A
Strain rate after 120 hours ($\%/\mathrm{h}$)	2.50×10^{-5}	N/A
Time at rate at $1 \times 10^{-4}\,\%/\mathrm{h}$ (hours)	35	20

Table 4.13: Creep strain rates

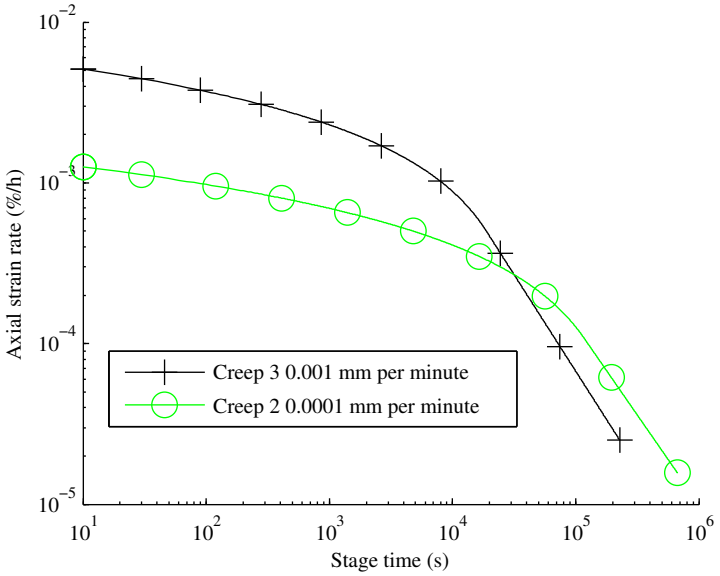

Figure 4.36: Axial strain rates for creep during test C2

4.7 Creep

Introduction

A series of drained creep stages of different durations were run after the conclusion of the drained approach paths within the RSH test series. The duration of each path is set out in Table 3.3 (p48) and the strain rate at the end of creep was expected to be similar to the dedicated creep test C2 creep 2 in Table 4.13. The initial results from applying the creep equation fit (detailed in Section 3.5.8 and demonstrated on test C2 in Section 4.6.2) produced a large degree of variability, as shown in Figure 4.37. The fit of the creep equation to the data was found to be broadly satisfactory and consistent with strains rates obtained from manually drawn tangents of the last $30\,\mathrm{minutes}$.

4.7.1 Potential effects of secondary consolidation

Primary consolidation was completed in all tests as indicated by an equalisation of pore pressure and back pressure, along with a degradation of the volumetric strain rate to below the rate resolvable from the refined data of $3 \times 10^{-3}\,\%/\mathrm{h}$. Secondary consolidation however continued through the tests as evidenced by a volumetric strain rate of up to $2.5 \times 10^{-5}\,\%/\mathrm{h}$, or $1.5\,\%/\mathrm{yr}$ found over the course of the creep stages. The linear portion at the end of the volume vs. log(time) plot for consolidation was used to provide an approximation of the continuing secondary consolidation. Expressed as volumetric strain per log cycle C_{sec}=7.83×10^{-3} to -3.73×10^{-3} this indicates both consolidation and swelling are occurring over a

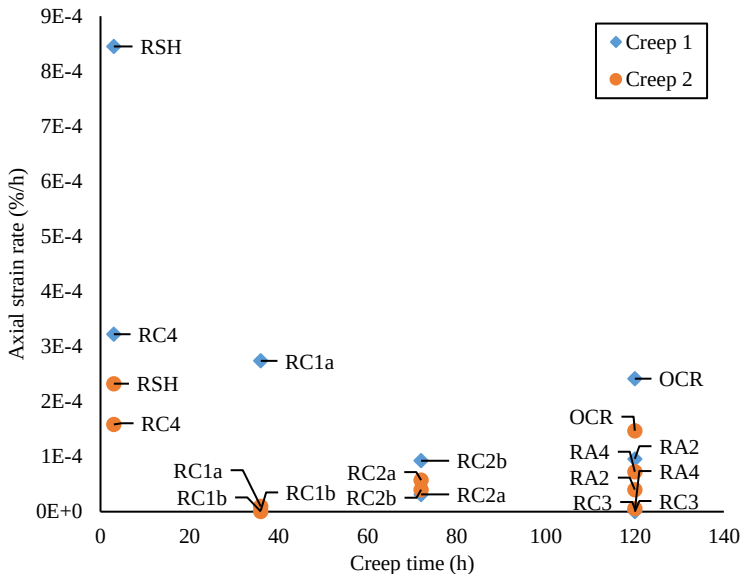

Figure 4.37: Initial results for axial strain rate at the end of creep

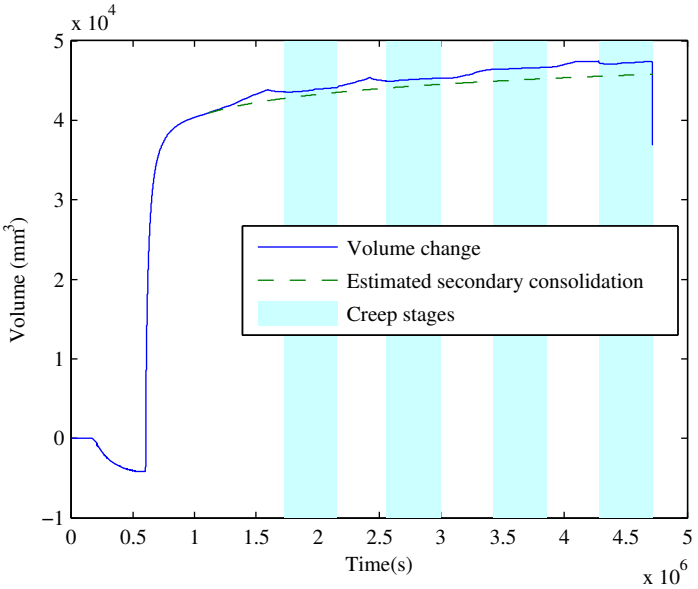

Figure 4.38: Volume change for test RA4

range of rates. Figure 4.38 shows this prediction alongside the actual volume change on a plot of sample volume change for the whole of test RA4. Due to the effects of the application of deviator stress along with the inherent uncertainty of the extrapolation, only a qualitative indication of the effect of secondary consolidation can be made.

The effect of the continuing consolidation on the observed creep degradation depends on the direction of the expected creep and consolidation. If the direction of the creep strain and the consolidation are complimentary, for example increasing axial strain (following a path from negative deviator stress to the isotropic stress state at creep) and consolidation, the axial strain rate is increased. If however the consolidation is counter to the creep strain the strain rate may be reduced or reversed.

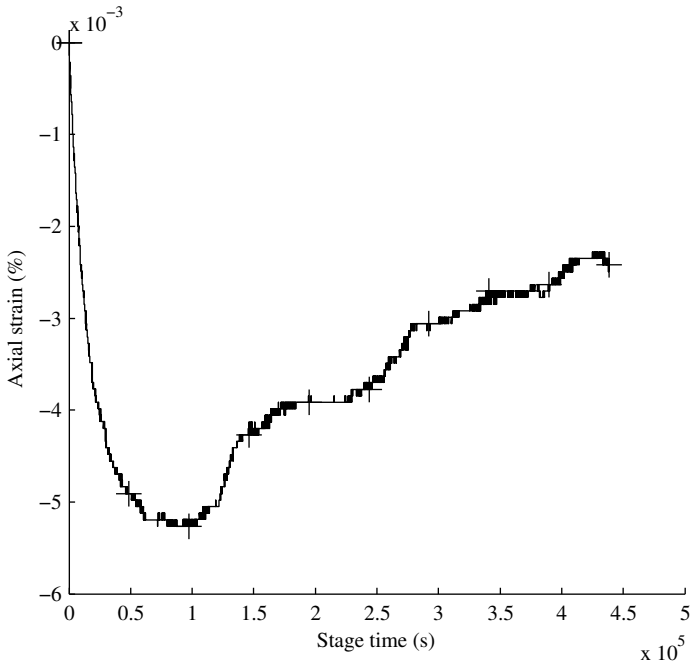

Figure 4.39: Example of reversing axial creep strain RA2 creep 1

Figure 4.39 shows an example where, as the strain rate of the negative creep strain decays the continuing consolidation eventually reverses the strain direction. Table 4.14 tabulates the volumetric strain rate predicted from the secondary consolidation for each creep stage, multiplied by -1 or 1 for decreasing or increasing expected shear strains. In this way both the magnitude and direction of the potential effect on the creep results can be assessed. The creep strain has been observed to reverse direction with a predicted strain rate with a magnitude as slow as -1 $\times$ 10^{-6} $\%/\mathrm{h}$. It is therefore not possible to make any meaningful statements on the drained creep behaviour resulting from the application of shear strains without the effect of secondary consolidation having an unknown influence.

4.7.2 Assessing the strain rate immediately prior to the shear probe stage

To allow comparison of the effect of creep an indication of the strain rate immediately prior to the shear probe is required. The axial strain can be influenced by both the isotropic consolidation and anisotropic creep that occur during the creep period. To avoid the influence of any isotropic consolidation the strain rate is assessed based on the triaxial shear strain $\varepsilon_q = (2/3)(\varepsilon_a - \varepsilon_r)$, where ε_a is the axial strain from local measurement and ε_r is a measure of radial strain obtained from the externally measured volumetric strain ε_v and the axial strain, such that $\varepsilon_r = (\varepsilon_v - \varepsilon_a)/2$. The primary consolidation was observed to be slightly anisotropic so this measure is affected by the secondary consolidation but in a reduced manner, as such only 5

Test	Predicted strain rate from secondary consolidation ($\%\,\mathrm{h}^{-1}\times10^{-6}$) modified to show effect direction		
	Creep 1	Creep 2	Creep 3
S1	-7.8		
S2	2.4	1.7	
C1	0.8	-0.5	-0.45
C2	-1.4	-0.6	-0.49
RC1b	-1.5	0.5	
RC2a	8.3	-3.0	
RC2b	2.7	-1.0	
RC3	-3.2	1.1	
RC4	-4.0	2.2	
RA2	-6.6	2.3	
RA4	-4.0	1.8	
HOCR	6.7	-2.2	
RC1a	14.1	-5.7	
HRSH	-4.0	1.4	

Table 4.14: Predicted strain rate from secondary consolidation ($\%\,\mathrm{h}^{-1}$) modified to show effect direction

stages are reversed compared to 9 for axial strains. The shear strain rates obtained from the creep equation fitting at the end of the creep stage are detailed in Table 4.15. For the 3 hour creep stages RC4 and HRSH the strain rate was determined by a tangent manually fitted to the last $30\,\mathrm{minutes}$ of the creep stage, as the model for strain rate decay did not fit well to the short data set.

An assessment was performed to give an indication of how the creep may have affected the shear stiffness G. The equivalent shear modulus discounting creep G_{nc} was calculated by discounting the shear strain associated with creep $\varepsilon_{q,c}$ from the shear strain measurement to give an equivalent shear strain without creep$\varepsilon_{q,nc}$ where $\varepsilon_{q,nc} = \varepsilon_q - \varepsilon_{q,c}$. As all shear probes were increasing shear strain paths when $\varepsilon_{q,c}$ is increasing discounting it reduces $\varepsilon_{q,nc}$ and so increases G_{nc}. The reverse is true when $\varepsilon_{q,c}$ is decreasing. As the creep process does not affect the stress the relative shear stiffness is the inverse of the relative shear strains and shear strain rates as given in Equation 4.2.

$$\frac{G_{nc}}{G} = \frac{\varepsilon_q}{\varepsilon_{q,nc}} = \frac{\dot{\varepsilon}_q}{\dot{\varepsilon}_{q,nc}} \tag{4.2}$$

It was assumed that for the undrained shear probe stages that the applied axial strain rate of $\dot{\varepsilon}_a = 3 \times 10^{-3}\,\%\,\mathrm{h}^{-1}$ was equal to the shear strain rate $\dot{\varepsilon}_q$. Using this it was possible to compute G_{nc}/G which is expressed in percentage terms in Table 4.16.

Test	Nominal creep time (h)	Absolute shear strain rate (%/h)	
		Creep 1	Creep 2
RC1b	36	1.01E-5	4.92E-5 *
RC2a	72	6.49E-4 *	6.27E-6
RC2b	72	3.25E-6	5.58E-5
RC3	120	7.51E-5	3.59E-5
RC4	3	2.67E-4	4.01E-4
RA2	120	3.00E-4	2.02E-4 *
RA4	120	1.21E-4	2.39E-5
HOCR	120	1.10E-4	2.15E-5 *
RC1a	36	7.06E-5 *	4.37E-5
HRSH	3	3.07E-4	2.69E-4

*Reversed from expected direction

Table 4.15: Absolute shear strain rates at the end of creep stages ($\%/\mathrm{h}$)

The results show that on average the G_{nc} is within $5.3\,\%$ of G. The continuing creep will thus have a small effect on observed stiffness. The adjustments here are however only approximate as the continuing decay of the creep strain rate was not accounted for nor individual variations in the shear strain rate. It was not possible to reliably assess $\dot{\varepsilon}_q$ or extrapolate the decay in the creep strain rate so this correction for creep was not used further.

Test	Nominal creep time (h)	Relative sheer modulus $G_{nc}G$ (%)	
		Creep 1	Creep 2
RC1b	36	100	98
RC2a	72	128	100
RC2b	72	100	98
RC3	120	98	101
RC4	3	92	115
RA2	120	91	94
RA4	12	96	101
HOCR	120	96	99
RC1a	120	98	99
HRSH	3	91	11

Table 4.16: Approximate effect of creep on shear modulus

4.8 Recent stress history

The remainder of the tests are those to establish the RSH effect a summary of these test is given in Table 4.17. This details the combinations of approach paths and creep times used as well as the state of the consolidation.

Sample name	Approach path maxima (kPa); 1st path, 2nd path	Creep time (h); 1st path, 2nd path	Initial effective stress	Void ratio prior to saturation	Void ratio after isotropic consolidation
RC1b	12.2 -12.3	36 36	263.4 [a]	0.748 [a]	0.747
RC2a	12.5 -12.1	71.9 64.7	212	0.805	0.8
RC2b	-12.6 12.5	74.9 71.9	230.1	0.794	0.772
RC3	10.7 -13.3	130.9 131.9	188.7	0.771	0.739
RC4[b]	12 -12.3	2.6 2.8	177.7	0.78	0.743
RA2	27.2 -27.4	121.8 119.9	195.4	0.789	No data [c]
RA3	42.1 -42	122.2 121.7	No data [d]	0.788	0.737
RA4	57.1 58.5	118.6 120.8	104.3[a]	0.843[a]	0.769
HOCR	12.8 -11.9	106 120.2	438.7	0.728	0.747
RC1a	-12.5 13.5	35.3 36.5	61.2[a]	0.861[a]	No data [e]
HRSH	58 -57.1	1.6 2	186.4	0.816	0.805

Table 4.17: Recent stress history tests

[a] Considered out of normal range
[b] Membrane leak during saturation stage that self-clogged
[c] Data acquisition hardware failed on isotropic consolidation stage
[d] Membrane leak invalidated result
[e] Transducer failure prevented sample volume measurement

4.8.1 Results at extreme points of approach path length and creep time

The recent stress history effect tests consisted of a series of constant p' stress paths following the isotropic consolidation. The shear probes on which the output was compared followed a variable length approach path with a $0°$ or $180°$ stress path rotation and a variable amount of creep. The tests performed are detailed in Figure 3.4 (Page 46) and in Table 3.3 (Page 48) where positive first approach path length indicates an $180°$ rotation for the first probe and $0°$ for the second and a negative first approach path is the reverse. For clarity the schematic diagrams of the tests at the extremes of the approach path and creep variables range are detailed in Figure 4.40. It can be noted in this figure that the long stress paths to q = $80\,\mathrm{kPa}$ are not consistently undrained as intended. The drained paths where a result of an error in the control software and indicate some change in the back volume occurred but not necessarily the active maintenance of a constant PWP. The parameters q and G are theoretical unaffected by the drainage and no significant differences were observed. Based on past results, the expected effect of recent stress history on the stiffness of the measured shear probes is for an increase in stiffness with an increase in rotation from the current path. The theoretical relationship being tested is for the RSH effect to increase with the approach path length and reduce with creep time. If the soil sample tested was to show a RSH effect it would therefore be most pronounced on test HRSH, where approach path length = $60\,\mathrm{kPa}$ and creep time = 3 hours. The results for test HRSH are shown in Figure 4.41 for the unrefined external radial stress strain path and Figure 4.42 for the stiffness degradation curve obtained by applying the bootstrap smoothing method to the external radial stress strain data. These results support a RSH effect with the typical increased stiffness at low strain for the $180°$ path and a degradation of this increase with further strain.

The effect of creep on long ($60\,\mathrm{kPa}$) approach paths can be observed on test RA4 with APL=$60\,\mathrm{kPa}$ and creep = 5 days. This is shown as stress strain in Figure 4.43 and stiffness in Figure 4.44. Compared to the HRSH test there is an increase in stiffness for the $0°$ rotation path and a reduction in stiffness for the $180°$ rotation path. This is combined with a reduction in the strain until stiffness mirrors the expected effect of creep on the RSH effect. It becomes clear however that the stiffness is very sensitive to small differences in the stress strain path as minimal difference can be detected in Figure 4.43.

Looking at the other extreme however the result is more complicated, for test RC3 (Fig 4.45 and Fig 4.46) with a $15\,\mathrm{kPa}$ approach path length and $5\,\mathrm{days}$ creep, the small RSH effect is expected to have been erased. The second shear probe with $0°$ path rotation has increased stiffness which is consistent with the reduction of the

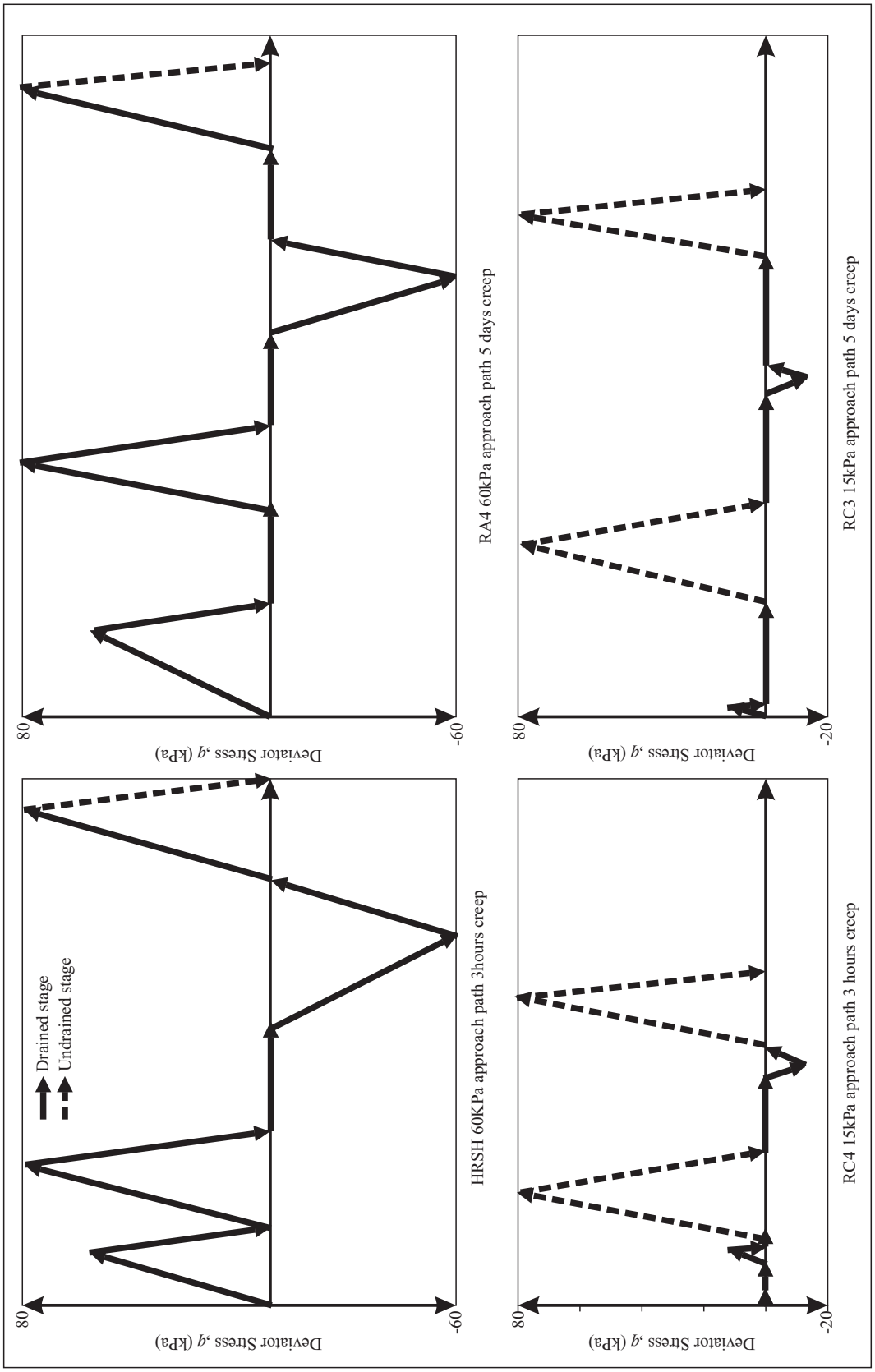

Figure 4.40: Schematic diagram of test plan for test at the extremes of creep and approach parameter range

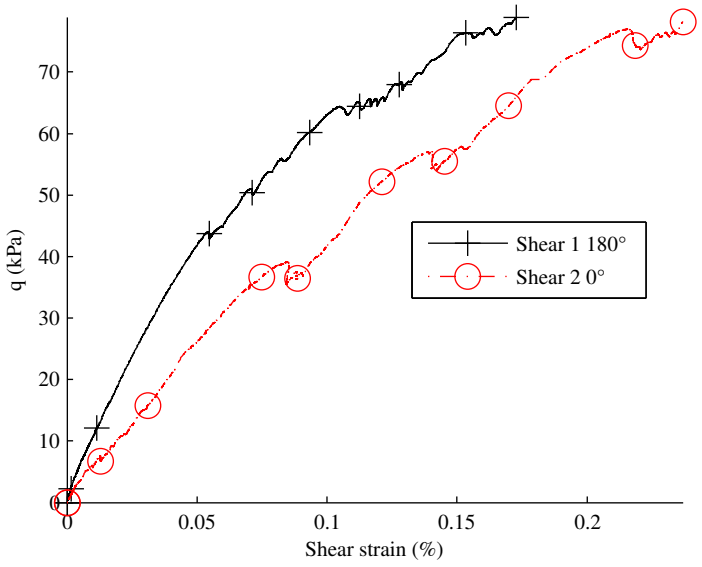

Figure 4.41: HRSH stress strain comparison

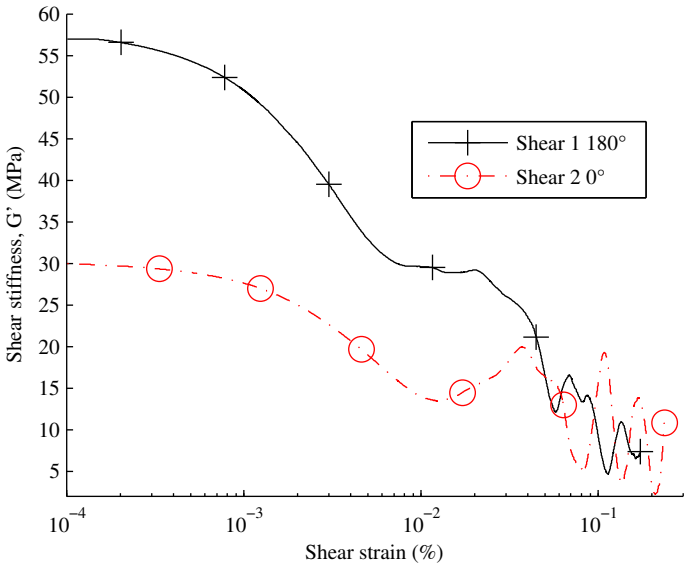

Figure 4.42: HRSH stiffness comparison

RSH effect. The stiffness of shear path 1 (the $180°$ rotation path) is increased however. This would indicate an increased stiffness and therefore an increased RSH effect. Judged by the initial stiffness magnitude the RSH effect is similar at this point to that observed on the HRSH test. If assessed by the point where the two stiffnesses become approximately equal, it could be observed that test RC3 achieves a stiffness parity after $5 \times 10^{-3}\,\%$ shear strain compared to $9 \times 10^{-3}\,\%$ and $5 \times 10^{-2}\,\%$ for RA4 and HRSH respectively. Due to the subjective nature of these slight comparisons and the sensitivity of the stiffness measurement, it is not possible to draw any conclusions from the comparison of test RC3 and RA4 as to the effect of approach path length on RSH effects.

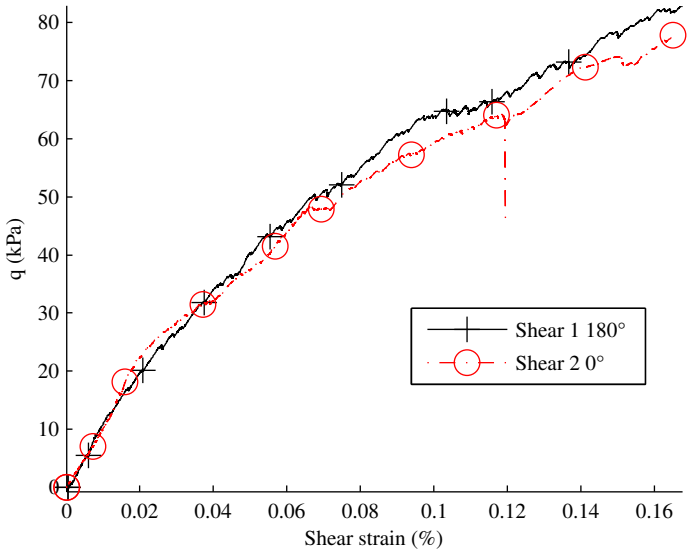

Figure 4.43: RA4 stress strain comparison

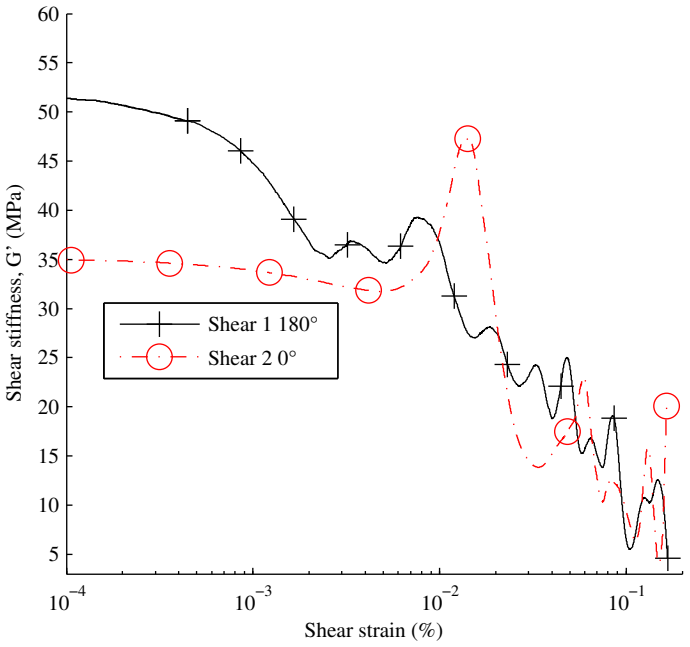

Figure 4.44: RA4 stiffness comparison

The final extreme point to compare is test RC4 with $3\,\mathrm{hours}$ creep and a $15\,\mathrm{kPa}$ approach path. The stress strain plot in Figure 4.47 shows a higher initial stiffness for the initial $180°$ rotation path than the later $0°$ rotation path. The stiffness plot in Figure 4.48 supports this observation however as both paths have an unusually low initial stiffness and demonstrate a peak in stiffness. The cause of this could be the low shear strain rate of approximately $3 \times 10^{-4}\,\%/\mathrm{h}$ or a tenth of the usual $3 \times 10^{-3}\,\%/\mathrm{h}$ which is observed up to $3 \times 10^{-3}\,\%$ shear strain. The effect of this would be a reduction in stiffness while the cause relates to the lower than expected

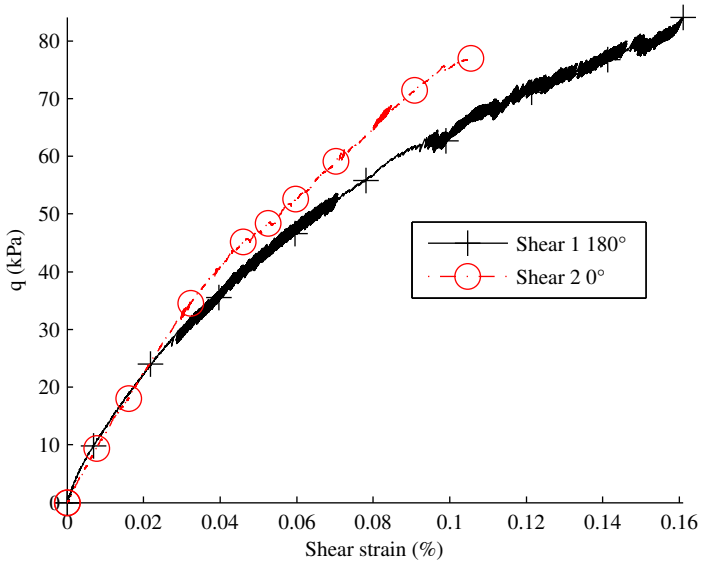

Figure 4.45: RC3 stress strain comparison

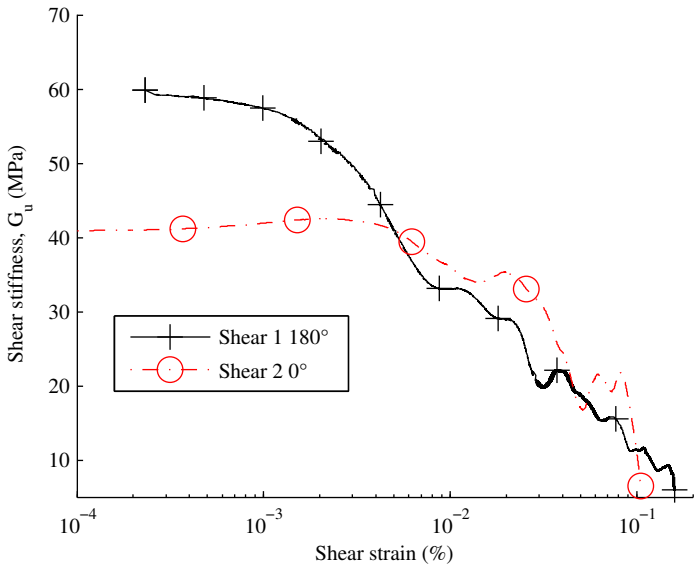

Figure 4.46: RC3 stiffness comparison

applied displacement, possibly resulting from compression of air inclusions within the lower chamber. This distortion makes judging the RSH effect difficult as the initial stiffness is lost. Shear 1 is however greater than shear 2 at the initial stages and the stiffness reaches parity at $2 \times 10^{-2}\,\%$. By this measure the RSH effect can be said to be less than HRSH but more than RC3 and RA4. A comparison between test RC4 and HRSH supports some increase in RSH effect with approach path length.

In conclusion it is possible to interpret the results at the extremes of the assessed range as a support for the tested hypothesis. However while the existence of the RSH effect on test HRSH is strong the rest of the trends stated could be the result

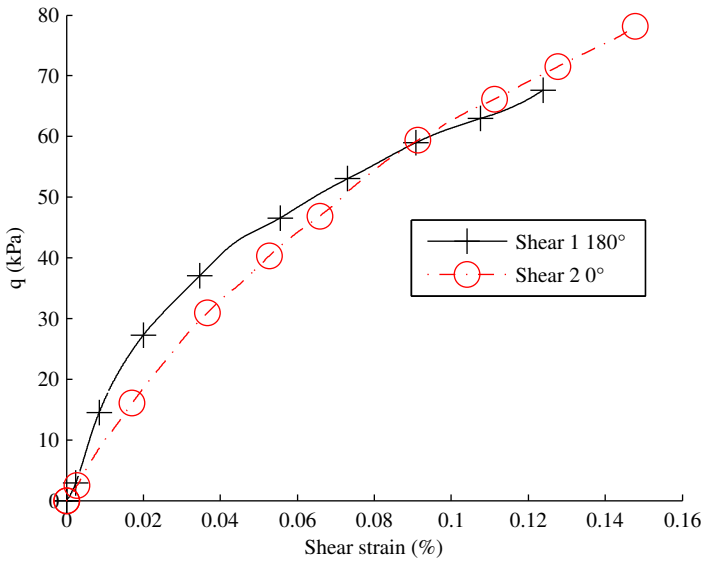

Figure 4.47: RC4 stress strain comparison

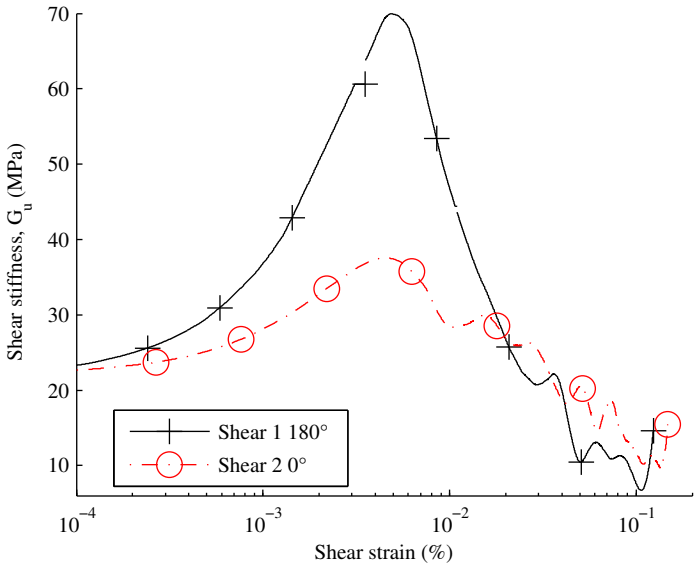

Figure 4.48: RC4 stiffness comparison

of natural variation in the test samples and errors in the testing methodology.

4.8.2 Trends observed from qualitative comparison of stress strain curves

Given the problems in obtaining reliable stiffness curves a qualitative assessment was made of the stress strain curves obtained for each shear path.

Stiffness of second shear path

A key observation was that the overall secant stiffness of the second shear probe was in many cases as stiff or stiffer than the first shear probe and had a lower variability. The possible influence of the void ratio being more consistent by the second stress path was not be supported by the observed data. Numerical modelling of the possible effects of volumetric creep, such as the observed secondary consolidation using the BRICK model, showed a possible increase in shear stiffness with increased volumetric creep. There was however no correlation between the observed stiffness increase and the observed change in volumetric strain. A rudimentary model of the effect of the multi stage testing approach used did indicate two possible mechanisms for the increased stiffness of the second shear probe. Firstly it was observed that with insufficient reset creep, the second shear probe could have an increased stiffness as a result of the RSH effect of the $180°$ rotation from the first shear probe. With a limited creep period the stiffening effects of the $80\,\mathrm{kPa}$ shear probe may have had more of an effect than the more recent approach path which was expected to reduce stiffness. Secondly the $90°$ rotation of the stress path from the consolidation to first approach path and then first shear path was found to reduce the stiffness on the shear path. This is to be termed the recent consolidation history (RCH) effect to distinguish it for the RSH effect caused by the intentional approach paths. This effect brings the validity of multi-stage testing into question.

Influence of creep

Both the stiffening of the second shear path and RCH effect were found to reduce with creep. The second shear probe was always allowed $5\,\mathrm{days}$ of 'reset' creep on top of the creep period under investigation, whereas the initial shear probe only allowed the investigated creep period to elapse. It is therefore anticipated that the stiffness reducing effect of the consolidation path on shear 1 is strong and the effect of creep on this is observable. The effect of the preceding shear probe on shear 2 is however thought to have been largely eliminated by creep. Looking at the stress strain probes for shear probe 1 of the test on the effect of creep (Figure 4.49) shows the high stiffness in test RC4 decay to the low stiffness at test RC2a, showing the degradation of the RSH effect. The increase in stiffness at test RC3 can then be interpreted as the reduction of the RCH effect. Looking at the stress strain plots for probe 2 of the test on the effect of creep (Figure 4.50), an increase in stiffness with creep can be interpreted if test RC2a is ignored. Given that RC2a was observed to start swelling from the mid-point of the consolidation stage, the assertion that the stiffness of RC2a was too low could be justified. It could also be explained that as test RC1b had a higher than average initial effective stress that its stiffness was too

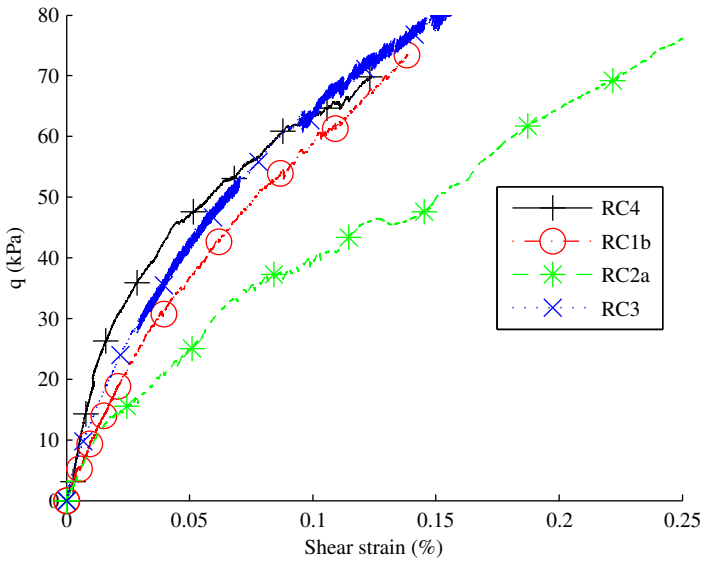

Figure 4.49: Effect of creep on shear probe 1

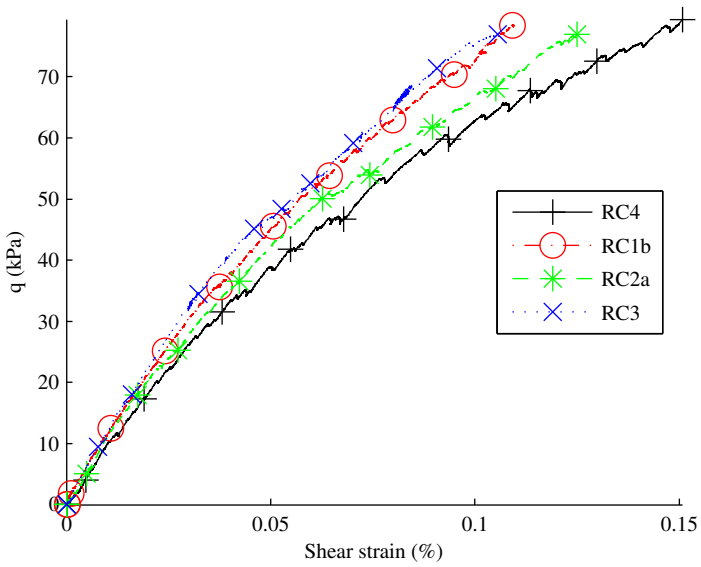

Figure 4.50: Effect of creep on shear probe 2

high.

Influence of approach path length

The effect of the approach path with $5\,\mathrm{days}$ creep is examined in Figure 4.51 and Figure 4.52 for shear probe 1 and 2 respectively. No overall trend is observed for shear path 1, however shear path 2 shows the expected reduction in stiffness with approach path length, as an increased RSH effect reduces the stiffness of the second $0°$ rotation path. It may be speculated that the lower than average initial effective stress caused a lowering of the stiffness for both shear probes of test RA4. A slight increase in the stiffness of both shear probes could result in shear probe 1 show-

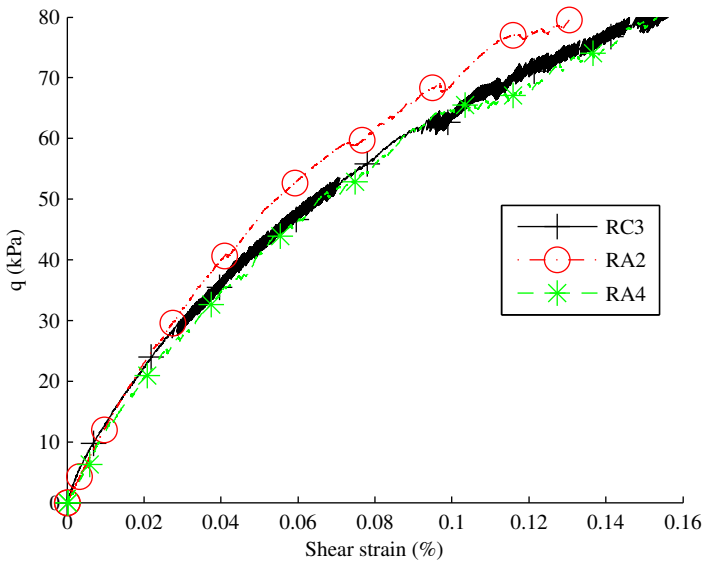

Figure 4.51: Effect of approach path length on shear probe 1

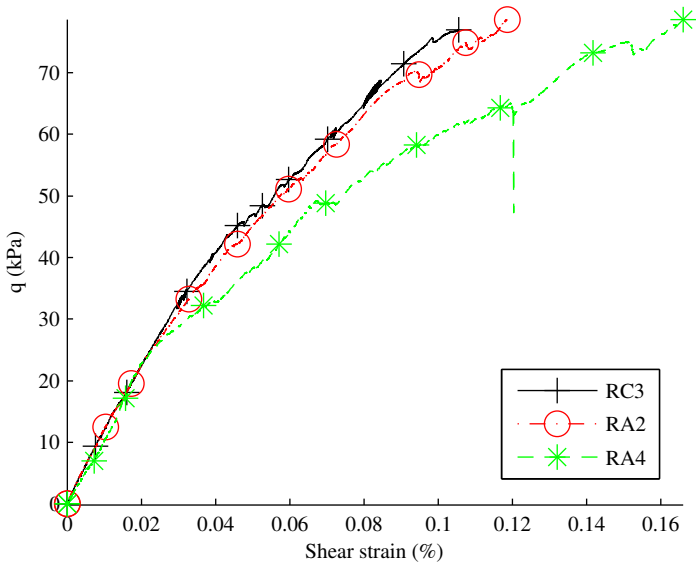

Figure 4.52: Effect of approach path length on shear probe 2

ing a increase in stiffness with approach path length without altering the trend of decreasing stiffness on shear probe 2.

Problems with test repeats

Two pairs of repeat test RC1a-b and RC2a-b were performed to gain insight into the effect of the multistage testing and provide a RSH comparison free of any multi stage effects. The problems with the test consistency meant that test RC1b was produced with a higher than average $263\,\mathrm{kPa}$ initial effective stress and RC1a was produced with a lower than average $61\,\mathrm{kPa}$ initial effective stress. It is therefore impossible to make reasonable comparisons between the tests. The low stiffness

on shear probe 1 of test RC2a associated with the swelling occurring in that test prevents comparison between RC2a and RC2b also.

4.8.3 Conclusions

The analyses of the data obtained on the RSH effect shows one example of a strong RSH effect on tests HRSH. If one accepts the proposed RCH effect for the reduction of stiffness on shear path, the other tests can be interpreted as supporting the tested hypothesis: a RSH effect that increases stiffness for $180°$ rotation and reduces it for $0°$ rotation, the magnitude of which increases with approach path length and reduces with creep time.
The robustness of the conclusion is hampered however by the quality of the data set available. Problems with sample variability prevented several of the planned comparisons. Additional problems such as membrane leaks and poor quality stress path control reduced the pool of reliable tests further. The need to undock the sample for creep stages introduced problems with defining the start of shear stages. This along with the temperature induced strain rate oscillation prevented a reliable quantitative comparison of stiffness. With the reduced data set and lack of quantified data for the RSH effect it is impossible to draw firm conclusions on the observed effects. A further insight into the reliability of the results will be obtained by modelling the testing process in the BRICK model as discussed in Chapter 6.

5

Alterations and additions to BRICK model

5.1 The BRICK model

5.1.1 Introduction

The BRICK model uses an analogy to describe the behaviour observed in soil at small strains. It accounts for the increase in stiffness at small strains and the effects of changes in stress path on small strain stiffness. The analogy as described by Simpson (1992) is one of a man dragging bricks on different lengths of string.

Figure 5.1 shows how when travelling in a straight line the bricks eventually move behind the man, but on a change in direction the movement of the bricks lags behind that of the man. This analogy is applied to practical soil behaviour by taking the

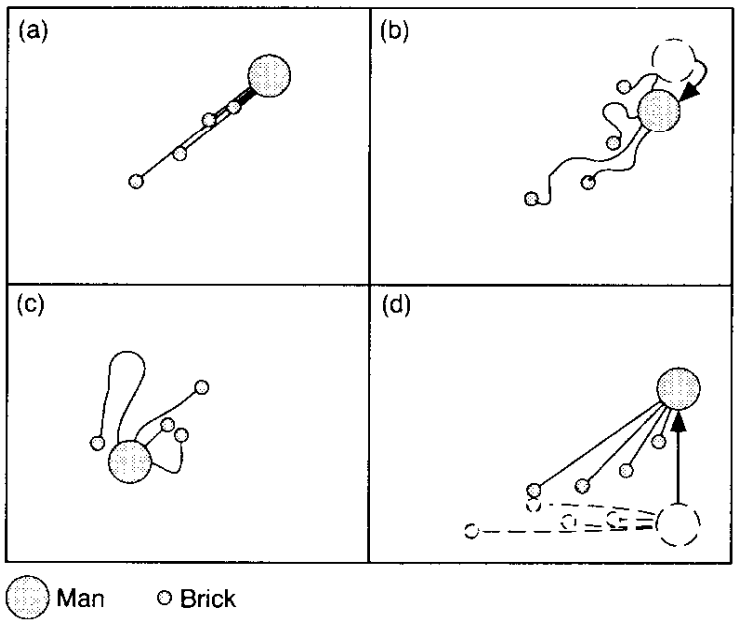

Figure 5.1: Illustration of BRICK model analogy, Simpson (1992)

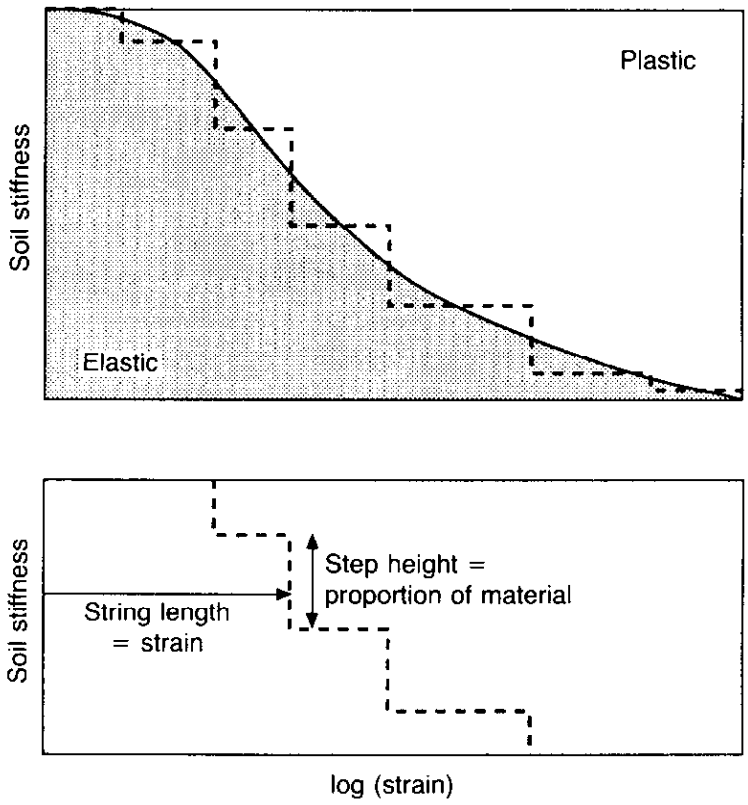

Figure 5.2: The S shaped stiffness curve represented in stepwise fashion, Simpson (1992)

man to represent the total strain of a soil element ε_t and the bricks to represent a portion of that soil element. Movement of a brick represents plastic strain ε_p while elastic strain ε_e is the difference between the movement of the man and sum movement of the bricks ε_t - ε_p. Thus pure elastic strain only occurs when none of the bricks are moving. It should be noted that ε_e, ε_p and ε_t are actually vectors that represent the strain state in multiple component directions, for example having both shear and volumetric strain. The s-shaped stiffness curve which may also represent the relative proportions of plastic and elastic strain can be modelled by a stepwise function as shown in Figure 5.2.

In the analogy, when a brick starts moving plastic strains are introduced giving a corresponding drop in the overall stiffness of the soil. The length of the steps represent an amount of strain or the string length. The height of the step is the proportion of the material represented by each brick. Figure 5.3 shows how the BRICK model can be used to model RSH effects where string lengths and proportions where chosen to fit path DOX and then used to generate the results for the other paths. The bumpiness of the stiffness plots is a result of the small number of steps used.

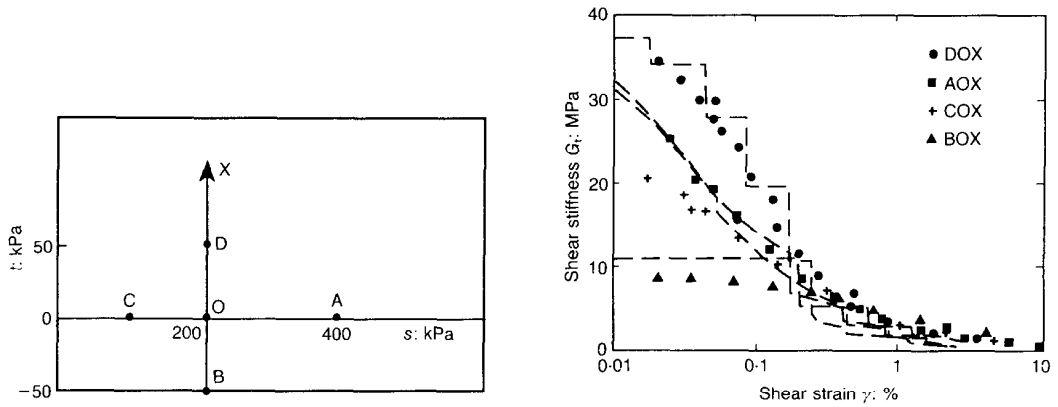

(a) (b)

Figure 5.3: Brick model predictions for (Richardson 1988) tests, Simpson (1992)

5.1.2 Parameters used in three dimensional BRICK

While the original formulation of the BRICK model described in Simpson (1992) was formulated in three stress and strain components, the work here uses the full three-dimensional form with six components of stress and strain. These components relate to volumetric and shear strains, and mean and shear stresses by either the bulk modulus K or shear modulus G as shown in Equation 5.1.

$$\begin{bmatrix} p' \\ t_{zx} \\ t_y \\ \tau_{xy} \\ \tau_{yz} \\ \tau_{zx} \end{bmatrix} = \begin{bmatrix} K & 0 & 0 & 0 & 0 & 0 \\ 0 & G & 0 & 0 & 0 & 0 \\ 0 & 0 & G & 0 & 0 & 0 \\ 0 & 0 & 0 & G & 0 & 0 \\ 0 & 0 & 0 & 0 & G & 0 \\ 0 & 0 & 0 & 0 & 0 & G \end{bmatrix} \bullet \begin{bmatrix} v \\ g_{zx} \\ g_y \\ \gamma_{xy} \\ \gamma_{yz} \\ \gamma_{zx} \end{bmatrix} \tag{5.1}$$

This may be abbreviated to $\boldsymbol{\sigma} = \mathbf{C} \times \boldsymbol{\epsilon}$ where $\boldsymbol{\sigma}$ and $\boldsymbol{\epsilon}$ are vectors containing all stress and strain terms respectively and $\mathbf{C}$ is the compatibility matrix containing G and K terms. While the final three stress and strain components are shear stress and strain terms in the conventional notion the first three components are defined as follows:

$$\text{Volumetric strain} = v = \varepsilon_x + \varepsilon_y + \varepsilon_z \tag{5.2}$$

$$\text{Shear strain component 1} = g_{zx} = \varepsilon_z - \varepsilon_x \tag{5.3}$$

$$\text{component 2} = g_y = \frac{(2\,\varepsilon_y - \varepsilon_x - \varepsilon_z)}{\sqrt{3}} \tag{5.4}$$

$$\text{Mean stress} = p' = \frac{(\sigma_x + \sigma_y + \sigma_z)}{3} \tag{5.5}$$

$$\text{Shear stress component 1} = t_{zx} = \frac{(\sigma_z - \sigma_x)}{2} \tag{5.6}$$

$$\text{component 2} = t_y = \frac{(2\,\sigma_y - \sigma_x - \sigma_z)}{2\sqrt{3}} \tag{5.7}$$

For modelling of standard tests p' is obtained directly as the first stress component while q can be calculated by 5.8 (Clarke 2009).

$$q = \sqrt{3}t_y + t_{zx} \tag{5.8}$$

In a similar manner to mean stress the volumetric strain v is directly defined. The shear strain ε_q, axial strain ε_a and radial ε_r are calculated by Equations 5.9, 5.10 and 5.11 respectively all of which are simplified to only use component 1 and 3.

$$\varepsilon_q = \frac{g_y}{\sqrt{3}} \tag{5.9}$$

$$\varepsilon_a = \frac{v + \sqrt{3} \times g_y}{3} \tag{5.10}$$

$$\varepsilon_r = \frac{2 \times v - \sqrt{3} \times g_y}{6} \tag{5.11}$$

Simulation of specific strain scenarios is achieved by specifying the six component strain vector so as to control the ratio of different strain components. Isotropic strain uses the strain vector with a ratio [1,0,0,0,0,0] i.e. no sheer strain components. For a undrained triaxial compression or extension a strain vector of [0, 0, 1, 0, 0, 0] is required as zero strain is permitted in the other strain components. One dimensional consolidation requires a strain vector with ratio [1, 0, 1.1547, 0, 0, 0] (Clarke 2009).

5.1.3 Computations used in the BRICK routine

Computations

The implementation of the BRICK model used the MATLAB version of the model produced by Clarke (2009). The flow of the program is illustrated in Figure 5.4 which shows the internal progression of the BRICK routine for a single BRICK increment. The control parameters, the current stress strain state and the applied

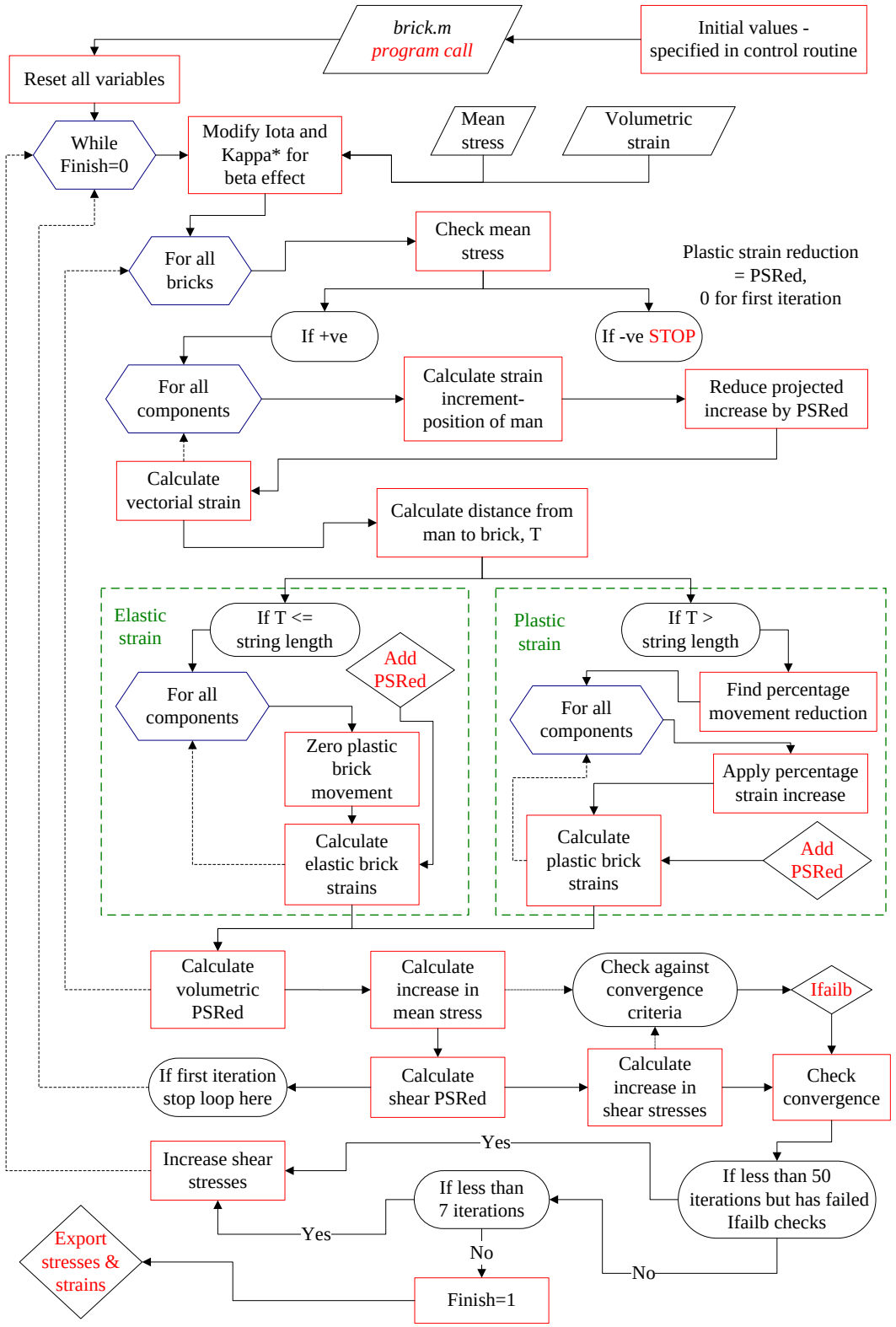

Figure 5.4: Flow chart showing internal workings of the BRICK model, (Clarke 2009)

strain increment are input into this code from an external control routine. Once within the BRICK code the first stage is to modify the gradient of the swelling line (in $\ln v - \ln p'$ space), κ*, and elastic constant, ι for the effect of OCR this is the 'beta effect' discussed in section 5.1.3. For each brick the distance T between the man after a strain increment and the current brick position is calculated using Equation 5.12. This is reduced slightly by the plastic strain reduction (PSRED) mechanism described in section 5.1.3. If T is greater than the relevant string length the brick moves and behaves plastically, otherwise it remains stationary and the movement of the man away from the brick contributes to the elastic strain. Once the strain of all bricks has been calculated the step height for each brick is used to calculate the total plastic strain. The volumetric plastic strain is then used to calculate the volumetric PSRED to be fed back into the next iteration.

$$T = \sqrt{\sum \left(\varepsilon_i + \delta\varepsilon_i - \varepsilon_{bi} - \varepsilon_{red,i}\right)^2} \tag{5.12}$$

for i = 1 : the number of components in the model, where:

T = separation of man and brick,

ε = current strain (position of the man),

$\delta\varepsilon$ = strain increment,

ε_b = position of the brick,

ε_{red} = plastic strain reduction.

By subtracting the calculated plastic strain change in each component from the applied strain change, the elastic strain change δv_e can be calculated. This can then be used to calculate an estimate of the change in the mean stress $\delta p'$ based on the current mean stress p' using equation Equation 5.13. This formulation has the bulk stiffness K increasing as a function of the current stress p' and the elastic constant ι.

$$\delta p' = \frac{p'\delta\varepsilon_e}{\iota} \tag{5.13}$$

A more accurate estimate of p' is calculated as the average stress for the increment $\bar{p} = p' + 0.5 * \delta p'$. This is then used to calculate the shear PSRED to be fed back in to the next increment. The new mean stress value $\bar{p}$ is then also used to calculate the change in each of the shear stress components using an equation of the form given in Equation 5.14 for δt_y. Where F is the ratio of the shear modulus G to the bulk modulus K which is a function of Poisson's ratio ν given by Equation 5.15.

$$\delta t_y = \Delta g_y \, \bar{p} \, \frac{F}{\iota} \tag{5.14}$$

$$F = \frac{3\,(1 - 2 * \nu)}{2\,(1 + \nu)} \tag{5.15}$$

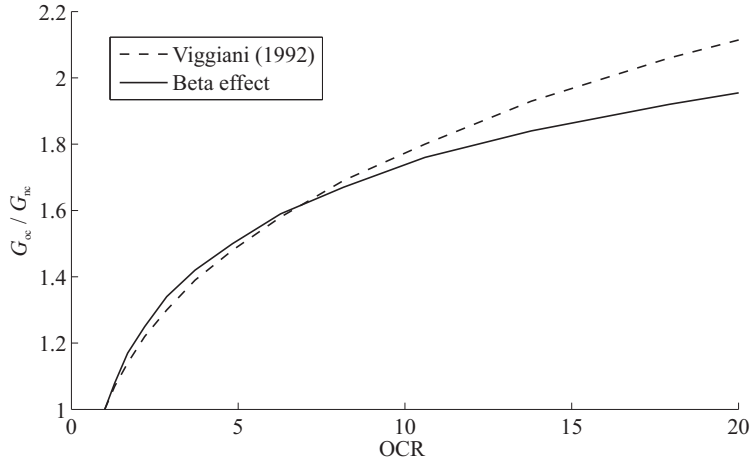

Figure 5.5: Comparison between models for the effect of overconsolidation on stiffness, (Clarke 2009)

The BRICK routine will continue to iterate and move PSRED towards an optimum solution. This is indicated when the change in mean and shear stress is stable between successive iterations being within a small tolerance of that observed on the previous iteration.

Beta effect

In the BRICK model the beta effect is used to allow stiffness to increase with overconsolidation ratio by using the parameter $\beta_{mod} = G_{max,oc}/G_{max,nc}$. This is calculated using Equation 5.16 and has been shown by Clarke (2009) to produce a similar result to that proposed by Viggiani (1992) from empirical results, as is shown in Figure 5.5.

$$\beta_{mod} = 1 + \beta \left(v - v_0 - \lambda^* \ln \left(\frac{p'}{p_0} \right) \right) \tag{5.16}$$

where:

β_{mod} = beta modification factor,
β = beta constant,
v_0 = initial volumetric strain,
λ* = gradient of the NCL plotted as ln v versus ln p',
p_0 = initial mean stress.

The constant β_{mod} is used to calculate a modified version of the stiffness constant ι, using Equation 5.17

$$\iota_\beta = \iota / \beta_{mod} \tag{5.17}$$

Plastic strain reduction

In the BRICK model the PSRED mechanism increases the elastic capacity in a strain increment. This allows stress changes in situations that would otherwise result in a zero stress increment due to all bricks moving and thus behaving plastically. The amount of PSRED is dependent on the direction of the applied strain. Volumetric PSRED generates the compression and swelling lines from the plastic volumetric strain δv_p by using Equation 5.18 and 5.19 when the soil is normal consolidated and overconsolidated respectively.

$$\varepsilon_{red,1} = \left(\frac{\iota}{\lambda^* - \iota} \right) \delta v_p \tag{5.18}$$

$$\varepsilon_{red,1} = \left(\frac{\iota_\beta}{\kappa^* - \iota_\beta} \right) \delta v_p \tag{5.19}$$

The formulation of PSRED in shear strain allows monotonic strain paths to approach a constant stress ratio e.g. the K_0 line in 1D consolidation. The mathematical formulation by which this is achieved is untouched by the work presented here and is described in detail by Ellison, Soga & Simpson (2012).

5.1.4 Prediction of failure in the BRICK model

Failure in the BRICK model is defined as the point where all of the applied strain results in plastic strain. When this occurs there is no generation of elastic strain and so no change of stress, resulting in an effectively zero stiffness. In order for this condition to exist it is first required that all bricks be taut so no elastic strains are being generated due to stationary bricks. Once this is achieved the prediction of failure is dependent on the PSRED mechanism. In volumetric strain PSRED is generated from plastic volumetric strains (as given by Equation 5.18 and 5.19) while for shear strains PSRED is also related to the change in elastic volumetric strain. From this it logicically follows that failure cannot occur when there is any change in plastic volumetric strain, as this will result in an elastic strain change due to the effects of PSRED. When there is no change in volumetric plastic strain however there will be no PSRED, and so if all strings are taut there will be no change in stress which would indicate failure. The failure point in BRICK is therefore defined as that where all strings are taut in shear with the same volumetric strain as the man.

5.1.5 Stress path finding routine

The BRICK routine is inherently strain controlled and so an iterative routine is used to enable the production of defined stress paths. This routine works for the mean

and shear stress components of the BRICK model used in triaxial tests. A bisecting iteration is run in each component to find the strain change that gives the appropriate stress output. As the strain in one component affects the stress in the other component, the process is repeated in an outer loop until the stress is within a tolerance of the target value. This routine works to a limited accuracy but employs a correction whereby the error in one increment is set to be removed on the subsequent increment thus avoiding cumulative errors. When the routine fails to reach a solution within the first 20 iterations the stress tolerances are relaxed as failure to find a solution would prevent a further continuation of the stress path.

5.1.6 Strain rate dependent string lengths

Modelling isotach behaviour

In order to implement strain rate dependent effects into the BRICK model it is first necessary to select a model to be used for isotach strain rate dependent behaviour. Whilst the general trends of the isotach behaviour are widely agreed upon, the numerical models that describe the effect of increasing strain rate on strength or stiffness are numerous. The general form of these is to take a parameter such as the peak strength q_f and determine a reference value $q_{f(ref)}$ which exists at a suitably low strain rate $\dot{\varepsilon}_{ref}$. A suitable function is then used to apply an increasing multiplication of the reference parameter with increase in strain rate. Examples include:
Soga & Mitchell (1996)

$$q_f = q_{f(ref)} \left(\frac{\dot{\varepsilon}}{\dot{\varepsilon}_{ref}} \right)^{\beta} \tag{5.20}$$

Graham et al. (1983)

$$q_f = q_{f(ref)} \left(1 + \lambda \log \left(\frac{\dot{\varepsilon}}{\dot{\varepsilon}_{ref}} \right) \right) \tag{5.21}$$

The values β and λ are soil constants. These functions allow strain rate effects to continue when the strain rate drops below the reference rate. This is however problematic very low rates can cause q_f to become negative or may fail numerically when $\dot{\varepsilon} = 0$. A common solution is to formulate the equation for strain rate effects so no rate effects occur for strain rates below the reference rate. The reference rate is usually selected well below that which can be practically tested; as such while there is little evidence for such a limit, there is also no practical situation in which the limit may be problematic. Several equations of this form are give below:
Soga & Mitchell (1996) as modified by Clarke (2009)

$$q_f = q_{f(ref)} \left(\frac{\dot{\varepsilon}}{\dot{\varepsilon}_{ref}} + 1 \right)^{\beta} \tag{5.22}$$

Graham et al. (1983) as modified by Clarke (2009)

$$q_f = q_{f(ref)} \left(1 + \lambda \log \left(\frac{\dot{\varepsilon}}{\dot{\varepsilon}_{ref}} + 1\right)\right) \tag{5.23}$$

Sorensen (2006)

$$q_f = q_{f(ref)} \left(1 + \beta \ln \left(\frac{\dot{\varepsilon}}{\dot{\varepsilon}_{ref}} + 1\right)\right) \tag{5.24}$$

Tatsuoka et al. (2002) proposes a more detailed model that demonstrates the strain rate effect across the whole stress strain curve. It should be noted that if this where defined for the peak strength it would simplify as follows, where m and α are constants and $\dot{\varepsilon}_{ir}$ is the strain rate of the irreversible (inelastic) component of the strain.

$$q_f = q_{f(ref)} \left(1 + \alpha \left[1 - exp\left\{1 - \left(\frac{|\dot{\varepsilon}^{ir}|}{\dot{\varepsilon}_{ref}} + 1\right)^m\right\}\right]\right) \tag{5.25}$$

Framework for implementation

Clarke & Hird (2012) implement and build on equations proposed by Sorensen (2006) to model strain rate dependency by introducing strain rate dependent string lengths (SRDSLs). The length of the string attached to each brick is a function of the plastic strain rate of the brick (Sorensen 2006). If the man moves at a constant rate this influences the string lengths, resulting in longer string lengths at higher rates. As a consequence there are higher levels of elastic strain and hence stiffness and strengths are observed. If the man were to halt the rate reduces to zero and the strings shorten to their reference values. This moves the bricks towards the man reducing elastic strains and increasing plastic strains. This has the effect of reducing the stress level and stress relaxation is shown. Upon a restart of movement strings become slack and therefore an initial stiff response is shown due to elastic strain being induced. Utilising the relationship between undrained shear strength and strain rate (Equation 5.24) and equating the string lengths directly to the undrained shear strength, the relationship between string length SL and strain rate $\dot{\varepsilon}$ can be found as Equation 5.26.

$$SL = SL_{ref} \left(1 + \beta \cdot \ln \left(\frac{|\dot{\varepsilon}|}{\dot{\varepsilon}_{ref}}\right)\right) \tag{5.26}$$

Here the reference string lengths SL_{ref} are the string lengths found at the low reference strain rate $\dot{\varepsilon}_{ref}$ which is taken as 1×10^{-13} $-/\mathrm{s}$ by (Clarke & Hird 2012). As the reference strain rate is low it is difficult to measure the string lengths at this rate. The reference string lengths are however calculable by Equation 5.27 (Clarke 2009), where SL_{test} = string lengths calculated from test at rate $\dot{\varepsilon}_{\text{test}}$.

$$SL_{ref} = \frac{SL_{test}}{1 + \beta \ln(\dot{\varepsilon}_{test}/\dot{\varepsilon}_{ref} + 1)} \tag{5.27}$$

It is suggested in the study of London clay by Sorensen (2006) that the relationship between volumetric and shear strain is independent of strain rate. It is also suggested that the expansion of a single state boundary surface with strain rate could govern the yield behaviour. Due to these two factors the strain rate used is the vector sum of the volumetric and shear strain rates Equation 5.28.

$$\dot{\varepsilon} = \sqrt{(\dot{\varepsilon}_v)^2 + (\dot{\varepsilon}_s)^2} \tag{5.28}$$

Brick led strain rate dependent

The brick led model makes the strain rate dependent upon the movement of the bricks. This allows different proportions of the soil to experience different strain rate effects simultaneously rather than being wholly dependent upon the applied strain rate. An iterative process is introduced as the string length is dependent on the strain rate of the bricks, while the strain rate of the bricks is dependent upon the string length (Clarke & Hird 2012). The iterative process used to converge upon a solution is liable to lead to unstable oscillations and so a damping routine is implemented, whereby only a fraction of the change in SL since the previous BRICK execution is applied.

Time dependent effects of creep and stress relaxation are implemented by forcing the decrease in brick strain rate to obey a logarithmic decay function with time. As the BRICK model only deals with increments of time Clarke & Hird (2012) used the following method to calculate the cumulative time required for creep. The previous strain rate $\dot{\varepsilon}_{previous}$ can be calculated from the known string lengths of the previous increment $SL_{previous}$ by Equation 5.29

$$\dot{\varepsilon}_{prev} = \dot{\varepsilon}_{ref} \left[e^{\left(\frac{(SL_{previous}/SL_{ref})-1}{\beta} \right)} - 1 \right] \tag{5.29}$$

If the creep is said to have a upper limit t_{max} at a long time taken as $1 \times 10^9\,\mathrm{s}$ seconds with a associated minimum strain rate $\dot{\varepsilon}_{min}$ taken from Bishop (1966) as $1 \times 10^{-12}\,\%\,\mathrm{s}^{-1}$, then the previous time can be calculated by Equation 5.30.

$$t_p = 10^{\left(\log(t_{max}) - \left(\log\left(\frac{\dot{\varepsilon}_{previous}}{\dot{\varepsilon}_{min}} \right) \frac{1}{m} \right) \right)} \tag{5.30}$$

This allows calculation of the current time t_c by $t_c = t_p + \Delta t$ where Δt is the time increment used. The current strain rate is then calculated by Equation 5.31. The whole calculation can be visualised by Figure 5.6.

$$\dot{\varepsilon}_{current} = 10^{\log \dot{\varepsilon}_{min} + max\left(0, \left(\frac{\log(t_{max}) - \log(t_c)}{1/m} \right) \right)} \tag{5.31}$$

A series of simulations were run; the efficacy of the model was evaluated and shown to represent a clear improvement in the modelling of strain rate and time dependent

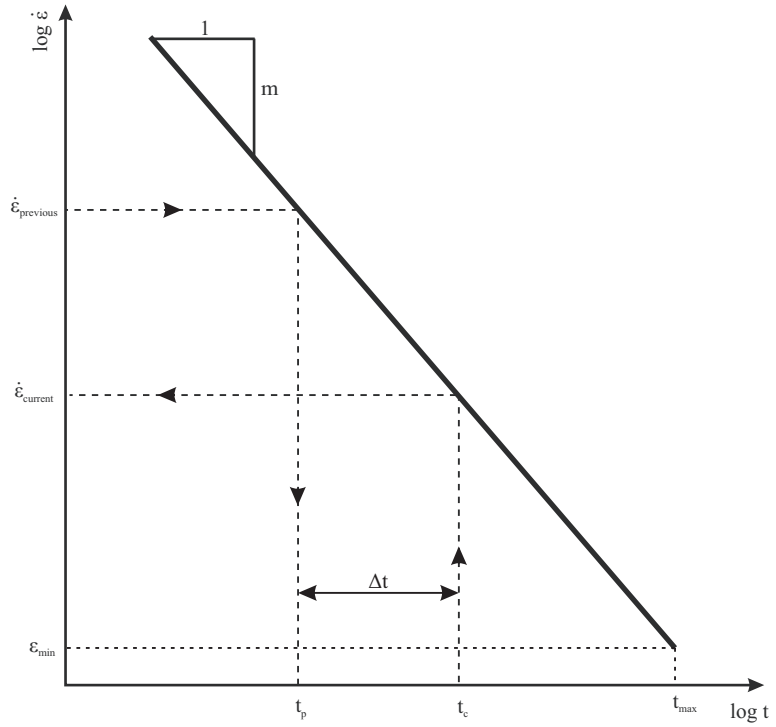

Figure 5.6: Visualisation of the framework for calculation of current strain rate in brick led SRD model, after Clarke (2009)

effects over previous approaches (Clarke 2009). It was also highlighted that the SRD BRICK model is able to deal with both isotach strain rate behaviour and time dependent effects such as creep and stress relaxation. These assertions are backed up by the successful simulation of the results presented by both Graham et al. (1983) and Gasparre (2005), showing that the model can not only replicate SRD behaviour but also the effect of creep on RSH (Clarke & Hird 2012).

5.1.7 Other expansions to the BRICK model

The BRICK model is expanded by several of the methods illustrated below in order to incorporate the strain rate and time dependent behaviours described.

Implementation of Pure and General TESRA behaviour

Sorensen (2006) proposed implementation of TESRA behaviour into the strain rate dependent model. The proposed implementation works by redefining the reference string length to those that define the unique CRS curve which is returned to after the temporary rate effects. The equation governing the string length is also redefined to Equation 5.32.

$$SL = SL_{ref}\left(1 + \beta \cdot \ln\left(\frac{|\dot{\varepsilon}|}{\dot{\varepsilon}_n}\right)\right) \tag{5.32}$$

The neutral strain rate $\dot{\varepsilon}_n$ tends towards the applied strain rate $\dot{\varepsilon}$ with increased strain at a rate which is a function of the difference $\dot{\varepsilon} - \dot{\varepsilon}_n$ Equation 5.33

$$\frac{\delta \dot{\varepsilon}_n}{\delta \varepsilon} = A\left[\dot{\varepsilon} - \dot{\varepsilon}_n\right] \tag{5.33}$$

The parameter A controls the rate at which $\dot{\varepsilon}_n$ tends towards $\dot{\varepsilon}$ and hence the rate at which the string lengths return to their reference state and the strain rate effects decay. Expanding to general TESRA involves making the parameter A a function of the strain. In Sorensen (2006) this is done by Equation 5.34.

$$A(\varepsilon) = A_f \cdot \left[1 - e^{-\frac{1}{c}\varepsilon}\right] \tag{5.34}$$

It was considered in the early stages that as TESRA behaviour was observed in reconstituted London clay it would be useful to implement into the BRICK model by the method described. It was however found that fitting additional parameters required for TESRA behaviour was therefore not straight forward. In addition it was clarified that the numerical modelling occurred at low strains where the Isotach model could be used. The implementation of TESRA behaviour is therefore not considered relevant to the rest of the thesis. It however represents a self contained aside and was therefore documented in Tuxworth & Clarke (2014) reproduced for convenience in Appendix D.

Anisotropic BRICK

A version of the BRICK model incorporating stiffness anisotropy was developed by Ellison, Soga & Simpson (2011), who describe improvements in field settlement calculations found by incorporating elastic stiffness anisotropy into the model. This model was not used in the current research however so is not described here.

5.2 Improvements made to SRD BRICK

5.2.1 Introduction

It was found that the SRD BRICK model used by Clarke (2009) had used a series of workarounds in the code implementation (Appendix E.1 contains the relevant section of the full code found in Appendix B.4.2 on pages 234-238 of (Clarke 2009)). These were all justified within the scope of that work however these caused problems in the more generalised cases presently investigated. This section will outline the issues with the original SRD code and the development made in the new strain rate dependent bisecting iteration (SRD-B) implementation. The SRD BRICK routine contains multiple levels of loop for clarity the following terminology is used:

- Increment = a call of the BRICK routine, each increment represents one step in applied strain.
- BRICK iteration = the outermost iteration in the BRICK code that checks for convergence on shear strain terms.
- SRD iteration = the iterative routine used to calculate the SRD string length. This is run separately for each brick but only on the first BRICK iteration

All modifications discussed are made to the calculation of strain rate dependent string lengths in the SRD iteration of the BRICK routine.

5.2.2 Problems and workarounds used in the SRD solution

Arbitrary limit for time dependent decay activation

Original implementation

The SRD BRICK model archives strain rate effects by relating SL to the brick strain rate using Equation 5.26 (p 154). Time dependent (TD) effects (creep and stress relaxation) are introduced by forcing the brick strain rate to decay logarithmically with time, using the framework given in Equation 5.29 to 5.31. This results in the SRD model effectively decaying into a time dependent string length (TDSL) model. In the MATLAB implementation of the SRD model TD effects are activated when $SL < SL_{previous}$ (the string length from the previous increment) indicating a reduction in strain rate for the current brick. There is however another condition to satisfy in order to engage the strain rate dependency, that of $t_c > 2$. In (Clarke 2009) the combination of parameters and strain rates used ensured $t_c > 2$ only when TD effects were required. In all other situations the TD effects would not be used.

By preventing the TD effects occurring on steady rate stages oscillation in the brick strains are avoided. Figure 5.7 shows the change in brick shear strain $\Delta g_{y,b}$ occurring on each step of a 1D consolidation. The applied shear strain change is Δg_y=1.15×10^{-3} therefore the brick strain change is expected to be 0 when initially slack and then increase to Δg_y when taut. In this case however Δt = 100 causing $t_c > 2$ and activating TD effects.

The SRD iteration runs by comparing the SL calculated in the current iteration to that from the previous iteration SL_{prev} and terminating when this differs by less than the set tolerance. The TDSL for a brick is constant within the BRICK increment as it is dependent on the fixed time increment and $SL_{previous}$. Given this set-up if the $SL < SL_{previous}$ condition to activate a TD effect occurs on consecutive SRD iterations the TDSL will be output. The reduction in SL causes the brick to move toward the man causing a spike in $\Delta g_{y,b}$. On the next increment SL begins to return to a rate appropriate value but as the brick starts closer to the man less strain is

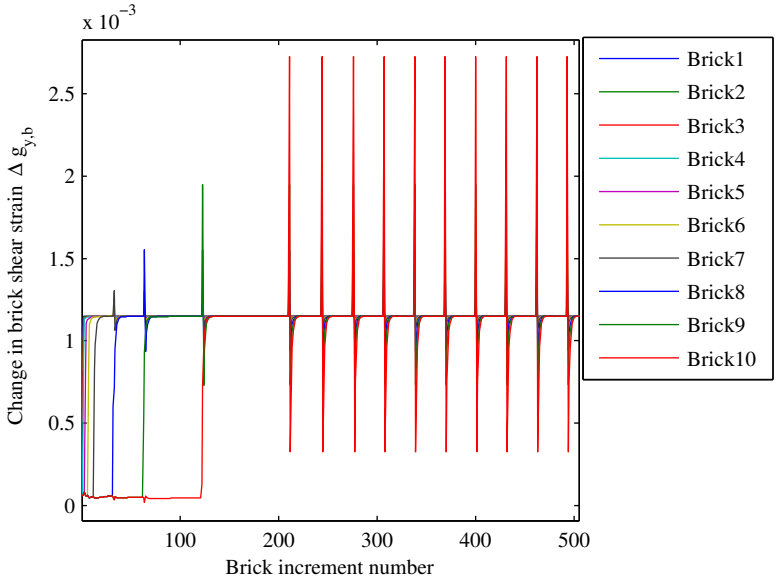

Figure 5.7: Oscillations caused by allowing time effects in constant rate consolidation

required so $\Delta g_{y,b}$ drops. The damping factor means that SL increases towards the rate appropriate value with each BRICK iteration and so the brick movement trends back to Δg_y. The problem then repeats when $SL_{previous}$ has increased to the point where the time decay can be activated again.

Problems caused

The use of the limit on t_c to work around this problem is problematic in two ways. First it is an arbitrary parameter hidden within the brick code that only functions correctly for a limited range of scenarios. Secondly it prevents the immediate time decay of parameters if there is a change in the brick strain rate. A more serious issue is that bricks will not follow the TD reduction in strain rate unless the test conditions are altered so $t_c > 2$. Figure 5.8 demonstrates this problem by plotting the normalised string length SL_{out} =SL/SL_{ref} versus iteration number for 1D swelling which had been preceded by 1D consolidation. A modified limit of t_c> 100 is used due to the slow test rate used in this example. After the initial oscillations the string length remains high and then drops suddenly before showing the curved form of the time dependent behaviour. The point at which SL_{out} drops is observed to increase with brick number. The drop point corresponds to the point where brick strain rate $||\dot{\boldsymbol{\varepsilon}}_{\boldsymbol{b}}||$, shown in Figure 5.9, has reached 0. $||\dot{\boldsymbol{\varepsilon}}_{\boldsymbol{b}}||$ is calculated for each brick as the magnitude of the vector of component strain changes for each brick $\boldsymbol{\Delta\varepsilon_b}$ divided by the applied change in time Δt.

In the test discussed the appropriate string length for a taut brick during the consolidation is SL_{out} =2.2. The swelling stage has however reversed the strain direction

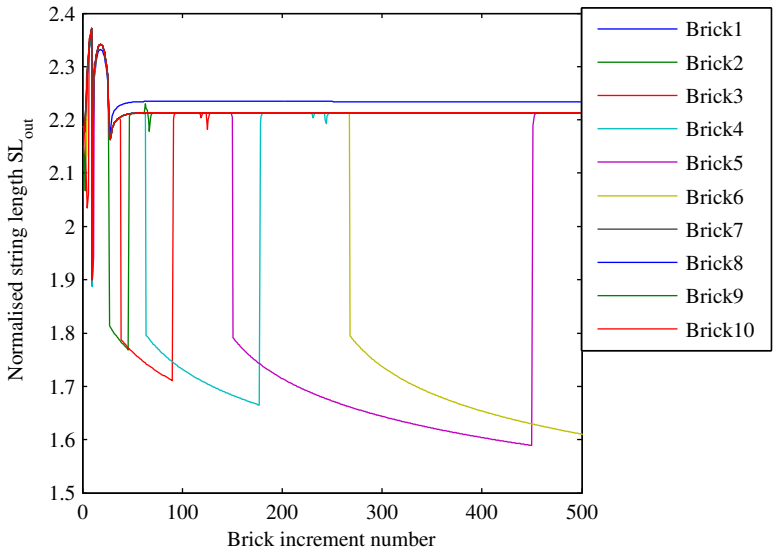

Figure 5.8: SL_{out} versus iteration number for a swelling stage when TC workaround used

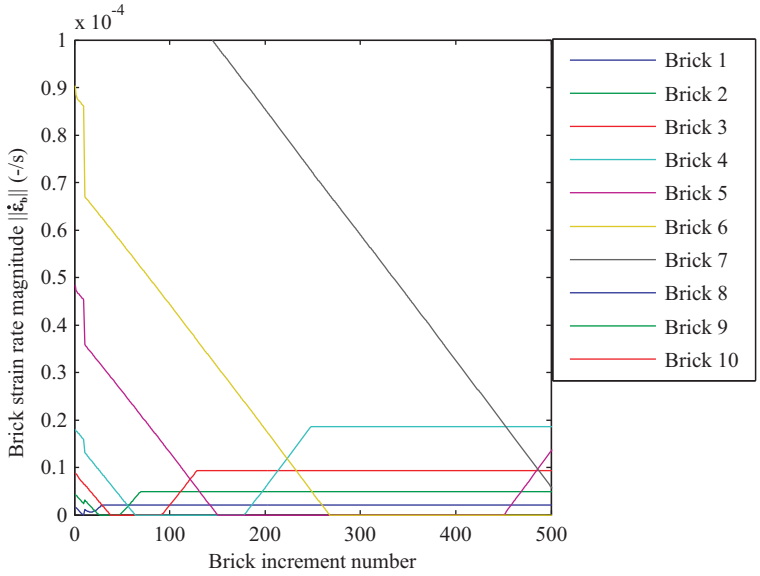

Figure 5.9: $||\dot{\varepsilon}_b||$ versus iteration number for a swelling stage when t_c workaround used

and initially all bricks are slack. If time effects were not in place all bricks would reset to their reference lengths SL_{out} =1. With TD effects all strings should shorten with increasing time. This continues until the combination of the applied strain and the shortened string lengths causes strings to become taut in the opposite direction and SL_{out} increases back to 2.2. The reason this is not happening is in part related to the limit of $t_c <$ 100 used to prevent oscillations during consolidation. The explanation for this requires an examination of the iteration process used:

1. The initial string length input into the SRD iteration is always set as SL_{ref}.

2. This results in a high initial brick strain and so $||\dot{\boldsymbol{\varepsilon}}_{\boldsymbol{b}}||$ is at its highest possible value.
3. If the distance between the man at the end of the brick iteration and the brick at the start T is greater than SL_{ref} $||\dot{\boldsymbol{\varepsilon}}_{\boldsymbol{b}}||$ will be non-zero.
4. A string length is generated to satisfy $||\dot{\boldsymbol{\varepsilon}}_{\boldsymbol{b}}||$ then averaged with the string length from the previous SRD iteration SL_{prev}.
5. At this point $SL < SL_{previous}$ TD effects should be activated however $t_c < 100$ so they are prevented.
6. Due to the 'rams workaround' (see next section) the strings do not become slack when SL increase within the SRD iteration but rather move bricks back generating a new value for $||\dot{\boldsymbol{\varepsilon}}_{\boldsymbol{b}}||$.
7. The process repeats until considered solved, as the strings do not become slack $||\dot{\boldsymbol{\varepsilon}}_{\boldsymbol{b}}||$ cannot be 0 unless on the first increment.

When the string becomes slack at SL_{ref} and $||\dot{\boldsymbol{\varepsilon}}_{\boldsymbol{b}}|| = 0$ on the first iteration SL is calculated as SL_{ref} from the applied strain rate, but due to damping SL is generated between this value and $SL_{previous}$. On the subsequent increment $SL_{previous}$ has dropped so t_p is higher resulting in $t_c > 100$ and activation of TD effects.

Rams work around

Original implementation

The rams workaround refers to a change in the brick analogy used in the SRD routine. In the original brick analogy the man is dragging bricks connected by strings that can only pull bricks. Strain rate dependency extends this by having the string length increased and decreased in relation to strain rate. The calculation of brick movements used within the SRD iteration does not prevent brick movement if the string length generated is longer than separation T. T is the distance between the applied strain that will exists at the end of the brick increment and the current strain of the brick. In cases where $SL > T$ the calculation used pushes bricks away from the man and so is more analogous to a hydraulic ram than a string.

This change allows a solution when strings where taut at SL_{ref} but slack at the rate appropriate string length SL_{app}. The SRD iteration is setup so for each brick the strain rate $||\dot{\boldsymbol{\varepsilon}}_{\boldsymbol{b}}||$ resulting from the brick strain change vector $\boldsymbol{\Delta\varepsilon_b}$ generated by a string of length SL, is the same at that used in Equation 5.35 from which SL originates.

$$SL = \frac{(SL_r \times (1 + (\beta * ln(\frac{||\dot{\boldsymbol{\varepsilon}}_{\boldsymbol{b}}||}{\dot{\varepsilon}_{ref}+1}))))) + SL_{prev}}{2} \tag{5.35}$$

When the string is slack at SL_{ref} the value $||\dot{\boldsymbol{\varepsilon}}_{\boldsymbol{b}}||$ is calculated from the initial SL value $SL = SL_{ref}$. There is no brick movement and so $||\dot{\boldsymbol{\varepsilon}}_{\boldsymbol{b}}|| = 0$. The value of SL calculated from $||\dot{\boldsymbol{\varepsilon}}_{\boldsymbol{b}}||$ is $SL = SL_{ref}$ and so the routine ends. When the string

is taut at SL_{app} value $||\dot{\boldsymbol{\varepsilon}}_{\boldsymbol{b}}||$ is determined by the applied strain rate. The iterative solution is however unstable when used to solve strings that are taut at SL_{ref} but not at SL_{app}. In this situation the unique string length solution is not found as the iteration proceeds as follows:

- String lengths shorter than the SL solution generate a strain rate $||\dot{\boldsymbol{\varepsilon}}_{\boldsymbol{b}}||$ in the SRD routine.
- The string length SL calculated from this strain rate makes strings slack.
- Slack strings result in a strain rate of 0.
- The string length SL is calculated to be the reference length SL_{ref}.
- The circular logic repeats until the effects of damping factors cause a solution to be declared.

The 'rams' approach avoids this error by ensuring that slack strains generate a high strain rate rather than zero strain rate. SL from this high strain rate is damped to be only a small change since the previous increment $SL_{previous}$. This results in a different strain rate from the slack strings and so over several iterations a solution is found where SL is within the tolerance of the SRD iteration. By the 'rams' workaround the first point to become taut at SL_{ref} generates a long string length. The string length then decays back to the rate appropriate length SL_{app} over several increments of the BRICK routine. This combined with the capping of the strain rate as that of brick 1 result in a satisfactory solution for consolidation. As the second brick iteration does not run the SRD iteration no brick strain is generated for the longer strings which become slack. As the longer strings remain slack there is no effect on output stress.

Problems caused

The 'rams' workaround results in a generation of a strain rate from what should be slack bricks. Along with the t_c limit on time decay, this prevents time decay from occurring at the start of a swelling stage.

Strain rate limited to that of brick 1

Original implementation

The value of the strain rate used within the SRD portion of the brick routine ($||\dot{\boldsymbol{\varepsilon}}_{\boldsymbol{b}}||$) is limited to that set for brick 1.

The purpose of this is to limit the string length of bricks in consolidation stages in the period between strings being taut at SL_{ref} and taut at SL_{app}. As brick 1 is the shortest of bricks, the peak caused by the rams approach increasing the string length for brick 1 after becoming taut at SL_{ref}, will have decayed before other bricks become taut at SL_{ref}. The effect of capping the strain rate means that the

peak in SL is suppressed for subsequent bricks.

Problems caused

The problem caused by this workaround is shown at the beginning of Figure 5.8. Due to the limit on when TD effects activate strings only shorten when $||\dot{\boldsymbol{\varepsilon}}_{\boldsymbol{b}}|| = 0$. This normally occurs when the string becomes slack at SL_{ref}. By limiting $||\dot{\boldsymbol{\varepsilon}}_{\boldsymbol{b}}||$ to that of brick 1, when string 1 becomes slack at SL_{ref} all strings shorten and produce a dip in SL. The unstable strain rate of brick 1 as it increases back to SL_{app} is then reflected on all bricks due to this mechanism.

Calculation of time

In the SRD code the TDSL is based on a calculation for the current strain rate $\dot{\varepsilon}_{current}$ given in Equations 5.29 to 5.31 (p 155). From this Equation 5.36 is used to calculate a string length appropriate to that strain rate SL_{calc} which is then damped to the string length output by Equation 5.37

$$SL_{calc} = SL_{ref} \times (1 + \beta \ln(\frac{\dot{\varepsilon}_{current}}{\dot{\varepsilon}_{ref}} + 1)) \tag{5.36}$$

$$SL = SL_{previous} + 0.05 \times (SL_{calc} - SL_{previous}) \tag{5.37}$$

This implementation causes problems with the correct calculation of time elapsed during a creep or stress relaxation stage. Figure 5.10 illustrates the progression of the code and how different calculations for time arise. The first method is a clock time taken from a cumulative sum of the applied time increments, in this case the first creep increment would start at $0\,\mathrm{s}$ and finish at $100\,\mathrm{s}$. This differs slightly from the current time approach that takes the value of t_c. While the increment is the same, $\dot{\varepsilon}_{previous}$ derived from $SL_{previous}$ results in $t_p = 0.0053$ so $t_c = 100.0053\,\mathrm{s}$ producing a minor difference in the calculated time. The major discrepancy is introduced when the string length calculated by Equation 5.36 for $t_c = 100.0053\,\mathrm{s}$ creep SL_{calc} is damped by Equation 5.37 increasing SL above that calculated from the given creep time. When the associated strain rate $\dot{\varepsilon}_{actual}$ and time t_{actual} are back calculated, the string length resulting from the 0.05 damping factor used in this example actually corresponds to a total creep time of $0.0086\,\mathrm{s}$. The effects of the time calculation on the SL versus time plot are shown in Figure 5.11. This shows how when the creep time does not relate to the actual string length output, the expected logarithmic decay is disturbed at the beginning for the current time approach or throughout when using clock time.

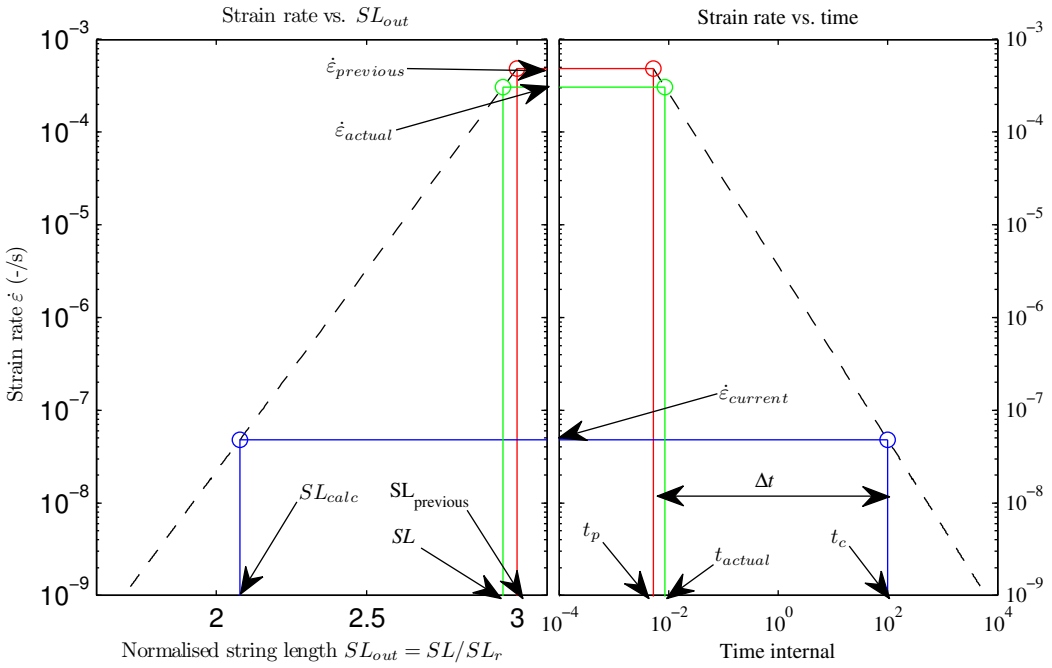

Figure 5.10: Calculation of time and string length

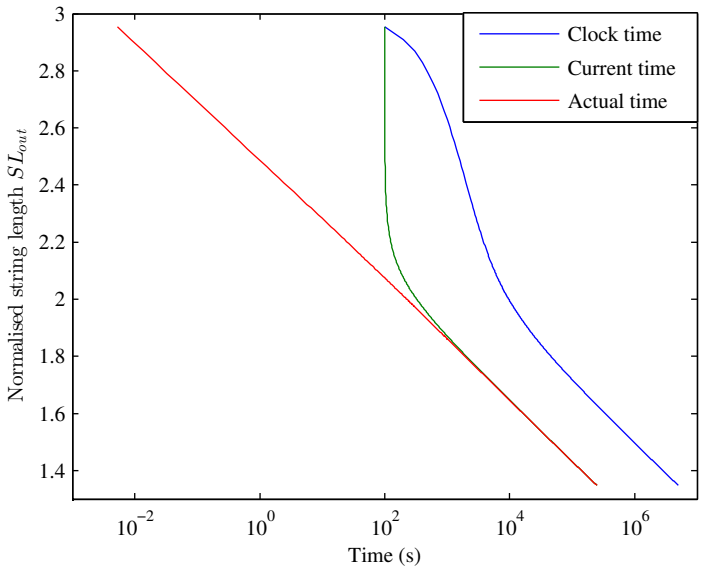

Figure 5.11: Effect of time calculation method on SL time relationship

5.2.3 Bisecting solution to SRD problem

To avoid the need for the workarounds used by Clarke (2009) a clearer picture of the problem to be solved is required. Equation 5.38 relates the string length of a brick SL to brick strain rate magnitude $||\dot{\boldsymbol{\varepsilon}}_{\boldsymbol{b}}||$ along with constants β and $\dot{\varepsilon}_{ref}$. An iterative solution is required as $||\dot{\boldsymbol{\varepsilon}}_{\boldsymbol{b}}||$ is related to SL by either Equation 5.39 or 5.40, refereed to as the 'rams' and 'strings' approaches respectively. The constant T is the distance between the position of a brick at the start of the current increment and the man after the application of the imposed strain change. This is controlled by

the input brick strain, applied strain and applied strain change. In both approaches the numerator is the magnitude of the strain change for a brick $||\boldsymbol{\Delta\varepsilon_b}||$. In the 'rams' approach this increases when $SL > T$ as bricks move away from the man while in the 'strings' approach no movement is allowed if $SL > T$.

$$SL = SL_{ref} \times (1 + \beta \ln(\frac{||\dot{\boldsymbol{\varepsilon}}_{\boldsymbol{b}}||}{\dot{\varepsilon}_{ref}} + 1)) \tag{5.38}$$

$$||\dot{\boldsymbol{\varepsilon}}_{\boldsymbol{b}}|| = \frac{|T - SL|}{\Delta t} \tag{5.39}$$

$$||\dot{\boldsymbol{\varepsilon}}_{\boldsymbol{b}}|| = \begin{cases} \frac{|T-SL|}{\Delta t}, & \text{if } SL<T. \\ 0, & \text{otherwise.} \end{cases} \tag{5.40}$$

Figure 5.12 and 5.13 show Equations 5.38, 5.39 and 5.40 plotted on axis of strain rate versus normalised string length SL/SL_{ref}. An indication of SL_{app} the string length appropriate to the applied strain rate is also given. Figure 5.12 shows one solution satisfying both Equation 5.38 and Equation 5.40 exists for a string length between SL_{ref} and SL_{app}. There are however several solutions between Equation 5.38 and Equation 5.39. The iteration used in Clarke (2009) converges on the upper solution. As the 'strings concept' is used outside the SRD iteration no brick strains are generated and so T increases by the applied strain change on each increment until the state shown in Figure 5.13 is reached. At this point the 'strings' and 'rams' approaches give the same result; this results in brick strains being generated equal to the applied strain so T remains constant on future increment at this rate.

Equation 5.40 can be reformulated to give string length as a function of strain rate, as given by Equation 5.41. When $T < SL_{ref}$ the solution is trivial as both Equation 5.38 and 5.40 solve $SL = SL_{ref}$. For other cases Equation 5.42 can be solved approximately by a bisecting iteration (Appendix E.2).

$$SL = \begin{cases} T - (\Delta t \times ||\dot{\boldsymbol{\varepsilon}}_{\boldsymbol{b}}||), & \text{if } T>SL_{ref}. \\ SL_{ref}, & \text{otherwise.} \end{cases} \tag{5.41}$$

$$0 = \left(SL_{ref} \times (1 + \beta \ln(\frac{||\dot{\boldsymbol{\varepsilon}}_{\boldsymbol{b}}||}{\dot{\varepsilon}_{ref}} + 1)) \right) - (T - (\Delta t \times ||\dot{\boldsymbol{\varepsilon}}_{\boldsymbol{b}}||)) \tag{5.42}$$

This new method dubbed SRD-B: $v1$ provides a string length solution that increases from SL_{ref} to SL_{app} in several steps. On each of these steps a brick strain change $\boldsymbol{\Delta\varepsilon_b}$ is produced. This has the effect of reducing T on the subsequent increment from what it would have been had a non-SRD solution with a string length SL_{app} been used. A simplified comparison was set up whereby SL_{ref}=0.5, SL_{app}=1 and the magnitude of the applied strain change $||\boldsymbol{\Delta\varepsilon}||$ = 0.01, this was run with both the non-SRD and the SRD-B codes. Figure 5.14 shows how for non-SRD brick T

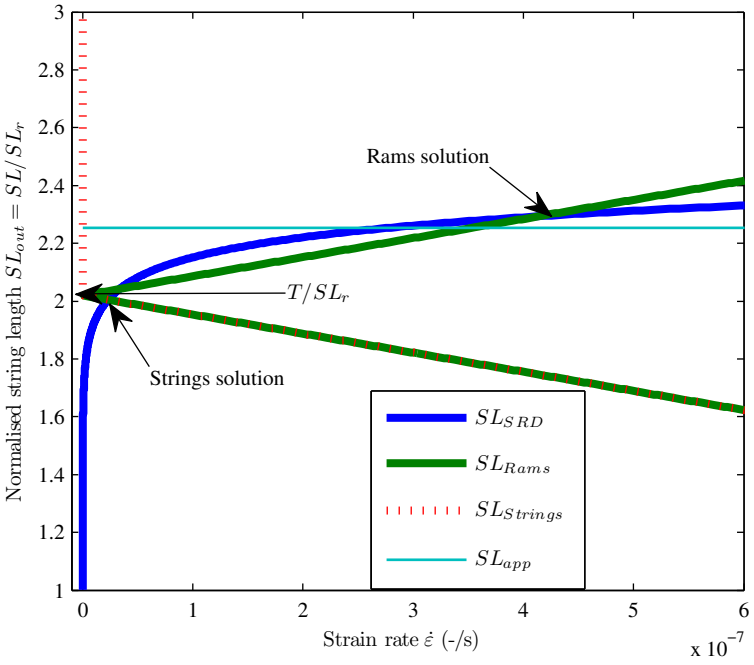

Figure 5.12: Illustration of string length calculation for SL less than SL_{app}

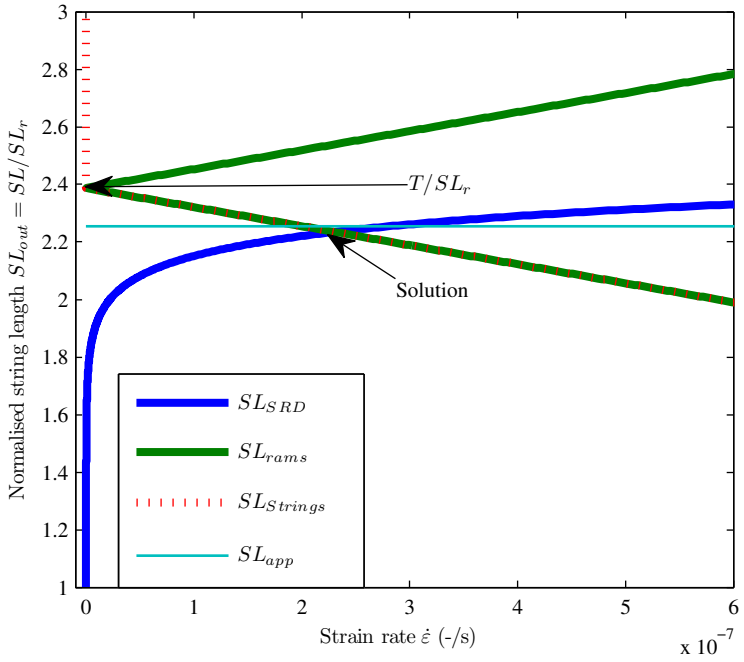

Figure 5.13: Illustration of string length calculation for SL approximately equal to SL_{app}

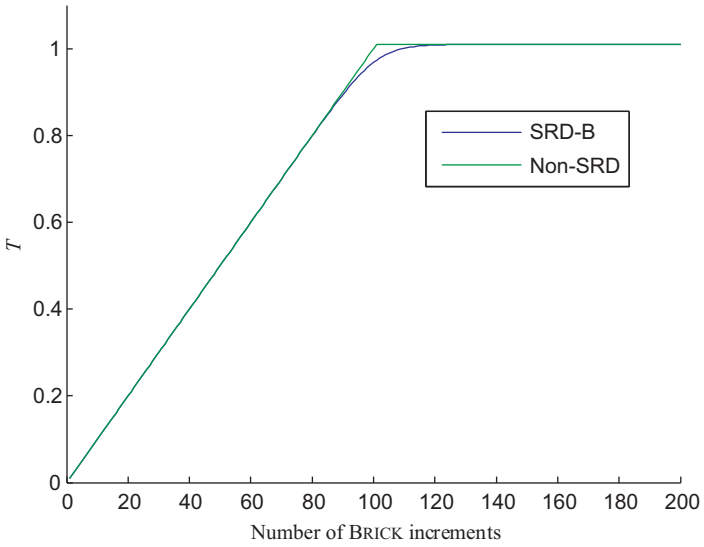

Figure 5.14: Comparison of how non-SRD and SRD-B BRICK calculate the brick to man distance T

increases linearly from $||\boldsymbol{\Delta\varepsilon}||$ to SL_{app} + $||\boldsymbol{\Delta\varepsilon}||$. At this point the string becomes taut causing a brick strain $||\boldsymbol{\Delta\varepsilon_b}||$ = $||\boldsymbol{\Delta\varepsilon}||$ to be generated therefore T is not increased on the next increment, as shown in Figure 5.15. The SRD-B model behaves differently: $||\boldsymbol{\Delta\varepsilon_b}||$ begins to be generated at SL_{ref} and approaches $||\boldsymbol{\Delta\varepsilon}||$ asymptotically (Figure 5.15) a corresponding reduction in T is shown in Figure 5.14. The total brick strain $||\boldsymbol{\varepsilon_b}||$ (as shown in Figure 5.16) increases earlier in the SRD-B model but becomes indistinguishable from the Non-SRD model with increasing increments. This result means that the SRD-B model will show smooth transitions in the stress path when bricks become taut but should have a minimal impact on the long term stress output.

5.2.4 Problems caused by limitations of double precision

The initial version of the SRD-B code encountered a problem whereby an oscillation of the string length would be induced at a constant strain rate. These consisted of sharp dips in SL followed by asymptotic increase towards SL_{app}, resulting from the activation of the TD effect when $SL < SL_{previous}$. For a constant strain rate SRD-B code however SL is asymptotic to SL_{app} so $SL < SL_{previous}$ is impossible. The problem was traced to the limit of the double precision numbers in MATLAB. These are only accurate to approximately 17 significant figures. In situations where $||\boldsymbol{\varepsilon_b}||$ was several orders of magnitude bigger than $||\boldsymbol{\Delta\varepsilon_b}||$, round off errors result in the actual brick strain change Δ $||\boldsymbol{\varepsilon_b}||$ not being equal to the applied change $||\boldsymbol{\Delta\varepsilon_b}||$. The distance T is calculated from Δ $||\boldsymbol{\varepsilon_b}||$; if this is calculated as greater than the applied strain change $||\boldsymbol{\Delta\varepsilon}||$ T reduces. This results in a small reduction of SL that

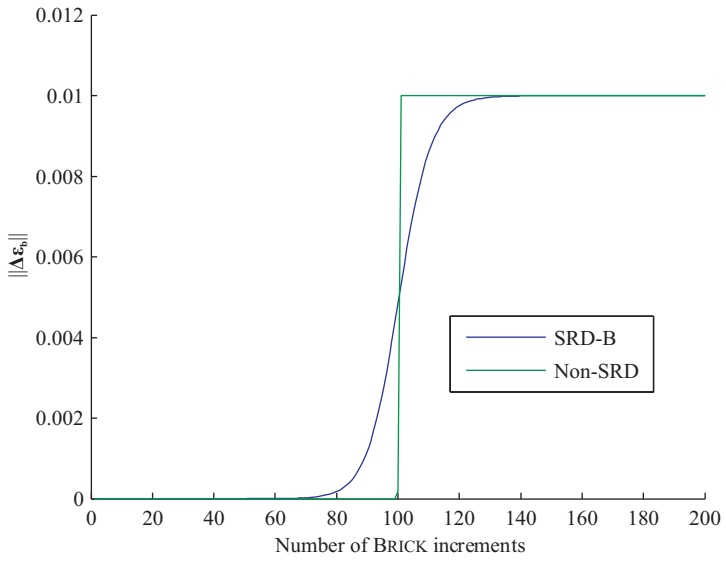

Figure 5.15: Comparison of how non-SRD and SRD-B BRICK calculate the brick strain change$||\boldsymbol{\Delta\varepsilon_b}||$

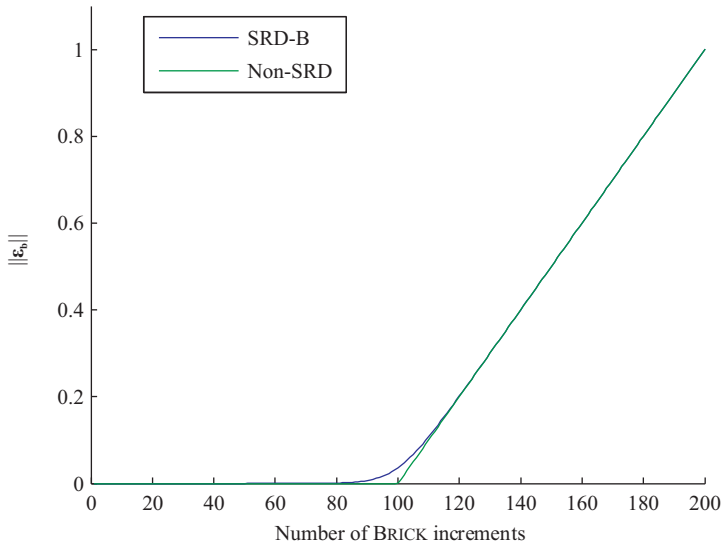

Figure 5.16: Comparison of how non-SRD and SRD-B BRICK calculate the brick strain $||\boldsymbol{\varepsilon_b}||$

activates a large reduction when a smaller TDSL is calculated.

To avoid this problem, TD effects are only allowed when the strain change vector $\boldsymbol{\Delta\varepsilon}$ has changed or TD effects were activated on the previous increment. Terms for these values on the previous increment where introduced and TD effects were activated only if at least one of the conditions was met (SRD-B: $v2$ Appendix E.3).

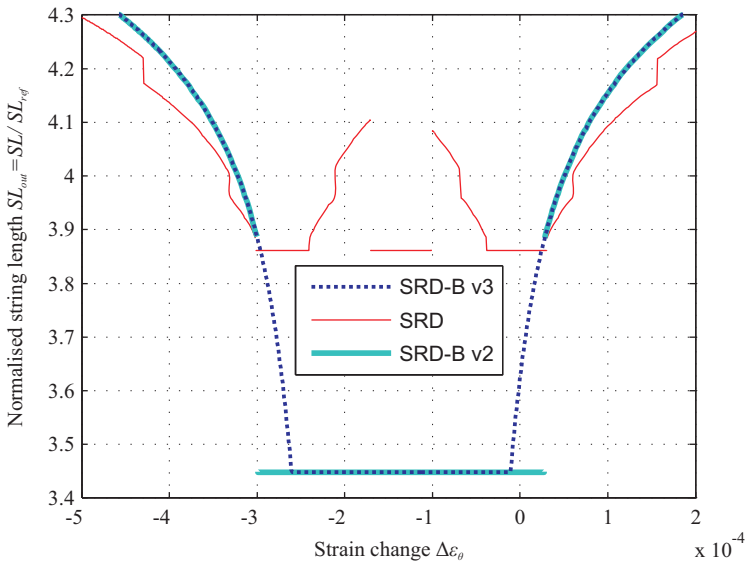

Figure 5.17: Effect of $\Delta\varepsilon_\theta$ on SL_{out} for fixed time creep stage

5.2.5 Refinement application of time dependent string lengths

The implementation of creep in the BRICK code is complicated by the strain controlled nature of the code, as creep requires the elastic strain ε_e to be held constant. The iterative routine discussed in the Section 5.3 is used to find the applied strain change vector $\boldsymbol{\Delta\varepsilon}$ that results in an equal plastic strain change vector $\boldsymbol{\Delta\varepsilon_p}$, thus producing no elastic strain change in any component. It was found however that a discontinuity in the plot of elastic strain versus applied strain change magnitude $||\boldsymbol{\Delta\varepsilon}||$ meant there was no solution for zero elastic strain.

This discontinuity was the result of the activation of TD effects when a reduced applied strain rate caused $SL < SL_{previous}$. This then resulted in a further drop in string length which had the effect of pulling the brick towards the man. This increased the plastic strain more than the total strain and so both elastic strain and stress reduced.

This problem was solved by limiting the string length to the maximum of the TDSL and that calculated from the string length solution. Figure 5.17 shows the effect of strain change $\Delta\varepsilon_\theta$ on the normalised string length SL_{out} of brick 6 for a fixed time creep stage. Here $\Delta\varepsilon_\theta$ defines the strain change along an axis passing through 0 and $\boldsymbol{\Delta\varepsilon}$ used by the stage prior to creep. This shows how the new version (SRD-B: $v3$ appendix E.4) prevents a sudden decrease in SL as it is allowed to decrease based on the change in strain rate until the point where the TD solution for string length is larger. Also shown is the SRD behaviour which contains several discontinuities and is unsuitable for the iterative solution.

Figure 5.18 shows how the strain rate degradation resulting from the new method-

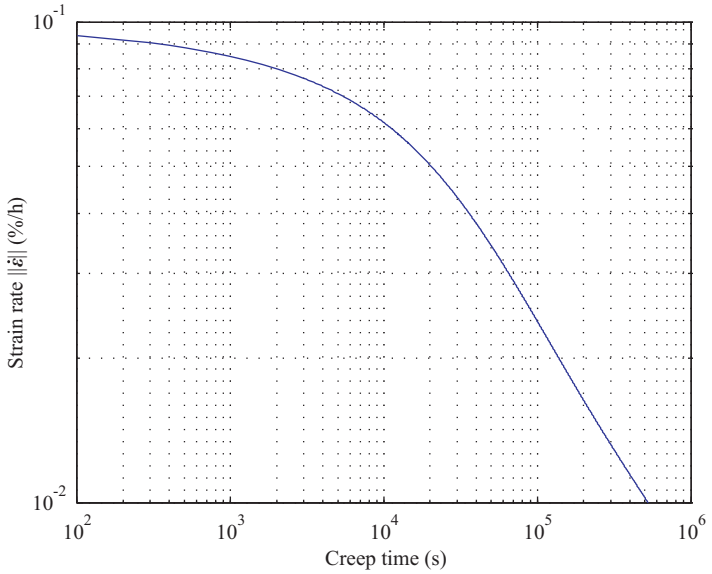

Figure 5.18: Example of strain rate decay with creep time

ology is a smooth decay to the log-log equation of strain rate versus time predicted for creep.

5.2.6 Evaluation of SRD-B model against SRD model

The new SRD-B code had be verified to run by running simulations of consolidation, creep, SRS test isotach strain rate effects, strain controlled shear, stress paths and stress relaxation. All of these tests types where observed and produce the expected form of output and correct behaviour of strings. There was however no data to which these test could be directly compared so the SRD-B code was evaluated against the original SRD code for a repeat of the evaluation tests found in section 5.3.4 to 5.3.6 of Clarke (2009). The parameters used for these simulations are given in Table 5.1 and were obtained either from Table 5.2 of Clarke (2009) or from a copy of the MATLAB code provided.

Step change in strain rate test

A SRS test was set up to show the differences between the SRD and SRD-B codes. This used a constant strain increment solution with $\boldsymbol{\Delta\varepsilon}$ = [0.0001,0,0.000 115,0,0,0] as used by Clarke (2009). The test setup given in Table 5.2 induces the reference CRS tests and the main SRS test.

The results of the SRD-B and SRD code are a close match as shown for ε_v versus p' in Figure 5.19 and for q versus p' in Figure 5.20. Two noticeable differences are; a slightly higher p', and lack of an overshoot when returning to the NCL in the SRD-B code variant.

BRICK parameter	Symbol	Code name	Value
Initial strains		`Sn(NC)`	[0, 0, 0, 0, 0, 0]
Initial stresses		`Ss(NC)`	[2, 0, 0, 0, 0, 0]
Reference string lengths [a]	SL_{ref}	`SLr(NB)`	[4.15×10^{-5}, 1.05×10^{-5}, 2.05×10^{-4}, 4.15×10^{-4}, 1.1×10^{-3}, 2.1×10^{-3}, 4.1×10^{-3}, 0.0105, 0.0205, 0.04]
Stiffness reduction		`GGmax(NB)`	[0.92, 0.75, 0.53, 0.29, 0.13, 0.075, 0.044, 0.017, 0.0035, 0]
Initial conditions		`Zero(2)`	[0,2]
Lambda*	λ*	`RLAM`	0.1
Kappa*	κ*	`RKAP`	0.02
Iota	ι	`RIOT`	0.0041
Beta constant		`BETA(1)`	4
Number of bricks		`NB`	10
Number of components		`NC`	6 - Full 3D (Triaxial testing)
Time decay constant [b]	m	`m`	0.9361
Reference strain rate	$\dot{\varepsilon}_{ref}$	`Neu`	$1 \times 10^{-13}\,\mathrm{s}^{-1}$
Viscous constant	β	`visc`	0.23
Poisson's ratio [c]	ν	`nu`	0.2
BRICK tolerance [c]		`TOLBR`	0.02
Time decay end time [d]	t_{max}	`TDtimeEnd`	$1 \times 10^{8}\,\mathrm{s}$
Time decay end rate [d]	$\dot{\varepsilon}_{min}$	`TDrateEnd`	$1 \times 10^{-12}\,\mathrm{s}^{-1}$
PSRED method [d]		`ips`	1
Second beta constant [d]		`BETA(2)`	3
Note: The string lengths are initially slack and the original position for all the bricks is the origin in strain space			

[a] Exact figures obtained from provided code not Clarke (2009)
[b] This is the inverse of the 1.0368 value in Clarke (2009) which had be used incorrectly
[c] Given in provided code
[d] Hard coded in BRICK routine of provided code

Table 5.1: BRICK parameters for the brick-led SRD-B model testing

The slightly higher p' value results from the fact that the SRD routine only calculates SL accurate to 0.1 SL_{out}, where the SRD-B routine finds $||\dot{\boldsymbol{\varepsilon}}_{\boldsymbol{b}}||$ accurate to $1 \times 10^{-15}\,\mathrm{s}^{-1}$ (the SL_{out} accuracy is approximately 1.5×10^{-12} at the $1 \times 10^{-4}\,\%/\mathrm{s}$ rate used and increases with $||\dot{\boldsymbol{\varepsilon}}_{\boldsymbol{b}}||$). The under-calculation of string length by the SRD routine may be equated to a slower strain rate, Table 5.3 gives the actual rates produced. These lower rates result in a NCL with a lower p' for a given strain. When the SRD-B code was run at these rates the result was a p' lower than the SRD

Test	Type	Rate ε_v (-/s)	Termination
1	CRS consolidation	1×10^{-2}	p'=500 kPa
2	CRS consolidation	1×10^{-3}	p'=500 kPa
3	CRS consolidation	1×10^{-4}	p'=500 kPa
4	SRS strain path	1×10^{-4}	ε_v= 15 %
		1×10^{-3}	ε_v= 20 %
		1×10^{-2}	ε_v= 25 %
		1×10^{-4}	ε_v= 40 %

Table 5.2: Setup of SRS test for SRD-B versus SRD comparison

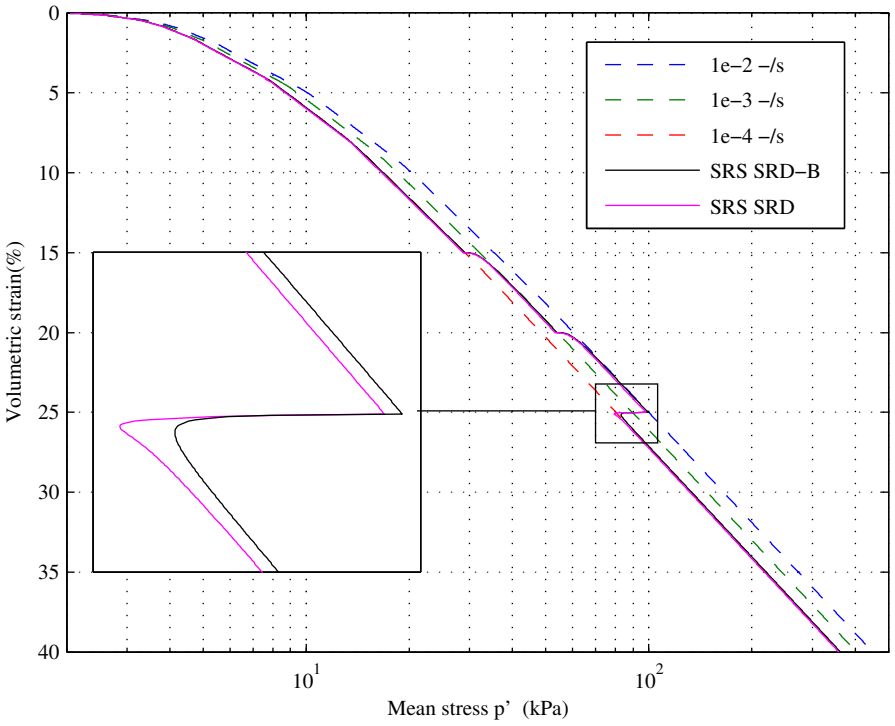

Figure 5.19: SRS test, SRD-B model versus SRD model ε_v -log p' plot

routine but by a smaller magnitude. This is because the SRD routine calculates $SL_{out}(1)$, the normalised string length for brick 1, as slightly longer than that for the rest of the bricks. This causes a slight increase in p' that cannot be accounted for in the SRD-B routine. The overshoot whereby p' dips below the appropriate CRS curve for the SRD code can be traced to the effect of the workarounds on the calculated string length. The cumulative effect of these workarounds in this case is for the string length to be controlled by the behaviour of brick 1. As shown in Figure 5.21 this results in many bricks reducing string length at lower strains than the exact solution predicts. The shorter strings result in more brick strains so that a greater plastic strain is generated and so elastic strains and hence stresses dip.

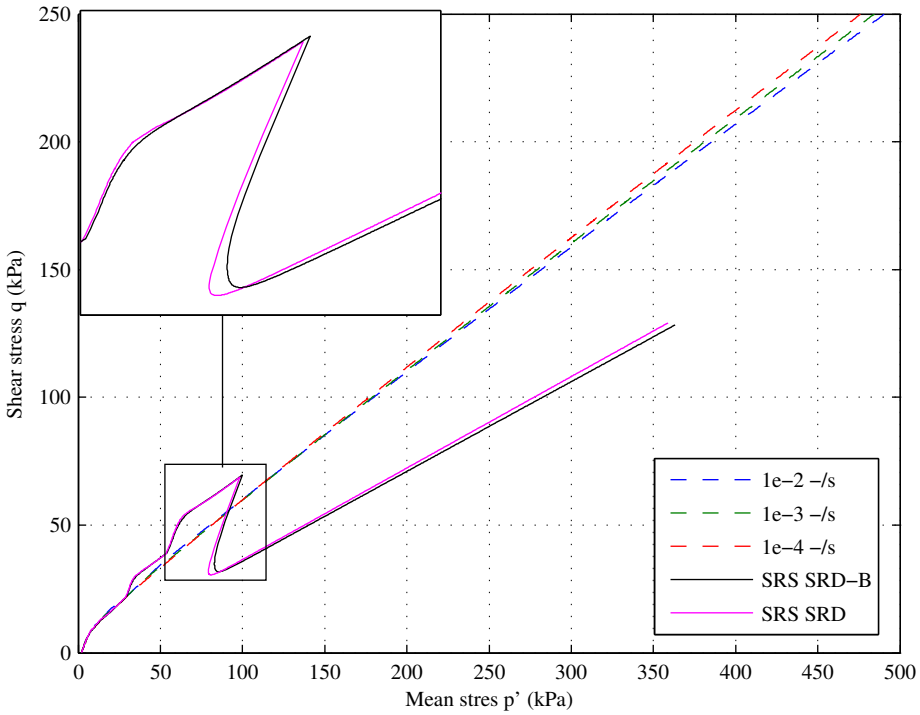

Figure 5.20: SRS test, SRD-B model versus SRD model q -log p' plot

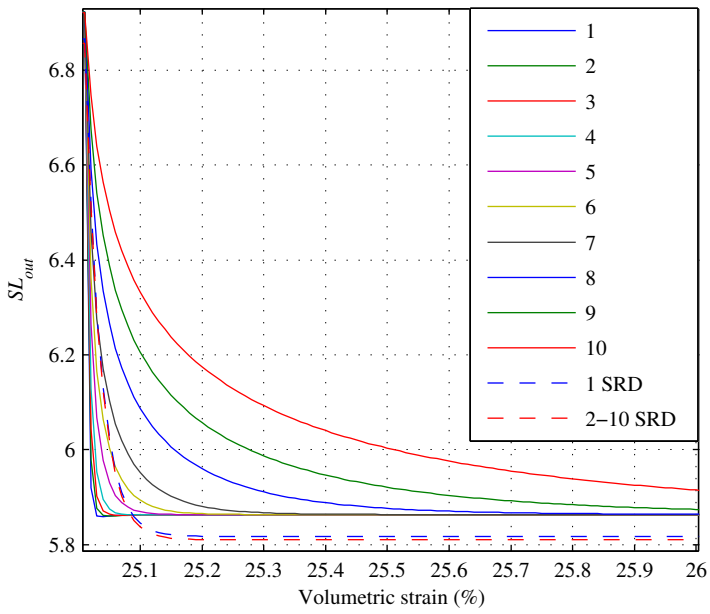

Figure 5.21: SRD-B model versus SRD model SL versus ε_v on lowering of strain rate

Rate nominal (-/s)	SL_{out}	Rate actual (-/s)
1×10^{-4}	5.81	8.18×10^{-5}
1×10^{-3}	6.33	7.73×10^{-4}
1×10^{-2}	6.86	7.53×10^{-3}

Table 5.3: Actual volumetric strain rates produced by SRD code

Stress relaxation

A stress relaxation for $5000\,\mathrm{s}$ with a time interval of $1\,\mathrm{s}$ was run after ε_v=20 % during CRS test at 3 strain rates, as detailed in Table 5.4.

Test	Type	Rate ε_v (-/s)	Termination
	CRS strain path	1.00×10^{-2}	ε_v= 20 %
1	Stress relaxation	N/A	$5000\,\mathrm{s}$
	CRS strain path	1.00×10^{-2}	ε_v= 40 %
	CRS strain path	1.00×10^{-3}	ε_v= 20 %
2	Stress relaxation	N/A	$5000\,\mathrm{s}$
	CRS strain path	1.00×10^{-3}	ε_v= 40 %
	CRS strain path	1.00×10^{-4}	ε_v= 20 %
3	Stress relaxation	N/A	$5000\,\mathrm{s}$
	CRS strain path	1.00×10^{-4}	ε_v= 40 %

Table 5.4: Setup of stress relaxation test for SRD-B versus SRD comparison

The difference between the stress relaxation in the SRD and SRD-B code is that the SRD-B code has a smaller stress change during stress relaxation. This can be seen by the smaller p' change in Figure 5.22 and the smaller p' and q change in Figure 5.23. The reason for this difference is that the SRD-B routine decays to approximately the same SL for all applied rates. This causes a smaller change in string length for the lower rate bricks which began at a slower strain rate, so these experience a smaller change in stress.

In the SRD implementation the reduction in string length is approximately equal at all rates. As shown in Figure 5.24 this is the result of the string length increasing before the end of the stress relaxation. This increase is a result of the iteration procedure used. For certain values of the initial brick strain rate $||\dot{\boldsymbol{\varepsilon}}_{\boldsymbol{b}}||$ calculated from SL = SL_{ref}, an increased string length may be calculated. Once this has occurred strings become slack and there is no movement of brick or man and the input condition is maintained for the rest of the stress relaxation. The string length increases towards that implied by the input $||\dot{\boldsymbol{\varepsilon}}_{\boldsymbol{b}}||$ over several iterations due to the damping routine.

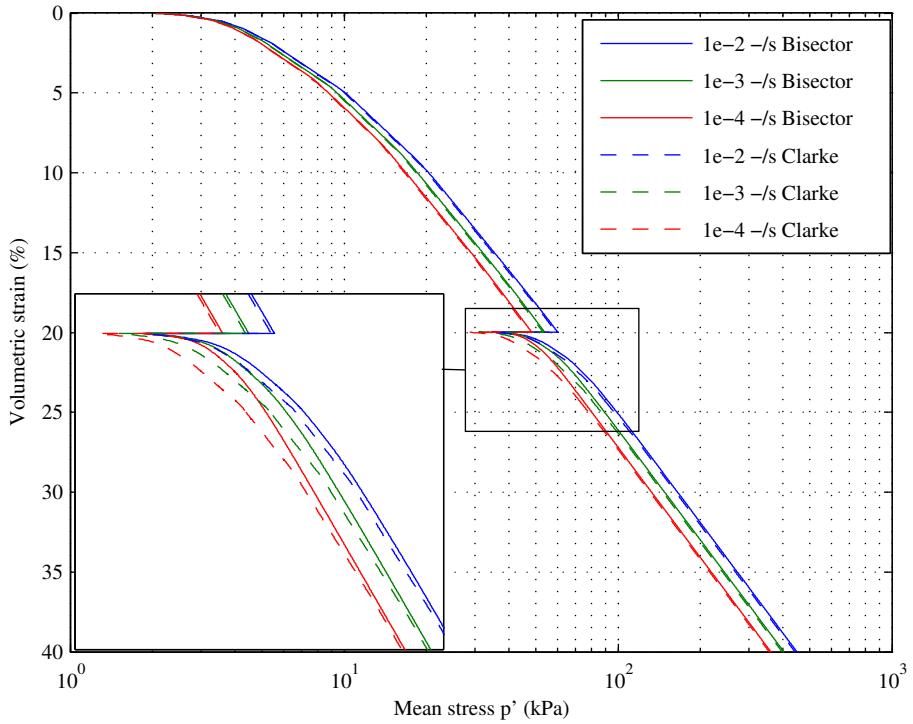

Figure 5.22: Stress relaxation test, SRD-B model versus SRD model ε_v -log p' plot

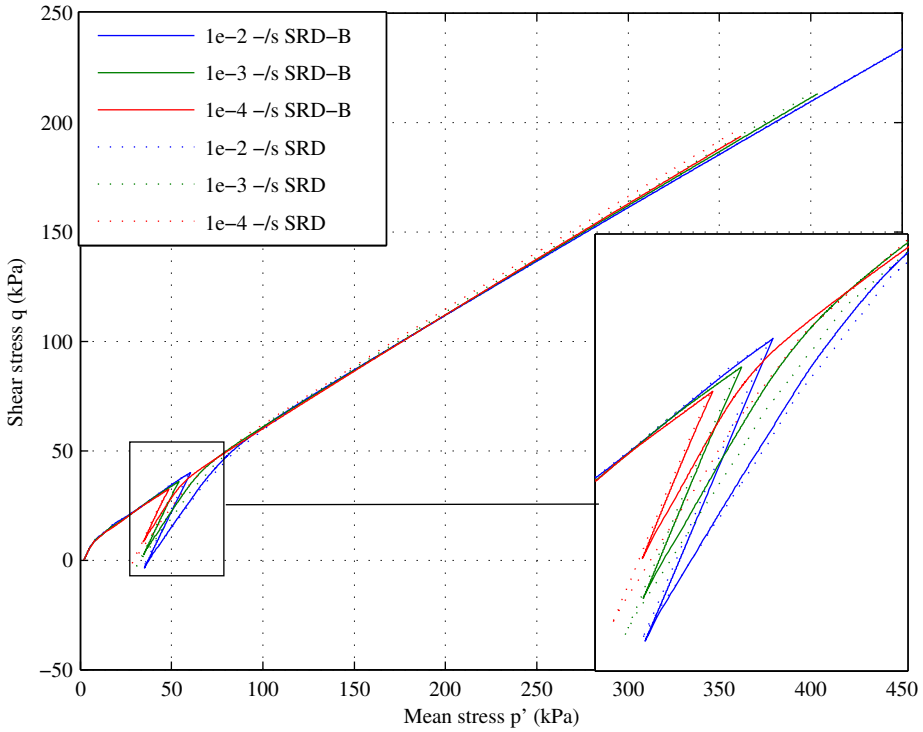

Figure 5.23: Stress relaxation test, SRD-B model versus SRD model q -log p' plot

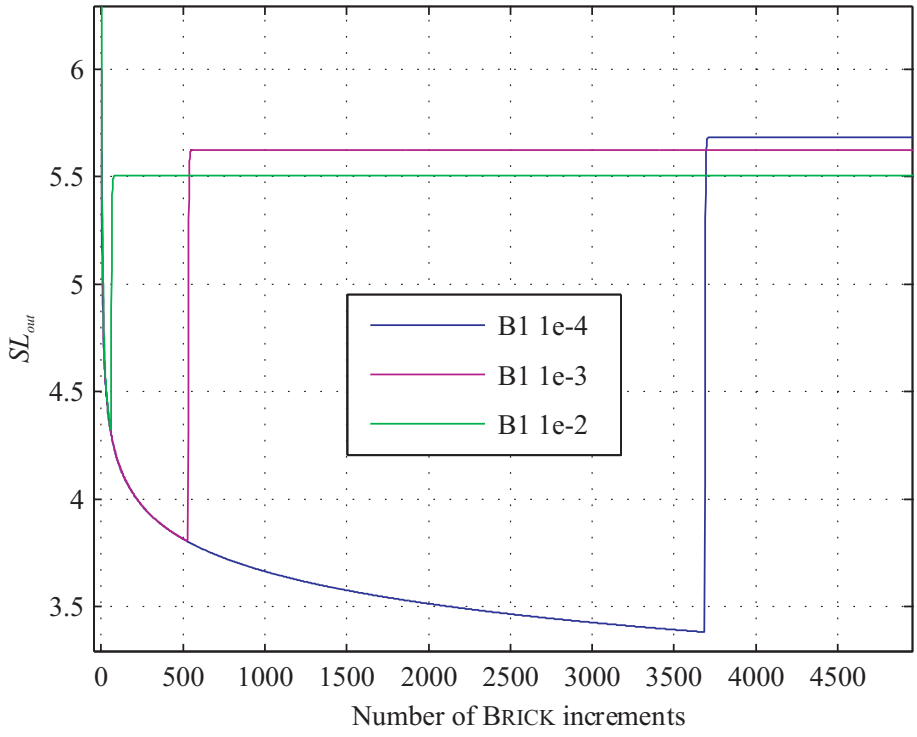

Figure 5.24: Stress relaxation SL_{out} versus BRICK increments for SRD code

One dimensional consolidation, swelling and reconsolidation

A one dimensional consolidation, swelling and reconsolidation test was run with consolidation and swelling at $1.00 \times 10^{-4}\,\mathrm{s}^{-1}$ and reconsolidation at 3 strain rates, as detailed in Table 5.5. The swelling was run to OCR=6.

Test	Type	Rate ε_v (-/s)	Termination
	CRS strain path	1.00×10^{-4}	ε_v= 20 %
1	CRS swelling	1.00×10^{-4}	OCR = 6
	CRS strain path	1.00×10^{-4}	ε_v= 40 %
	CRS strain path	1.00×10^{-4}	ε_v= 20 %
2	CRS swelling	1.00×10^{-4}	OCR = 6
	CRS strain path	1.00×10^{-3}	ε_v= 40 %
	CRS strain path	1.00×10^{-4}	ε_v= 20 %
3	CRS swelling	1.00×10^{-4}	OCR = 6
	CRS strain path	1.00×10^{-2}	ε_v= 40 %

Table 5.5: Setup of reconsolidation test for SRD-B versus SRD comparison

Due to the inaccuracies in the SL_{out} calculation, the SRD code produces a lower p' as discussed in Section 5.2.6. The SRD-B code was repeated with the strain rates found in Table 5.3 to better show the difference in return to the NCL. The ε_v versus p' plot in Figure 5.25 for the adjusted strain rates shows how the SRD-B code

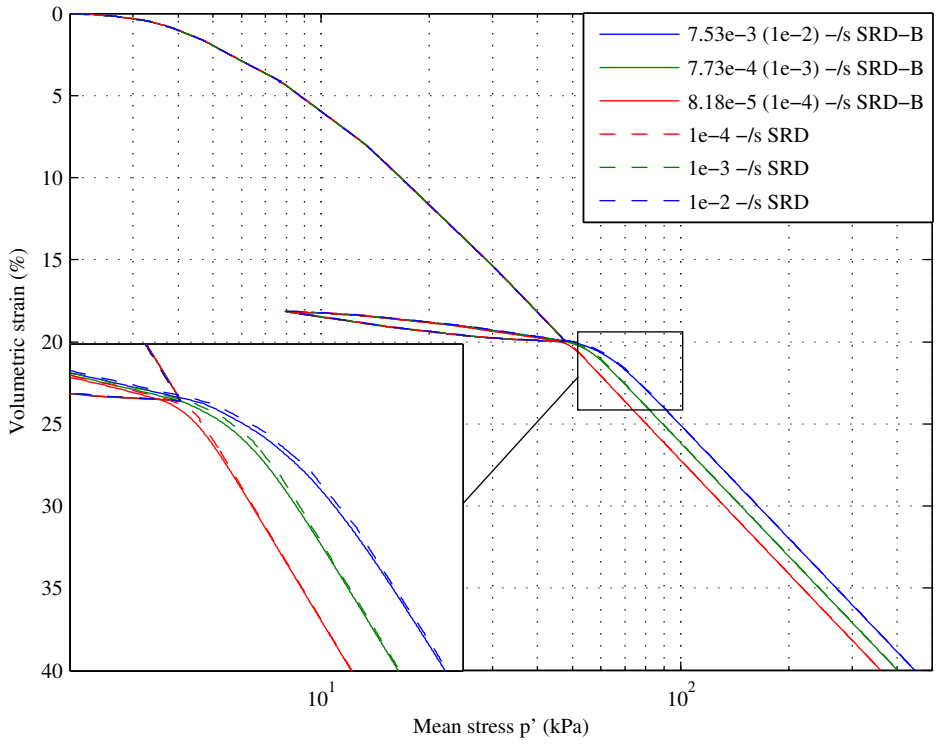

Figure 5.25: Consolidation, swelling and reconsolidation test, SRD-B model versus SRD model ε_v -log p' plot

produces a smooth asymptotic return to the NCL.This slight difference can also be seen on the stress path plot in Figure 5.26.

The major difference however is in the logic of the change in string length. In the SRD-B code shown in 5.27 all strings immediately begin to reduce in length. This is due to the string becoming slack as the strain direction reverses and so bricks undergo some creep. The reduction in string length and applied strain then causes shorter strings to become taut and so increase SL as they strain in the swelling direction. At the end of the swelling stage the those strings that had become taut become slack again and the process reverses. The longer strings that had not become taut during swelling may continue to reduce until they become taut in the new strain direction. For the SRD code however the string lengths shown in 5.28 result form the interplay of the workaround used and cannot be related to the expected positions of bricks within the brick model.

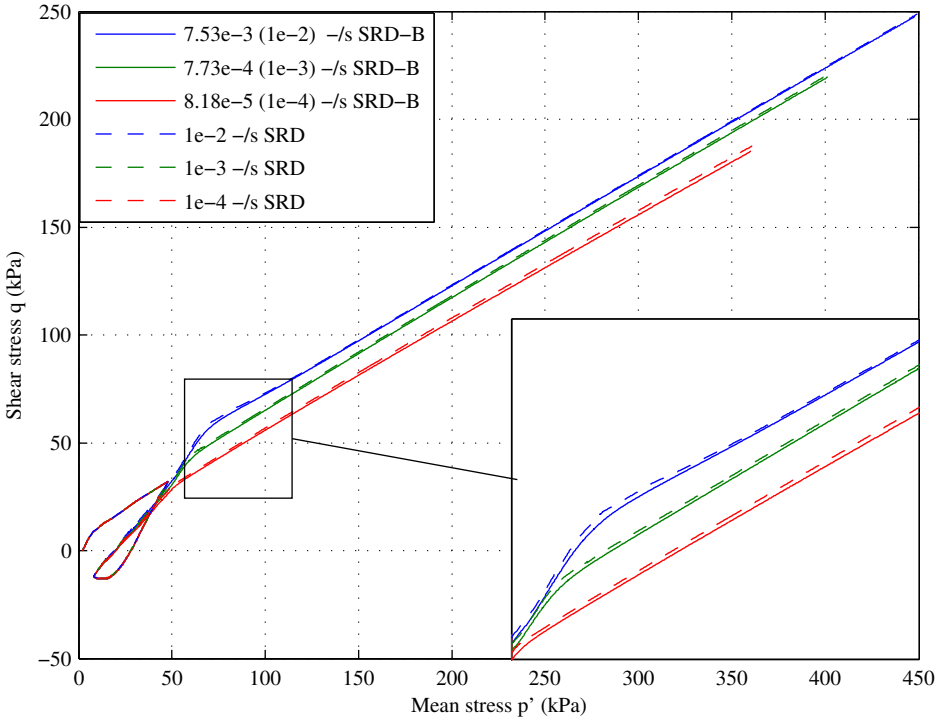

Figure 5.26: Consolidation, swelling and reconsolidation test, SRD-B model versus SRD model q -log p' plot

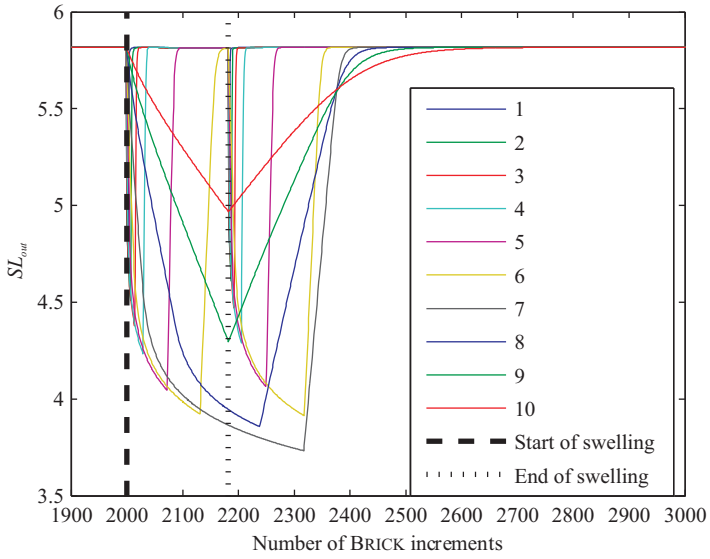

Figure 5.27: Swelling string lengths SRD-B model $\dot{\varepsilon}_v$ =$1 \times 10^{-4}\,\mathrm{s}^{-1}$

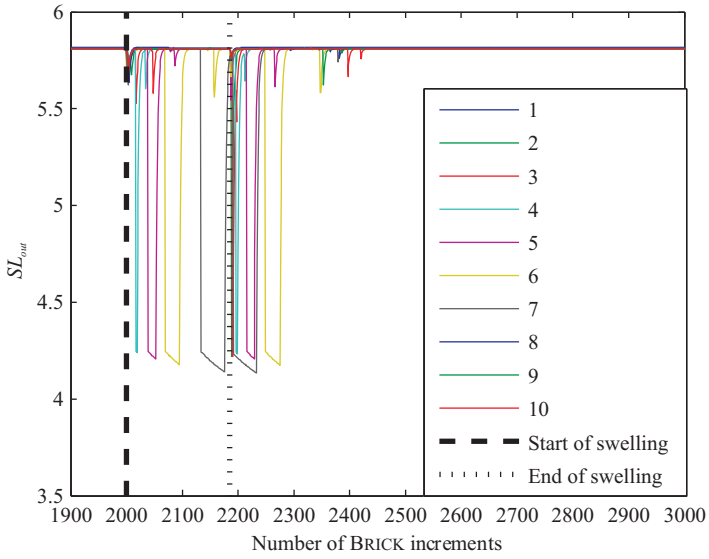

Figure 5.28: Swelling string lengths SRD model $\dot{\varepsilon}_v$ =1 $\times$ $10^{-4}\,\mathrm{s}^{-1}$

5.3 Achieving creep in the BRICK control routine

5.3.1 Introduction

To achieve creep the reduction in string length that would result in a stress relaxation must be balanced by a small applied strain such that there is no stress change. In this set-up the stress path routine commonly used does not converge on a solution consistently and the stress tolerance cannot be reduced sufficiently to provide an accurate result. A separate method is therefore required to solve creep. It should be clarified that the term creep refers specifically to strains that result in no stress change and it is this for which a specialised routine is required. The time dependent mechanism by which SL reduces with time (see Section 5.1.6 p 155) is always available.

5.3.2 Set-up used for creep tests

A 1D consolidation stage was run at a vectoral strain rate of $1 \times 10^{-3}\,\%\,\mathrm{h}^{-1}$ using a strain increment $\boldsymbol{\Delta\varepsilon}$= [0.0001,0,0.000 115,0,0,0] for 1D consolidation or $\boldsymbol{\Delta\varepsilon}$= [0.0001,0,0,0,0,0] for isotropic consolidation. At $20\,\%$ volumetric strain a $100\,\mathrm{day}$ creep stage evaluated every $100\,\mathrm{s}$ was run and then the consolidation resumed and ran until $40\,\%$ volumetric strain. The testing used the 18 brick model used by Clarke (2009) which is given along with all other parameters used in table Table 5.6.

BRICK parameter	Code name	Value
Initial strains	`Sn(NC)`	[0, 0, 0, 0, 0, 0]
Initial stresses	`Ss(NC)`	[2, 0, 0, 0, 0, 0]
Reference string lengths	`SLr(NB)`	$[5 \times 10^{-7},\ 1.5 \times 10^{-6},\ 3.125 \times 10^{-6},\ 5 \times 10^{-6},\ 1 \times 10^{-5},\ 1.75 \times 10^{-5},\ 2.5 \times 10^{-5},\ 3.5 \times 10^{-5},\ 5 \times 10^{-5},\ 1.05 \times 10^{-4},\ 2 \times 10^{-4},\ 3.5 \times 10^{-4},\ 5 \times 10^{-4},\ 1 \times 10^{-3},\ 2 \times 10^{-3},\ 4 \times 10^{-3}, 0.01, 0.0323]$
Stiffness reduction	`GGmax(NB)`	[0.9, 0.85, 0.815, 0.79, 0.74, 0.69, 0.61, 0.5, 0.4, 0.3, 0.22, 0.17, 0.13, 0.09, 0.06, 0.02, 0.009, 0]
Initial conditions	`Zero(2)`	[0,2]
Lambda*	`RLAM`	0.1
Kappa*	`RKAP`	0.02
Iota	`RIOT`	0.0054
Beta constant	`BETA(1)`	4
Number of bricks	`NB`	18
Number of components	`NC`	6 - Full 3D (Triaxial testing)
Time decay constant [a]	`m`	0.888
Reference strain rate	`Neu`	$1 \times 10^{-13}\,\mathrm{s}^{-1}$
Viscous constant	`visc`	0.23
Poisson's ratio	`nu`	0.2
BRICK tolerance	`TOLBR`	0.02
Time decay end time [a]	`TDtimeEnd`	$1 \times 10^{11}\,\mathrm{s}$
Time decay end rate [a]	`TDrateEnd`	$2.2 \times 10^{-14}\,\mathrm{s}^{-1}$
PSRED method	`ips`	2
Second beta constant	`BETA(2)`	3
Note: The string lengths are initially slack and the original position for all the bricks is the origin in strain space		

[a] From analysis of Bishop (1966)

Table 5.6: BRICK parameters for use in creep testing

5.3.3 Alternating stress relaxation - stress path method

This method works by separating the reduction in string lengths and the output stress. A stress relaxation stage is run to a small stress change. During this stage the measured time is allowed to increase and the string lengths reduce. The strain rate effects are then turned off and the string lengths are fixed at the value output from the stress relaxation stage. A stress path is then run to return the stress to that at the

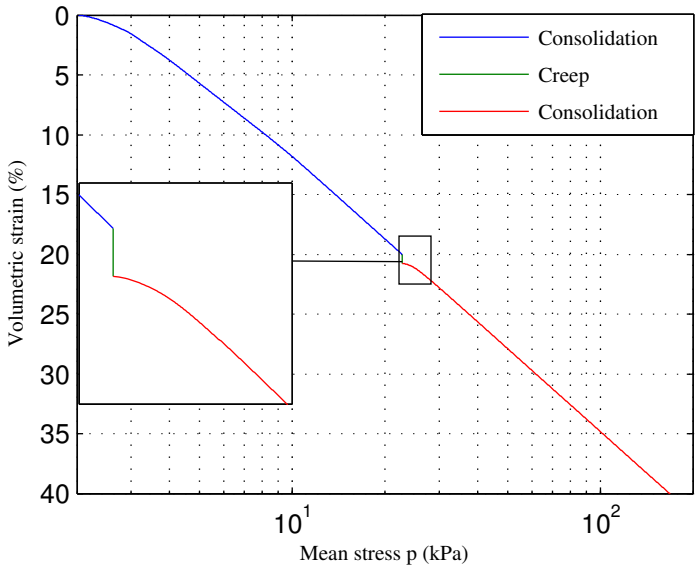

Figure 5.29: Isotropic creep ε_v -log p' plot, alternating stress relaxation - stress path method

beginning of creep. In this way the string length has become shorter and no stress change has been imposed. Stress relaxation and stress path stages are alternated to produce a creep solution. This method was only implemented to hold the mean stress component p' constant. This was because the stress path finding routine was modified to achieve a high accuracy in finding the target stress. This routine could not be extended easily to more than one stress component. The holding of only the mean stress was however appropriate for creep performed at $q = 0\,\mathrm{kPa}$. The result of this method for an isotropic consolidation is that the mean stress is kept within $0.001\,\mathrm{kPa}$ stress change allowed for the stress relaxation as shown in Figure 5.29. The strain rate, taken from the end of the returning stress path stages, degrades with time and then reaches the log-log strain rate versus time relation expected for a creep stage, as shown in Figure 5.30.

5.3.4 Coordinate descent creep routine

Principle

In order to achieve creep stress needed to be held at zero in all stress components. A single target parameter could be found by taking the magnitude of the stress $||\boldsymbol{\sigma}||$. Figure 5.31 shows the variation of $||\boldsymbol{\sigma}||$ with the imposed change in the brick strain components Δv and Δg_y for a $30\,\mathrm{min}$ creep step applied during the 1D consolidation. This shows that there exists a single point at which $||\boldsymbol{\sigma}||$=0 and that $||\boldsymbol{\sigma}||$ decreases monotonically towards this point from all directions.

Under this set of circumstances a coordinate descent routine could be used to find

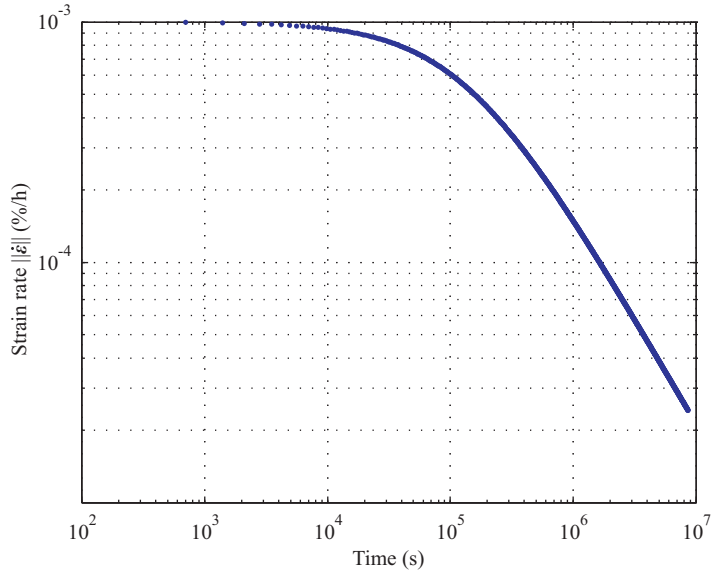

Figure 5.30: Isotropic creep log ($\dot{\varepsilon}$) - log(t) plot, alternating stress relaxation - stress path method

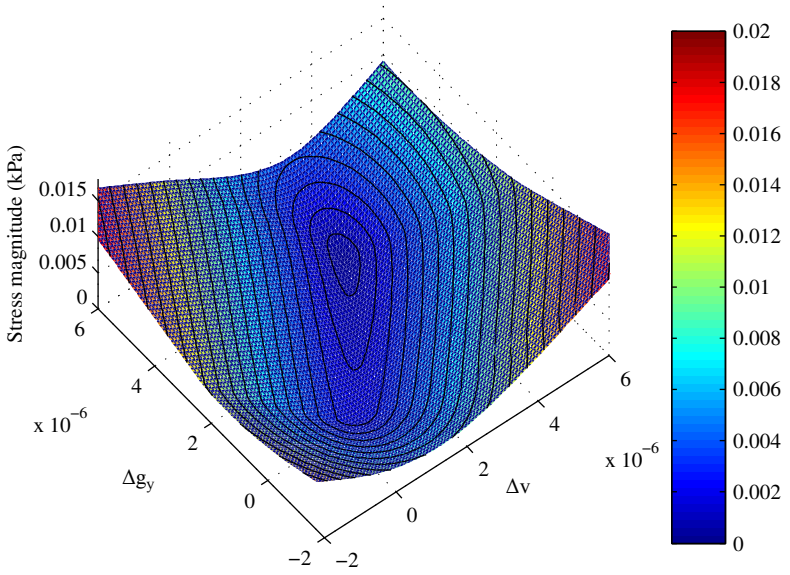

Figure 5.31: The effect of strain change Δv and Δg_y on stress magnitude $||\boldsymbol{\sigma}||$

the strain change that would result in creep. The Matlab based coordinate descent creep routine (Appendix F) used several creep increments of fixed time step to reach a target creep duration or strain rate. The strain change was calculated by the following algorithm:

1. Use a stress relaxation where Δv = 0 , Δg_y = 0 to define a point $P = (\Delta v, \Delta g_y)$.
2. Calculate $||\boldsymbol{\sigma}||$ at point P and term it S.
3. Calculate six points $p_{1-6} = (\Delta v, \Delta g_y)$ located at the points of a hexagon

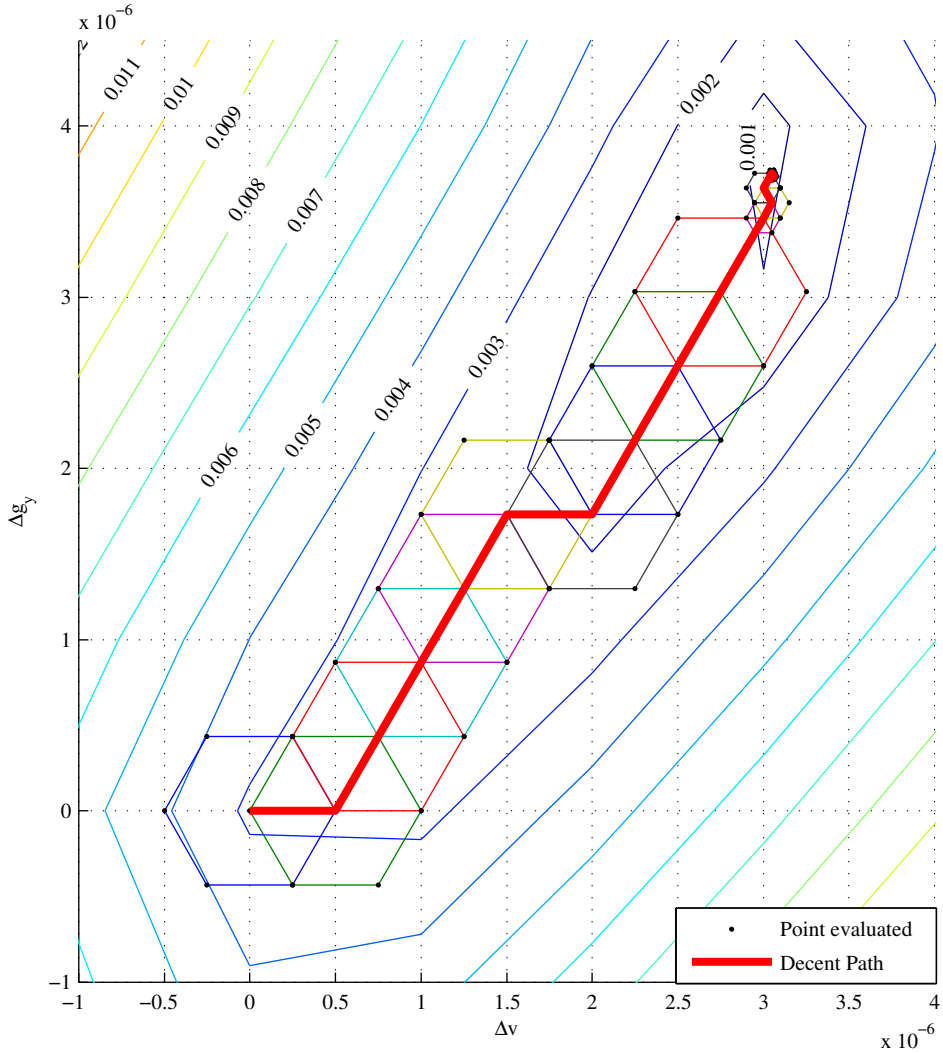

Figure 5.32: Progress of coordinate descent creep routine shown on contour plot of $||\boldsymbol{\sigma}||$ versus Δv and Δg_y

(shown in Figure 5.32) inscribed by a circle of radius R and centred on point P.

4. Calculate stress magnitudes s_{1-6} at each of the points p_{1-6}.
5. Find the point p which gives the lowest stress magnitude s.
6. If s is less than S the P is given value of p, otherwise R is reduced to $R/5$.
7. Stages 2-6 are repeated until $R < R_{tol}$ or $S < S_{tol}$ where R_{tol} is taken as three times the floating point accuracy of R and S_{tol} $=1 \times 10^{-7}$ kPa.

Hexagons are used as they form a regular grid allowing for repeats to be omitted and allow for movement in both components simultaneously. Both of these improve the efficiency of the algorithm by lowering the number of BRICK executions. Figure 5.32 shows the points evaluated in the coordinate descent routine overlaid on a contour plot of the mesh shown in Figure 5.31.

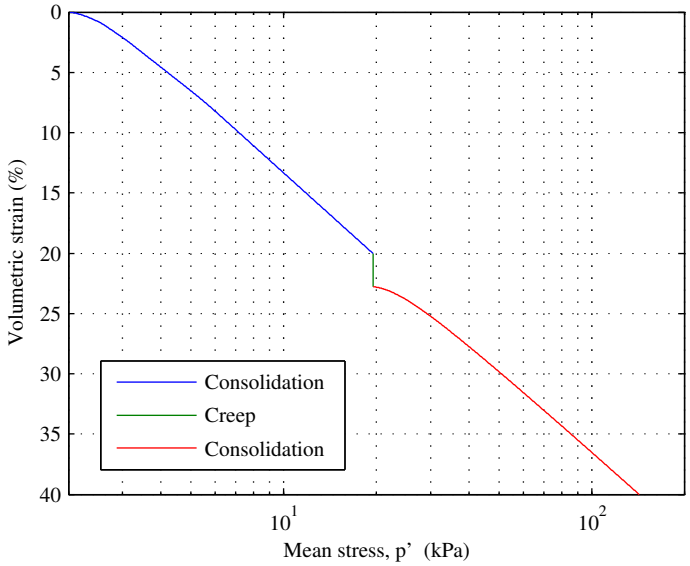

Figure 5.33: 1D creep ε_v -log p' plot, coordinate descent method

Initial results

A one dimensional version of the creep test was run using the coordinate descent method for creep. The creep time was extended to $1 \times 10^{10}\,\mathrm{s}$ and the time step was multiplied by 1.002 on each stage to form a geometric progression of the time step, and allow a reasonable run time and a manageable amount of data. Despite the $1 \times 10^{-7}\,\mathrm{kPa}$ stress tolerance used the cumulative effect over the 1722 steps resulted in to total change of Δq to $1.4 \times 10^{-5}\,\mathrm{kPa}$ and $\Delta p'$ to $9.5 \times 10^{-6}\,\mathrm{kPa}$. Figure 5.33 shows the extended creep that results from the long creep duration and the expected return to the 1D NCL on continuing consolidation. The strain rate degradation plotted in Figure 5.34 however shows effects of creep rupture resulting in the strain rate becoming constant after about $1 \times 10^{9}\,\mathrm{s}$. The plot of shear strain versus log time in Figure 5.35 shows the effect more clearly as shear strain increases rapidly rather than linearly against log time as expected.

Mechanism for rupture and its detection within the brick code

Creep rupture refers to the process whereby the creep strains accelerate towards failure and is shown to occur from a shear stress of 60 to $90\,\%$ of the failure stress (Singh & Mitchell 1968). For the 1D consolidation example q is at $77\,\%$ of the predicted failure so prediction of creep rupture is acceptable. In BRICK the prediction of failure is when all bricks are taut with the same volumetric strain as the man. The nature of the SRD-B routine where $\boldsymbol{\Delta\varepsilon_b}$ approaches $\boldsymbol{\Delta\varepsilon}$ asymptotically complicates the solution as negligible elastic strain will always be generated.

The very low or zero stiffness generated at creep rupture was problematic for the

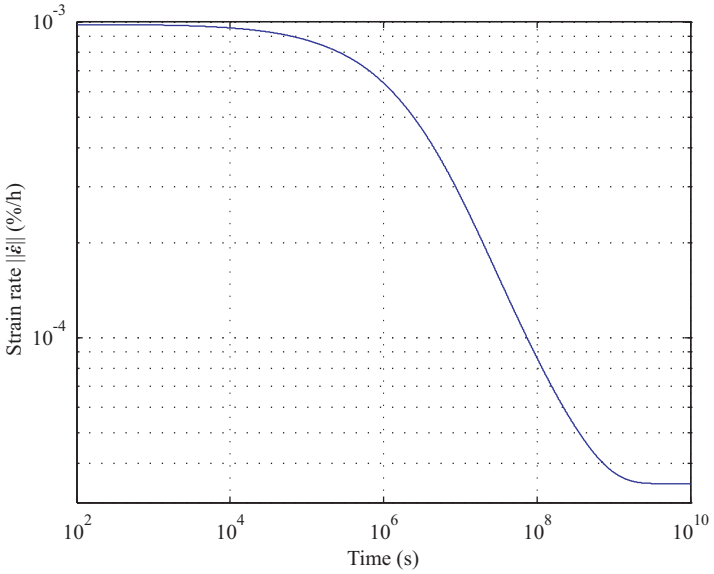

Figure 5.34: 1D creep log ($\dot{\varepsilon}$) -log(time) plot, coordinate descent method

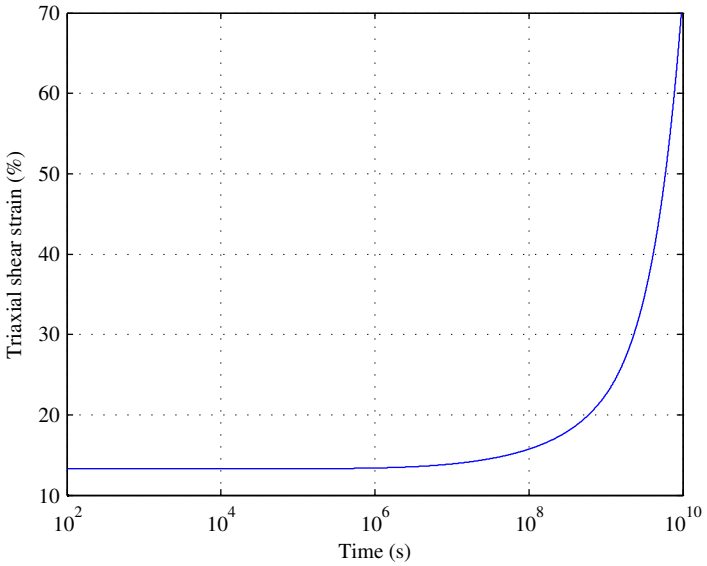

Figure 5.35: 1D creep ε_q -log(time) plot, coordinate descent method

creep routine so a detection mechanism for creep rupture was implemented. Creep rupture was detected when the path taken to find the creep solution in the coordinate descent creep routine was within $0.02°$ of being in pure shear for all bricks. An additional check was to ensure that there had been a change in brick strain. Creep would be terminated early if these conditions were met ten times consecutively and the strain in brick component 3 (measured from the first detection) was more than the initial strain change magnitude R. .

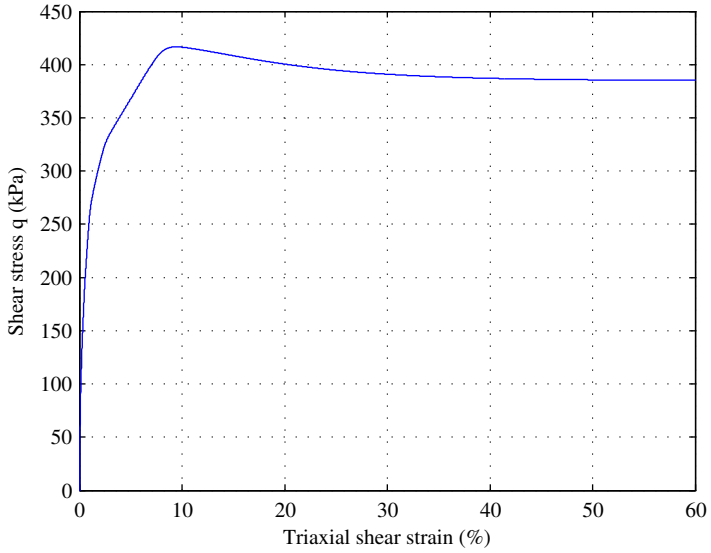

Figure 5.36: Shear stress strain path indicating failure of simplified rupture trial

5.3.5 An investigation of creep rupture behaviour

Creep rupture was studied by holding deviator stress steady at various different percentages of the failure stress. This is based on the creep tests illustrated in Bishop (1966) but is run as a simplified model that does not attempt to recreate the full stress history. Instead the test runs an isotropic consolidation to p' =600 kPa at a volumetric strain rate of $1\,\%\,\mathrm{yr}^{-1}$. An undrained shear path is then applied at an axial strain rate of $2\,\%\,\mathrm{h}^{-1}$. Running this to triaxial shear strain ε_q=40 % revealed a peak stress q_{peak} = 416 kPa as shown in Figure 5.36. A 1×10^9 s or 31.69 yr creep stage was run at q=10, 20, 40, 80, 160, 240, 280, 320, 360, 400 and 410 kPa, the time step started at 1 s and was multiplied by 1.002 on each step.

The presence of creep rupture at higher stress is shown clearly when the axial strain is plotted against time in Figure 5.37. This shows how as q approaches failure the strains become excessive after shorter creep times. The higher initial axial strain for higher stress creep is the axial strain incurred during the shear stage, the start of which is the datum for strain measurement. This behaviour mirrors that shown by Vaid & Campanella (1977) in Figure 5.38.

The effect of creep upon the axial strain rate (as shown in Figure 5.39) differs in several respects to the that observed in tests by Vaid & Campanella (1977) in Figure 2.26 (p 23). The most major is the lack of an increasing strain rate after rupture. In the SRD-B BRICK model an increase in the applied rate would require the applied $\boldsymbol{\Delta\varepsilon}$ to increase. An increase in $\boldsymbol{\Delta\varepsilon}$ would result in an elastic strain change as the change $\boldsymbol{\Delta\varepsilon_b}$ would be less than $\boldsymbol{\Delta\varepsilon}$. Any increase in strain rate would therefore not produce a zero stress change creep solution. The linear trend between log time and log $\dot{\varepsilon}_a$ is shown to exist for paths above 80 kPa between 100 s and rupture. The

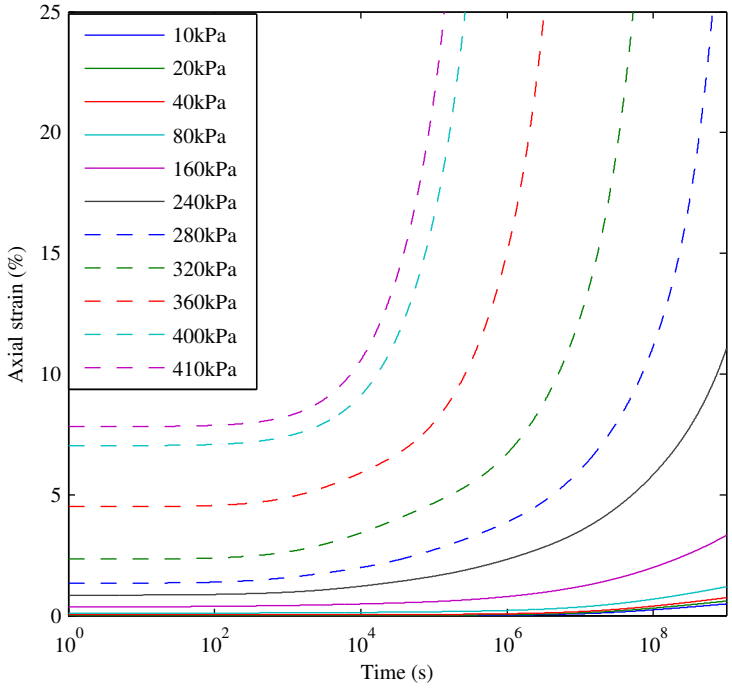

Figure 5.37: The effect of creep on axial strain

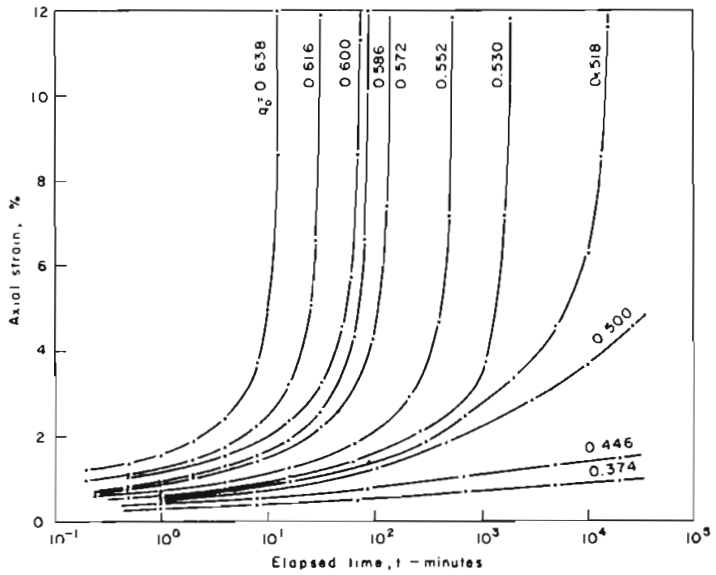

Figure 5.38: Results of constant stress creep tests on undisturbed Haney clay, Vaid & Campanella (1977)

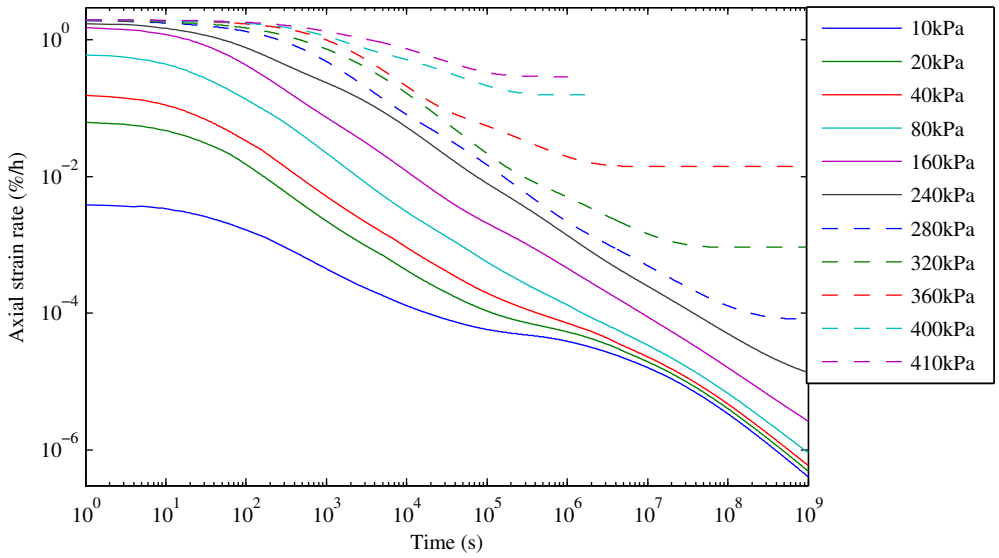

Figure 5.39: The effect of creep on axial strain rate

transition to the linear trend early on is a result of using the exact calculated SL in situations where using a TDSL would result in a discontinuity not conducive to a creep solution. The tests at lower q values have distorted axial strain rate degradations as the longer bricks which are positioned along the volumetric strain axis only acquire a $\Delta g_{y,b}$ component of strain as creep progresses.

The plot of axial strain versus strain rate in Figure 5.40 is shown to closely resemble that from Bishop (1966) in Figure 5.41. The difference here as that those stages experiencing rupture do not increase in strain rate. The prediction of increasing axial strain with time and a higher isochrone position with increasing q are both exaggerated from the trends shown by Bishop (1966). The exaggerated effect is due to a combination of the excessive creep times allowed and the lower stiffness resulting from the simplified stress history of the model. The effect of stress on axial strain rate shown in Figure 5.42 is the same as that shown by Campanella (1965) in Figure 2.24 (p 22). This behaviour can be described by Equation 2.6 (Singh & Mitchell 1968) in the stress range where there is a linear relationship between log $\dot{\varepsilon}_a$ and q. The upper limit of this stress range is shown to reduce with creep duration in Figure 5.40 and to a lesser degree in Figure 2.24 (Campanella 1965). The maximum stress at which each strain rate is observed may be described by a linear trend between q and $\log(\dot{\varepsilon}_a)$. This indicates the rupture stress at which the strain rate accelerates. Given the linear relationship between $log(t)$ and $log(\dot{\varepsilon}_a)$ it can be seen that the time to creep rupture will increase logarithmically as q/q_{peak} decreases. There is however no evidence for a limiting stress below which creep rupture will not occur, as proposed by Vaid & Campanella (1977) and illustrated in Figure 2.27 (p 24).

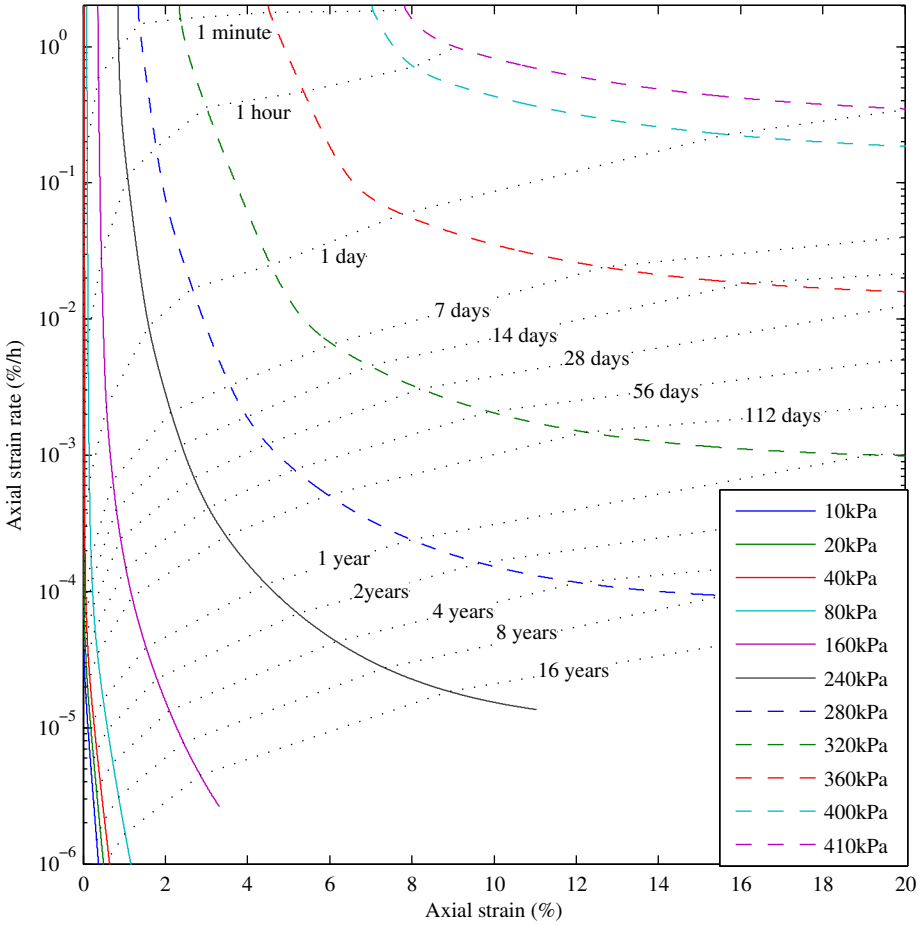

Figure 5.40: The effect of creep axial strain rate versus axial strain

5.3.6 Evaluation of coordinate descent creep routine

The coordinate descent creep routine has been shown to produce a near constant stress state in component 1 and 3 of the BRICK routine. Only strain components 1 and 3 are needed to model 1D consolidation, isotropic consolidation and triaxial strain paths, all other stress components remain zero so the whole stress state is held and stress component 1 = p' and component 3 =$q/\sqrt{3}$. Under this constant stress state the BRICK routine has been shown to replicate the effects of creep and creep rupture observed in experimental data. The discrepancies shown in modelling creep rupture (the lack of a strain rate increase and no minimum stress below which creep will never occur) do not result from the coordinate descent creep routine, but from limitations of the BRICK modelling of time dependent string lengths which may be investigated in future work now a mechanism exists for maintain creep conditions.

The coordinate descent routine could be expanded in future to utilise all 6 stress and strain components in the BRICK routine; this would however represent a exponential

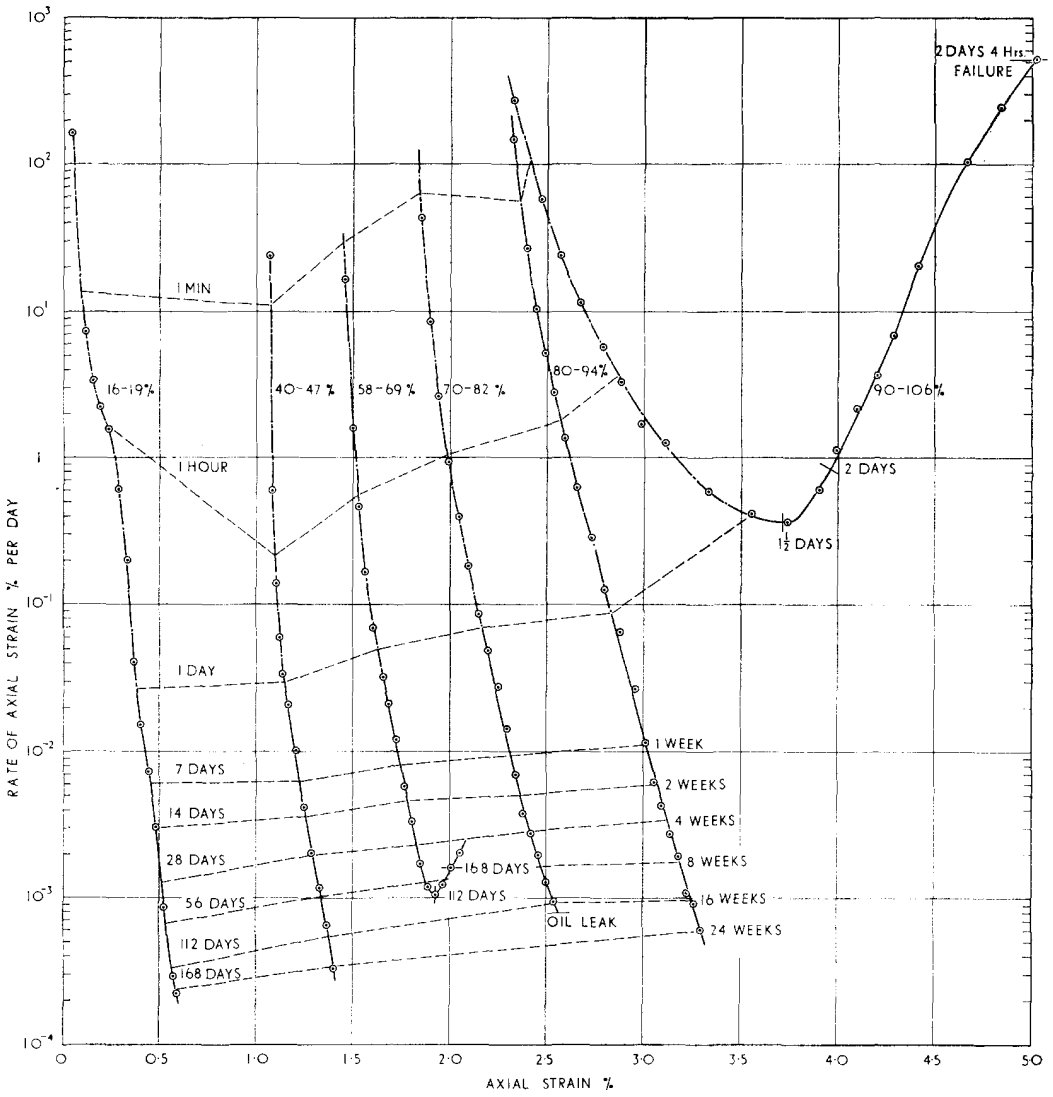

Figure 5.41: The effect of creep on axial strain rate versus axial strain after Bishop (1966)

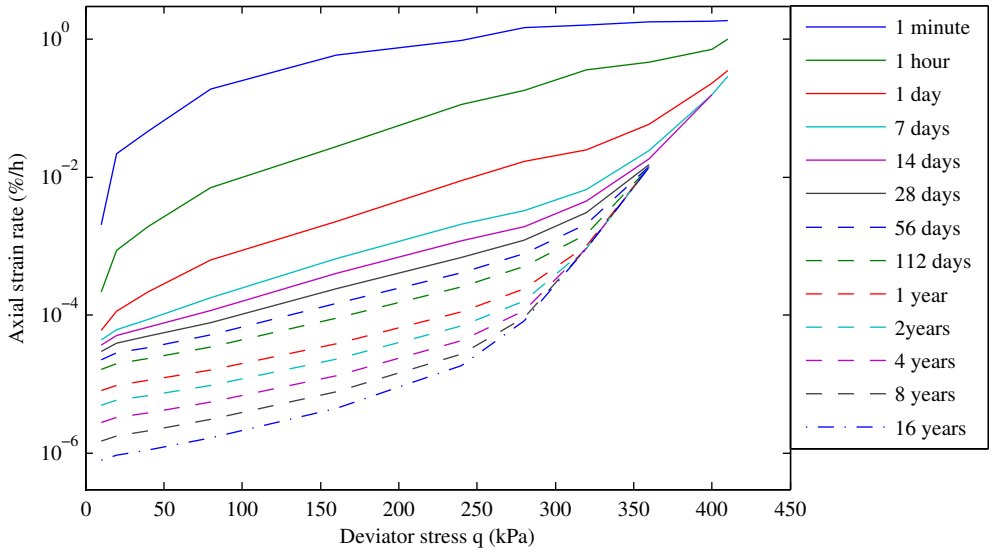

Figure 5.42: The effect of creep on axial strain rate versus testing stress

increase in complexity and computing requirements and is only required for very specialised modelling. A more immediate improvement would be to reduce the computation time by minimising the number of points at which BRICK is run to calculate a stress magnitude. The hexagonal gird is used for this reason as it ensures overlaying test points can be reused. It has also been shown that approaching the creep solution in a straight line, not a zig zag, and using an appropriate initial strain step can reduce computation dramatically. The strain change on the previous result or the plastic strain movement from the initial stress relaxation may be used to give a refined guess as to the position of the creep solution, and so more optimally set the orientation and size of the test hexagon.

5.4 Incremental strain energy contours

5.4.1 Introduction

The concept of using incremental strain energy contours as a method of displaying stiffness anisotropy was first used in Burland & Georgiannou (1991). In that case it was used to show the effect of OCR on clayey sands. The concept of incremental strain energy is to measure the strain energy required for the strain increment since a key point in the straining of the soil e.g. the end of consolidation or swelling. The strain energy U being the area under the stress-strain graph is calculated by Equation 5.43 when in triaxial stress space.

$$U = \sum_{0}^{\varepsilon_v} \Delta p' \delta\varepsilon_v + \sum_{0}^{\varepsilon_s} \Delta q' \delta\varepsilon_q \tag{5.43}$$

When plotted in the stress space the incremental strain energy contours will indicate a high stiffness when widely spaced and low stiffness when closely spaced. This has the effect of showing the lowering of stiffness towards the yield surfaces, as shown in Figure 5.43. ISE contours also provide a clear indication of the change in stiffness caused by RSH.

Within the BRICK model a routine was developed to evaluate ISE on a series of stress paths rotating out from a datum stress point. The calculation of ISE U was reformulated from Equation 5.43 in order to calculate the change in ISE δU caused by each step of the stress path. This is shown in Equation 5.44 where $\Delta p'$ and Δq are stress changes measured from the start of the stress path, while $\delta\varepsilon_v$ and $\delta\varepsilon_q$ are strain changes produced during the current step of the stress path.

$$\delta U = \Delta p' \delta\varepsilon_v + \Delta q \delta\varepsilon_q \tag{5.44}$$

In addition to the calculation of U, mechanisms were developed to detect failure of the stress paths. This could be either a soil failure where the BRICK model predicted

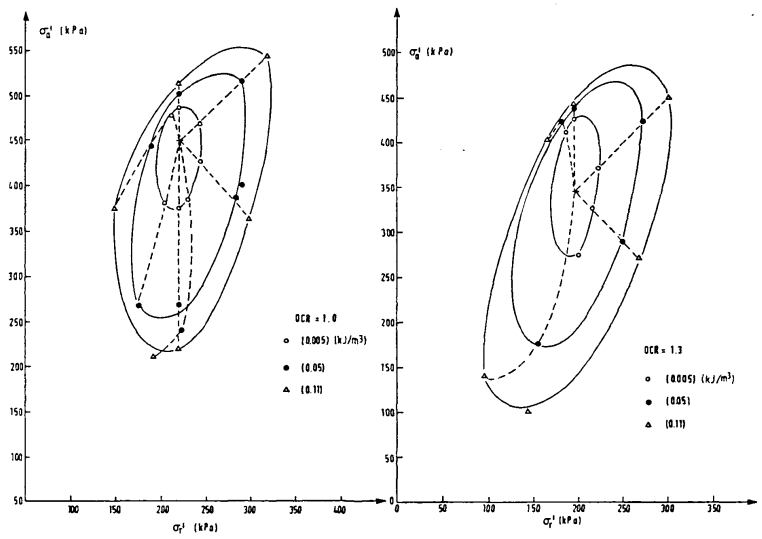

Figure 5.43: Effect of OCR on incremental strain energy contours from Burland & Georgiannou (1991)

a yield point, or a calculation failure. Calculation failure refers to times when the stress path control routine did not converge on a strain solution that satisfies both p' and q targets due to the unusual nature of the stress paths investigated.

5.4.2 Using ISE to illustrate brick behaviour

Introduction and method

The effects of the BRICK model on the stiffness anisotropy were demonstrated by producing plots of ISE contours at several points of a 1D consolidation, swelling and reconsolidation test. The test as illustrated in Figure 5.44 was a 1D consolidation at run $\dot{\varepsilon}$ =$0.1\,\%/\mathrm{h}$ using a strain step of $\boldsymbol{\Delta\varepsilon}$=$[0.0001, 0, 0.000115, 0, 0, 0]$ for consolidation and $\boldsymbol{\Delta\varepsilon}$=$[-0.0001, 0, -0.000115, 0, 0, 0]$ for swelling, all other parameters are defined in Table 5.6. The initial consolidation ran until p' =$1000\,\mathrm{kPa}$ swelled until p'=$200\,\mathrm{kPa}$ before a reconsolidation to p'=$500\,\mathrm{kPa}$. ISE contours were produced at the points illustrated in Figure 5.44.

The test was repeated with three set-ups of the BRICK model. Two inviscid models were used where string lengths were set appropriately for the applied strain rate and remained constant. In the first of these, the 'reset' model, all bricks were moved to the position of the man at the start of the ISE stress paths to erase all RSH effects. The second 'inviscid' model was allowed to proceed and demonstrate RSH effects. In the final 'SRD' model the SRD-B code was utilised throughout the consolidation stages and ISE stress paths. In addition an increased strain rate of $\dot{\varepsilon}$ =$10\,\%/\mathrm{h}$ was tested for the ISE paths.

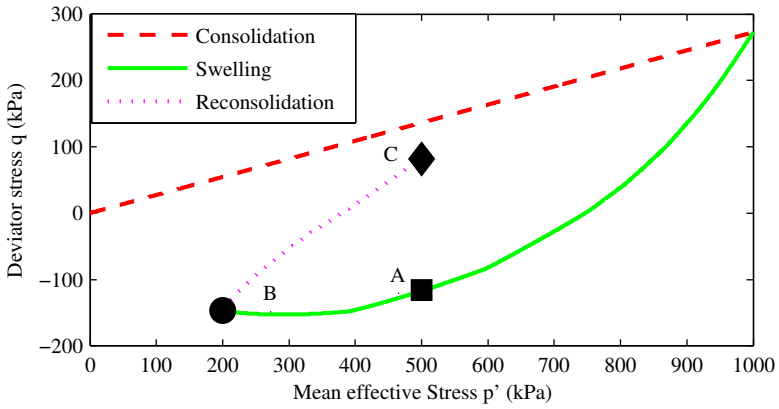

Figure 5.44: Position of ISE contour plots

Reset bricks

When the bricks are reset at the start of the ISE paths the effects of brick positions on stiffness are removed. This is shown in Figure 5.45 for point A and Figure 5.46 for point C, neither of which show a distortion towards direction of the approaching stress path (the swelling and reconsolidation path respectively), thus produce very similar results. The small differences between Figure 5.45 and Figure 5.46 relate to the stiffness anisotropy caused by the PSRED mechanism and the dependence of stiffness on p'. The result is an increased stiffness for increasing p' and a reduced stiffness normal to the approach path. Point C shows a greater degree of anisotropy as it is closer to yielding at q=82 kPa than point A was at q=−116 kPa. The result for path B shown in Figure 5.47 shows that the stiffness has reduced with p' as indicated by the generally closer ISE contours. As the stiffness is related to $\log(p')$ there is greater evidence of stiffness increasing along the p' axis at this lower value of p'. It is also apparent that the failure is being approached in compression and extension, as evidenced by closer contours to the top and bottom left of the figure.

Inviscid bricks

Using the inviscid version of the BRICK routine allows for the development of RSH effects. This is best seen by the comparison of points A and C in Figure 5.48 and 5.49 respectively. These clearly show that the ISE contours are bunched when the stress path continues from the approaching path and spaced when the path direction reverses. This indicates a reduced stiffness for continuing paths and an increased stiffness when the path is reversed. Comparing the contours on path reversal with those from the reset model indicates a greater stiffness. This is because strings typically have to move twice their string length to become taut when reversing the path direction compared to just once when brick positions were reset.

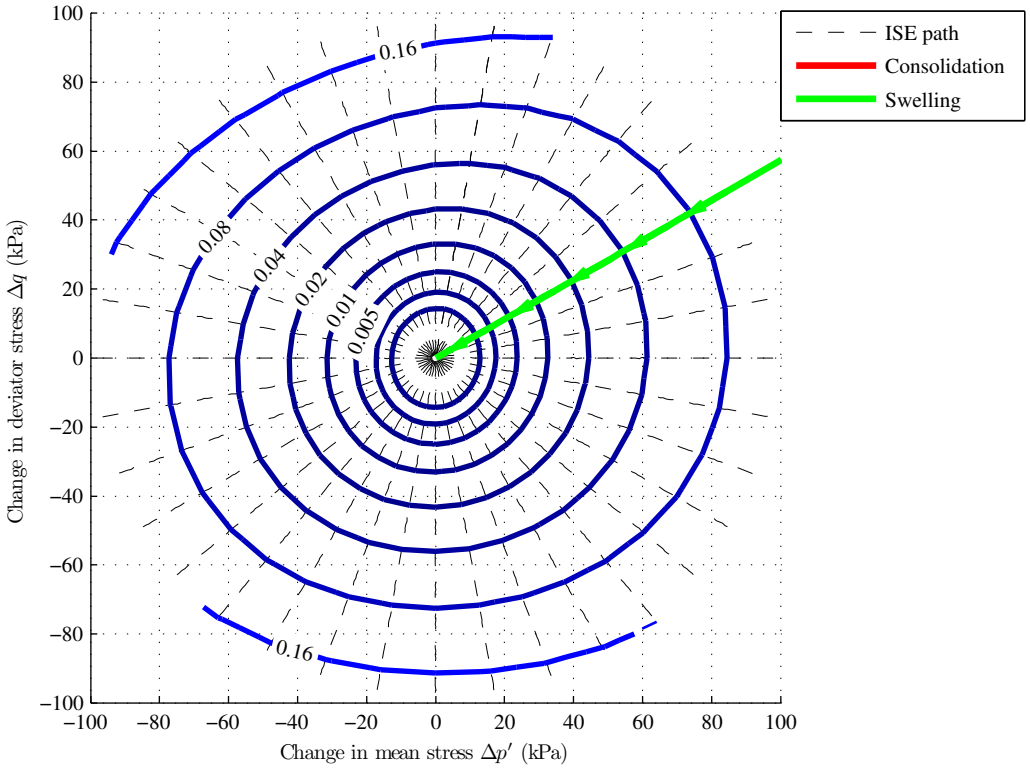

Figure 5.45: Plot of ISE contours for stress change from point A with reset bricks

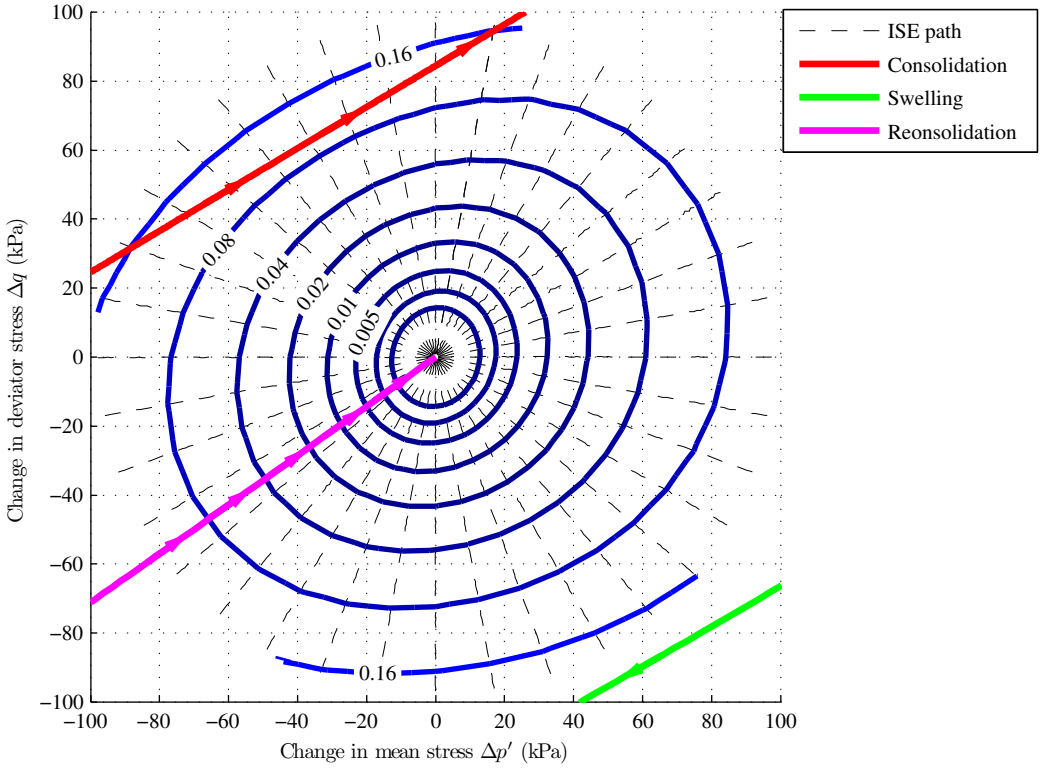

Figure 5.46: Plot of ISE contours for stress change from point C with reset bricks

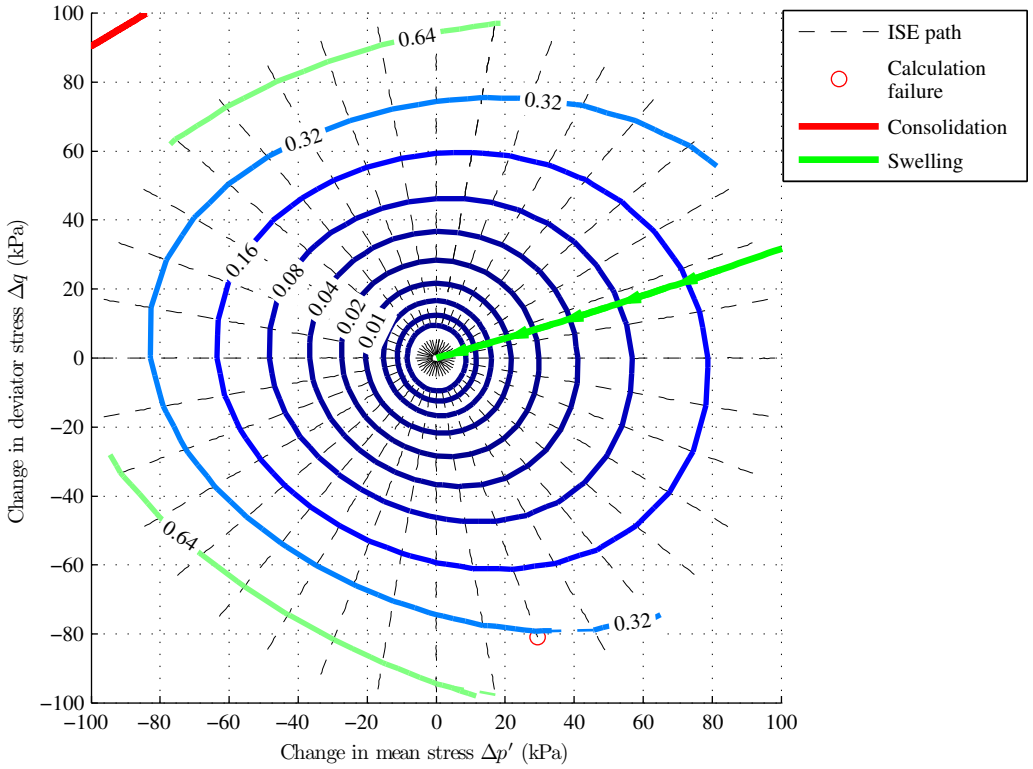

Figure 5.47: Plot of ISE contours for stress change from point B with reset bricks

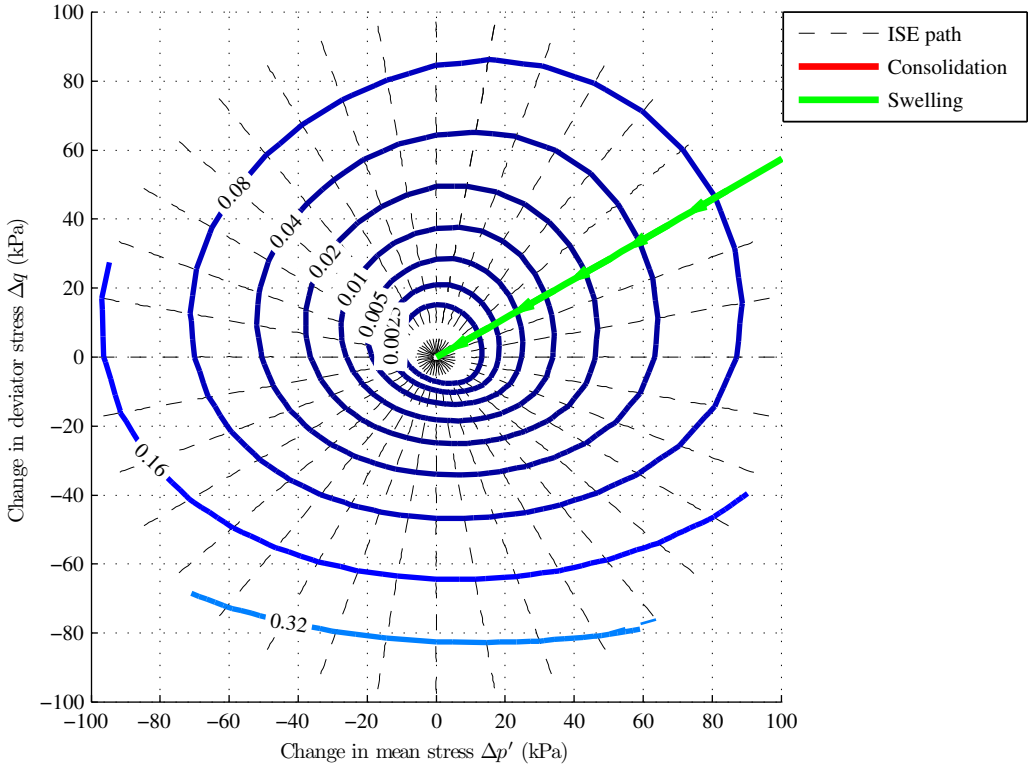

Figure 5.48: Plot of ISE contours for stress change from point A with inviscid bricks

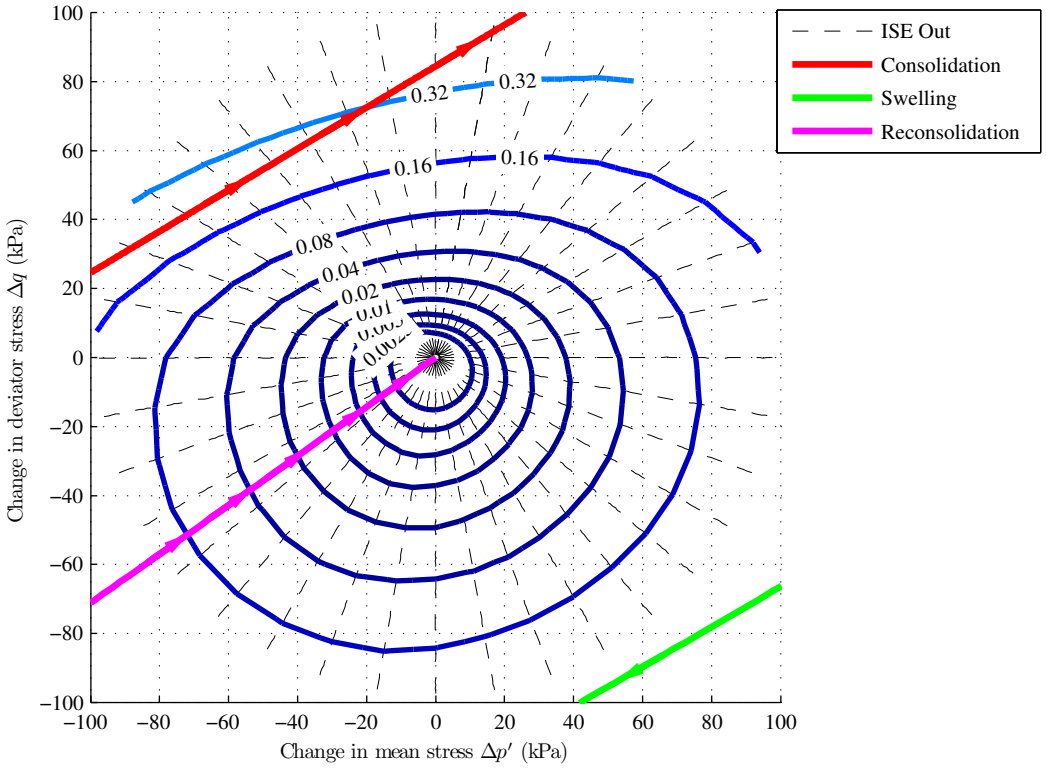

Figure 5.49: Plot of ISE contours for stress change from point C with inviscid bricks

Influence of SRD string lengths

Using the SRD BRICK model at a strain rate of $\dot{\varepsilon}$ =0.1 %/h produces the same results as the inviscid model. This confirms that the SRD-B version of the brick code produces the correct solution as the string lengths have reached the same values when controlled for rate effects individually as when set globally. What is shown by using SRD effects is the effect of increasing the strain rate of the ISE stress paths. The effect can be shown by comparing Figure 5.50 and Figure 5.51 which show point C with $\dot{\varepsilon}$ =0.1 %/h and $\dot{\varepsilon}$ =10 %/h respectively. At the higher rate the stiffness is increased in all directions as the longer strings associated with the increased rate allow for more elastic strain to occur before bricks become taut and the plastic strain increases. The effect is minor for stress reversals where the strings are already slack. A continuous stress path however results in several shorter strings being slack at the higher rate that were taut at the slower rate and so a greater elastic capacity is available.

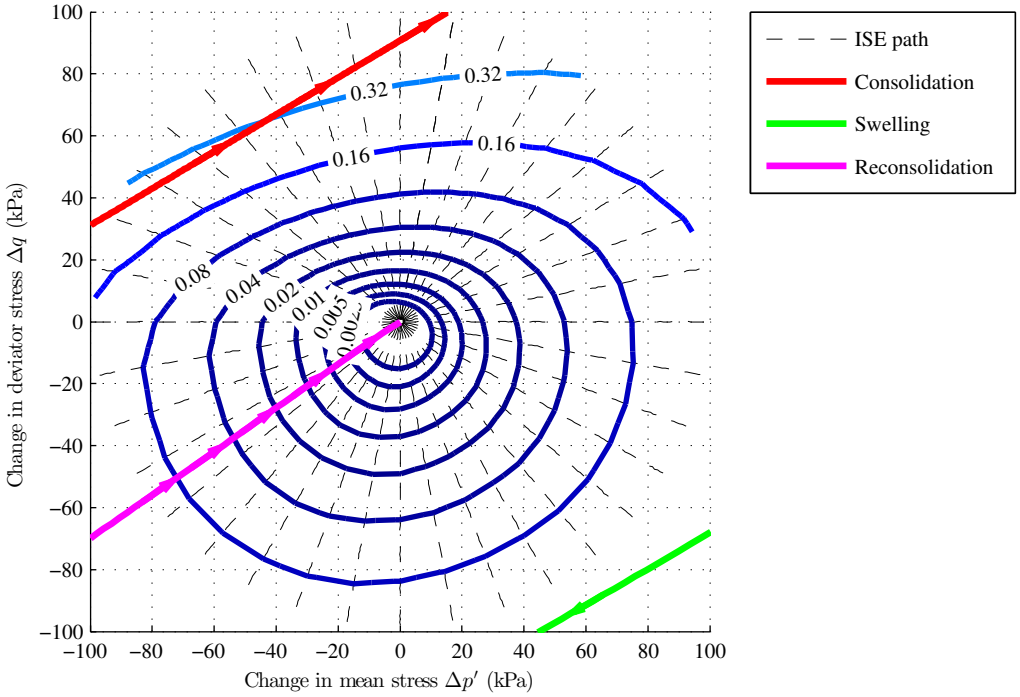

Figure 5.50: Plot of ISE contours for stress change from point C using SRD behaviour when $\dot{\varepsilon}$ =0.1 %/h

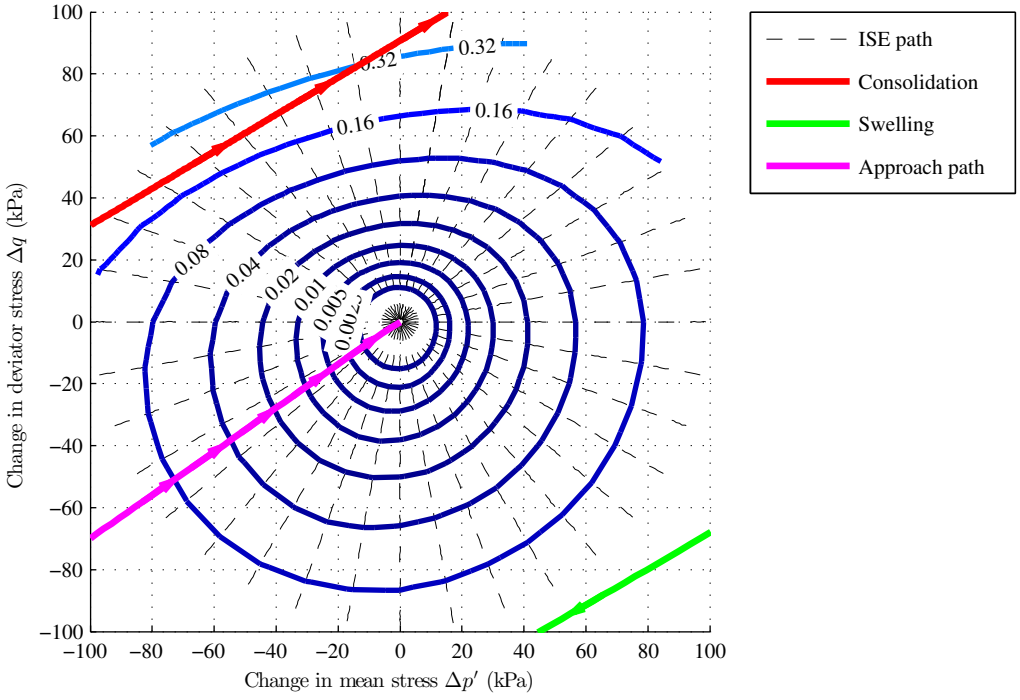

Figure 5.51: Plot of ISE contours for stress change from point C using SRD behaviour when $\dot{\varepsilon}$ =10 %/h

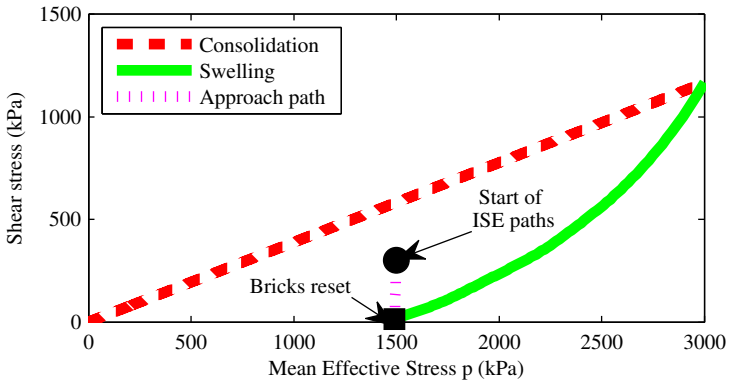

Figure 5.52: Diagram of test to show effect of creep on RSH

5.4.3 Using ISE to show effect of creep

Introduction and method

A series of ISE contour plots were produced to demonstrate how the BRICK model interpreted the effect of creep on RSH effects. In order to achieve this a simplified test was set up to produce strong RSH effects. The test again uses the parameters defined in Table 5.6 and is illustrated in Figure 5.52.

A 1D consolidation run at $\dot{\varepsilon}$ =1 %/yr until p' =3000 kPa with $\boldsymbol{\Delta\varepsilon}$=[0.0001, 0, 0.000 115, 0, 0, 0] is followed by a 1D swelling to p' =1500 kPa where $\boldsymbol{\Delta\varepsilon}$=[−0.0001, 0, −0.000 115, 0, 0, 0]. This point was chosen as it allows for the application of a large increase in q to a point that is not near failure and does not exhibit creep rupture. In order to both maximise and simplify the RSH effect the bricks are reset to the man position at the start of the approach path. The approach path itself is run to the point p'=1500 kPa, q=300 kPa at a strain rate of $\dot{\varepsilon}$=2 %/h.

A series of ISE probes of 300 kPa length were run immediately after the approach path and after the creep strain rate had been allowed to degrade to either $\dot{\varepsilon} = 2 \times 10^{-3}$ or 2×10^{-6} % h^{-1}. The strain rate used for the ISE paths was set to represent two scenarios. Setting the strain rate to $\dot{\varepsilon}$=2 %/h, the same as the approach path, represents the situation 'after' a strain rate acceleration has been applied. This provides an illustration of the effect of creep on a typical test for RSH effects where the testing path is performed at the same rate as the approach path. The other set of ISE paths are performed at the strain rate reached by the creep. These 'before' tests illustrate the effect of creep on stiffness without the effects of a strain rate acceleration.

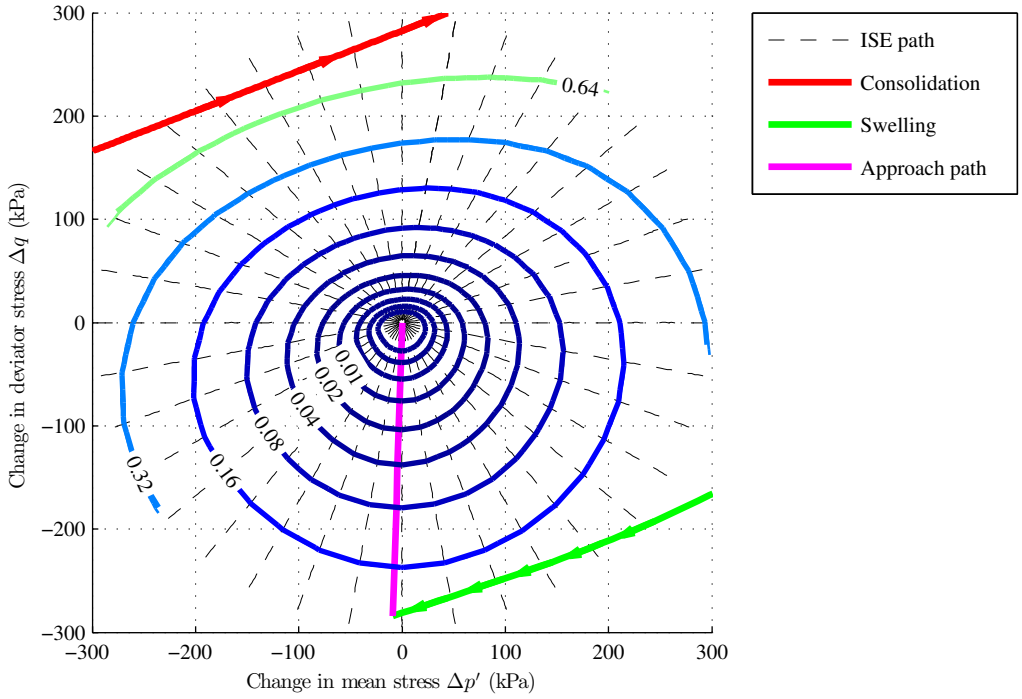

Figure 5.53: ISE contour plot showing RSH effects

Results

The maximum RSH effect is shown in Figure 5.53 which was produced before any creep was applied. This shows the expected behaviour whereby there is a reduced stiffness for a continuation of the approach path. The effect of creep is shown for creep with residual strain rates of $\dot{\varepsilon}$ =2×10^{-3} and $2 \times 10^{-6}\,\%/\mathrm{h}$ in Figure 5.54 and 5.55 respectively. Due to the logarithmic relationship between creep strain rate and time this equates to a creep time of $6.3\,\mathrm{hours}$ and $3.4\,\mathrm{years}$.

As creep progresses string lengths become shorter, whereas when the strain rate is not increased the string lengths remain shorter. The effect of this is a reduced stiffness for a continuing approach path as more strings have become taut and the capacity for elastic strain has reduced. There is also a reduction in stiffness when the stress path is reversed as creep has moved bricks closer to the man and so less strain is required to re-engage bricks and reduce the stiffness.

The effect of creep after the strain rate acceleration is shown for residual strain rates of $\dot{\varepsilon}$ = 2×10^{-3} and $2 \times 10^{-6}\,\%/\mathrm{h}$ in Figure 5.56 and 5.57 respectively. In this case the only impact of creep is to have moved the bricks closer to the man. This results in an increased stiffness for a continuing stress path as strings have become initially slack at $\dot{\varepsilon}$ =$2\,\%/\mathrm{h}$. For reversing paths the movement of bricks now means the movement required to engage bricks is lowered from $2 * SL$ required without creep.

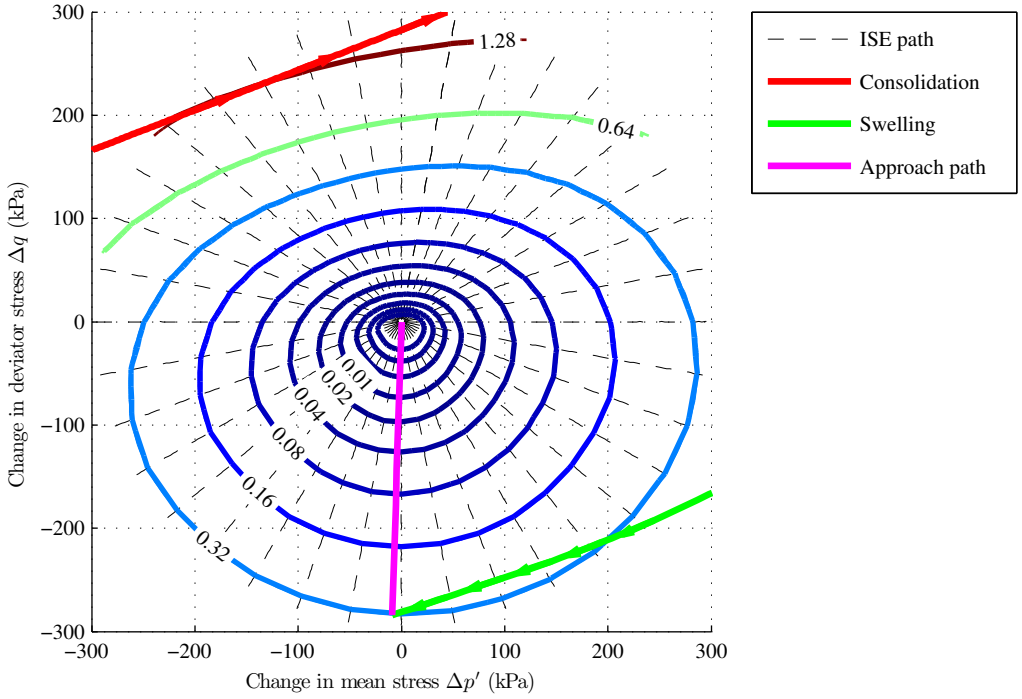

Figure 5.54: ISE contour plot showing effect of creep to $\dot{\varepsilon}$=2 $\times$ 10^{-3} %/h before strain rate acceleration

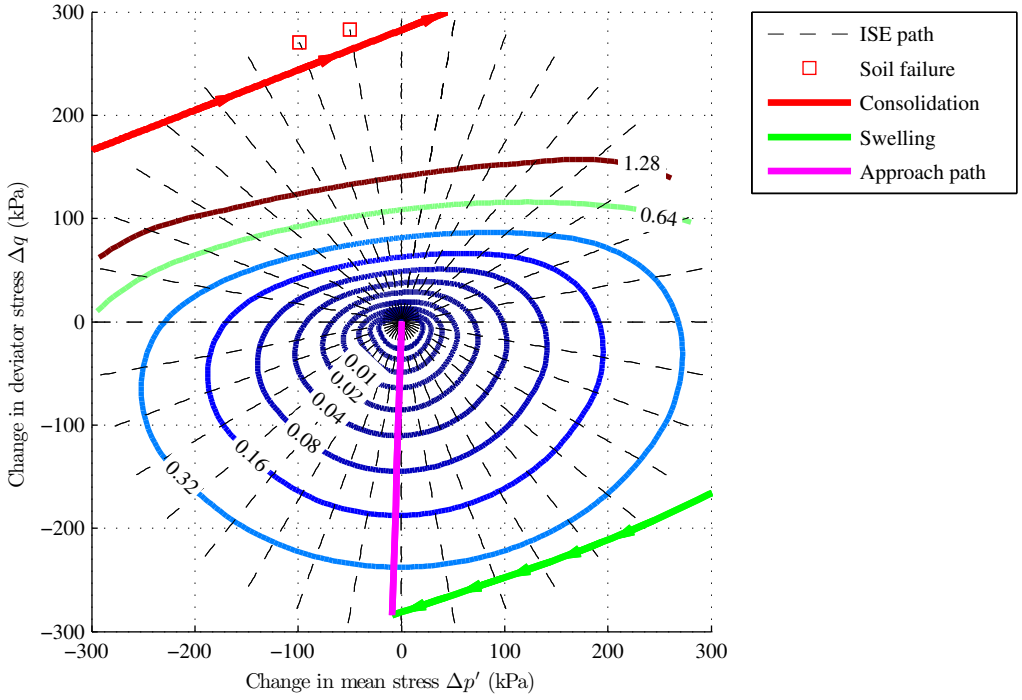

Figure 5.55: ISE contour plot showing effect of creep to $\dot{\varepsilon}$=2 $\times$ 10^{-6} %/h before strain rate acceleration

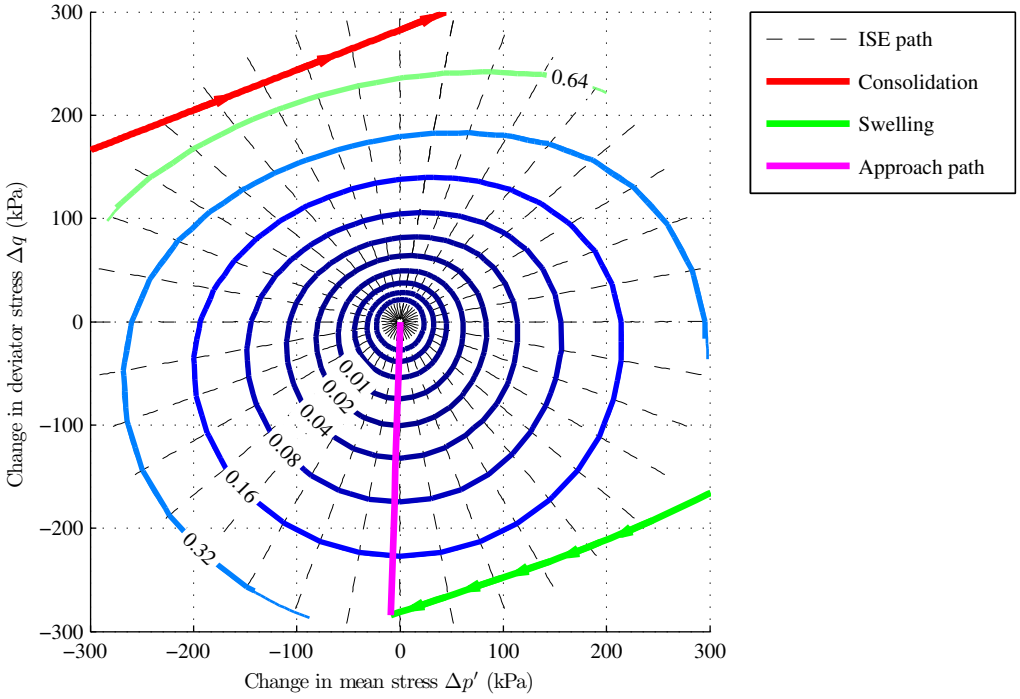

Figure 5.56: ISE contour plot showing effect of creep to $\dot{\varepsilon}$=2 × 10^{-3} %/h after strain rate acceleration

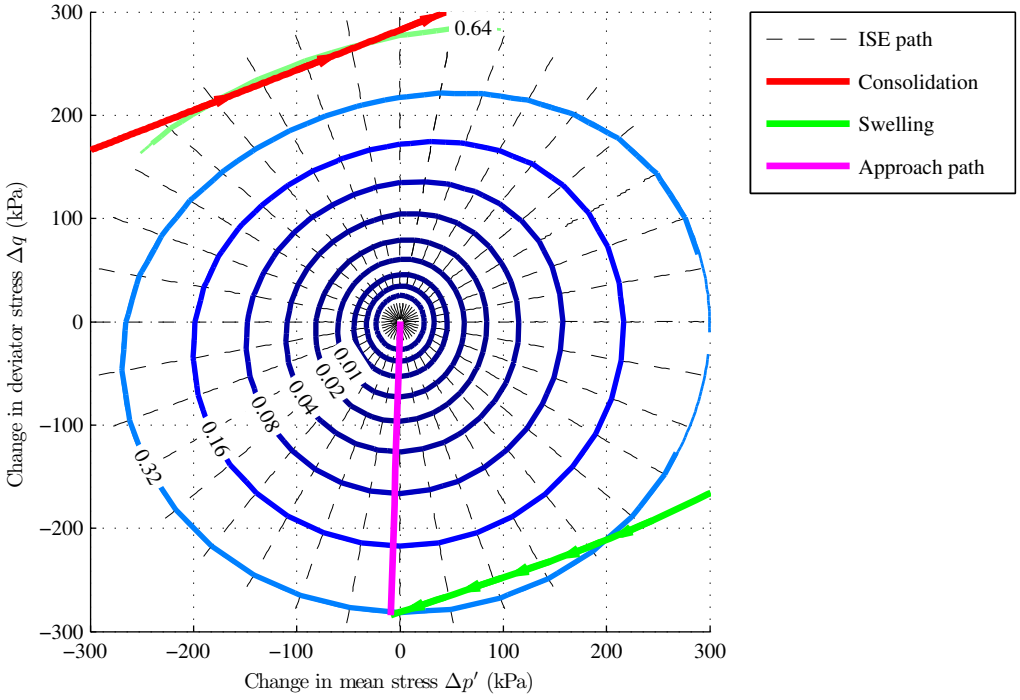

Figure 5.57: ISE contour plot showing effect of creep to $\dot{\varepsilon}$=2 × 10^{-6} %/h after strain rate acceleration

It is by this mechanism that BRICK predicts RSH effects will be reduced. This mechanism does not permit RSH effects to be fully erased as SL cannot reduce below SL_{ref}, so the bricks will continue to reside on one side of the man even after excessive creep. If the term erased is taken to mean 'too small to be detected in physical testing', the erasing of the RSH effect was found to be related purely to the duration of creep. The suggestion by Gasparre et al. (2007) of an approach path length above which RSH effects cannot be erased is therefore not demonstrated in the BRICK model.

5.4.4 Simulation of results from Pierpoint (1996)

Introduction and method

The BRICK model was used to repeat a test on an unweathered heavily overconsolidated Oxford clay performed by Pierpoint (1996). The purpose of the test was to illustrate the capabilities of the combination of the improved SRD-B model and ISE contour output to repeat complex stress paths and yield interpretable results. Due to the relative lack of supporting data it was decided to continue to use the standard London clay parameters found in Table 5.6 and not produce a new fit for Oxford clay. Table 5.7 lists the stages used; two stages of geological history are followed by four for lab consolidation before the 18 stress path stages required to repeat test T03. The geological consolidation was run as a strain controlled 1D consolidation at an arbitrary strain rate $\dot{\varepsilon}$= $1\,\%\,\mathrm{yr}^{-1}$ to an estimated preconsolidation pressure of $10\,\mathrm{MPa}$, before swelling to a measured initial effective stress of $140\,\mathrm{kPa}$. The estimation of preconsolidation pressure is based upon the, highest value obtained by Pierpoint (1996) from a high pressure oedometer test, as an approximation of the eroded overburden was $11.1\,\mathrm{MPa}$ (Jackson & Fookes 1974). The lab consolidations consist of a stress path for deviator stress release and then stress paths for the documented consolidation and swelling stages, all of which were performed at $\dot{\varepsilon}$= $0.03\,\%\,\mathrm{h}^{-1}$ approximated from strains during the consolidation stages. All stress path stages were run as stress paths with at a constant stress rate determined by their duration.

Results

Figure 5.58 shows the result of simulation along with an overlay of the results obtained from the original test. In both cases U is calculated from the start of the relevant stress path. In cases where the test stress paths are within $5°$ of each other an average position was used at each values U used to fit the ISE contours. In the simulation the position on each stress path at the contour value U, expressed in polar

coordinates, was interpreted by a spline fit to generate a contour position between stress paths in all directions.

In the original test it was observed that the initial approach from q = $0\,\mathrm{kPa}$ to q = $-115\,\mathrm{kPa}$ caused a significant RSH effect. This resulted in increasing q paths ($180°$) being stiffer than increasing p' paths ($90°$) and themselves being stiffer than decreasing q paths ($10°$). It was also observed that the decreasing q paths were initially stiffer than increasing p' paths indicating either a reduction in RSH effect caused for smaller strains, or that the test was approaching failure towards the end of the stress path.

Comparing the simulation to the original tests shows a broadly similar magnitude for ISE but differs in several other ways. The shear stiffness is shown to be generally reduced, a RSH effect is still observed but is constant rather than showing a reduction in stiffness at the end of the decreasing q path. The bulk stiffness in increasing p' is observed to be higher than the test both in terms of magnitude and proportion of the shear stress. The ratio of shear to bulk stiffness observed in the testing cannot be achieved in the BRICK model by adjustment of Poisson's ratio and so must be derived by brick positions.

This test has illustrated that the SRD routine can model a test with complex stress history involving several strain and stress rates, and produce a usable output without failure of the routine to solve. It is however also apparent that such tests would require that the BRICK model parameters be fitted to simpler tests. A greater detail of the testing conditions is also required as slight changes in consolidation rates or undocumented pauses in the test may alter brick positions and thus the resulting stiffness.The results obtained are however good considering no parameter fitting was performed.

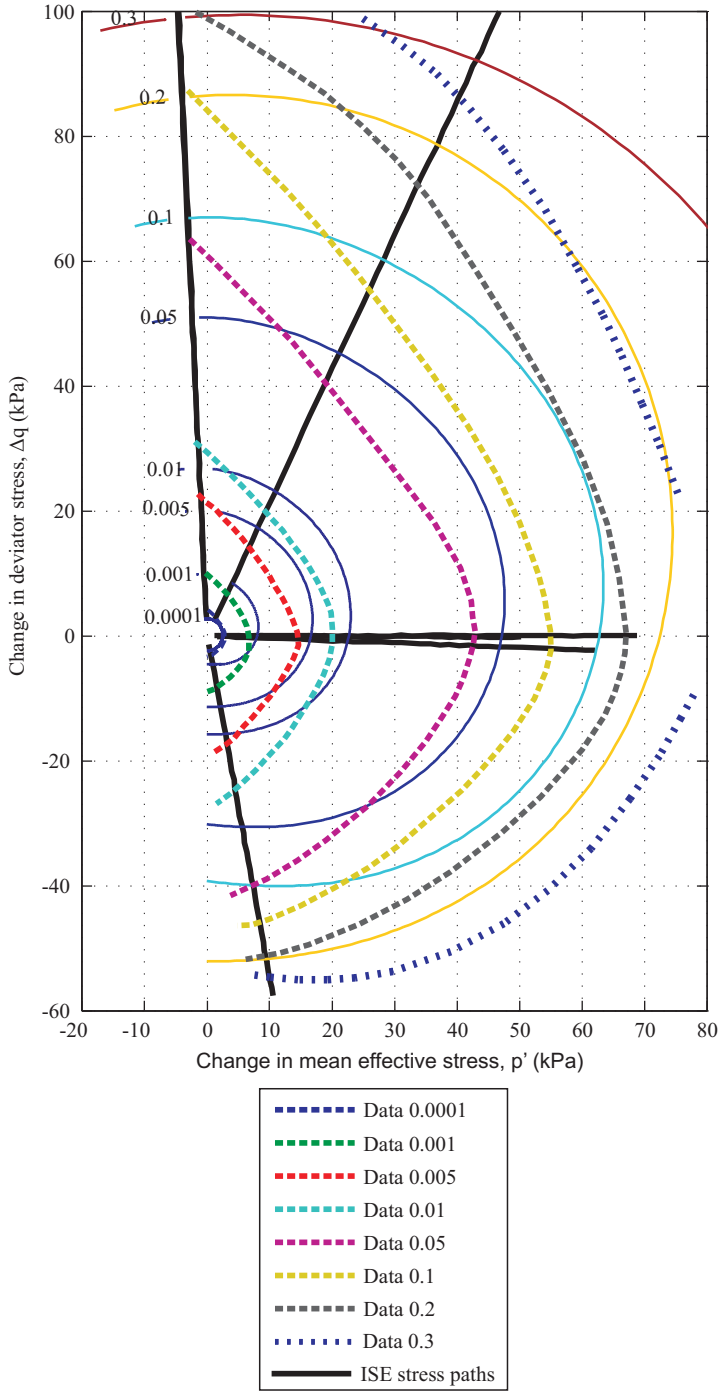

Figure 5.58: Plot of ISE contours for simulation of T03 (Pierpoint 1996) expressed in stress space

Geological history			
Stage description	p' target (kPa)	q target (kPa)	Strain rate $\dot{\varepsilon}$ ($\%\,\mathrm{yr}^{-1}$)
Strain controlled 1D consolidation	10000	N/A	1
Strain controlled 1D swelling	140	N/A	1
Sampling and lab consolidation			
Stage description	p' target (kPa)	q target (kPa)	Strain rate $\dot{\varepsilon}$ ($\%\,\mathrm{h}^{-1}$)
Stress path for shear stress relief	140	0	0.03
Stress controlled isotropic consolidation	218	0	0.03
Stress controlled isotropic swelling	83	0	0.03
Stress controlled isotropic reconsolidation	150	1.1	0.03
Stress paths			
Stress path number	p' target (kPa)	q target (kPa)	Stress rate $\dot{\sigma}$ ($\mathrm{kPa\,h}^{-1}$)
1	150.8	-84	0.754
2	146.5	-115.8	0.909
3 ISE measured	215.5	-115.7	0.789
4	154.5	-117.1	0.994
5	209	-114.3	0.522
6	158.4	-114.5	0.515
7 ISE measured	153.9	-14.4	2.101
8	154.8	-115.8	0.279
9 ISE measured	216.8	-118.1	0.754
10	161.7	-117.5	0.712
11 ISE measured	209.1	-16.4	2.087
12	209.6	-117.2	1.836
13	161.7	-117.8	0.894
14 ISE measured	156.9	-15.3	1.621
15	159.4	-115.5	2.029
16 ISE measured	209.6	-115.8	0.984
17	153.9	-117.2	37.145
18 ISE measured	164.5	-174.9	1.195

Table 5.7: Stages used for simulation of T03 (Pierpoint 1996)

6

BRICK simulations of RSH effects

6.1 Introduction

In this chapter a series of BRICK simulations are presented which increase in complexity to approach a simulation of the physical tests performed. This has been made possible by the improvements to the BRICK model given in Chapter 5. The SRD-B formulation allows a wider range of stress paths to be modelled with strain rate effects. The addition of the coordinate descent creep routine enables extended creep periods to be modelled without stress change.

Section 6.2 details the BRICK simulation of the testing until the end of the isotropic consolidation. Due to the variable and ill-defined nature of the stresses, strains and strain rates of these stages, the simulation in BRICK is a simplified representation of an ideally executed physical test. This is in contrast to the shear and creep stages in the standard triaxial test which are trivial to model as the clearly defined testing conditions can be directly entered into the BRICK model. The selection of the parameters controlling the BRICK model is discussed in Section 6.3.

In the remainder of the chapter brick positions are reset to the strain of the man at different points to show how different aspects of the test performed would influence the observed behaviour. Section 6.4 shows the idealised effect of RSH by resetting the bricks immediately prior to the approach path and running a separate test for the $180°$ and $0°$ stress path rotations. Section 6.5 shows the effect of multistage testing by modelling the whole test (where the $180°$ path rotation is followed by the $0°$), but with bricks reset after the isotopic consolidation. Section 6.6 demonstrates the effect of recent consolidation history (RCH) by resetting the bricks prior to an exaggerated isotropic consolidation stage. By modelling the whole test without resets in Section 6.7 the combined effects of multistage testing, RCH and RSH are demonstrated along with the potential impact of 1D consolidation.

6.2 Consolidation process modelling

In order to model a RSH test in the BRICK model one must first model the full consolidation history. The first stage is an approximation of the consolidation from a slurry. In BRICK this is run as a constant strain rate one dimensional strain path with $\boldsymbol{\Delta\varepsilon}$ = [0.0001, 0, 0.000 115 47, 0, 0, 0] until the maximum mean effective stress p'_m is reached. As was discussed in Section 4.3.4 (p 109) the PWP measurement was inaccurate and gave a wide range of values for σ'_{vc}. It was therefore decided to use the mean result obtained from the oedometers tests σ'_{vc} =544 kPa equivalent to p'_m=415.5 kPa using $K_0 = 1 - sin\phi'$ where ϕ' = 20.9°. Swelling was performed in a similar manner with $\boldsymbol{\Delta\varepsilon}$ = [−0.0001, 0, −0.000 115 47, 0, 0, 0] to p'_i = 172 kPa the mean of the initial effective stress measurements for samples from consolidation tube 1 (excluding HOCR and RA3). The strain rates were based on mean logarithmic axial strains ε_a=78 and −1.7 % for consolidation and swelling respectively. Given the consolidation and swelling durations of 432 and 186 hours, the approximate constant strain rates were $\dot{\varepsilon}_a$ = 0.181 and 0.0093 % h^{-1} respectively.

At the end of the 1D swelling stage both shear and deviator stress are present in the sample. When the sample is removed from the consolidation tube negative pore water pressures develop and maintain p'_i but not q. A stress path at constant p' is therefore used to reduce the deviator stress to q = 0. The strain rate for this path is arbitrarily set at a shear strain rate of $\dot{\varepsilon}_q$= 1 % h^{-1}.

On placing the sample in the triaxial cell several test stages are performed which do not alter p' in a permanent fashion. The B-check type tests apply a change in cell pressure without sample drainage and so p' remains constant if saturation is complete. The saturation stage increases the cell and back pressure simultaneously to maintain a constant p' and sample volume. The small strains that the flow of pore water and dissolution of air cause in these stages are considered negligible and not modelled. The fact that the sample has been held at an almost constant p' for approximately 8 days may however have an influence in the positions of bricks at the start of the RSH stages. As such the omitted saturation and B-check stages may be modelled as a creep stage in some cases.

The isotropic consolidation is modelled by a stress path from the stress at the end of stress release (p'=172 kPa, q=0 kPa) to that from which the RSH stages start (p'=300 kPa, q=0 kPa). A stress path is required as the 1D consolidation history will have left bricks positioned such that an isotopic strain will generate some deviator stress. The volumetric strain that would occur in this idealised consolidation stage was approximated as ε_v=3 % from local transducer measurements. This gives a volumetric strain rate of $\dot{\varepsilon}_v$=0.025 % h^{-1} given the 120 h duration of the consolidation stage.

The planned simulation of the consolidation stages may therefore be summarised by Table 6.1.

Stage	Modelling type	End condition	Strain rate
1D consolidation	1D strain path $\boldsymbol{\Delta\varepsilon}$ = [0.0001, 0, 0.000 115 47, 0, 0, 0]	p'=415.5 kPa	$\dot{\varepsilon}_a$=0.181 % h^{-1}
1D swelling	1D strain path $\boldsymbol{\Delta\varepsilon}$ = [−0.0001, 0, −0.000 115 47, 0, 0, 0]	p'=172 kPa	$\dot{\varepsilon}_a$=0.0093 % h^{-1}
Stress relief	9 step stress path	p'=172 kPa, q=0 kPa	$\dot{\varepsilon}_q$=1 % h^{-1}
Saturation and B-checks	Not modelled or creep stage	8 days	N/A
Isotropic consolidation	19 step stress path	p'=300 kPa, q=0 kPa	$\dot{\varepsilon}_v$=0.025 % h^{-1}

Table 6.1: Modelling of consolidation

6.3 Selection of testing parameters

The BRICK model contains multiple parameters which interact with the modelled stress history to produce the stress-strain output. The fit of the model to the data may therefore be influenced as much by the stress points and strain rates used in the modelling of the tests as the BRICK parameters. Rather than fitting a set of parameters to the output from the modelled test conditions, the effects of possible variations in test conditions were studied using the standard set of parameters found in Table 5.6 (p 180). These parameters are a modification of the original BRICK parameters for London clay (Simpson 1992) by Clarke (2009) to fit the stiffness degradation curves observed for RSH effects in London clay by Gasparre et al. (2007), and are assumed to be representative of London clay.

The use of the 18 brick parameter set is justified by its improved fit to the experimental data, as shown in Figure 6.1. This shows the normalised stiffness degradation curves for test S1-1 and HRSH approach path 1, based on the bootstrap stiffness of the triaxial strains using the external measurement of radial strain, along with the 18 brick (Clarke 2009) and 10 brick (Simpson 1992) stepped approximations. Test S1-1 and approach path 1 of HRSH are used for this comparison because they are without RSH effects and were produced at the testing axial strain rate of $\dot{\varepsilon}_a$ = 3×10^{-3} % h^{-1}.

Tests for undrained shear strength CU3, CU1 and CU2 which ran from p' = 200, 300 and 400 kPa respectively were simulated in BRICK. The tests were run using

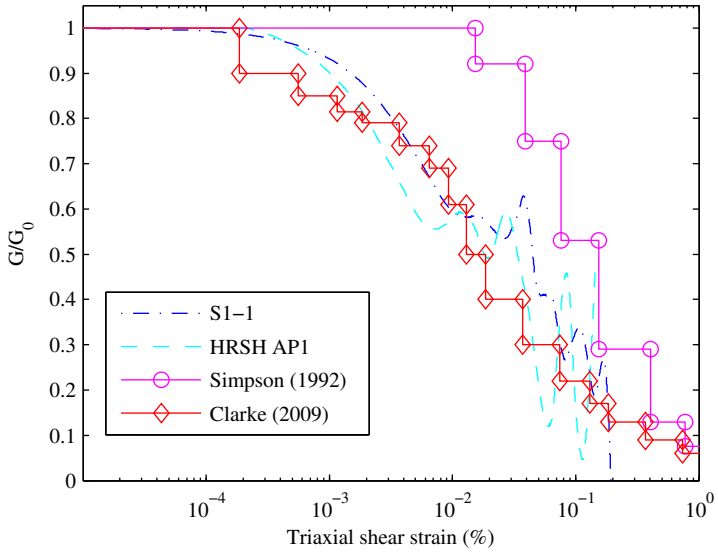

Figure 6.1: Fitting of stiffness degradation curve

Test	Stage	Modelling type	End condition	Strain rate (%/h)
Common	1D consolidation	1D strain path $\boldsymbol{\Delta\varepsilon}$ = [0.0001, 0, 0.000 115 47, 0, 0, 0]	p'=415.5 kPa	$\dot{\varepsilon}_a$= 0.181
	1D swelling	1D strain path $\boldsymbol{\Delta\varepsilon}$ = [−0.0001, 0, −0.000 115 47, 0, 0, 0]	p'=172 kPa	$\dot{\varepsilon}_a$=0.0093
	Stress relief	9 step stress path	p'=172 kPa, q=0 kPa	$\dot{\varepsilon}_q$=1
CU3	Isotropic consolidation	19 step stress path	p'=200 kPa q=0 kPa	$\dot{\varepsilon}_v$=0.025
CU1	Isotropic consolidation	19 step stress path	p'=300 kPa q=0 kPa	$\dot{\varepsilon}_v$=0.025
CU2	Isotropic consolidation	19 step stress path	p'=400 kPa q=0 kPa	$\dot{\varepsilon}_v$=0.025
Common	Undrained shear	Undrained strain path $\boldsymbol{\Delta\varepsilon}$ = [0,0,0.0001,0,0,0]	$\Delta\ \varepsilon_q$ =40 %	$\dot{\varepsilon}_a$=0.15

Table 6.2: Stages used for CU tests

the test stages detailed in Table 6.2 and the standard parameter set (Table 5.6). Given the fixed limits of p' the volumetric strains generated during the consolidation shown in Table 6.3 provided an indicator of the effect of parameter change. It can be seen that volumetric strain change is lower in the BRICK simulations than the actual

	Volumetric strain (%)		
	1D consolidation	1D swelling	Isotopic consolidation to 300 kPa
Experimental result	78	-1.7	3
Standard parameters	49.5	-1.3	0.8

Table 6.3: Volumetric strain in consolidation stages

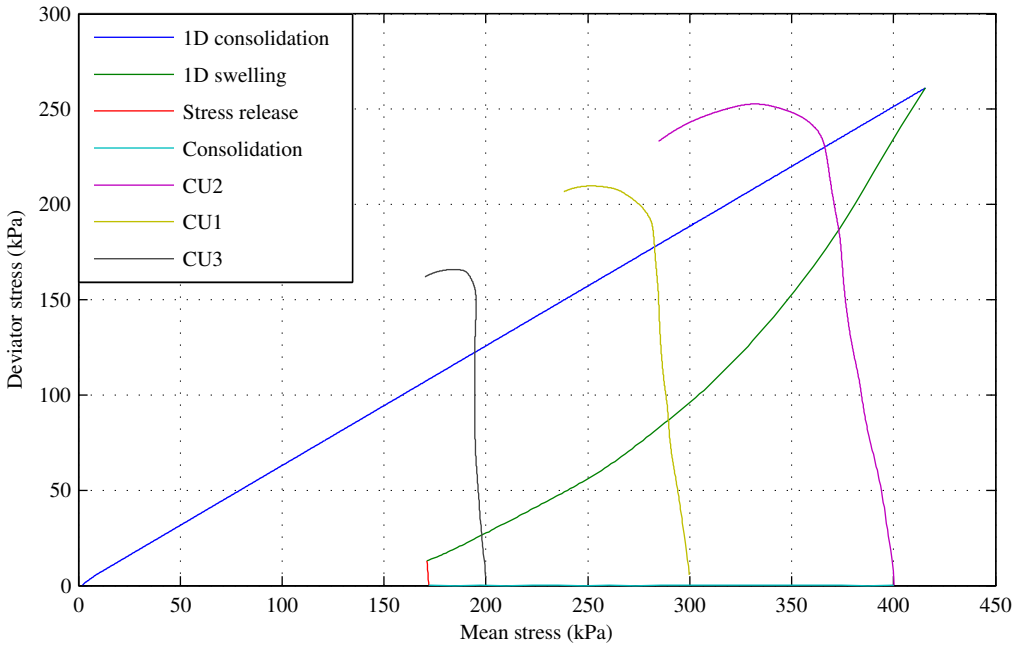

Figure 6.2: Stress path for CU tests, standard parameters

test data. The stress paths for the standard and fitted data are shown in Figure 6.2. The stress paths to failure are shown to correlate well with the experimental results in Figure 4.27 (p 122). The differences are attributed to the effect of stiffness anisotropy observed in the experimental data that is not modelled in this version of the BRICK model.

6.4 Idealised RSH effect

In the BRICK model the stiffness degradation curve is determined by the positions of the bricks at the start of the measured shear probe. In actual test conditions this is influenced by the whole stress history. In order to show just the RSH effect the test set-up in Table 6.4 was run for approach path length (APL) = 15 and 60 kPa, and creep time (CT) 3 and 120 hours. This setup eliminated any effects of brick position from the consolidation history by resetting the bricks after the isotopic consolidation. Effects of multistage testing are avoided by modelling the 180° and 0° sets of shear paths as separate tests immediately after the isotropic consolidation. This test shows the expected theoretical effect of both creep and approach path

Number	Description	Modelling type	End condition	Strain rate ($\%\,\mathrm{h}^{-1}$)
1	1D consolidation	1D strain path $\boldsymbol{\Delta\varepsilon}$ = [0.0001, 0, 0.000 115 47, 0, 0, 0]	p'=415.5 kPa	$\dot{\varepsilon}_a$= 0.181
2	1D swelling	1D strain path $\boldsymbol{\Delta\varepsilon}$ = [−0.0001, 0, −0.000 115 47, 0, 0, 0]	p'=172 kPa	$\dot{\varepsilon}_a$=0.0093
3	Stress relief	9 step stress path	p'=172 kPa, q=0 kPa	$\dot{\varepsilon}_q$=1
4	Isotropic consolidation	19 step stress path	p'=300 kPa q=0 kPa	$\dot{\varepsilon}_v$=0.025
		Strain of bricks rests to strain of man		
5 [180°]	Approach path out	Stress path 0.1 kPa steps.	p'=300 kPa q=APL kPa	$\dot{\varepsilon}_a$=3 × 10^{-3}
6 [180°]	Approach path back	Stress path 0.1 kPa steps.	p'=300 kPa q=0 kPa	$\dot{\varepsilon}_a$=3 × 10^{-3}
5 [0°]	Approach path out	Stress path 0.1 kPa steps.	p'=300 kPa q= -APL kPa	$\dot{\varepsilon}_a$=3 × 10^{-3}
6 [0°]	Approach path back	Stress path 0.1 kPa steps.	p'=300 kPa q=0 kPa	$\dot{\varepsilon}_a$=3 × 10^{-3}
7	Creep period	Creep stage	Creep time has elapsed	N/A
8 [a]	Shear probe	Stress path 0.1 kPa steps.	p'=300 kPa q=80 kPa	$\dot{\varepsilon}_a$=3 × 10^{-3}

[a] The 'NO RSH' probe runs stages 1,2,3,4 and 8

Table 6.4: Stages used for illustration of idealised RSH effect

length on the observed RSH effect. The effect of the approach path length can be seen by comparing Figure 6.3 and Figure 6.4 for 3 hours creep after 15 and 60 kPa long approach paths respectively. The key effect of increasing the length of the approach path is to increase the strain at which the RSH lines diverge from the 'NO RSH' line. The ''NO RSH' line is a shear probe performed without an approach path and so represents the stiffness degradation curve produced by undisturbed bricks.

The approach path stages act to disturb the brick positions in two ways. Those bricks moved by the approach path in the 180° stress path rotation test are left in the

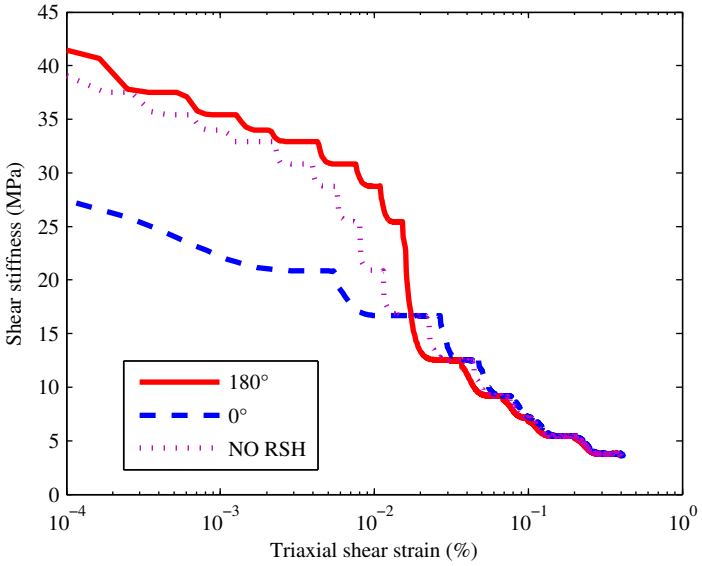

Figure 6.3: Idealised RSH effect, 3 hours creep, 15 kPa approach path

strain path of the shear probe. The amount of strain required to move a brick and reduce the stiffness is therefore up to double that required for the 'NO RSH' probe. This increases the stiffness at any point in strain but does not alter the maximum stiffness observed when no bricks are moving.

For a 0° stress path rotation the bricks affected by the approach path will be left behind the man in the opposite direction to the strain path of the shear probe. The amount of strain required to move these bricks is therefore reduced up to the point of strings becoming taut. This has the effect of reducing the stiffness at a point in strain and can reduce the initial stiffness if strings are initially taut. The impact of the approach path on these processes is that the longer approach paths disturb more bricks and so more strain is required to reach the point where bricks have not been disturbed; the 'NO RSH', 0° and 180° paths are the same.

The effect of creep on the observed RSH effect can be seen by comparing the 15 kPa approach path after 3 hours and 120 hours in Figure 6.3 and Figure 6.5 respectively. In the BRICK routine the effect of creep is to move the bricks towards the man while applying a small total strain change which maintains no change in stress. By moving the bricks closer to the man the RSH effect on both 180° and 0° paths is reduced. On the 180° path a small reduction in the strain to each drop in stiffness is observed. The 0° path shows a clearer effect as some bricks have moved to have initially slack strings and so the initial stiffness increases. The effect of creep will be limited to the point where SL has reached SL_{ref} during the creep stage. In this case the strings of those bricks affected by the approach path will be in a position to become taut at strains given by SL_{app} + SL_{ref} or SL_{app} - SL_{ref} for 180° and 0° path rotations respectively, where SL_{app} is the string length at the testing strain rate.

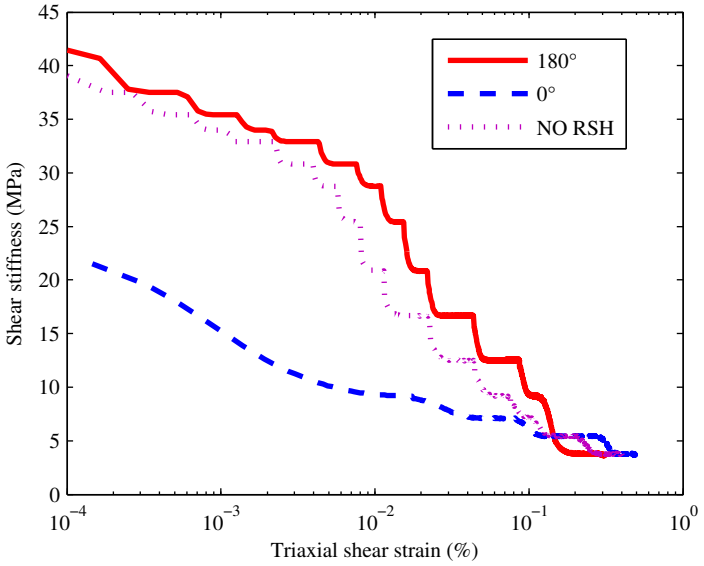

Figure 6.4: Idealised RSH effect, 3 hours creep, 60 kPa approach path

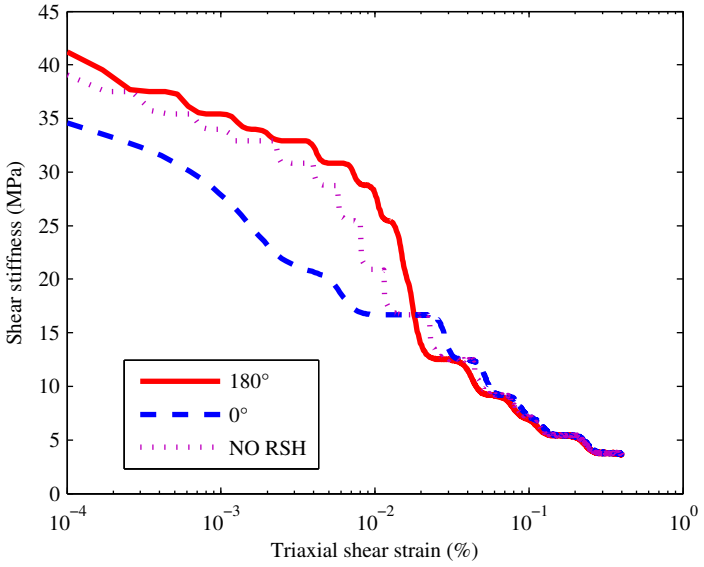

Figure 6.5: Idealised RSH effect, 120 hours creep, 15 kPa approach path

6.5 Effect of multistage testing

To study the effects of multistage testing without any effects from the consolidation stages, the actual test program where the 180° and 0° rotation paths were run sequentially was modelled while resetting the bricks after isotopic consolidation. Table 6.5 gives the set-up for this test and includes the stress path to q =0 kPa after the first shear probe along with a 5 day reset creep period.

The effect of the multistage testing approach is to increase the stiffness on the second shear probe. This is best shown on the 15 kPa approach path tests shown with 3 or 120 hours of creep in Figure 6.6 and 6.7 respectively. In comparison to the re-

Number	Description	Modelling type	End condition	Strain rate ($\%\,\mathrm{h}^{-1}$)
1	1D consolidation	1D strain path $\boldsymbol{\Delta\varepsilon}$ = [0.0001, 0, 0.000 115 47, 0, 0, 0]	p'=415.5 kPa	$\dot{\varepsilon}_a$= 0.181
2	1D swelling	1D strain path $\boldsymbol{\Delta\varepsilon}$ = [−0.0001, 0, −0.000 115 47, 0, 0, 0]	p'=172 kPa	$\dot{\varepsilon}_a$=0.0093
3	Stress relief	9 step stress path	p'=172 kPa, q=0 kPa	$\dot{\varepsilon}_q$=1
4	Isotropic consolidation	19 step stress path	p'=300 kPa q=0 kPa	$\dot{\varepsilon}_v$=0.025
		Strain of bricks reset to strain of man		
5	Approach path 1 out	Stress path 0.1 kPa steps	p'=300 kPa q=APL kPa	$\dot{\varepsilon}_a$=3 × 10^{-3}
6	Approach path 1 back	Stress path 0.1 kPa steps	p'=300 kPa q=0 kPa	$\dot{\varepsilon}_a$=3 × 10^{-3}
7	Creep period 1	Creep stage	Creep time has elapsed	N/A
8[a]	Shear probe 1 [180°]	Stress path 0.1 kPa steps.	p'=300 kPa q=80 kPa	$\dot{\varepsilon}_a$=3 × 10^{-3}
9	Reset path	Stress path 0.1 kPa steps	p'=300 kPa q=0 kPa	$\dot{\varepsilon}_a$=3 × 10^{-3}
10	Reset creep	Creep stage	5 days	N/A
11	Approach path 2 out	Stress path 0.1 kPa steps	p'=300 kPa q=-APL kPa	$\dot{\varepsilon}_a$=3 × 10^{-3}
12	Approach path 2 back	Stress path 0.1 kPa steps	p'=300 kPa q=0 kPa	$\dot{\varepsilon}_a$=3 × 10^{-3}
13	Creep period 2	Creep stage	Creep time has elapsed	N/A
14[b]	Shear probe 2 [0°]	Stress path 0.1 kPa steps	p'=300 kPa q=80 kPa	$\dot{\varepsilon}_a$=3 × 10^{-3}

[a] Path NO RSH 1 runs stages 1,2,3,4 and 8
[b] Path NO RSH 2 runs stages 1 to 10 and 14

Table 6.5: Stages used for illustration of effect of multistage testing

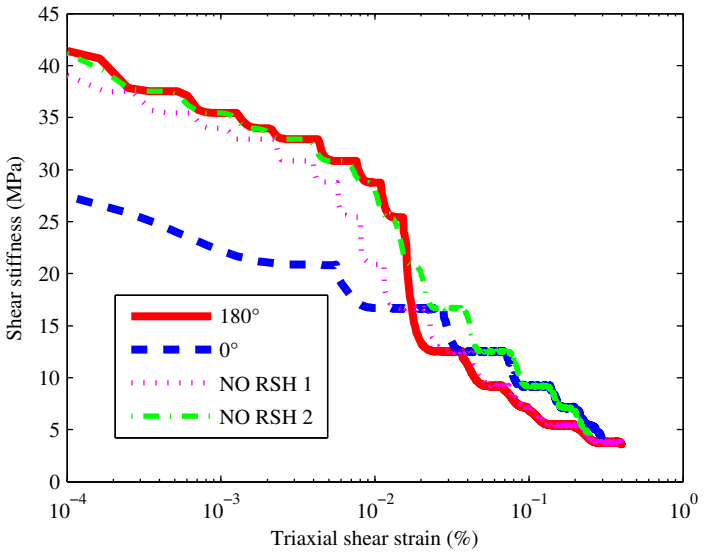

Figure 6.6: RSH test with effects of multistage testing, 3 hours creep, 15 kPa approach path

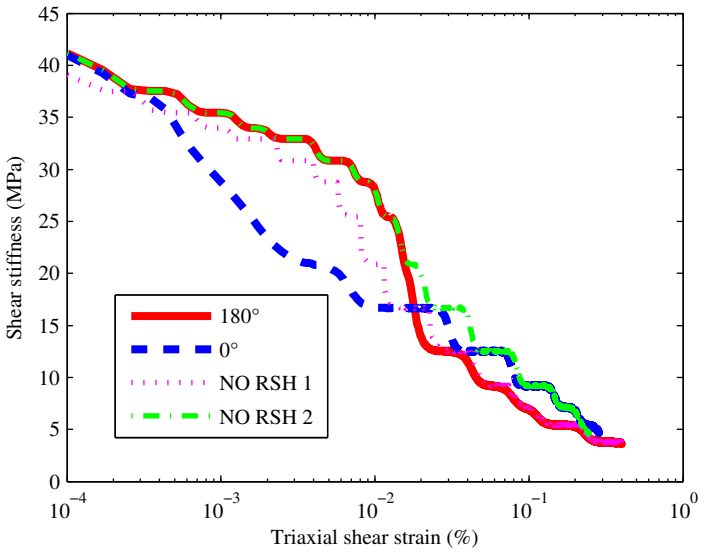

Figure 6.7: RSH test with effects of multistage testing, 120 hours creep, 15 kPa approach path

spective plots with single test stages Figure 6.3 and 6.5, the stiffness of the 0° path is increased.

The cause of the change is that the state of bricks before the application of the approach paths has been changed by the first shear probe. Figure 6.8 and 6.9 show the shear strain paths of the man and the bricks against the applied deviator stress for lines 'NO RSH1' and 'NO RSH 2' respectively. The line 'NO RSH 1' shows no RSH effect indicating the stress at which undisturbed bricks start moving. The line 'NO RSH 2' shows how shear probe 1 has moved bricks 1-14 to strains above the man which have not been greatly reduced by the reset creep stage. This results in

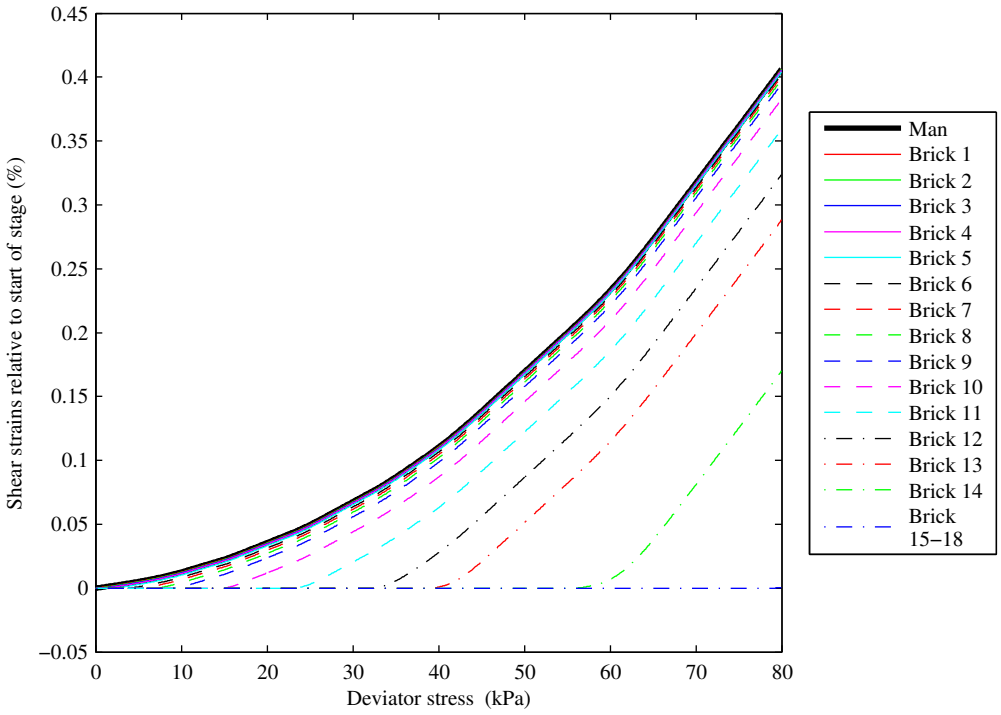

Figure 6.8: Illustration of brick shear strains for theoretical shear probe 'NO RSH 1'

an increase in the stress point where each of these bricks starts moving.

The effect of the multistage testing approach is therefore to change the stiffness degradation path from which the measured shear probe has been diverted and creeps back to. The $180°$ path therefore matches line 'NO RSH 1' in areas unaffected by the approach path and will return towards it as creep occurs. The $0°$ path is shown to match 'NO RSH 2' for those parts of the degradation curve unaffected by the approach path and even exhibits a stiffness in excess of the $180°$ path in some areas. The effect of multistage testing on brick strains is shown in Figure 6.10 and 6.11 for a $15\,\mathrm{kPa}$ approach path after $3\,\mathrm{hours}$ creep for idealised and multistage tests respectively. The idealised RSH effect shows how bricks (1-9) which are moved by a $15\,\mathrm{kPa}$ stress in Figure 6.8 now begin moving sooner and cause a lowering of stiffness. The remaining bricks however move at the same point shown for the 'NO RSH 1' line in Figure 6.8. In the multistage case the effect on bricks 1-9 is the same however the remaining bricks act as those shown for the 'NO RSH 2' line in Figure 6.9.

The effect of creep at modest creep times is to move the path towards line 'NO RSH 2'. At longer creep times however creep will affect the bricks last affected by the previous shear probe as well as those affected by the approach path.

The increase in the stiffness at larger shear strains produces an increased shear stress

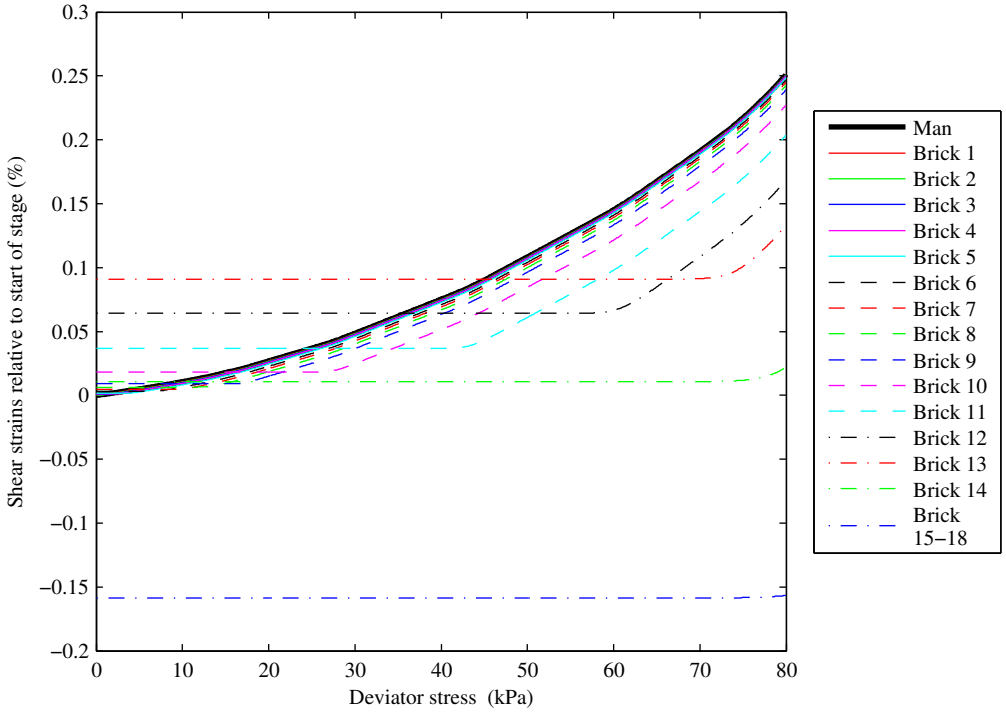

Figure 6.9: Illustration of brick shear strains for theoretical shear probe 'NO RSH 2'

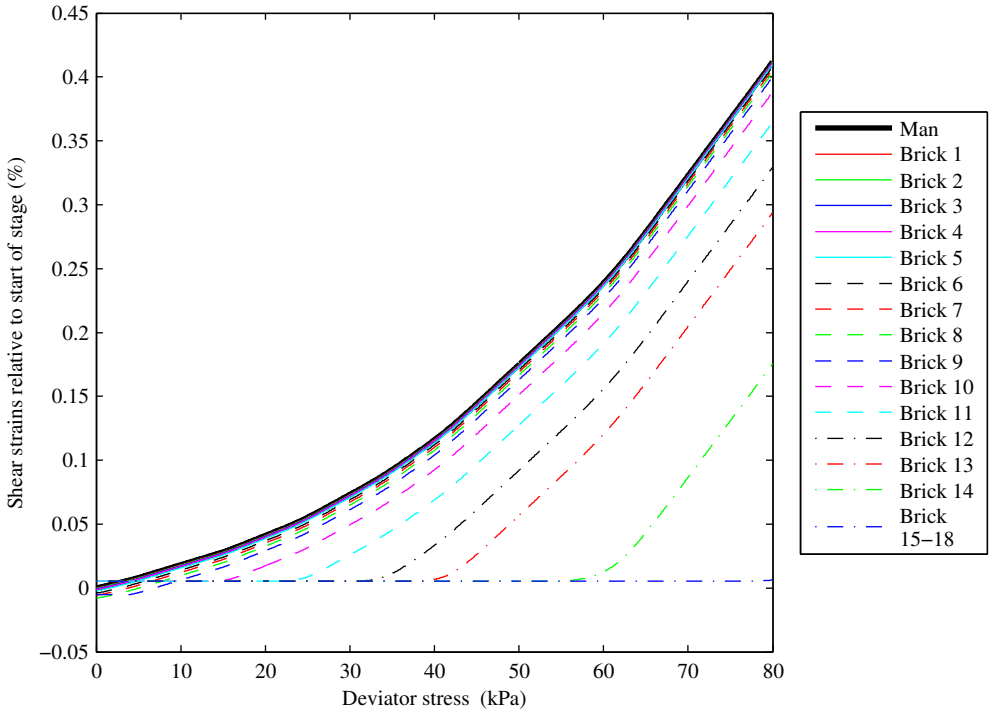

Figure 6.10: Illustration of brick shear strains idealised RSH effect, 3 hours creep, 15 kPa approach path

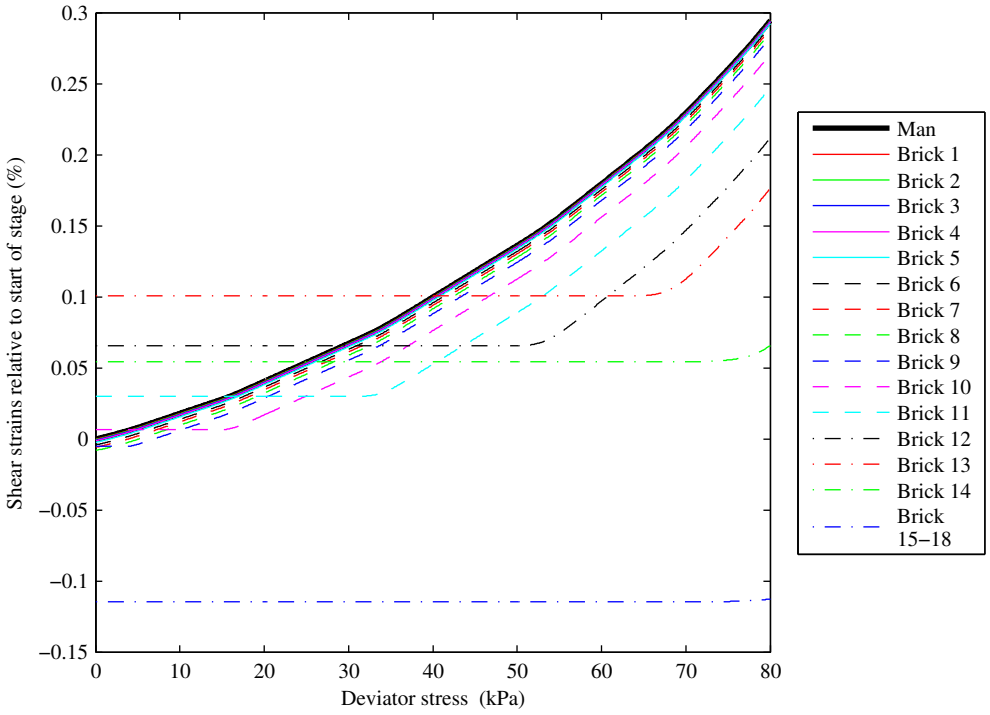

Figure 6.11: Illustration of brick shear strains modelling of multistage testing shear probe after $3\,\mathrm{hours}$ creep and $15\,\mathrm{kPa}$ approach path

at high strains. This is shown by Figure 6.12 the stress-strain plot for a $15\,\mathrm{kPa}$ approach path with $3\,\mathrm{hours}$ creep. This compares well with the equivalent test RC4 shown in Figure 4.47 (p 140). Both the experimental and numerical results show the $180°$ paths have initially higher stresses before the more rapid stiffness degradation results in a higher strain for the $180°$ path than the $0°$ path at the end of the stress path.

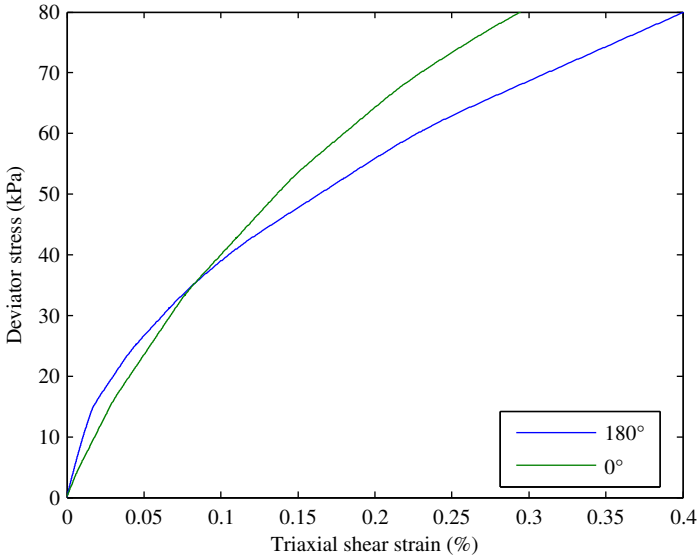

Figure 6.12: Stress strain path for multistage simulation of test with 3 hours creep and a 15 kPa approach path

6.6 Effect of recent consolidation history

The other problem that affects the stiffness of a shear probe within the BRICK model has been termed recent consolidation history (RCH). The RCH effect is limited in scope to the most recent consolidation path. For the current tests this is the isotropic consolidation stage. This limitation eliminates complexities arising from the 1D consolidation and swelling paths and release of deviator stress. In order to demonstrate RCH effects the consolidation sequence was modified to that in Table 6.6. The amount of isotropic consolidation was exaggerated compared to the standard procedure and bricks were reset prior to the isotropic consolidation to eliminate any effect from the prior stages. A second brick reset at the end of isotropic consolidation was used to remove the RCH effects for comparison.

The principle of RCH is that at the end of the isotropic consolidation bricks will be positioned in a line behind the man in decreasing volumetric strain. This has the effect of reducing the shear stiffness as less strain is required to move bricks. This can be seen in Figure 6.13 which shows how the RCH effect influences the 180° stress path rotation tests shear probe 1 when APL = 15 kPa and CT = 3 hours..

The application of a shear strain will cause brick positions to move in the shear strain direction and so reduce the influence of the volumetric strain positions of the bricks. In the tests performed the effect of the RCH on the first shear probe will be dependent on the length of the approach path. Figure 6.14 shows the reduced impact of the RCH effect on shear probe 1 when APL = 60 kPa and CT = 3 hours.

On the second shear path all bricks moved will have been previously moved by the

Number	Description	Modelling type	End condition	Strain rate ($\%\,\mathrm{h}^{-1}$)
1	1D consolidation	1D strain path $\boldsymbol{\Delta\varepsilon}$ =[0.0001, 0, 0.000 115 47, 0, 0, 0]	p'=600 kPa	$\dot{\varepsilon}_a$= 0.2
2	1D swelling	1D strain path $\boldsymbol{\Delta\varepsilon}$ = [−0.0001, 0, −0.000 115 47, 0, 0, 0]	p'=50 kPa	$\dot{\varepsilon}_a$=0.2
3	Stress relief	9 step stress path	p'=50 kPa, q=0 kPa	$\dot{\varepsilon}_q$=0.2
		Strain of bricks reset to strain of man		
4	Isotropic consolidation	Isotropic strain path $\boldsymbol{\Delta\varepsilon}$ =[0, 0, 0.0001, 0, 0, 0]	p'=600 kPa q=0 kPa	$\dot{\varepsilon}_v$=3 × 10^{-3}
		Strain of bricks reset to strain of man for RCH off paths		
5	Approach path 1 out	Stress path 0.1 kPa steps	p'=600 kPa q=APL kPa	$\dot{\varepsilon}_a$=3 × 10^{-3}
6	Approach path 1 back	Stress path 0.1 kPa steps	p'=600 kPa q=0 kPa	$\dot{\varepsilon}_a$=3 × 10^{-3}
7	Creep period 1	Creep stage	Creep time has elapsed	N/A
8	Shear probe 1 [180°]	Stress path 0.1 kPa steps.	p'=600 kPa q=80 kPa	$\dot{\varepsilon}_a$=3 × 10^{-3}
9	Reset path	Stress path 0.1 kPa steps	p'=600 kPa q=0 kPa	$\dot{\varepsilon}_a$=3 × 10^{-3}
10	Reset creep	Creep stage	5 days	N/A
11	Approach path 2 out	Stress path 0.1 kPa steps	p'=600 kPa q=APL kPa	$\dot{\varepsilon}_a$=3 × 10^{-3}
12	Approach path 2 back	Stress path 0.1 kPa steps	p'=600 kPa q=0 kPa	$\dot{\varepsilon}_a$=3 × 10^{-3}
13	Creep period 2	Creep stage	Creep time has elapsed	N/A
14	Shear probe 2 [180°]	Stress path 0.1 kPa steps	p'=600 kPa q=80 kPa	$\dot{\varepsilon}_a$=3 × 10^{-3}

Table 6.6: Stages used for demonstration of RCH effects

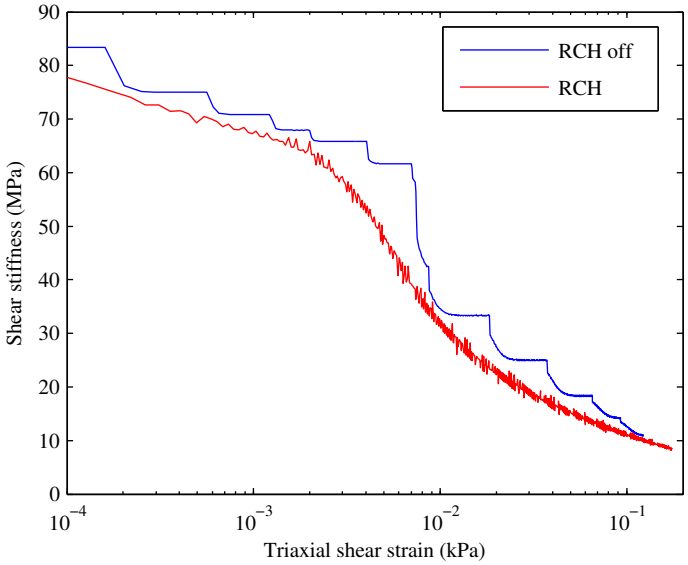

Figure 6.13: Impact of RCH effect on stiffness degradation, 3 hours creep, 15 kPa approach path

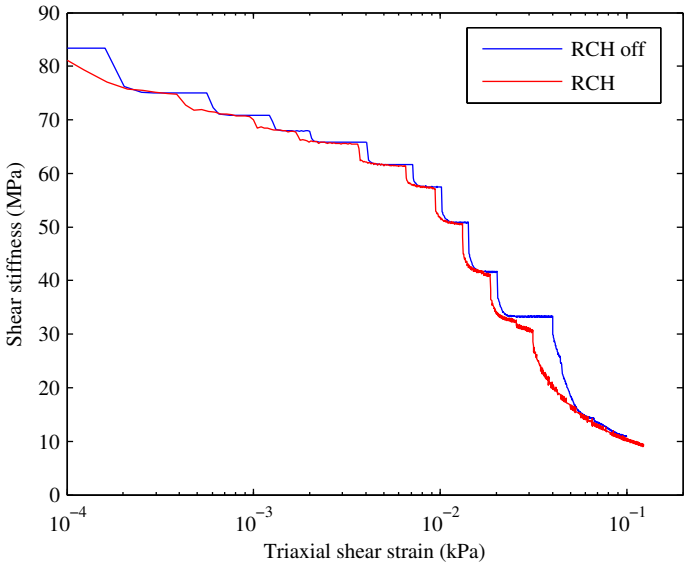

Figure 6.14: Impact of RCH effect on stiffness degradation, 3 hours creep, 60 kPa approach path

first shear path and so the RCH effect is reduced. This effect is shown in Figure 6.15 which shows shear probe 2 for APL = 15 kPa and CT = 3 hours. As detailed in Table 6.6 the testing program was altered so shear probe 2 has a 180° stress path rotation. This eliminates stress path rotation as a cause for the observed reduction in RCH effect. It is not possible however to show the effect of shear probe 1 on the volumetric strains of the bricks without also showing the effect on the shear strains of the bricks. As such when compared to Figure 6.13, there is a stiffness increase both with and without RCH effects due to the effect of multistage testing discussed previously. It is still clear however that the RCH effect is reduced on the second

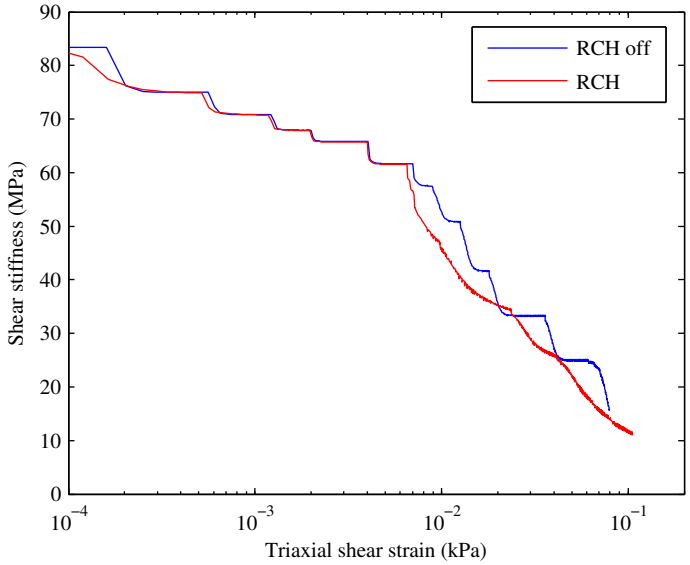

Figure 6.15: Impact of RCH effect on stiffness degradation of second shear path flowing 3 hours creep and a 15 kPa approach path

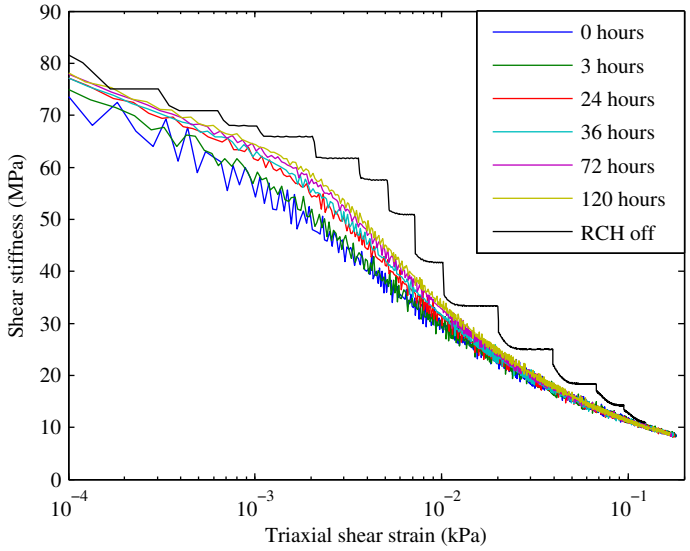

Figure 6.16: Effect of creep on the RCH effect, stiffness degradation curves

stress path.

The effect of creep on the RCH effect is to reduce its impact. When bricks are moved closer to the man along the volumetric strain axis, the shear strain required to make a string taut and move a brick will increase and result in a stiffer shear path. The effect of creep on the RCH effect is shown in Figure 6.16 for tests without approach paths (stages 1 to 4, 7 and 8 of Table 6.6). The limitations of the accuracy of the stress path finding routine cause the stiffness degradation curve to oscillate under these conditions, so a clearer illustration is provided by the curve of q versus ε_q in Figure 6.17. This shows the stress-strain path moving towards that predicted without RCH effects with increasing creep duration.

The omission of approach paths when demonstrating the effect of creep on RCH

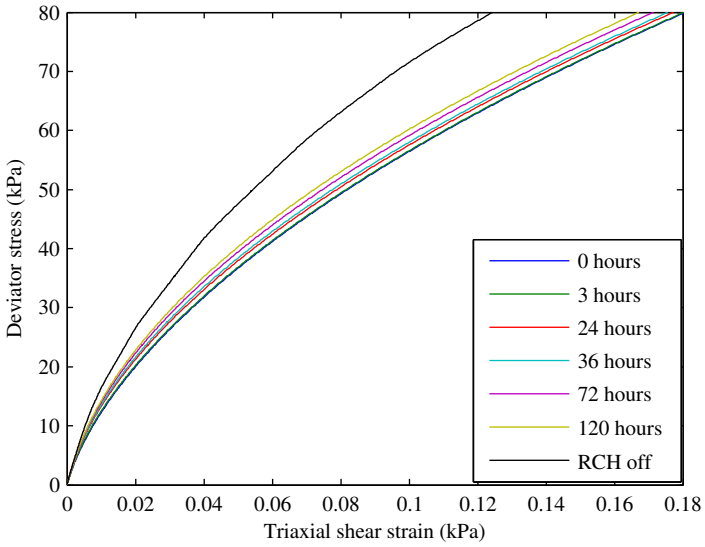

Figure 6.17: Effect of creep on the RCH effect, stress strain plots

effects was to eliminate the contrary effects of creep on RSH effects. Creep reduces both RSH and RCH effects, however in the case of a $180°$, stress path rotation a reduction in the RSH effect causes a decrease in the stiffness opposing the increase in stiffness caused by reducing the RCH effect. The precise interaction of the opposing effects of creep will be dependent on many factors including the approach paths lengths, the isotopic consolidation path, the creep duration, and the strain rates of all these stages. One outcome of interest however is that of an initial reduction in stiffness as RSH effects are erased, before an increase in stiffness as RCH effects are erased. This form of behaviour was observed when studying the effect of creep on the first shear path of the experimental results, as shown in Figure 4.49 (p 142). In order to demonstrate the effects of creep on both RSH and RCH, the simulation set-up must incorporate all effects. For this reason a new simulation was run with APL = $30\,\mathrm{kPa}$ and stages 1 to 8 of Table 6.6 to increase the RSH effect without too much detriment to the RCH effect. Creep was run at the experimental creep times of 3, 36, 72 and $120\,\mathrm{hours}$ as well as an extended creep of $760\,\mathrm{hours}$. The results are shown as a stiffness degradation curve and a stress strain plot in Figure 6.18 and 6.19 respectively. It is shown that at strains under $1 \times 10^{-2}\,\%$, where the stiffness is influenced by RSH, the effect of creep is to reduce the stiffness. The remainder of the curve is influenced by the RCH effect and so creep causes an increase in stiffness in that region. When plotted as stress strain curves, the effect of creep is shown to lower stress in the small strain but result in a higher stress at the end of the tests. This effect can be seen by comparing the 3 and $760\,\mathrm{h}$ creep paths, the trend of which mirrors the relationship between test RC4 and RC3 observed in Figure 4.49 (p 142).

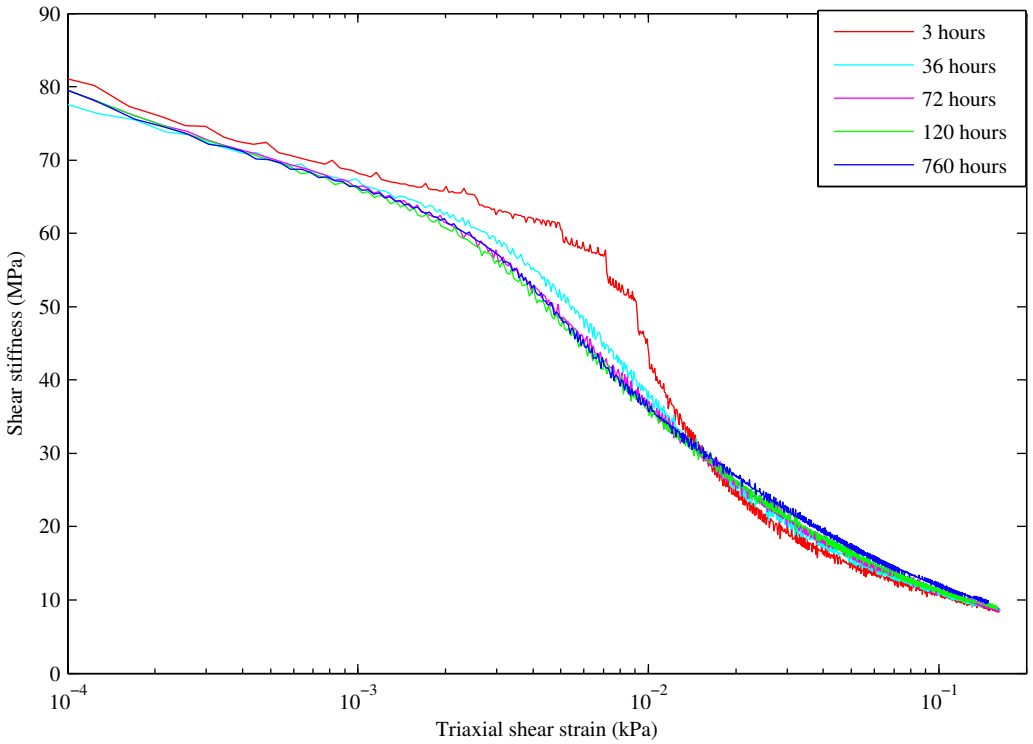

Figure 6.18: Effect of creep on the RCH and RSH effects for a $30\,\mathrm{kPa}$ approach path test, stiffness degradation curves

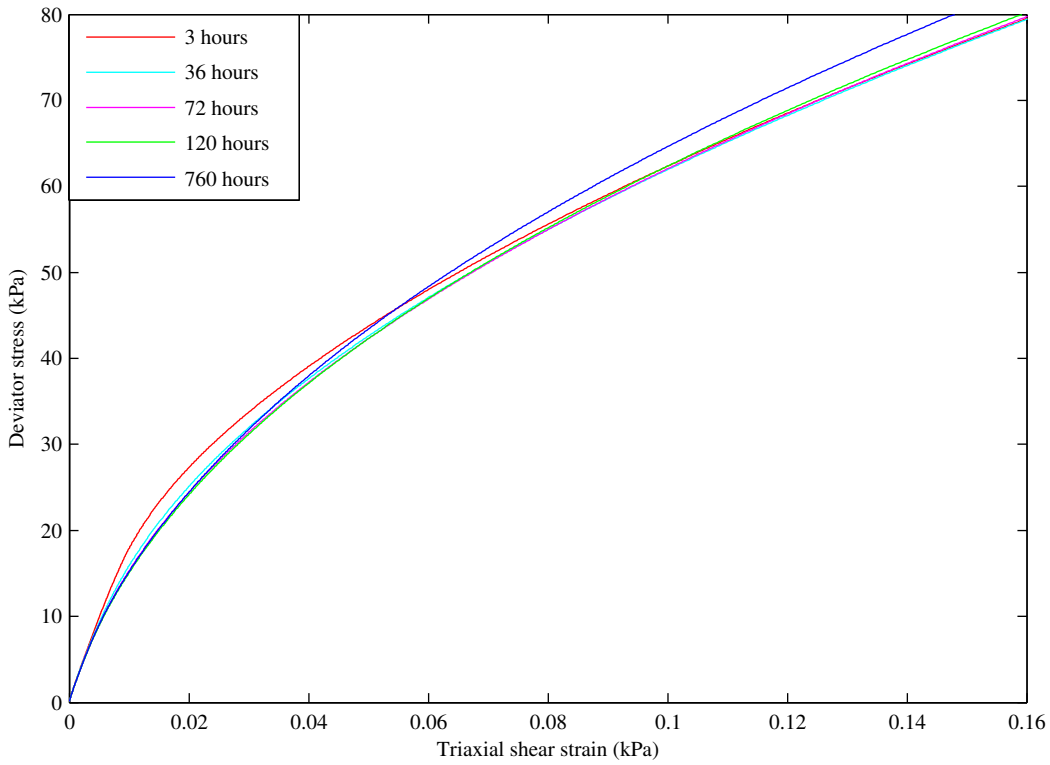

Figure 6.19: Effect of creep on the RCH and RSH effects for a $30\,\mathrm{kPa}$ approach path test, stress strain curves

6.7 Simulation of the experimental data

A simulation of the experimental results was performed using the test stages detailed in Table 6.7. This demonstrates how the effects of RSH, RCH and multistage testing combine with the effects from the 1D consolidation, 1D swelling and deviator stress release. The maximum observed shear stiffness remains at G_0 = 42 MPa as it was when bricks were reset after the isotropic consolidation stage. This confirms that the G_0 is unaffected by brick positions. As the shear stiffness is lower than the G_0=60 MPa observed in the experimental results, trends are discussed rather than making direct comparison to the experimental results.

The effect of creep on the first shear probe which underwent a 180° stress path rotation is shown in Figure 6.20. The effect of creep is a small reduction in shear stiffness G_0 below ε_q = 0.02 % shear strain and a slight increase above. The cumulative effect is a very slight increase in G_Ω (the secant shear stiffness measured to the end of the shear probe, illistrated in Figure 6.22). This shows a reduction in only the RCH effect in contrast with the experimental results (Figure 4.49, p 142), which shows the effect of a combined reduction in RSH and RCH effects as well as a greater variation in G_Ω.

The effect of creep on the second path with a 0° stress path rotation angle is an increase in G for strains below ε_q = 0.01 %, as shown in Figure 6.21. The increase in stiffness with creep is consistent with the experimental results (Figure 4.50 p 142) however the magnitude of the effect is reduced. G_Ω increases by only 2 % between test RC4 and RC3 in the BRICK simulation compared to 36 % in the experimental

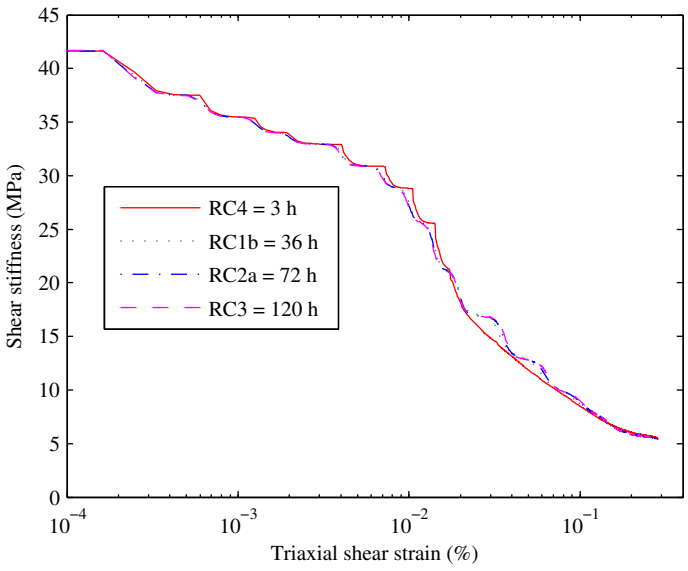

Figure 6.20: Effect of creep on the stiffness degradation curve of shear probe 1 simulated without resetting bricks

Number	Description	Modelling type	End condition	Strain rate ($\%\,\mathrm{h}^{-1}$)
1	1D consolidation	1D strain path $\boldsymbol{\Delta\varepsilon}$ =[0.0001, 0, 0.000 115 47, 0, 0, 0]	p'=415.5 kPa	$\dot{\varepsilon}_a$= 0.2
2	1D swelling	1D strain path $\boldsymbol{\Delta\varepsilon}$ = [−0.0001, 0, −0.000 115 47, 0, 0, 0]	p'=172 kPa	$\dot{\varepsilon}_a$=0.2
3	Stress relief	9 step stress path	p'=172 kPa, q=0 kPa	$\dot{\varepsilon}_q$=0.2
Strain of bricks reset to strain of man for tests without effect of 1D consolidation				
4	Isotropic consolidation	Isotropic strain path $\boldsymbol{\Delta\varepsilon}$ =[0, 0, 0.0001, 0, 0, 0]	p'=300 kPa q=0 kPa	$\dot{\varepsilon}_v$=3 × 10^{-3}
5	Approach path 1 out	Stress path 0.1 kPa steps	p'=300 kPa q=APL kPa	$\dot{\varepsilon}_a$=3 × 10^{-3}
6	Approach path 1 back	Stress path 0.1 kPa steps	p'=300 kPa q=0 kPa	$\dot{\varepsilon}_a$=3 × 10^{-3}
7	Creep period 1	Creep stage	Creep time has elapsed	N/A
8	Shear probe 1 [180°]	Stress path 0.1 kPa steps.	p'=300 kPa q=80 kPa	$\dot{\varepsilon}_a$=3 × 10^{-3}
9	Reset path	Stress path 0.1 kPa steps	p'=300 kPa q=0 kPa	$\dot{\varepsilon}_a$=3 × 10^{-3}
10	Reset creep	Creep stage	5 days	N/A
11	Approach path 2 out	Stress path 0.1 kPa steps	p'=300 kPa q=APL kPa	$\dot{\varepsilon}_a$=3 × 10^{-3}
12	Approach path 2 back	Stress path 0.1 kPa steps	p'=300 kPa q=0 kPa	$\dot{\varepsilon}_a$=3 × 10^{-3}
13	Creep period 2	Creep stage	Creep time has elapsed	N/A
14	Shear probe 2 [180°]	Stress path 0.1 kPa steps	p'=300 kPa q=80 kPa	$\dot{\varepsilon}_a$=3 × 10^{-3}

Table 6.7: Stages used for demonstration repeat of actual tests

results.

The effect of the approach path length is shown in terms of stress versus strain in Figure 6.22 and 6.23 for shear probe 1 and 2 respectively. In terms of G_Ω the effect of the approach path length is seen to increase the RSH effect. This increase in stiffness on the 180° path and reduction on the 0° path conforms with the idealised RSH effect. This result supports the supposition that test RA4 exhibited an erroneously low stiffness on shear probe 1 of the experimental results.

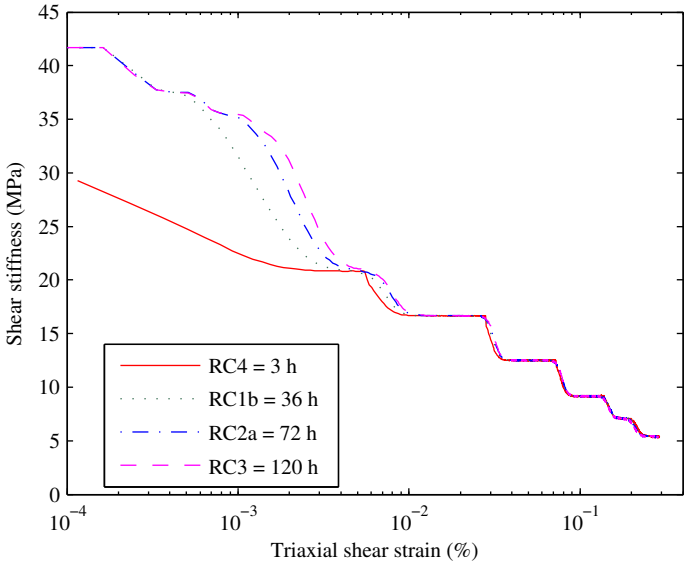

Figure 6.21: Effect of creep on the stiffness degradation curve of shear probe 2 simulated without resetting bricks

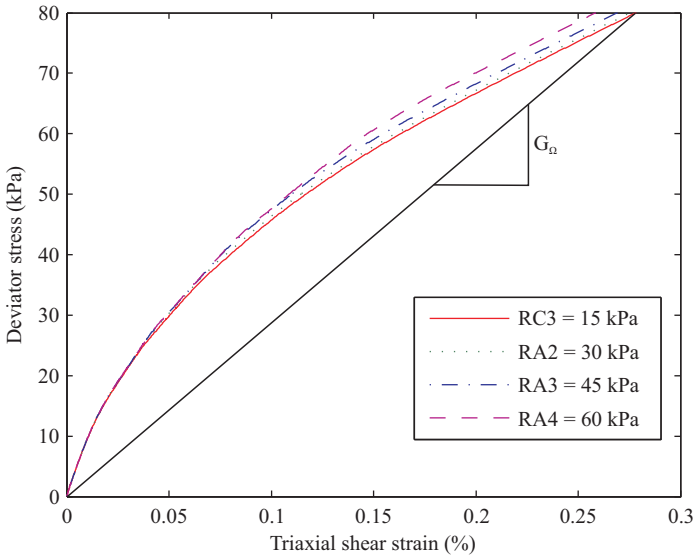

Figure 6.22: Effect of approach path length on shear stress strain curve of shear probe 1 simulated without resetting bricks

The stiffness degradation of shear probe 1 (Figure 6.24) shows a lower impact of approach path length than is suggested by comparison between Figure 6.13 and 6.14 for the idealised RSH effect. The effect of approach path length on the stiffness degradation of shear probe 2 (Figure 6.25) however, show a larger impact of approach path length consistent with the effects of multistage testing. These results indicate that all bricks moved by shear probe 1 resided at a higher shear strain than the man prior to the commencement of the approach paths. As such shear probe 1 produces the stiffness degradation plot for a 180° stress path rotation throughout

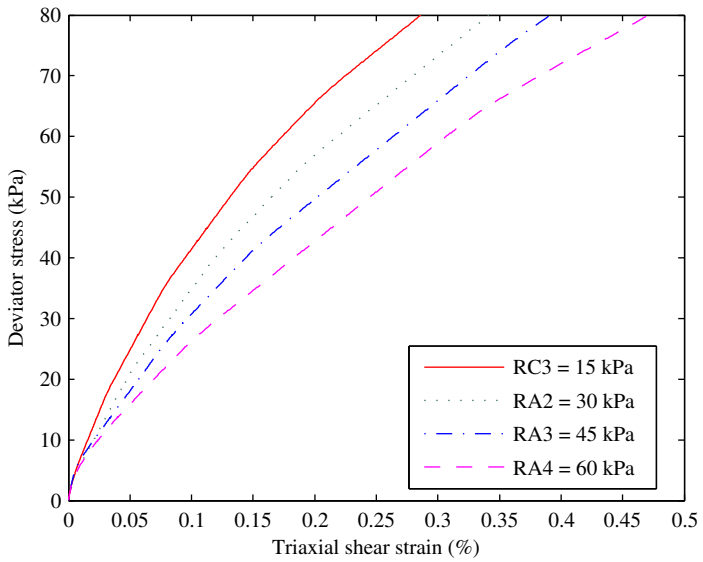

Figure 6.23: Effect of approach path length on shear stress strain curve of shear probe 2 simulated without resetting bricks

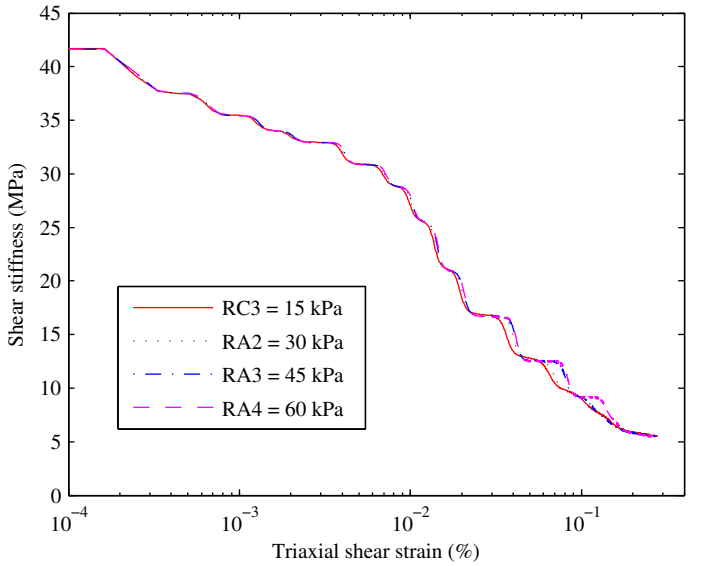

Figure 6.24: Effect of approach path length on stiffness degradation curve of shear probe 1 simulated without resetting bricks

the stress path no matter the approach path length. The slight increase in stiffness observed is due to the reduction of the RCH effect.

The test was rerun with bricks reset just prior to the isotropic consolidation stage in order to demonstrate the impact of the 1D consolidation, 1D swelling and deviator stress release. On the second shear probes this causes no notable effects on the observed trends, just a small reduction in G_Ω. A significant difference is seen by comparing the effect of creep on the stiffness degradation plot of shear probe 1 in Figure 6.26 and Figure 6.20, with and without brick resetting respectively. These

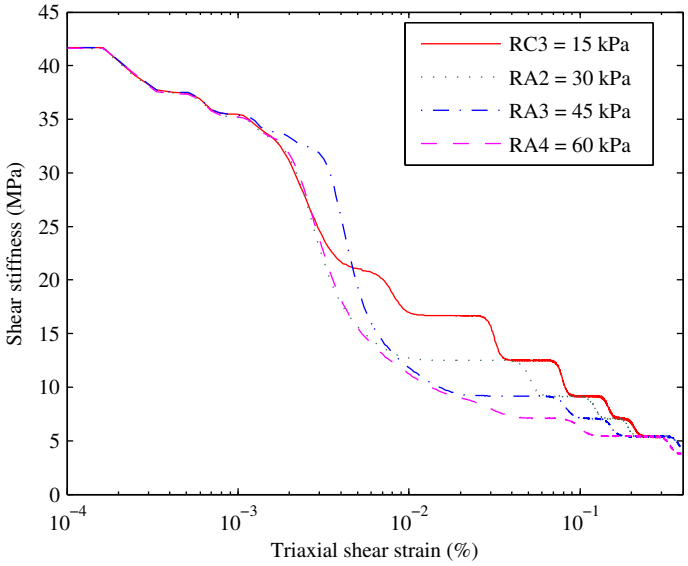

Figure 6.25: Effect of approach path length on stiffness degradation curve of shear probe 2 simulated without resetting bricks

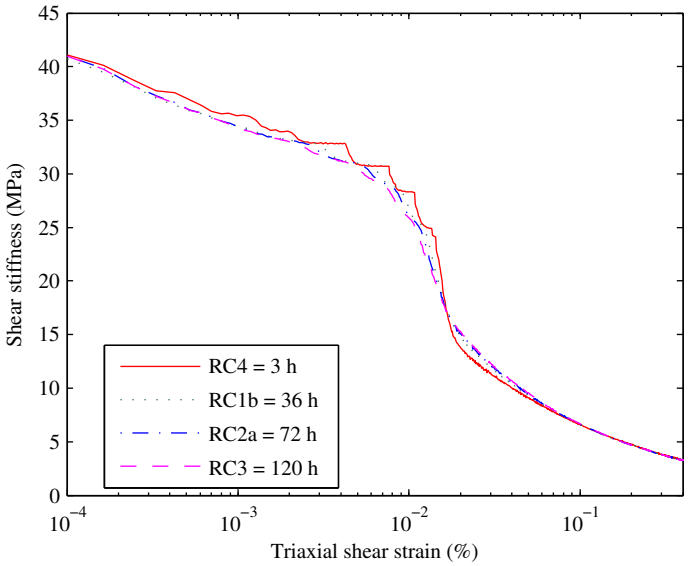

Figure 6.26: Effect of creep on the stiffness degradation curve of shear probe 1 simulated with bricks reset prior to isotropic consolidation

examples show how resetting brick positions has increased the RSH effect so there is now a significant reduction in stiffness at low strains due to reduction of the RSH with creep. This combines with the increase in stiffness due to reduction of the RCH effect, resulting in behaviour similar to that seen in Figure 6.19. The trend in G_Ω now matches the experimental work. The magnitude of the effect of creep however remains much reduced.

The effect of resetting bricks prior to isotropic consolidation is most clear when looking at the effect of the approach path on shear path 1. In Figure 6.27 the stress

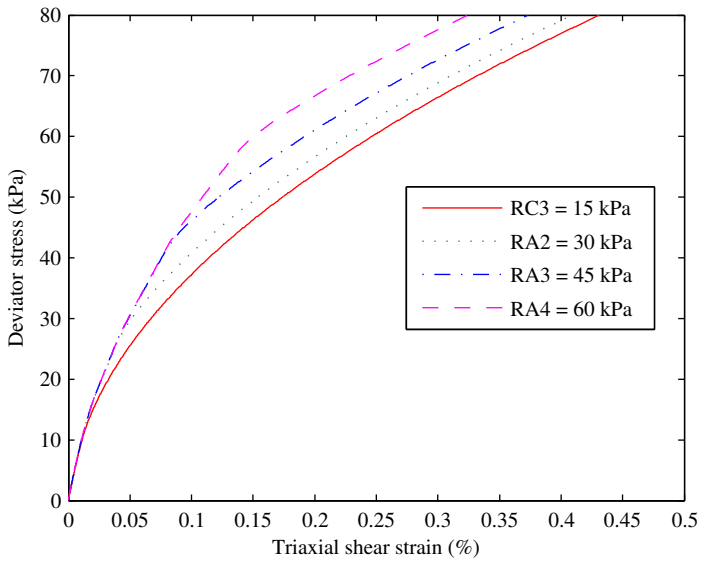

Figure 6.27: Effect of approach path length on shear stress strain curve of shear probe 1 simulated with bricks reset prior to isotropic consolidation

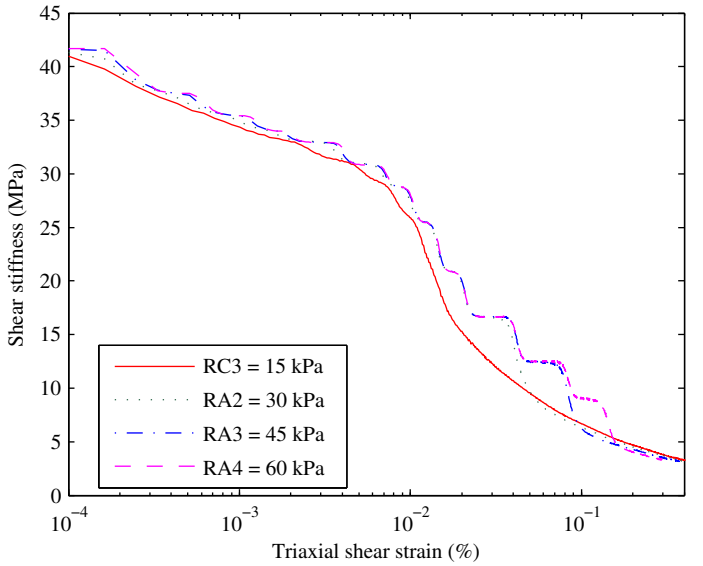

Figure 6.28: Effect of approach path length on stiffness degradation curve of shear probe 1 simulated with bricks reset prior to isotropic consolidation

paths now drop in stiffness once the stress reaches the approach path length. In Figure 6.28 the strain at which stiffness drops is now seen to clearly increase with approach path length. The observed effect of approach path length and the generally reduced stiffness confirms that one of the first 3 test stages left bricks at a higher shear strain than the man.

The trace of brick positions through the consolidation stage in Figure 6.29 shows how the elevated shear strain of the bricks arose. In the initial 1D consolidation all bricks are behind the man along the line traced by the man in volumetric and shear

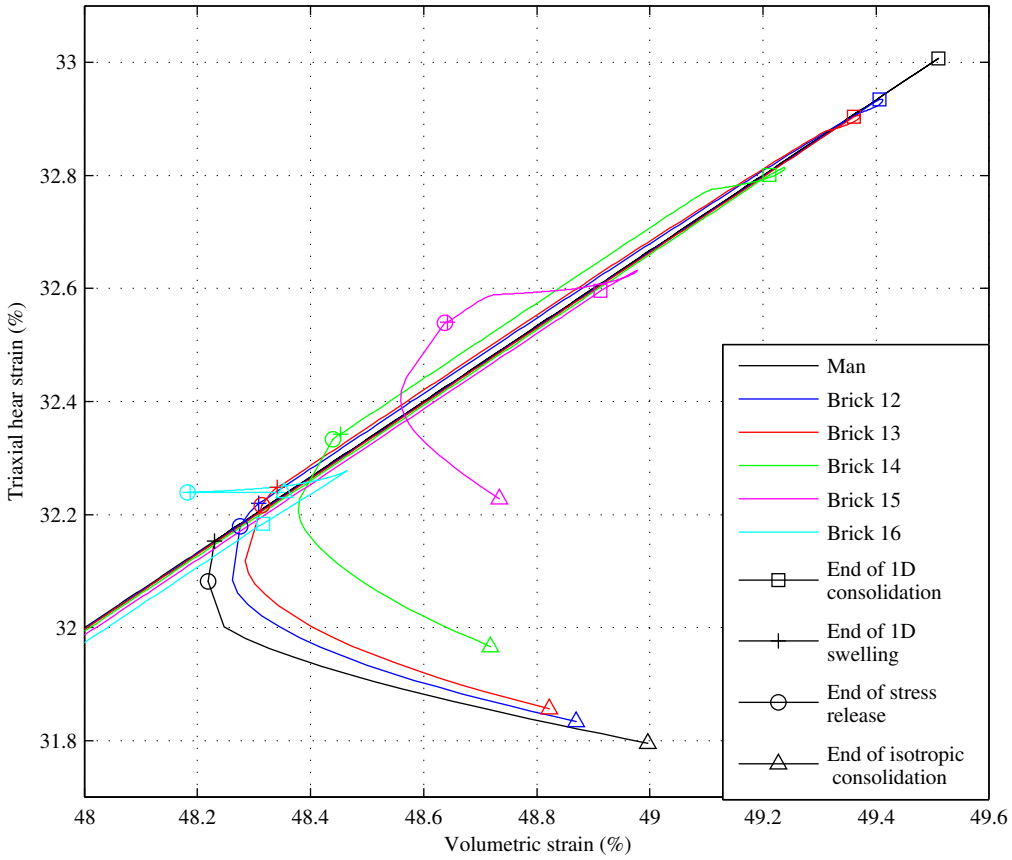

Figure 6.29: Trace of brick positions during consolidation simulation. Bricks 1-11 omitted for clarity, 17 and 18 are not in observed strain range

strain. The 1D swelling returns the man along the same path. Strings are initially made slack, begin to shorten under the effects of the time decay mechanism, and are affected solely by the PSRED which causes some movement off the path. At the end of the swelling stage the strings of bricks 1 to 15 become taut and bricks lie at a greater shear and volumetric strain than the man. Brick 16 is slack with a higher shear strain but lower volumetric strain than the man, while bricks 17 and 18 are slack at much lower shear and volumetric strains. The stress release stages causes a small change in total and brick strains that does not substantially affect the relative positions. The elevated brick shear strains and the resulting distortions are therefore the result of the 1D consolidation and swelling. A small reduction in the difference between the shear strain of the bricks and the man occurs during isotropic consolidation.

6.8 Conclusions

The BRICK simulations presented in this chapter have shown how different stress paths within the simulations influence the resulting behaviour. It was shown that

the ideal RSH effect would increase stiffness for the $180°$ probes and reduce it for $0°$ probes, when compared to a shear probe with no stress history. The approach probe was shown to increase the section of the stiffness degradation curve that was diverted from the result without stress history, while creep brought the stiffness back to this path. It was shown that when two paths were run in succession, the first shear probe would have increased the stiffness at the higher strains unaffected by the $0°$ approach path, producing an increased G_Ω.

The results also demonstrated the RCH mechanism by which the stiffness of the first shear probe was lowered. This was shown to reduce with approach path length as well as creep. A reduction due to the effect of the first shear probe caused an additional increase in the stiffness observed on the second shear probe. The effects of creep on the RCH effect were shown to increase stiffness on the first shear probe, while reducing the stiffness as the RSH effect reduced. As such it could be demonstrated that creep would cause an initial decrease in G_Ω as the RSH effect reduced before an increase as the RCH effect reduced.

When the whole test was simulated the effect of the 1D consolidation path was shown. This caused the same effect as a large $180°$ approach path and so reduced the effects of the modelled approach paths and altered the creep trend. A brick reset prior to the isotropic consolidation was used to remove the effect of 1D consolidation which was not observed in the experimental results. The same effect could be achieved through a combination of creep and the isotropic consolidation. This would require the BRICK parameters to be altered to increase the effect of creep and the volumetric strain during isotropic consolidation.

When the influence of the 1D consolidation was removed, the trends for the modelled effects of creep and approach path length matched those observed in the experimental work. When comparing physical tests to the simulations the main differences were the shear stiffness and the magnitude of the creep effect. The correct maximum shear stiffness could be found by increasing the OCR by changing the maximum consolidation pressure to $p'_m = 1785\,\mathrm{kPa}$. Increasing the impact of creep however would require a change in the model parameters. Simply using slightly higher creep parameters obtained from test C2 in section 4.6.2 (p 127) had a minimal effect.

There were no further attempts to fit the output of the BRICK model to the experimental results. This would require an expansive parametric study, encompassing both BRICK parameters and those parameters governing the model stress path which are variable or uncertain. Given the number of parameters this encompasses this would require an excessive amount of time. There is also too little experimental data that exists outside the RSH set of tests to provide sufficient cross validation to justify any parameter set that may have been obtained.

7

Summary and conclusions

7.1 Introduction

The work presented in this thesis was performed to provide an enhanced understanding of the interactions between the recent stress history (RSH) effect, creep and approach path length. In this chapter the work performed will be summarised, the key conclusions highlighted and finally suggestions made for future work.

7.2 Summary

The work performed can be categorised into two main sections, experimental and numerical. The experimental program consisted of a series of multistage constant p' triaxial tests. The samples used for the testing were of weathered London clay which had been reconstituted one dimensionally in order to produce a consistent sample and eliminate the structural effects of weathering. The apparatus used was a stress path triaxial cell with local instrumentation to provide actuate control of stress and measurement of strains.

The stages within each test were arranged to demonstrate the RSH effect; first with a 180° rotation between approach path and shear probe and then after a suitable reset for a 0° rotation. The length of the approach path and the duration of a creep period between an approach path and a shear probe were varied between tests to investigate their impact on the RSH effect. The test results indicated an increase in RSH effect with approach path length and a decrease with creep duration. The impacts of the multistage testing approach however caused the greatest effect.

The numerical work utilised the strain rate dependent (SRD) BRICK model as this had been previously shown to be capable of simulating RSH effects. It was found however that the existing implementation of the model had utilised a series of workarounds in order to allow the string length to increase from its reference length to one appropriate to the applied strain rate. These workarounds caused problems in simulating a more generalised set of stress paths, particularly swelling stages. In

order to avoid these problems an improved version of the code, dubbed strain rate dependent bisecting iteration (SRD-B), was developed. This utilised a bisecting iteration to find $||\dot{\boldsymbol{\varepsilon}}_{\boldsymbol{b}}||$ that would result in the same string length from the strain rate dependency equation (Equation 5.38 p 165) and the difference between the position of the brick and the man (Equation 5.41 p 165). This method improved both the stability and accuracy when compared to the original SRD implementation.
A further element missing from the BRICK model was the ability to successfully implement creep. The SRD model had introduced a time dependent mechanism by which string lengths would shorten with time. At a constant total strain this mechanism would move bricks and result in a stress relaxation. To achieve creep however the applied strain change had to be set to match the plastic strain change caused by brick movements and so produce no change in stress. A new method for finding the appropriate strain to achieve creep was developed. This utilised a coordinate descent method to continually move in the direction of the lowest stress magnitude on a surface of stress magnitude vs. shear and volumetric strain. This allowed creep to be run accurately at any stress point and demonstrated creep rupture behaviour.
The improved SRD-B BRICK model and creep routine were then applied to demonstrate the RSH effect. Firstly the mechanisms by which stress path rotation increased stiffness and how creep reduced the effects of stress path rotation were demonstrated using incremental strain energy (ISE) contour plots. A series of simulations of the physical testing program were then performed. These showed that the experimental work did not conform to the simplified model of RSH. In the simplified model the $180°$ rotation produced a consistently stiffer result and the overall RSH effect is increased by approach path length and reduced by creep time. Instead it was shown that the RSH effect combined with the recent consolidation history (RCH) effect and the multistage effect. The RCH effect is a reduction in stiffness on the first shear probe caused by the $90°$ stress path rotation from the isotropic consolidation path. The multistage effect is a stiffening of the second shear probe due to the $180°$ stress path rotation from shear probe 1.

7.3 Conclusions

7.3.1 Experimental results and their simulation in the BRICK model

- Temperature variations of $\pm 1\,^{\circ}\mathrm{C}$ within the lab caused oscillations in the stress and strain readings of the triaxial tests. These caused the measurement of tangent shear stiffness G to vary to the point where a stiffness degradation curve could not be easily discerned. A bootstrap smoothing routine was

developed which improved the stiffness degradation curves.

- The samples of London clay used were found to have index properties within the expected range. The clay fraction obtained from laser diffraction was however initially lower than expected. An adjustment to the clay threshold was made to account for the different effects of non-spheroidal particles on the laser diffraction and pipette methods. The adjusted result was consistent with previous studies although it would be more rigorous to obtain particle size distribution by both methods for comparison.
- The consistency of the 1D consolidation method was found to be significantly affected by clogging of the porous discs. This was determined as the only strong correlation that accounted for the decrease in initial effective stress and increase in final void ratio was with the test number when numbered by condsolidation apparatus used. In future test awareness of this problem would enable a more rigorous cleaning and monitoring regime to be used as trends in results were not immediately apparent when altering between two consolidation apparatus.
- The attempts made to quantify the stress condition in the one dimensional consolation were largely impeded by the quality of data acquisition and transducer calibrations. In future work using data acquisition which allowed stable multipoint calibration and a transducer less susceptible to drift would improve the pore water pressure readings. The measurement of earth pressure at the ends of the sample however must be redesigned. It was found that the use of ceramic pressure transducers surrounded by an annular porous disk were susceptible to unknown bridging effects and could not be reliably calibrated. Measuring the pressure over the whole ends surface via a load cell arrangement may be a more reliable method for obtaining a measurement of the pressure at the end of the consolidation tube.
- The degree of consolidation during the one dimensional consolidation was found to be incomplete. This lead to the maximum vertical effective stress σ'_{vc} = $544\,\mathrm{kPa}$ estimated from oedometer test. Significantly less than the σ'_{vc} = $2800\,\mathrm{kPa}$ expected from complete consolidation. Obtaining a higher degree of consolidation would require an excessive consolidation time for the $100\,\mathrm{mm}$ samples. In future work using a smaller sample is recommended if the problems of transducer resolution associated with a smaller measurement span can be overcome.
- The expected linear relationship between the logarithm of strain rate to the logarithm of time could only be fitted to long term results. In the short term the strain rate was linear with logarithm of time. These two relationships could be combined by incorporating a fixed transition. This relationship for

strain rate vs. time was then integrated to allow fitting to the strain vs time data. This gave a parametric fit for the strain rate during creep. This allowed the creep strain rate to be examined in situations where the noise in the strain data made it impossible to reliably obtain a strain rate directly.

- The strain rate degradation was observed to fit the parametric relationship on initial tests used to setup the durations allowed for creep. When comparing the final axial strain rates of the creep periods within the main test sequence however, there was no clear trend. It was found that the creep strain following the shear stages was disturbed from the expected parametric fit by a persistent secondary consolidation. This caused the final strain rate at the end of the creep stage to be increased, decreased or even reversed depending on the relation of the expected creep strain to the continuing volumetric strain. Due to this effect the strain rate at the end of the creep periods was not considered a reliable indicator of creep progress and so creep duration was used.
- A clear RSH effect was shown for a $60\,\mathrm{kPa}$ approach path with a $3\,\mathrm{hour}$ creep. This proved that the RSH was present in the reconstituted samples of the weathered London clay used.
- In other tests performed, G was observed to be higher for a $180°$ stress path rotation at small strain. By larger strains however the $0°$ stress path rotation was observed to have a higher stiffness. This effect along with the oscillation in the stiffness degradation effect made it impossible for a single metric to correctly quantify the RSH effect.
- Simulations of the experimental work demonstrated that the multistage testing approach produced a result significantly different from that expected from single stage tests.
- BRICK simulations without any stress history effects prior to the approach paths produced a simple model for the effect of approach path length and creep on RSH effect.

  The approach path length was shown to increase the strain at which the stiffness degradation path returned to a neutral stiffness degradation path. The neutral path was one performed without approach paths. A $180°$ stress path rotation increased the strain at which the strings became taut and therefore increased the stiffness. A $0°$ stress path rotation reduced the strain at which strings became taut and therefore reduced stiffness.

  The effect of creep was shown to reduce the RSH effect as the stiffness degradation curve approached the neutral stiffness degradation curve.
- It was shown by BRICK simulations that the multistage testing approach would cause an increase in stiffness on the second shear probe. This was not initially apparent as small strains were affected by the approach path and

so had a reduced G associated with a $0°$ stress path rotation. At higher strains however G increased to the $180°$ stress path rotation relative to the first shear probe. This effect resulted in the secant shear stiffness at the end of the shear probe G_Ω being higher for the $0°$ stress path rotation probe. This effect was also observed in the experimental results.

- It was shown in BRICK simulations that the isotropic consolidation stage would reduce the stiffness on the first shear probe. This effect was termed RCH and was a result of the brick positions along the volumetric strain axis resulting in lower strain being required to move bricks and thus lower stiffness. This effect was shown to be reduced by the approach path length and was almost eliminated by the first shear probe. Creep also reduced the RCH effect.
- In the BRICK simulations a combination of the RCH effect and $180°$ stress path rotation RSH effect was shown to cause G_Ω to decrease and then increase as creep time increased. This is caused by contrary effects of creep which first reduced stiffness at low strains as the RSH effect was reduced, before a stiffness increase at high strains occurred as the RCH effect reduced. On the second shear probe any remaining influence of RCH acted with the $0°$ RSH effect and so both G and G_Ω increased with increasing creep time.
- When simulated in the BRICK model the one dimensional consolidation and swelling stage was shown to produce a change in brick positions. This acted as a $180°$ stress path rotation and therefore increased the stiffness of the first shear probe. The effect of approach path length on the first shear probe was also reduced, as the whole path acted as if a $180°$ stress path rotation had occurred regardless of the approach path length.
- When an allowance was made for the inconsistencies in the sample preparation, the trends in the experimental results analysed in stress versus strain paths were:

  G_Ω on the first shear probe with a $180°$ stress path rotation increased with approach path length.

  G_Ω on the second shear probe with a $0°$ stress path rotation decreased with approach path length.

  G_Ω on the first shear probe with a $180°$ stress path rotation decreased with creep up to $72\,\text{hours}$. G_Ω then increased after $120\,\text{hours}$ of creep.

  G_Ω on the second shear probe with a $0°$ stress path rotation increased with creep duration.
- The trends in the experimental work were reflected by a simulation of the whole test with the bricks reset immediately prior to the isotopic consolidation. In this case the effects of RSH, RCH and multistage testing were com-

bined but the effect of the 1D consolidation was discounted. The shear stiffness magnitudes and the impact of creep however were lower in the BRICK simulations than the experimental results.

- The BRICK simulations were assumed to represent the behaviour of the real soil and so allow the soil behaviour to be explored at various levels of simplification. The simplified effects of RSH, RCH and multistage testing could then be combined to provide a plausible mechanism for the observed behaviour. It should however be remembered that BRICK is a model and so any conclusions made do not necessarily represent the behaviour of real soils.

7.3.2 Improvements made to the BRICK model

- The SRD BRICK model was only capable of simulating a limited selection of stress or strain paths. This limitation was due to a number of specialisations in the numerical solution for string length which produced particularly erroneous string lengths during swelling stages. The key problem was that the measured strain rate of a brick would not be equal to the strain rate used to calculate the string length.
- A mathematical formulation (Equation 5.39 p 165) was found that described the actual strain rate of a brick $||\dot{\boldsymbol{\varepsilon}}_{\boldsymbol{b}}||$ in terms of two fixed input parameters and the string length vector SL. The fixed parameters were Δt the time step and T the distance between the total strain point reached at the end of the BRICK increment and the strain of the brick at the start of the increment.
- Ensuring the correct relationship between the actual strain rate of a brick and the string length associated with it resulted in an improved calculation of SL. This was achieved by using a bisecting iteration to find $||\dot{\boldsymbol{\varepsilon}}_{\boldsymbol{b}}||$ that produced the same SL from the strain rate dependency equation (Equation 5.38 p 165) and the actual brick movement (Equation 5.41 p 165). Dubbed SRD-B this model allowed the calculated SL to increase gradually between reference string length SL_{ref} and the string length for the applied strain rate SL_{app}, a region that had previously required SL to be artificially increased.
- The SRD-B BRICK model caused an expansion in the number of BRICK increments required for the change brick strain $||\boldsymbol{\Delta\varepsilon}_{\boldsymbol{b}}||$ to match the change in applied strain $\boldsymbol{\Delta\varepsilon}$. In standard BRICK with a set of strings at SL_{app} when a string became taut $||\boldsymbol{\Delta\varepsilon}_{\boldsymbol{b}}||$ instantly increased to $\boldsymbol{\Delta\varepsilon}$. In the SRD-B BRICK $||\boldsymbol{\Delta\varepsilon}_{\boldsymbol{b}}||$ produces an s-shaped curve when plotted against the iteration number. This began with an initial increase when the string became taut at SL_{ref}, had a point of inflection at $||\boldsymbol{\Delta\varepsilon}_{\boldsymbol{b}}|| = 0.5 \times \boldsymbol{\Delta\varepsilon}$, before $||\boldsymbol{\Delta\varepsilon}_{\boldsymbol{b}}||$ became asymptotic to $\boldsymbol{\Delta\varepsilon}$.

- In the stepped rate of strain (SRS) test SRD-B exhibited two key improvements over the SRD model. Firstly a slight overshoot in p' when lowing the applied strain rate was avoided. Secondly the SRD-B model had a slightly higher p' at each strain rate due to the SRD model under-calculating SL due to a large iteration tolerance.
- In a stress relaxation test the SRD-B model produced a smooth reduction in SL which reached the same final SL independent of the starting strain rate. In the SRD model however the reduction in SL is halted prematurely as the iteration workarounds cause an increase in SL.
- In a swelling and reconsolidation test the SRD-B model predicts a logical effect of swelling; where strings become slack causing SL to reduce due to time dependent (TD) effects, before increasing when strings become taut again. This is in contrast to the SRD model in which the SL is a function of the iteration process used.
- An instant application of TD effects was found to prevent a creep solution as it caused a discontinuous space where $\Delta\varepsilon_e = 0$ did not exist. This problem was rectified by only applying the TD effect in situations where the resulting SL was greater than that generated without TD effects.
- As the BRICK model is strain based, achieving creep is difficult and requires that the stresses be held constant. The control routine must find the applied strain that results in no elastic strain. The accuracy required prevented the standard stress path finding routine being used. Other methods such as alternating stress relaxations and stress paths were also found to be insufficient at holding stress constant.
- A method for achieving creep was developed for triaxial test situations that utilised volumetric strain and just one shear strain component. The magnitude of the stress change during a BRICK increment was plotted against the change in volumetric and shear strain. The surface formed was found to have only a single minima where the stress change magnitude was equal to zero. A coordinate descent routine was utilised to enable this minima to be found accurately and rapidly.
- With a high accuracy of stress path holding and the SRD-B BRICK routine, reliable prediction of creep was observed. The strain rate during creep was observed to decay smoothly from testing strain rate to the $log(t)$ versus $log(||\dot{\boldsymbol{\varepsilon}}_{\boldsymbol{b}}||)$ trend specified by the equation for TD effects.
- The effects of creep rupture predicted by the BRICK model were shown when the coordinate descent creep routine was used. The creep rupture in the BRICK model was characterised by the strain rate ceasing to decrease. This was in contrast to the increasing strain rates observed for creep rupture in ex-

perimental testing. An increasing strain rate is however not possible in the current implementation of the BRICK model. Up to the point of rupture, the effect of stress on the relationship between creep time and strain rate has been shown to match experimental results. This is shown from comparison of the BRICK model to Bishop (1966) in Figure 5.40 and 5.41 respectively.

- The relationship between q and strain rate shown by the BRICK model demonstrates a region of linear trend between stress and $log(\dot{\varepsilon})$ as suggested by Singh & Mitchell (1968) and shown by Campanella (1965).
- Adding contours of ISE to the BRICK model provided a simple method demonstrating the effects of stress paths on stiffness.
- The experimental program was found to have been insufficient to directly fit a parameter set for the SRD BRICK model. Many parameters had not been measured during the experimental program and just changing those for which a value was know did not produce sensible effects on the output. The large number of parameters also prevented a parametric fitting to the results. For this reason the SRD BRICK model in its current form is not easily applied to industry where any benefits obtained by using the model are outweighed by the difficulty in obtaining reliable parameters.

7.4 Future work

The following topics for potential future work were established:

- The experimental program could be vastly improved if repeated. Firstly the consistency of sample production could be improved by avoiding clogging of the porous drainage disks. As well as investigating the use of smaller stress steps and termination at fixed height or void ratio rather than fixed time. The measurement of the applied stress during consolidation could be improved by more accurate pressure transducers and calibrations that account for bridging effects. The triaxial testing could be made more consistent by improved insulation and temperature control. Improving the data logging system to log multiple readings per second would allow for time averaging for the small strain results. Improving the control software to allow docked creep would permit creep at a variety of stress levels and would eliminate the problematic determination of the docking point. With these changes a repeat of the results would more conclusively demonstrate the trend shown.
- The coordinate descent creep routine would require an extensive optimisation in its run time to be of use outside of academia. The key limit on the computational time is currently the number of times the BRICK model is required to run. This may be reduced by having the path to the solution be straight and

with as few steeps as possible. The results from preceding creep stages may be used to optimise the strain steps used and their orientation to improve this. The strain step reduction factor when no lower points are found could also be optimised through a parametric study.

- The coordinate descent creep routine could be expanded to use all six strain and stress components in the BRICK model. This would allow it to be used in a general sense rather than the set of triaxial conditions currently permitted.
- The increase in strain rates associated with creep rupture in actual testing should be investigated. This has been made possible by the improved creep finding routine.
- A more detailed experimental study on the RCH effect and its influence on multistage testing to properly investigate how the model of RCH from BRICK simulations is observed in physical testing.
- The interplay between RSH and RCH effect has been shown on only a limited number of tests. There is scope to investigate this relationship in detail.
- A full parametric study would be required to fit the BRICK model to the experimental results. If this were done the predictive power of the BRICK simulations would be better established.
- Further study is required to show how finite element modelling with the SRD-B BRICK model compares to that using the SRD BRICK model by Clarke (2009). In this way the impact of the model changes on the real world predictive capacity of the BRICK model can be observed. This would show if the improvements to SRD brick can be usefully applied in geotechnical design and back analysis.

  The improvements made to SRD BRICK as well as the implementation of creep have improved the range of problems that can be run with the model. The

References

Aboshi, H., Matsuda, H. & Okuda, M. (1973). An experimental investigation on the similitude in the consolidation of a soft clay, including the secondary creep settlement., *Proceedings of the 8th International Conference on Soil Mechanics and Foundation Engineering* **4**, 3: 88.

Arulanandan, K., Shen, C. K. & Young, R. B. (1971). Undrained creep behaviour of a coastal organic silty clay, *Geotechnique* **21**, 4: 359–375.

Atkinson, J. (2000). Non-linear soil stiffness in routine design, *Géotechnique* **40**, No. 5: 487–508.

Atkinson, J., Richardson, D. & Stallebrass, S. (1990). Effect of recent stress history on the stiffness of overconsolidated soil, *Géotechnique* **40**, No. 4: 531–540.

Baldi, G., Hight, D. & Thomas, G. (1988). State of the art paper a revaluation of conventional triaxial test methods, *Advanced Triaxial Testing of Soil and Rock*, American Socity for Testing and Materials, Philadelphia, pp. 219–263.

Bishop, A. (1966). The strength of soils as engineering materials, *Géotechnique* **16**, No. 2: 91–130.

Bishop, A. & Wesley, L. (1975). A hydraulic triaxial apparatus for controlled stress path testing, *Géotechnique* **25**: 657–670.

Bishop, A. W., Webb, D. L. & Lewin, P. I. (1965). Undisturbed samples of london clay from the ashford common shaft: strength-effective stress, *Geotechnique* **15**, 1: 1–31.

Bjerrum, L. (1967). Engineering geology of norwegian normally-consolidated marine clays as related to settlements of buildings, *Géotechnique* **17**, No. 2: 81–118.

Black, D. K. & Lee, K. L. (1973). Saturating laboratory samples by back pressure., *ASCE J Soil Mech Found Div* **99**, SM1: 75–93.

Burland, J. & Maswoswe, J. (1982). Insitu measurement of horizontal stress in overconsolidated clay using push-in spade-shaped pressure cells-discussion, *Geotechnique* **32**, 3: 285–286.

Burland, J. & Symes, M. (1982). a simplel axial displacement guage for use in triaxial aperatus, *Géotechnique* **32**, No. 1: 62–65.

Burland, J. B. & Georgiannou, V. N. (1991). Small strain stiffness under generalised stress changes, *Proceedings of the 10th European Conference on Soil Mechanics and Foundation Engineering, ' Deformation of Soils and Displacement of Structures'*, Vol. 1, Florence, Italy, pp. 41–44.

Burland, J. B., Simpson, B. & St. John, H. D. (1979). Movements around excavations in london clay., *Design parameters in geotechnical engineering.Proc.7th European conference on soil mechanics and foundation engineering, Brighton, 1979.Vol.1, (British Geotechnical Society; distributed by T.Telford, London)* pp. 13–29.

Campanella, R. (1965). *Effcet of Temperature and Stress on the Time Defomation Behavior in Saturated Clays*, PhD thesis, University of California, Berkeley.

Cekerevac, C., Laloui, L. & Vulliet, L. (2005). A novel triaxial apparatus for thermo-mechanical, *Geotechnical Testing Journal* **28**, No. 2: 1–10.

Chandler, R. J. & Apted, J. P. (1988). The effect of weathering on the strength of london clay, *Quarterly Journal of Engineering Geologyl* **21**, 1: 59–68.

Clarke, S. (2009). *Enhancement of the BRICK constitutive model to incorporate viscous soil behaviour*, PhD thesis, University of Sheffield.

Clarke, S. D. & Hird, C. C. (2012). Modelling of viscous effects in natural clays, *Canadian Geotechnical Journal* **49**, 2: 129–140.

Clayton, C. I. & Heymann, G. (2001). Stiffness of geomaterials at very small strains, *Géotechnique* **51**, No. 3: 245–255.

Crawford, C. (1965). Resistance of soil structre to consolidation, *Canadian Geotechnical Jornal* **2**, No. 2: 90–115.

Cuccovillo, T. & Coop, M. (1997). The measurement of local axial strains in triaxial tests using lvdts, *Géotechnique* **47**, No. 1: 167–171.

Da Re, G., Santagata, M. & Germaine, J. (2001). Lvdt based system for the measurement of the pre-failure behavior of geomaterials, *Geotechnical Testing Journal* **24**, No. 3: 288–298.

Degago, S. A., Grimstad, G., Jostad, H. P., Nordal, S. & Olsson, M. (2011). Use and misuse of the isotache concept with respect to creep hypotheses a and b, *Geotechnique* **61**, 10: 897–908.

El-Rimawi, J. (1996). *The behaviour of flexural members under fire conditions*, PhD thesis, University of Sheffield.

Ellison, K. C., Soga, K. & Simpson, B. (2012). A strain space soil model with evolving stiffness anisotropy, *Geotechnique* **62**, 7: 627–641.

Ellison, K., Soga, K. & Simpson, B. (2011). A strain space model with evloving stifness anistropy, *(in press)* .

Eshel, G., Levy, G. J., Mingelgrin, U. & Singer, M. J. (2004). Critical evaluation of the use of laser diffraction for particle-size distribution analysis, *Soil Science Society of America Journal* **68**, 3: 736–743.

Finnie, I. & Heller, W. (1959). *Creep Engineering of Materials*, McGraw-Hill Book Co., Inc, New York.

Finno, R. J. & Cho, W. (2011). Recent stress-history effects on compressible chicago glacial clays, *Journal of Geotechnical and Geoenvironmental Engineering* **137**, 3: 197–207.

Gasparre, A. (2005). *Advanced laboratory characterisation of London Clay*, PhD thesis, Imperial College London.

Gasparre, A. & Coop, M. (2006). Techniques for performing small-strain probes in the triaxial apparatus, *Géotechnique* **56**, No. 7: 491–495.

Gasparre, A., Nishimura, S., Minh, N., Coop, M. & Jardine, R. (2007). The stiffness of natural london clay, *Géotechnique* **57**, No. 1: 33–47.

Graham, J., Crooks, J. A. & Bell, A. (1983). Time effects on the stress-strain behaviour of natural clays, *Géotechnique* **33**, No. 3: 327–340.

Hajj, A. (1990). *The simulation of sampling disturbance and its effects on the deformation behaviour of clays*, PhD thesis, University of Sheffield.

Head, K. (1998). *Manual of Soil Laboratory Testing*, Vol. 3, John Wiley and Sons.

Henkel, D. J. (1957). Investigations of two long-term failures in london clay slopes at wood green and northolt, *Proc 4th Int. Conf. Soil Mech* **2**: 315–320.

Hight, D., McMillan, F., Powell, J., Jardine, R. & Allenou, C. (2003). Some characteristics of london clay, *in* T. T.S., K. Phoon, D. Hight & L. S. (eds), *Proc. Conf. Characterisation and Engineering*, Vol. 2, Balkema, National University Singapore, pp. 851–907.

Imai, G. & Tang, Y.-X. (1992). Constitutive equation of one-dimensional consolidation derived from inter-connected tests, *Soils and Foundations* **32**, 2: 83–96.

Jackson, J. & Fookes, P. (1974). relationship of estimated former burial depth of lower oxford clay to some soil properties, *Quarterly Journal of Engineering Geology and Hydrogeology* **7**: 137–179.

Jardine, R. (1992). Some observations on the kinematic nature of soil stiffness, *Soils and Foundations* **32**, No. 2: 111–124.

Jardine, R., Brooks, N. & Smith, P. (1985). The use of electrolevel guages in triaxial tests on weak rock, *Int. J. Rock. Mech. Min. Sci. and Geomech Abstr* **22**, No. 5: 331–337.

King, C. (1981). The stratigraphy of the london clay and associated deposits, *Tertiary Research Special Paper* **6**.

Konert, M. & Vandenberghe, J. (1997). Comparison of laser grain size analysis with pipette and sieve analysis: A solution for the underestimation of the clay fraction, *Sedimentology* **44**, 3: 523–535.

Konovalov, P. A. & Bezvolev, S. G. (2005). Analysis of results of consolidation tests of saturated clayey soils, *Soil Mechanics and Foundation Engineering* **42**, 3: 81–85.

Kuwano, R., Connolly, T. & Jardine, R. (2000). Anisotropic stiffness measurements in a stress-path triaxial cell, *Geotechnical Testing Journal* **23**, No. 2: 141–157.

Ladd, C. C., Foott, R., Ishihara, K., Schlosser, F. & Poulos, H. G. (1977). Stress-deformation and strength characteristics. state-ofthe- art report, *Proc. 9th Int. Conf. Soil Mech. Found. Engng*, Vol. 2, Tokyo, pp. 421–494.

Leroueil, S. & Marques, M. S. (1996). Importance of strain rate and temperature effects in geotechnical engineering, *Geotechnical Special Publication* **61**: 1–60.

Leroueil, S., Kabbaj, M., Tavenas, F. & Bouchard, R. (1985). Stress-strain-strain rate relationship for the compressibility of sensitive natural clays., *Géotechnique* **35**, No. 2: 159–180.

Lo Presti, D. F., Jamoilkowski, M., Pallara, O. & Cavallaro, A. (1996). Rate and creep effect on the stiffness of soils., *Geotechnical Special Publication* **61**: 166–180.

Lo Presti, D. F., Pallara, O., Raino, M. & Maniscalco, R. (1993). A computer-controlled triaxial apparatus- preliminary results, *Rivista Italiana di Geotecnica, in English* .

Mitchell, J. & Campamella, R. (1964). Creep studies on saturated clays, *Laboratory shear testing of soils, ASTM special thechnical pulication No 316*, American Socity for Testing and Materials, Philadelphia, pp. 90–103.

Pantelidou, H. & Simpson, B. (2007). Geotechnical variation of london clay across central london, *Géotechnique* **57**, No. 1: 101–112.

Pierpoint, N. (1996). *The prediction and back analysis of excavation behavior in Oxfrod clay*, PhD thesis, University of Sheffield.

Richardson, A. & Whitman, R. (1963). Effect of strain rate upon undrained shear resistance of a saturated remoulded fat clay, *Géotechnique* **13**, No. 3: 310–324.

Scholey, G., Frost, J., Lo Presti, D. F. & Jamiolkowski, M. (1995). A review of instrumentation for measuring small strains during triaxial testing of soil specimens, *Geotechnical Testing Journall* **18**, No. 2: 137–156.

Shibuya, S., Mitachi, T., Hosomi, A. & Hwang, S. C. (1996). Strain rate effects on stress-strain behaviour of clay as observed in monotonic and cyclic triaxial tests, *Geotechnical Special Publication* , 61: 214–227.

Simpson, B. (1992). Retaining structures: displacement and design, *Géotechnique* **42**, No. 4: 541–576.

Singh, A. & Mitchell, J. (1968). General stress-strain-time function for soils, *Journal of the Soil Mechanics and Foundations Division* **94**, No. 2: 21–46.

Sivakumar, V., Mackinnon, P., Zaini, J. & Cairns, P. (2010). Effectiveness of filters in reducing consolidation time in routine laboratory testing, *Geotechnique* **60**, 12: 949–956.

Skempton, A. W. (1961). Horizontal stresses in an overconsolidated eocene clay, *Proc. 5th Int. Conf. Soil Mech. Found. Engng* **1**: 351–357.

Skempton, A. W. & Henkel, D. J. (1957). Tests on london clay from deep borings at paddington, victoria and the south bank, *Proc 4th Int. Conf. Soil Mech* **1**: 100–106.

Smith, P., Jardine, R. & Hight, D. (1992). The yeilding of bothkennar clay, *Géotechnique* **42**, No. 2: 257–274.

Smith, T. J. (1978). *Consolidation and other geotechnical properties*, PhD thesis, University of Durham.

Soga, K. & Mitchell, J. (1996). Rate-dependent deformation of structured natural clays, *Geotechnical Special Publication* **61**: 243–257.

Sorensen, K. (2006). *Influence of viscosity and ageing on the behaviour of clays*, PhD thesis, University College, London.

Sorenson, K., Baudet, A. & Simpson, B. (2007). Influence of structure on the time-dependent behaviour of a stiff sedimentary clay, *Géotechnique* **57**, No. 1: 113–124.

Tatsuoka, F. (2007). Keynote lecture: Inelastic deformation characteristics of geomaterial, *Soil stress-strain behaviour: measurement, modelling and analysis. Proceedings of the Geotechnical Symposium*, Rome, pp. 1–108.

Tatsuoka, F., Ishihara, M., Di Benedetto, H. & Kuwano, R. (2002). Time-dependent shear deformation characteristics of geomaterials and their simulation, *Soils and Foundations* **42**, No. 2: 531–540.

Tatsuoka, F., Santucci de Magistris, F., Hayano, K., Koseki, J. & Momoya, Y. (2000). Some new aspects of time effects on the stress-strain behaviour of stiff geomaterials., *The Geotechnics of Hard Soil - Soft Rocks, Proc. 2rd Int. Symp. Hard Soils and Soft Rocks*, Balkema, Napoli, pp. 1285–1371.

Taylor, D. (1942). Research on consolidation of clays, *Massachusetts Institue of Technology, Department of Civil and Sanitary Enginering Serial* **82**: 147.

Tuxworth, A. & Clarke, S. (2014). Incorporating tesra behaviour in an advanced constitutive model, *Numerical methods in geotechnical enginering: NUMGE 2014* **1**: 127–132.

Vaid, Y. & Campanella, R. (1977). Time-dependent behaviour of undisturbed clay, *Journal of the Geotechnical Engineering Division* **103**, No. GT7: 693–709.

Viggiani, G. (1992). Dynamic measurement of small strain stiffness of fine grained soils in the triaxial apparatus, *Proc. workshop on experimental characterization and modelling of soils and soft rocks, Napoli* pp. 75–97.

Viggiani, G. & Atkinson, J. (1995). Stiffness of fine-grained soil at very small strains, *Géotechnique* **45**, No. 2: 249–265.

A

Apparatus details

A.1 Calibrations

Tube	Piston	Sensitivity (kPa sample / kPa applied to piston)	Y intercept kPa sample at 0 kPa applied (kPa)	ς_r (pascal)
1	4	4.01	29.00	14.46
2	3	4.06	28.86	31.37

Table A.1: Calibration of loading piston

Tube	1	2
Transducer SN	10143574	10143587
Initial zero (div)	10583	10571
Initial FSD at 5000 kPa (div)	31387	31566
Initial sensitivity (Div/kPa)	4.1608	4.199
Initial Y int (Div at 0 kPa)	10583	10571
Error trend gradient (Pa error/kPa applied)	10.289	3.1748
Error trend intercept (Pa error at 0 applied stress.	-2085	2804.8
Zero (div)	10575.20	10582.25
FSD at 5000 kPa (div)	31592.08	31644.61
Sensitivity (Div/kPa)	4.203	4.212
Y int (Div at 0 kPa)	10575.204	10582.255
ς_r (Pa)	9244	5633

Table A.2: PWP calibration

Tube	1 Base	1 Top	2 Base	2 Top
Transducer SN	149236	149238	175154	175152
Zero (div)	-753	-163	4	-7
FSD (value)	3000	3000	2799.9	2799.9
FSD (div)	18780	19683	20632	17843
	Calibration prior to 16/08/2012		Calibration for test C2	
Zero (div)	-741.00	-226.00	200	262
FSD (value)	3000	3000	2799.9	2799.9
FSD (div)	19786	19828	20632	17843

Table A.3: EPC calibration

Cell	1	1	1	2	2	2
Transducer	Axial 1	Axial 2	Radial	Axial 1	Axial 2	Radial
S/N	149968	149970	50954	149967	149969	50953
Sensitivity $\mu\mathrm{m\,mV^{-1}}$)	-0.223	-0.223	-0.174	-0.222	-0.222	-0.178
Offset (μm at 0 mV)	-2.49	2.15	-1.68	6.98	-5.18	0.296
ς_r (μm)	1.8517	2.5081	3.5229	1.2419	1.7992	1.1241
Error between readings. (mean of SD at point) (μm)	1.1398	0.675	0.5384	0.8731	1.2303	0.4672
Error over time (Mean of SD at point) (μm)	0.0518	0.0374	0.0303	0.0366	0.0595	0.0292

Table A.4: LVDT calibration summary

	Cell Pressure		Back Pressure	
Cell number	1	2	1	2
Manufacturer	Maywood Instruments		DRUCK Ltd	
Model	P-102 500 PSI g		PDCR 810 7 bar g 10 volts	PDCR 810 10 bar 10 volts
SN	84642	84647	320409	436855
Sensitivity ($\mathrm{kPa\,mV^{-1}}$)	17.1819	17.1434	-4.4312	-6.6277
Zero (kPa at 0 mV)	23.5282	20.5907	10.4274	-4.4803
Standard error of calibration	907.73	324.74	398.82	2559.66

Table A.5: Pressure transducer calibrations

Cell number	1	2
Manufacturer	Applied Measurements	
Model	STALC3 -15Kn	
SN	25992	25991
Sensitivity (N/mV)	700.0900	689.0292
Zero (N at 0 mV)	835.6088	40.2659
ς_r (N)	39.031	79.75

Table A.6: Load cell calibration

A.2 Sample preparation details

Sample	Tube used	Fill height (mm)	Comments
O1	1	168	Short sample using low loading pattern
S1	1	599	
S2	1	544	
C1	1	544	
C2	1	530	
O2	2	544	Formally RC1a
RC1b	1	530	
RC2a	2	544	Extended 1d consolidation due to errors
RC2b	1	544	Extended 1d consolidation due to errors
RC3/RA1	2	544	
RC4	1	542	
RA2	1	542	
RA3	2	541	
RA4	1	545	
HOCR	2	544	Long duration consolidation stage
RC1a	1	554	
HRSH	2	544	
CU1	1	541	
CU2	1	543	Re-batched London clay
CU3	2	544	Re-batched London clay

Table A.7: Samples preparation

B

Data processing code

B.1 Docking point selection

B.1.1 Boxes code

```
function [CENTRESX,CENTRESY,boxextents,GRADXPLOT,GRAD]=...
    Boxes5(DISPLACEMENT,TIME,Direction,fig)
Colours={'r','b','g','y','m','c','k'};%colour order for ploting
res=1e-4;                              %specify the resolution
%-------------------INCREASING ROUTINE--------------------
if Direction>0
    boxlow(1)=min(DISPLACEMENT);
    boxhigh(1)=min(DISPLACEMENT(DISPLACEMENT>boxlow(1)+0.5*res));
    %the box goes up to the point at least 0.5 res above the
    %minimum
    boxextents=[1,1]; %set up box extents [start,end] for 1st box.
    a=1;
    %continue while the upper limit is not at the maximum
    while a<=max(size(TIME));
        %First point to stratify boxlow.
        LOOKBEYOND=find(DISPLACEMENT==boxlow(a),1,'first');
        %Must also increase from the start point by at least 1
        LOOKBEYOND=max(LOOKBEYOND,boxextents(a,1)+1);
        %See when transition occurs last point to be at lower
        %bound
        TRANSLOW=find(DISPLACEMENT==boxlow(a),1,'last');
        if isempty(TRANSLOW)
            TRANSLOW=max(size(TIME)); %last data value if empty.
        end
        TRANSHIGH=find(DISPLACEMENT(LOOKBEYOND:end)>boxhigh(a)...
            ,1,'first')-1+LOOKBEYOND-1; %First point to exceed
                                        %upper bound -1
        if isempty(TRANSHIGH)
```

```
            TRANSHIGH=max(size(TIME));
            %make last data value if empty.
        end
        %Only consider data beyond the first point to satisfy
        %boxlow. need to add the number of rows not considered at
        %the beginning.
        TRANSROW=min(TRANSLOW,TRANSHIGH); %transition at 1st point
        if TRANSROW>=max(size(TIME)); %Break the loop if
            %transition row is greater than the size of the data
            boxextents(a,2)=max(size(TIME)); %end box
            boxextentsTIME(a,:)=TIME(boxextents(a,:)); %In time
            a=a+1;%increase counter
            break
        end

        boxextents(a,2)=TRANSROW; %end box at the transition row.
        boxextentsTIME(a,:)=TIME(boxextents(a,:)); %In time
        %start new box
        boxextents(a+1,1)=TRANSROW+1;%new box at transition row +1

        if TRANSLOW==TRANSROW %if transition on the lower bound
            boxlow(a+1)=min(DISPLACEMENT( (DISPLACEMENT>...
               boxlow(a)) & TIME>=(TIME(TRANSROW)) ));
            %minimum of everything higher than previous low i.e.
            %next low point that is also beyond the transition
            %point.
        else
            boxlow(a+1)=boxlow(a);
            %No change if transition not lower
        end

        if TRANSHIGH==TRANSROW %if a transition on the higher
            %bound given that the transition is set at the point
            %before an increase aplly the increase to the point
            %after transition.
            boxhigh(a+1)=DISPLACEMENT(TRANSHIGH+1);
        else
            boxhigh(a+1)=boxhigh(a); %do not change if not higher
        end
        a=a+1;%increase counter
    end
else
    %------------------DECREASING ROUTINE-----------------------
```

A repeat of the increasing routine inverted for decreasing data.

```
%--------------------------TRIMING-------------------------------
figure(fig)
hold off
plot(TIME,DISPLACEMENT)
hold all
for b=1:a-1;
    %Trim box to contents in box
    boxlowtrim(b)=max(min(DISPLACEMENT(boxextents(b,1):...
        boxextents(b,2))),boxlow(b)); %Use maximum of box low and
            %trimmed boxlow i.e. trimming cannot pull start down.
    boxhightrim(b)=min(max(DISPLACEMENT(boxextents(b,1):boxextents...
        (b,2))),boxhigh(b)); %Use minimum of box high and trimmed
        %box high. i.e. trimming cannot push start up.
    %plot trimmed boxes
    figure(fig)
    fill([boxextentsTIME(b,1),boxextentsTIME(b,1),...
        boxextentsTIME(b,2),boxextentsTIME(b,2)],[boxlowtrim(b)...
        -0.1*res,boxhightrim(b)+0.1*res,boxhightrim(b)+0.1*res,...
        boxlowtrim(b)-0.1*res],Colours{rem(b,6)+1})
end
figure(fig)
plot(TIME,DISPLACEMENT)

%Add a plot connecting the box centres
CENTRESX=mean(boxextentsTIME,2);
CENTRESY=(boxlowtrim+boxhightrim)/2;
CENTRESY=CENTRESY';

figure(fig)
plot(CENTRESX,CENTRESY);
xlabel('Time(s)')
ylabel('Displacement (mm)')
title('Box fitting algorithm trimmed')

%Gradient of the lines between centres
GRAD=diff(CENTRESY)./diff(CENTRESX);
GRAD=GRAD*60; %covert in to mm/min.
GRAD=GRAD*(200/70); %rough scaling to the approximate whole
%sample displacement rate.
GRADXPLOT=(CENTRESX(2:end)+CENTRESX(1:end-1))/2;

figure(fig+1)
hold off
plot(GRADXPLOT,GRAD);
title('Box fitting algorithm trimmed centre difference rates')
xlabel('Time (s)')
ylabel('Displacement rate (mm/min)')
```

B.2 Refinement

B.2.1 SpapsNew code

Due to the large data matrixes involved an out of memory error was occurring on a regular basis. This error was the result of transformation of a 5 line diagonal space matrix to a sparse matrix with a value in each element. This was the result of a division by zero which resulted in the value Inf. As 0*Inf =NaN all zero elements became NaN rather than 0 so are no longer sparse. The problem results from the error measure E not changing since the previous occasion. The approach taken is to add a reference to the previous error E0. If the error is at the previous value the control parameter rho is changed by the change in rho delrho again until the error changes. The relevant code section is shown below winch replaces line 358 to 380 in Revision: 1.30.4.4 of spaps.m the smoothing spline routine in Matlab.

```
if tol<0      % we are to work with a specified rho
    rho = -tol;
    u = (ctwic + rho*A)\cty; ymf = wic*u; values = (yi - ymf).';
else          % determine  rho  from the tolerance requirement
    u = ctwic\cty; ymf = wic*u; E = trace(u'*Ct*ymf);
    E0=E;
    if E<tol
        values = (yi - ymf).'; rho = 0;
        sp = spmak(augknt(xi([1 n]),m), values(:,ones(1,m)));
        must_integrate = 0;
    else
        oost = 1/sqrt(tol); g0 = 1/sqrt(E) - oost;
        rho = -g0*E*sqrt(E)/trace(u'*A*u); delrho = rho;
        count=0;
        while ~isnan(rho) && (rho-(rho+delrho))~=0
            count=count+1;
            u = (ctwic + rho*A)\cty; ymf = wic*u;
            E = trace(u'*Ct*ymf);
            count2=0;
            while E==E0; %if the error is unchanged. which would
                %cause delrho = inf on the next calculation of delrho
                rho = rho+delrho; %apply the increase in rho again
                %Recalculate E
                u = (ctwic + rho*A)\cty; ymf = wic*u;
                E = trace(u'*Ct*ymf);
                %This can take a long time to execute if
                %circumstances are bad added code to double rho
                %after 1000 iterations, breaking results in
```

```
                %memory error as allows E to remain at E0
                count2=count2+1;
                if count2>1000, rho=rho*2;  end
            end
            if 100*abs(E-tol)<tol, break, end
            grho = 1/sqrt(E) - oost;
            delrho = delrho/(g0/grho-1);
            g0 = grho; rho = rho+delrho;
            E0=E;
        end
        values = (yi - ymf).';
    end
end
```

B.3 Smoothing

B.3.1 Biline code

```
function [qOut,MINSSE,TRANSITIONSTRAIN,stiff]=...
    BiLineCalc(Strain,q,transratios)
%Covert the stress strain to a 2 line solution.
a=0;
%preassign for speed
amax=max(size(transratios));
FittedqOUT=cell(amax,1);
stiff=cell(amax,1);
SSE=ones(amax,1);
transratioUsed=ones(amax,1);

for transratio=transratios
    a=a+1;
    rowsset1=find(Strain<transratio*max(Strain));
    rowsset2=find(Strain>=transratio*max(Strain));

    strainset1=Strain(rowsset1);
    qset1=q(rowsset1);
    strainset2=Strain(rowsset2);
    qset2=q(rowsset2);

    fitset1=polyfit(strainset1,qset1,1); %coefficients for Mx +C
    fitset2=polyfit(strainset2,qset2,1); %coefficients for Mx +C
    %calculate the strain at the intercept of the equations
    IntX=(fitset2(2)-fitset1(2))/(fitset1(1)-fitset2(1));
    rowseq1=find(Strain<IntX);
```

```
    rowseq2=find(Strain>IntX);              %calculate the output
    %based on eq1 below intercept and eq 2 above.

    FittedqOUT{a}=zeros(size(Strain));
    FittedqOUT{a}(rowseq1)=Strain(rowseq1)*fitset1(1)+fitset1(2);
    %calculate q for points in set 1
    FittedqOUT{a}(rowseq2)=Strain(rowseq2)*fitset2(1)+fitset2(2);
    %calculate q for points in set 2
    stiff{a}(rowseq1)=fitset1(1)*100/3;
    %gradient of stress vs. strain %
    stiff{a}(rowseq2)=fitset2(1)*100/3;
    ERRORq=FittedqOUT{a}-q;
    SSE(a)=sum(ERRORq.^2);
    transratioUsed(a)=transratio;
end

[MINSSE,IND]=min(SSE);
TRANSITIONSTRAIN=transratioUsed(IND)*max(Strain);
%transition strain
qOut=FittedqOUT{IND};
stiff=stiff{IND}; %select the stiffness for the correct index
```

B.3.2 Ramberg-Osgood code

```
function [stressout,strainout,stiffout,ROfit,ROstats]...
    =ROfitting(Strain,q);
%model outputs strain from stress so stress on x axis
direction=mean(q)/abs(mean(q)); %gives -1 if stress is decreasing

%data fitted on absolute values
x=abs(q);
y=abs(Strain);

%create fit object
%create options
ROopts = fitoptions('Method','NonlinearLeastSquares',...
               'Lower',[0,0,0,0],...
               'Upper',[Inf,Inf,Inf,Inf],...
               'Startpoint',[1,1,1,1]);
%create fit object
ROfittype=fittype('(x/A)+B*(x/C)^n','options',ROopts);
[ROfit,ROstats] = fit(x,y,ROfittype);

%% data from cfit object
Coeffs = coeffvalues(ROfit);
```

```
A=Coeffs(1);
B=Coeffs(2);
C=Coeffs(3);
n=Coeffs(4);

NoPs=size(q,1); %number of points
stressout=linspace(0,max(abs(q)),NoPs);
stressout=stressout'; %convert to column vector
strainout=(stressout./A)+B.*(stressout./C).^n;

%Correct for direction
stressout=direction*stressout;
strainout=direction*strainout;

%Calculate stiffness
stiffout=1./((1/A)+(n*B/C).*(stressout./C).^(n-1));
%stiffness is expressed as dq/ deq(%) needs to be converted to
%stiffness.
stiffout=(stiffout*100)/3;
```

B.3.3 Bootstrap code

```
function [StressOUT,StressOUT10,StressOUT90,StiffOUT,StiffOUT10...
    ,StiffOUT90]=LimBS2(strain,q,qspace,bootstraps,refstrain)
%limited point of strain q plot at q spacing of qspace with
%bootstraps fold bootstrapping.

numpoints=ceil((max(q)-min(q))/qspace);
%calculate section bounds approximately q space wide
Sectionbounds=linspace(min(q),max(q),numpoints+1);
%set q at NaN start and end to avoid errors when start or end
%point selected at random
qmod=q;
qmod(1)=NaN;
qmod(end)=NaN;
%preassign for speed
SampleIndex=ones(numpoints+2,bootstraps);
Stressfits=zeros(max(size(strain)),bootstraps);
Stiff=zeros(max(size(strain)),bootstraps);
for b=1:bootstraps
    for a=2:size(Sectionbounds,2)
        Indexlist=find(qmod>Sectionbounds(a-1)&...
            qmod<Sectionbounds(a)); %indexes of points in section
        SampleIndex(a,b) = randsample(Indexlist,1);
    end
```

```
    SampleIndex(size(Sectionbounds,2)+1,b)=size(q,1); %set end
                                                %index at the end
    %Sort all the sample indexes by strain
    [~,SORTIND]=sort(strain(SampleIndex(:,b)));
    SampleIndexcol=SampleIndex(:,b);
    SampleIndex(:,b)=SampleIndexcol(SORTIND);
    splinestrain=strain(SampleIndex(:,b));

    [splinestrain,IND,~]=unique(splinestrain); %remove repeats
    splineQ=q(SampleIndex(:,b));
    splineQ=splineQ(IND); %remove the repeated points from Q

    splineeq=spline(splinestrain,splineQ);%spline fit to a ppform
    splineeq=fnxtr(splineeq);              %extrapolate correctly

    %evaluate at refstrain points
    Stressfits(:,b)=fnval(splineeq,refstrain);
    stiffeq=fnder(splineeq);          %differentiate to stiffness
    Stiff(:,b)=fnval(stiffeq,refstrain)*100/3; %Adjust the
    %stiffness calculation
end
%stress
StressOUT=median(Stressfits,2); %stress out Median
StressOUT10=prctile(Stressfits,10,2) ;%10 percentile
StressOUT90=prctile(Stressfits,90,2)    ;%90 percentile

%stiffness
StiffOUT=median(Stiff,2);     %stiffness out Median
StiffOUT10=prctile(Stiff,10,2)    ;%10 percentile
StiffOUT90=prctile(Stiff,90,2)    ;%90 percentile
```

C

Experimental data

	O1B	O1T	O2B	O2M	O2T	S1B	S1T	Mean
0-50	-0.208	-0.113	-0.129	-0.038	0.020	0.028	0.063	-0.054
50-100	0.135	0.131	0.011	0.010	0.015	0.019	0.001	0.046
100-200	0.189	0.169	0.007	0.066	0.007	-0.033	0.026	0.062
200-300						0.046	0.068	0.057
200-400	0.179	0.187	0.088	0.101	0.066			0.124
300-400						0.054	0.067	0.060
400-800	0.157	0.155	0.074	0.122	0.083	0.061	0.069	0.103
800-1600	0.084	0.084	0.051	0.056	0.058	0.058	0.059	0.064
1600-2200						0.042	0.043	0.043
1600-2600					0.046			0.046
1600-2800	0.046	0.045	0.038	0.046				0.044
2200-2800						0.033	0.035	0.034

Table C.1: m_v values from oedometer tests ($\mathrm{m^2\,MN^{-1}}$)

	O1B	O1T	O2B	O2M	O2T	S1B	S1T	Mean
50-100	0.238	0.169						0.203
100-200	0.192	0.128		0.129				0.149
200-300						0.268	0.268	0.268
200-400	0.233	0.132	0.421	0.071	0.112			0.194
300-400						0.151	0.157	0.154
400-800	0.138	0.060	0.352	0.052	0.139	0.240	0.281	0.180
800-1600	0.124	0.058	0.327	0.260	0.106	0.150	0.203	0.175
1600-2200						0.066	0.096	0.081
1600-2600					0.083			0.083
1600-2800	0.107	0.058	0.211	0.066				0.111
2200-2800						0.055	0.087	0.071

Table C.2: c_v values from oedometer tests sqrt method ($\mathrm{m^2\,yr^{-1}}$)

	O1B	O1T	O2B	O2M	O2T	S1B	S1T	Mean
50-100	0.483	0.374						0.429
100-200	0.268	0.174						0.221
200-300						0.551	0.431	0.491
200-400	0.233	0.145	0.362	0.060	0.100			0.180
300-400						0.132	0.150	0.141
400-800	0.138	0.067	0.365		0.187	0.193	0.265	0.203
800-1600	0.122	0.055	0.261	0.223	0.100	0.158	0.199	0.160
1600-2200						0.058	0.085	0.071
1600-2600					0.071			0.071
1600-2800	0.123	0.059	0.188	0.050				0.105
2200-2800						0.046	0.069	0.058

Table C.3: c_v values from oedometer tests log method ($\mathrm{m^2\,yr^{-1}}$)

	O1B	O1T	O2B	O2M	O2T	S1B	S1T	Mean
50-100	9.976	6.817						8.397
100-200	11.217	6.723		2.622				6.854
200-300						3.778	5.658	4.718
200-400	12.946	7.628	11.497	2.226	2.275			7.314
300-400						2.513	3.242	2.878
400-800	6.693	2.913	8.059	1.976	3.576	4.524	6.052	4.827
800-1600	3.238	1.515	5.208	4.476	1.896	2.678	3.705	3.245
1600-2200						0.854	1.287	1.070
1600-2600					1.170			1.170
1600-2800	1.527	0.820	2.523	0.950				1.455
2200-2800						0.571	0.938	0.754

Table C.4: k values from oedometer tests sqrt method ($\mathrm{pm\,s^{-1}}$)

	O1B	O1T	O2B	O2M	O2T	S1B	S1T	Mean
50-100	20.289	15.148						17.719
100-200	15.724	9.118						12.421
200-300						7.773	9.099	8.436
200-400	12.946	8.382	9.879	1.878	2.023			7.022
300-400						2.191	3.093	2.642
400-800	6.693	3.233	8.358		4.824	3.650	5.712	5.412
800-1600	3.186	1.432	4.164	3.835	1.800	2.829	3.621	2.981
1600-2200						0.753	1.139	0.946
1600-2600					1.008			1.008
1600-2800	1.755	0.836	2.240	0.715				1.386
2200-2800						0.479	0.745	0.612

Table C.5: k values from oedometer tests log method ($\mathrm{pm\,s^{-1}}$)

D

Introduction of TESRA to BRICK model

Numerical Methods in Geotechnical Engineering – Hicks, Brinkgreve & Rohe (Eds)

Incorporating TESRA behaviour in an advanced constitutive model

A.J. Tuxworth & S.D. Clarke
Department of Civil and Structural Engineering, The University of Sheffield, Sheffield, UK

ABSTRACT: The Strain Rate Dependent (SRD) BRICK model (Clarke and Hird 2012) is a constitutive model based on BRICK (Simpson 1992) modified to incorporate Isotach behaviour. BRICK is formulated within strain space and approximates the stiffness degradation curve of a soil in a stepwise manner. SRD BRICK varies the shape of this degradation curve depending upon the magnitude of the applied strain rate. This produces a unique relationship between applied strain rate and stress level known as Isotach behaviour (Tatsuoka et al. 2002). The Isotach model has been shown to have wide application to the analysis of natural clays. In some reconstituted clays and sands however the soil response is temporary with the stresses returning to their previous level after a change in strain rate. In this paper a new set of laws is introduced into SRD BRICK to incorporate TESRA behaviour and simulations of previous work are presented.

1 INTRODUCTION

It is generally accepted that the behaviour of a soil is dependent upon the rate at which it is strained. The effects of strain rate can be measured by shearing different samples at different constant rates of strain (CRS) or a single sample at a stepped rate of strain (SRS) and interpolating between sections at the same strain rate. For SRS tests to be used an Isotach model of rate effects must be assumed.

The Isotach concept describes behaviour where the stress state during both creep and shearing is uniquely defined by the current strain and its strain rate (Leroueil et al. 1985). There exists a wealth of experimental data to confirm the presence of Isotach behaviour. A review of literature by Sorensen (2006) concluded that most soft clays in both undisturbed and reconstituted states, undisturbed natural stiff clays and some soft rocks, show Isotach viscous behaviour.

Work by Soga & Mitchell (1996) on one dimensional compression and Graham et al. (1983) on triaxial compression showed a linear relationship between stress and the logarithm of strain rate at the criterion point used. This forms the basis of several equations used to describe Isotach behaviour (Graham et al. 1983, Soga and Mitchell 1996, Tatsuoka et al. 2002, Sorensen 2006).

The Temporary Effects of Strain Rate and Acceleration (TESRA) model is relevant to soils which exhibit a temporary effect of change in strain rate which decays with further strain (Tatsuoka et al. 2002). Where the increase in stress caused by a change in strain rate decays over time to a reference CRS curve that is considered to be independent of strain rate.

In the current work, the TESRA effect is achieved by applying a decay function to the equation used to determine the viscous effect which reduces the viscous effect with further strain. For clarity the term Pure TESRA is used to distinguish from General TESRA behaviour where Isotach behaviour is observed at small strains and TESRA at large strains. This is implemented by increasing the TESRA effect parameter as a function of strain.

2 SRD BRICK MODEL

2.1 *BRICK model*

The Strain Rate Dependent (SRD) BRICK model (Clarke and Hird 2012) used as basis for this work is a variation on the BRICK model (Simpson 1992). BRICK is most readily explained using an analogue of a man walking around a room and dragging a series of bricks tied to him with separate strings of differing lengths. The bricks represent portions of soil while the strings indicate strain occurring before that soil portion strains plastically. The room represents strain space with axes of volumetric and shear strain. Movement of the man though this strain space represents the strain applied to the soil. Initially all strings are slack and no bricks move, hence all the strain is elastic. With increasing strain a string will become taught the attached brick will move and the portion of soil it represents strains plastically. As more bricks move a greater portion of the strain becomes plastic and the soil stiffness decreases. This stiffness degradation is represented by a stepped S-shaped stiffness curve in the BRICK model as shown in Figure 1. Only elastic strains are used to calculate stress changes however provision is made for stress levels to increase in full plastic consolidation.

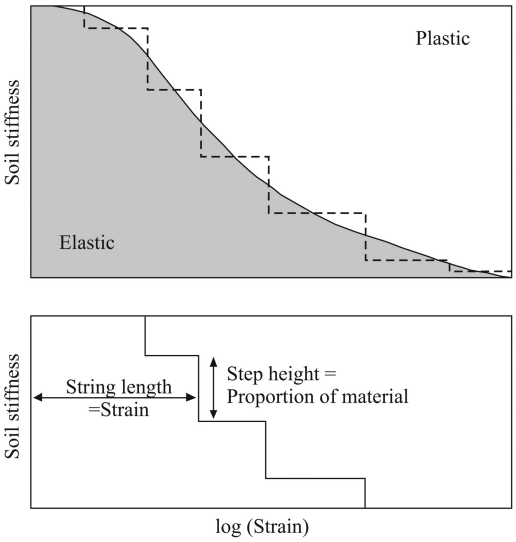

Figure 1. Stiffness degradation represented in stepwise fashion (after Simpson (1992)).

2.2 *Strain rate dependence*

Introducing strain rate dependent behaviour relies on string length being proportional to strength in BRICK. Equations developed to show strain-rate dependent strength can be used to govern string lengths. Work linking the undrained shear strength of a clay soil to applied strain rate by Graham, Crooks, & Bell (1983) was adapted to string lengths by Sorensen (2006) to give:

$$SL = SL_{ref}\left[1+\beta\ln\left(\frac{|\dot{\varepsilon}|}{\dot{\varepsilon}_{ref}}+1\right)\right] \quad (1)$$

where SL is string length SL_{ref} is a reference string length, β is rate sensitivity coefficient (Tatsuoka 2005), $\dot{\varepsilon}$ is strain rate and, $\dot{\varepsilon}_{ref}$ is reference strain rate. Equation 1 is calculated for each brick separately and the rate $\dot{\varepsilon}$ is the magnitude of the brick strain vector. The brick-led approach allows different portions of the soil to strain at different rates crucial for modelling complex behaviour.

2.3 *Control of strain rate reduction*

Allowing a rapid reduction in string length upon a change of strain rate precludes modelling of creep and stress relaxation. Therefore a limit to the maximum rate of strain rate reduction is derived from work by Singh & Mitchell (1968) on the natural decay of strain rate with time under constant stress conditions.

$$\dot{\varepsilon} = \dot{\varepsilon}_1\left(\frac{t_1}{t}\right)^m \quad (2)$$

where $\dot{\varepsilon}_1$ is the strain rate at an arbitrary time t_1, t is the current time and m is the negative slope of the relation between logarithm of strain rate and logarithm of time. In the SRD BRICK model used an arbitrary upper time limit of 10^9 s or roughly 31 years and 8 months is used as t_1. A rate A of $1e^{-12}$ and coefficient m of 0.888 fit Equation 2 to data from Bishop (1966). The actual implementation into the incremental BRICK routine (Simpson 1992) is complicated by the lack of time base. The interaction of string length, strain rate and time is used to derive the current time from the previous string length and the time increment as described in detail by Clarke & Hird (2012).

3 TESRA IMPLEMENTATION

3.1 *Theoretical model*

The implementation of TESRA behaviour into BRICK is based on a modification of the method proposed by Sorensen (2006). The calculation of SL is redefined as Equation 3. $\dot{\varepsilon}_n$ is a movable 'neutral' strain rate that tends towards the applied strain rate in TESRA conditions. SL_u is the unique set of string lengths that are returned to when $\dot{\varepsilon}_n = \dot{\varepsilon}$.

$$SL = SL_u\left[1+\beta\times\ln\left(\frac{|\dot{\varepsilon}|}{\dot{\varepsilon}_n}\right)\right] \quad (3)$$

The string lengths SL_u are set using Equation 1 where the strain rate used is set $\dot{\varepsilon} = \dot{\varepsilon}_u$ the unique strain rate. Conceptually SL_u is the set of string lengths attained by a constant rate of strain (CRS) stress path at rate $\dot{\varepsilon}_u$.

The trend of the neutral strain rate towards the applied strain rate is also given by Sorensen (2006) as:

$$\frac{\delta\dot{\varepsilon}_n}{\delta\varepsilon} = A[\dot{\varepsilon}-\dot{\varepsilon}_n] \quad (4)$$

The TESRA effect is controlled by the parameter A which controls the rate of convergence of the neutral rate with the applied rate. When $A = 0$ the neutral rate does not move giving Isotach behaviour. When A is high the neutral strain rate moves to the applied rate and so negates any increase caused by a change of rate. Using a constant value of A is the so called Pure TESRA behaviour where effects of rate increase are temporary throughout. It was observed by Tatsuoka, Ishihara, Di Benedetto, & (2002) that some soils exhibit Isotach behaviour at low strains and transition to TESRA at higher strains. This General TESRA case is handled by tying the parameter A to the strain level. The equation used derived again from Sorensen (2006) is:

$$A(\varepsilon_d) = A_f\left[1-e^{-\frac{1}{c}\varepsilon_d}\right] \quad (5)$$

where A_f and c are constants and ε_d is the strain from a suitable datum. The need for taking the strain from a datum is due to the requirement to model the whole

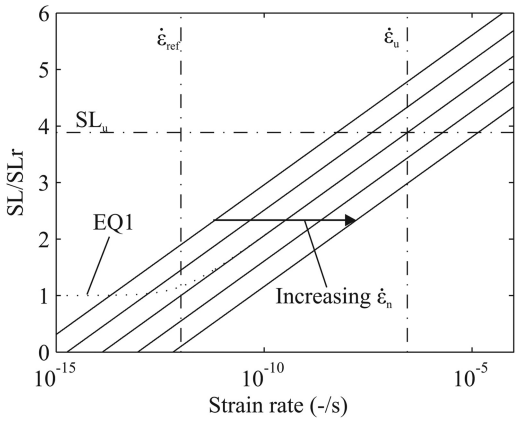

Figure 2. String lengths calculated by TESRA using Equation 3 and 6.

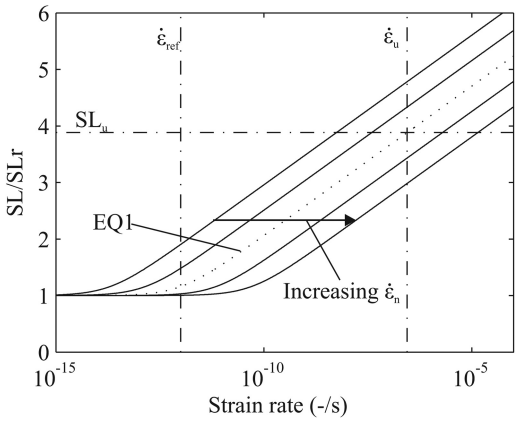

Figure 3. String lengths calculated by TESRA using Equation 7 and 8.

geological history of a soil in the BRICK model. If the large strains occurring in the consolidation stages where to be included it is impossible to fit the degradation of the A parameter to occur over the relatively small strain of a simulated test. Using a very small c parameter allows the formulation to revert to Pure TESRA behaviour.

3.2 *Brick implementations*

The original implementation used Equation 3 to control the string lengths. In order for this to function however the constant β requires adjustment:

$$\beta_{ad} = \frac{\beta}{SL_u} \tag{6}$$

where β_{ad} is the adjusted value of β. This was required as the change of the reference point resulted in a change to the angle of the SL vs. $\ln(\dot{\varepsilon})$ trend. This original formulation however had the problem that a string length below SL_{ref} could be generated. Figure 2 shows that if the neutral strain is higher than the unique strain rate this could occur at rates above the reference rate and cause problems with the stability of the BRICK routine.

A new formulation was devised to shift the SL vs. rate trend on the rate axis only and maintain the minimum at SL_{ref}. A new reference rate $\dot{\varepsilon}_T$ is introduced and Equation 1 reformulated:

$$SL = SL_{ref}\left[1 + \beta \ln\left(\frac{|\dot{\varepsilon}|}{\dot{\varepsilon}_T} + 1\right)\right] \tag{7}$$

It is defined that for the TESRA model when $|\dot{\varepsilon}| = \dot{\varepsilon}_n$then $SL = SL_u$. Solving Equation 7 for $\dot{\varepsilon}_T$ at this point:

$$\dot{\varepsilon}_T = \frac{|\dot{\varepsilon}_n|}{e^{\frac{\left(\frac{SL_u}{SL_{ref}}\right)-1}{\beta}} - 1} \tag{8}$$

By using Equation 7 and 8 the string length can be calculated for any neutral strain rate and will not drop below SL_{ref} (Fig. 3).

The neutral strain rate calculation can be rearranged from Equation 8 to an explicit calculation:

$$\dot{\varepsilon}_n = \frac{\dot{\varepsilon}_{n,prev} + \delta\varepsilon \times \dot{\varepsilon}}{1 + \delta\varepsilon \times A} \tag{9}$$

This calculates the rate based $\dot{\varepsilon}_{n,prev}$ the neutral strain rate in the previous increment, the factor A, the current strain rate $\dot{\varepsilon}$ and the strain change $\delta\varepsilon$. All the strains and strain rates are the magnitude of the strain vectors used in the BRICK routine.

3.3 *Brick-led vs. man-led neutral strain rate*

There are two options for the migration of the neutral strain rate: man-led where the neutral strain rate approached the strain rate applied to the whole of the soil. Brick-led when the neutral strain rate approaches the strain rate of the portion of soil represented by the current brick. The implementation of the man-led approach is straight forward as $\delta\varepsilon$ and $\dot{\varepsilon}$ are input parameters to the BRICK routine. The brick-led approach is complicated as the brick strain rate $\dot{\varepsilon}_b$ and brick strain increment $\delta\varepsilon_b$ are controlled by:

$$SL = T - \delta\varepsilon_b \tag{10}$$

where T is the strain distance between the brick at the beginning of a increment of the BRICK routine and the man at the end of the increment and SL is the string length. As each increment has a fixed duration t the brick strain rate is defined:

$$\delta\varepsilon_b = \dot{\varepsilon}_b \times t \tag{11}$$

Using $\delta\varepsilon_b$ and $\dot{\varepsilon}_b$ in Equation 7 and 8 makes SL dependent on $\delta\varepsilon_b$. An existing bisecting iteration used

to find $\dot{\varepsilon}_b$ that satisfies Equation 1 and 10 simultaneously for the Isotach code formulation is reused. Given Equation 11 the solution for $\dot{\varepsilon}_b$ also provides $\delta\varepsilon_b$ and allows the calculation of $\dot{\varepsilon}_n$ for each brick.

4 ISOTACH BEHAVIOUR WITH THE TESRA MODEL

In order to confirm that Isotach behaviour can be simulated with the TESRA model. A simulation of Sorenson, Baudet, & Simpson (2007) test S1LC for an intact London Clay was performed using the parameters and assumptions form Clark & Hird (2012) detailed in Table 1. The test modelled a 1D consolidation to $p_{max} = 2000$ kPa, swelling to $p_{swell} = 285$ kPa, before application of an set of undrained shear stages detailed in Table 2. The model was run in both the TESRA SRD formulation and original SRD formulation (Clarke 2009).

The results shown in Figure 5 show a close match between the TESRA SRD and original SRD model as well as a similar form to the original data in Figure 4. The smother transitions on change of strain rate observed are the result of other model improvements beyond the scope of this paper.

Table 1. Isotach BRICK model parameters.

Parameter	Value	Parameter	Value
λ	0.1	t_1	10^8
κ	0.02	$\dot{\varepsilon}_1$	$1e^{-13}$
ι	0.0029	$\dot{\varepsilon}_{ref}$	$1e^{-13}$
m	0.936	β	0.23

Table 2. Isotach test strain rates.

Isotach		TESRA	
Shear Strain rate %/h	Shear Strain limit %	Axial strain rate %/h	Axial Strain limit %
0.05	0.58	0.05	0.10
Unload Reload	–	0.90	0.32
0.80	0.68	0.05	1.00
0.05	0.80	0.20	1.16
0.80	0.92	0.90	1.50
0.2	1.02	0.05	2.00
0.05	1.11	0.90	2.50
0.80	1.34	0.05	3.40
Unload Reload	–	0.90	4.40
0.80	1.63	0.05	6.60
0.05	2.31	0.90	8.80
Unload Reload	–	Stress Relax	8.80
0.80	2.73	0.90	9.50
0.20	2.91		
0.05	3.00		

5 TESRA BEHAVIOUR

5.1 *Test set-up*

A simulation of Sorenson et al. (2007) test S1LCrA2 for a reconstituted London Clay was performed using the parameters in Table 3. The test modelled a 1D consolidation to $p_{max} = 90$ kPa, swelling to $p_{swell} = 10$ kPa, a release of any shear stress and a isometric consolidation to $p_{test} = 300$ kPa. The set of undrained shear stages detailed in Table 2 were then applied to mirror the SRS path shown in Figure 6. The calibration

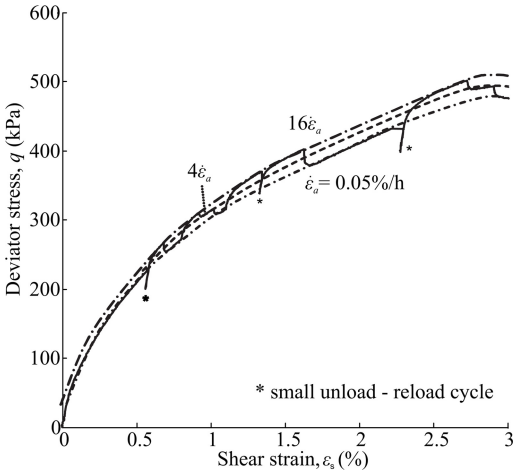

Figure 4. Strain rate behaviour of normally consolidated London Clay (after Sorenson, Baudet, & Simpson (2007)).

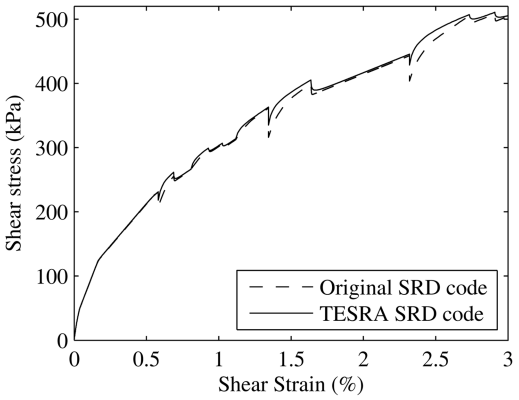

Figure 5. Comparison of SRD and TESRA SRD codes in modelling Isotach behaviour.

Table 3. TESRA BRICK model parameters.

Parameter	Value	Parameter	Value
λ	0.1	t_1	10^9
κ	0.02	$\dot{\varepsilon}_1$	$1e^{-12}$
ι	0.0054	$\dot{\varepsilon}_{ref}$	$1e^{-12}$
m	0.888	β	0.23

of BRICK parameters to match the stress magnitude has not been performed so results are assessed on the variation around a central CRS path.

5.2 *Brick-led pure TESRA model*

The brick-led model with $A_f = 200$ and $c = 1e^{-15}$ is shown in Figure 7. The form of the SRS stage does not conform to the original data in Figure 4 and oscillates unstably.

The problem with a brick-led approach is illustrated in the simplified schematic in Figure 8. This shows a 3 brick model having just experienced a strain rate increase. Figure 8a shows an Isotach test simplified so that SL increases at the point where a string at the new applied rate would be taut. Longer strings require more strain to occur before the string length increases. In the man-led approach (Fig. 8b) $\dot{\varepsilon}_n$ transition begins immediately and is the same for all bricks. Consequently the increase in *SL* for longer strings is reduced. In the brick-led approach (Fig. 8c) $\dot{\varepsilon}_n$ does not begin to transition until $\dot{\varepsilon}_b$ increases with *SL*. Each brick to become engaged therefore has a *SL* greater than that for bricks with previously taut strings. The increase in *SL* results in an increase in elastic strain and therefore a spike in stress.

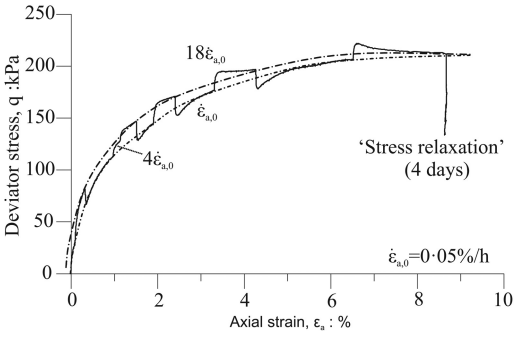

Figure 6. Strain rate behaviour of normally consolidated reconstituted London Clay (after Sorenson, Baudet, & Simpson (2007)).

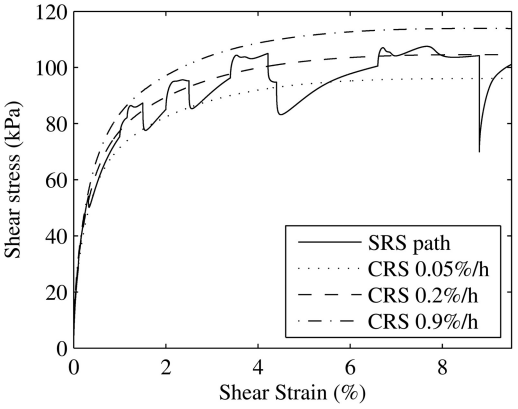

Figure 7. Brick-led Pure TESRA model of SRS stress path.

5.3 *Man-led Pure TESRA model*

The man-led Pure TESRA formulation (Fig. 9) was produced using $A_f = 200$ and $c = 1e^{-15}$. The results agree well with the experimental data (Fig. 6) when comparing the SRS paths. The small peaks on increasing rate and larger troughs on decreasing are shown. The CRS indications differ because in Figure 6 these are interpolated lines from the SRS test but represent a theoretical CRS path in Figure 9. The major difference is the slow return from the stress relaxation.

5.4 *Man-led General TESRA model*

The man-led General TESRA formulation (Fig. 10) was produced using $A_f = 200$ and $c = 0.2$. The General TESRA effect shown is a transition from Isotach behaviour at the start where the SRS path moves to and remains at the CRS for the applied rate and a TESRA

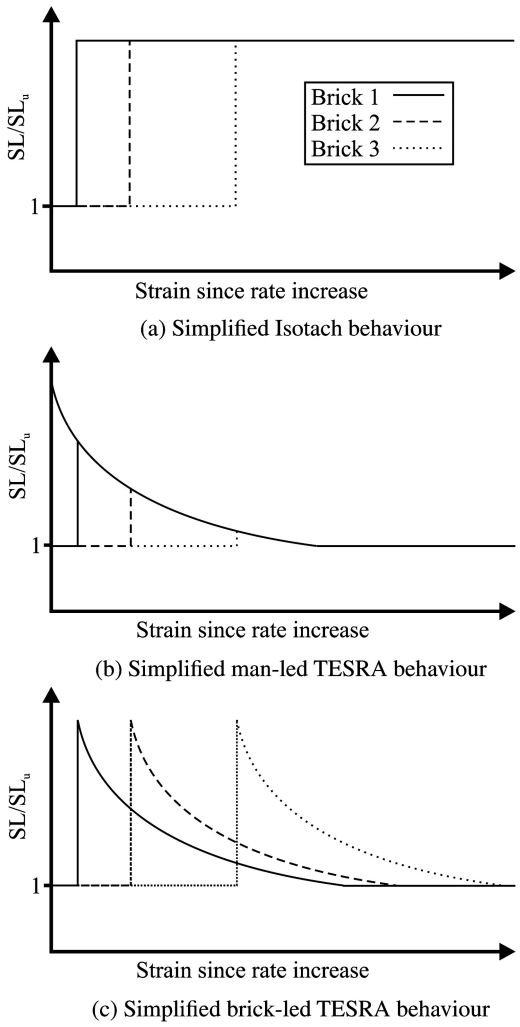

Figure 8. TESRA model types behaviours.

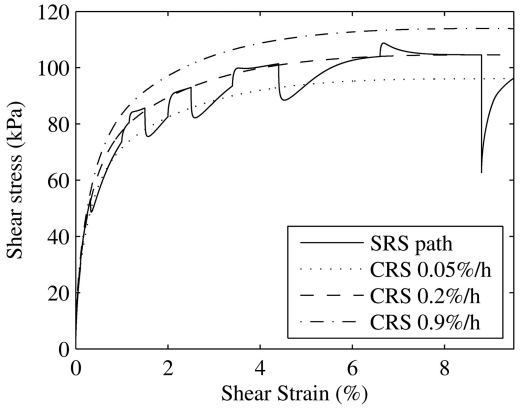

Figure 9. Man-led Pure TESRA.

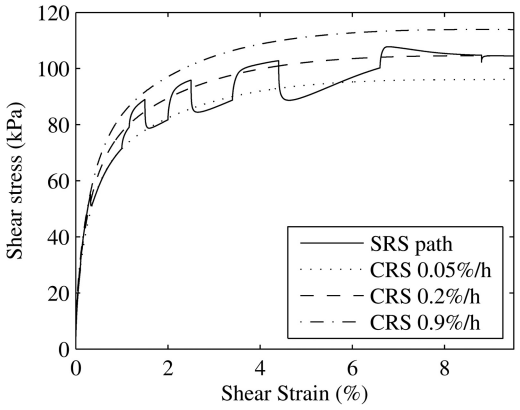

Figure 10. Man-led General TESRA.

behaviour at higher strain where the SRS path tends to the unique stress path.

6 CONCLUSIONS

The implementation of a TESRA model based on the work of Sorenson (2006) into the framework of a SRD BRICK model based on Clarke and Hird (2012) has been successful in replicating the Isotach results. When implementing TESRA behaviour two approaches are possible; brick-led (where the neutral strain rate decays to the brick strain rate), and man-led (where the neutral strain rate decays to the applied strain rate). It has been demonstrated that the brick-led approach produces erroneous results in TESRA conditions. The man-led approach generates a response to strain rate change observed in experimental data as shown in the Pure TESRA model of Sorenson et al. (2007) test S1LCrA2. General TESRA behaviour functions as expected within the model but is not compared to actual results.

REFERENCES

Bishop, A. (1966). The strength of soils as engineering materials. *Géotechnique 16*(No. 2), 91–130.

Clarke, S. (2009). *Enhancement of the BRICK constitutive model to incorporate viscous soil behaviour, PhD Thesis*. University of Sheffield.

Clarke, S. D. & C. C. Hird (2012). Modelling of viscous effects in natural clays. *Canadian Geotechnical Journal 49*(2), 129–140.

Graham, J., J. A. Crooks, & A. Bell (1983). Time effects on the stress-strain behaviour of natural clays. *Géotechnique 33*(No.3), 327–340.

Leroueil, S., M. Kabbaj, F. Tavenas, & R. Bouchard (1985). Stress-strain-strain rate relationship for the compressibility of sensitive natural clays. *Géotechnique 35*(No. 2), 159–180.

Simpson, B. (1992). Retaining structures: displacement and design. *Géotechnique 42*(No. 4), 541–576.

Singh, A. & J. Mitchell (1968). General stress-strain-time function for soils. *Journal of the Soil Mechanics and Foundations Division, ASCE 94*(No. 2), 21–46.

Soga, K. & J. Mitchell (1996). Rate-dependent deformation of structured natural clays. *ASCE Geotechnical Special Publication 61*, 243–257.

Sorensen, K. (2006). *Influence of viscosity and ageing on the behaviour of clays, PhD Thesis*. London: University College.

Sorenson, K., A. Baudet, & B. Simpson (2007). Influence of structure on the time-dependent behaviour of a stiff sedimentary clay. *Géotechnique 57*(No. 1), 113–124.

Tatsuoka, F. (2005). Effects of viscous properties and ageing on the stress-strain behaviour of geomaterials. *Geotechnical special publication 143*(No. 1-60).

Tatsuoka, F., M. Ishihara, H. Di Benedetto, & R. Kuwano (2002). Time-dependent shear deformation characteristics of geomaterials and their simulation. *Soils and Foundations 42*(No. 2),531–540.

E

Matlab code for SRD section

E.1 Original SRD code

```
%SRD segment from Clarke (2009)
if ITERBR==1 && On==1;
    SLerr=1;
    % Convergence criteria for SRD model
    SRDcount=0;
    while SLerr>(SLr(JB)/10)
        SRDcount=SRDcount+1;
        % Calculate vectoral strain rate
        Vecstrain(JB) =norm(DSNB(:,JB))/Time;
        % limit minimum strain rate;
        Vecstrain(JB)=max(1e-13,Vecstrain(JB));
        % Limit Vecstrain to that of brick 1
        if Vecstrain(JB)>Vecstrain(1)
            Vecstrain(JB)=Vecstrain(1);
        end
        % Deassign string length
        SLprev(JB)=SL(JB);
        % Calculate SRD string lengths and apply half of the
        % change
        SL(JB)=((SLr(JB)*(1+(visc*log((abs(Vecstrain(JB))/Neu)...
            +1))))+SLprev(JB))/2;
        %Apply time dependent effects if string length decreases
        if SL(JB)>=SLprevious(JB)
            %Damp the application relative to previous execution
            SL(JB)=SLprevious(JB)+AppfacUP*(SL(JB)-SLprevious(JB));
        else
            % Calculate time dependent decay
            Vecprevious(JB)=((exp(((SLprevious(JB)/SLr(JB))-1)...
                /visc))-1)*Neu;          %previous strain rate
            Tp=10^(log10(TDtimeEnd)+(log10(Vecprevious(JB)/...
                TDrateEnd)*TDECAY));     %previous time
```

```
            Tc=Tp+Time;                    %current time
            % Calculate rate dependent string lengths if Tc>2
            if Tc>2;
                CurVec(JB)=10^((max(0,(log10(Tc)-log10...
                    (TDtimeEnd))/(TDECAY)))+log10(TDrateEnd));
                SL(JB)=SLr(JB)*(1+(visc*log((abs(CurVec(JB))...
                    /Neu)+1)));
                SL(JB)=SLprevious(JB)+AppfacDOWN*(SL(JB)...
                    -SLprevious(JB));
            else
                SL(JB)=SLprevious(JB)+AppfacDOWN*(SL(JB)...
                    -SLprevious(JB));
            end
        end
        %Calculation of brick strain using 'rams' approach
        %T is distance between the man and the brick
        %T-SLprev(JB) is the strain of the brick along a vector
        %in the previous iteration.
        Distance=DSNB(:,JB)*(T/(T-SLprev(JB))); %distance is a
        %vector of the difference in position between the man and
        %the brick in each component.
        DSNB(:,JB)=Distance*((T-SL(JB))/T);     %the change in
        %each brick component strain is the component distance
        %to the man multiplied by the ratio of change on the
        %vetoral distance
        SLerr=SL(JB)-SLprev(JB);
    end
    SLout(JB)=SL(JB)/SLr(JB);
end
```

E.2 SRD-B code version 1: Bisecting iteration for SL calculation

```
% SRD-B code with bisecting solution for string lengths
if ITERBR==1 && On==1;
    % Convergence criteria for SRD model
    Vecstrain(JB) =norm(DSNB(:,JB))/Time;
    %===============Find exact SL solution=====================
    if T>SLr(JB) %solution for bricks taut at SLr
        RATEhigh=5e-2;
        RATElow=0;
        ITTERerror=1;
        while abs(ITTERerror)>SRDITTTOL
            RATEmid=(RATEhigh+RATElow)/2;
```

```
            ITTERerror=(SLr(JB)*(1+(visc*log((abs(RATEmid)...
                /Neu)+1))))-(T-(Time*RATEmid));
            if ITTERerror>0
                RATEhigh=RATEmid;
            else
                RATElow=RATEmid;
            end
        end
        SL(JB)=(SLr(JB)*(1+(visc*log((abs(RATEmid)/Neu)+1))));
    else %trivial solution for distance less than SLr
        SL(JB)=SLr(JB); %SL cannot be less than SLr
        RATEmid=0;
    end
    %==============Time decay ================================
    if SL(JB)>=SLprevious(JB);
        % Allow instantaneous increase in string lengths
    else
        % Calculate time dependent decay
        Vecprevious(JB)=((exp(((SLprevious(JB)/SLr(JB))-1)/...
            visc))-1)*Neu;              %previous strain rate
        Tp=10^(log10(TDtimeEnd)+(log10(Vecprevious(JB)/...
            TDrateEnd)*TDECAY));        %previous time
        Tc=Tp+Time;                     %current time
        CurVec(JB)=10^((max(0,(log10(Tc)-log10(TDtimeEnd))/...
            (TDECAY)))+log10(TDrateEnd)); %current strain rate
        %calculate string length
        SL(JB)=SLr(JB)*(1+(visc*log((abs(CurVec(JB))/Neu)+1)));
    end
    %================Calculate brick strains====================
    SLJB=SL(JB);
    if T<=SLJB              %No brick movement if string slack
        for JC=(1:NC)
            DSNB(:,JB)=0;
        end
    else
        Tout=(T-SLJB)/T; %correctly proportioned moment if taut
        for JC=(1:NC)
            DSNB(JC,JB)=(SN(JC)+DSN(JC)-SNB(JC,JB))*Tout;
        end
    end
    SLout(JB)=SL(JB)/SLr(JB);
    %=======recalculate Vecstrain from output SL===============
    Vecstrain(JB) =norm(DSNB(:,1))/Time;
end
```

E.3 SRD-B code version 2: Workarounds for double precision problems

```
% SRD-B code with workarounds for double precision problems
% SRD-B code with bisecting solution for string lengths
if ITERBR==1 && On==1;
    % Convergence criteria for SRD model
    Vecstrain(JB) =norm(DSNB(:,JB))/Time;
    %===============Find exact SL solution=====================
    if T>SLr(JB) %solution for bricks taut at SLr
        RATEhigh=5e-2;
        RATElow=0;
        ITTERerror=1;
        while abs(ITTERerror)>SRDITTTOL
            RATEmid=(RATEhigh+RATElow)/2;
            ITTERerror=(SLr(JB)*(1+(visc*log((abs(RATEmid)...
                /Neu)+1))))-(T-(Time*RATEmid));
            if ITTERerror>0
                RATEhigh=RATEmid;
            else
                RATElow=RATEmid;
            end
        end
        SL(JB)=(SLr(JB)*(1+(visc*log((abs(RATEmid)/Neu)+1))));
    else %trivial solution for distance less than SLr
        SL(JB)=SLr(JB); %SL cannot be less than SLr
        RATEmid=0;
    end
    %==============Time decay ==================================
    if SL(JB)>=SLprevious(JB);
        % Allow instantaneous increase in string lengths
        TIMEDECAYPREV(JB)=0; %set as time decay did not occur
    else
        % Calculate time dependent decay
        Vecprevious(JB)=((exp(((SLprevious(JB)/SLr(JB))-1)/...
            visc))-1)*Neu;              %previous strain rate
        Tp=10^(log10(TDtimeEnd)+(log10(Vecprevious(JB)/...
            TDrateEnd)*TDECAY));        %previous time
        Tc=Tp+Time;                     %current time
        % Added rules for the application of time dependent SL
        if  any(APPSNR~=APPSNRPREV) || TIMEDECAYPREV(JB)==1;
           CurVec(JB)=10^((max(0,(log10(Tc)-log10(TDtimeEnd))...
           /(TDECAY)))+log10(TDrateEnd)); %current strain rate
           %calculate string length
```

```
            SL(JB)=SLr(JB)*(1+(visc*log((abs(CurVec(JB))/Neu)+1)));
            TIMEDECAYPREV(JB)=1; %set as time decay occurred
        else
            TIMEDECAYPREV(JB)=0; %set as time decay did not occur
        end
    end
    %================Calculate brick strains====================
    SLJB=SL(JB);
    if T<=SLJB              %No brick movement if string slack
        for JC=(1:NC)
            DSNB(:,JB)=0;
        end
    else
        Tout=(T-SLJB)/T;%Correctly proportioned movement if taut
        for JC=(1:NC)
            DSNB(JC,JB)=(SN(JC)+DSN(JC)-SNB(JC,JB))*Tout;
        end
    end
    SLout(JB)=SL(JB)/SLr(JB);
    %=======Recalculate Vecstrain from output SL================
    Vecstrain(JB) =norm(DSNB(:,1))/Time;
end
```

E.4 SRD-B code version 3: Limited application of time dependent SL

```
% SRD-B code with limited application of time dependent SL
if ITERBR==1 && On==1;
    % Convergence criteria for SRD model
    Vecstrain(JB) =norm(DSNB(:,JB))/Time;
    %===============Find exact SL solution=====================
    if T>SLr(JB) %solution for bricks taut at SLr
        RATEhigh=5e-2;
        RATElow=0;
        ITTERerror=1;
        while abs(ITTERerror)>SRDITTTOL
            RATEmid=(RATEhigh+RATElow)/2;
            ITTERerror=(SLr(JB)*(1+(visc*log((abs(RATEmid)...
                /Neu)+1))))-(T-(Time*RATEmid));
            if ITTERerror>0
                RATEhigh=RATEmid;
            else
                RATElow=RATEmid;
            end
```

```
        end
        SL(JB)=(SLr(JB)*(1+(visc*log((abs(RATEmid)/Neu)+1))));
    else %trivial solution for distance less than SLr
        SL(JB)=SLr(JB); %SL cannot be less than SLr
        RATEmid=0;
    end
    %==============Time decay ================================
    if SL(JB)>=SLprevious(JB);
        % Allow instantaneous increase in string lengths
        TIMEDECAYPREV(JB)=0; %set as time decay did not occur
    else
        % Calculate time dependent decay
        Vecprevious(JB)=((exp(((SLprevious(JB)/SLr(JB))-1)/...
            visc))-1)*Neu;              %previous strain rate
        Tp=10^(log10(TDtimeEnd)+(log10(Vecprevious(JB)/...
            TDrateEnd)*TDECAY));        %previous time
        Tc=Tp+Time;                     %current time
        % Added rules for the application of time dependent SL
        if  any(APPSNR~=APPSNRPREV) || TIMEDECAYPREV(JB)==1;
           CurVec(JB)=10^((max(0,(log10(Tc)-log10(TDtimeEnd))...
              /(TDECAY)))+log10(TDrateEnd)); %current strain rate
           TDSL(JB)=SLr(JB)*(1+(visc*log((abs(CurVec(JB))...
              /Neu)+1)));%calculate time dependent string length
           TIMEDECAYPREV(JB)=1; %set as time decay occurred
        else
           TIMEDECAYPREV(JB)=0; %set as time decay did not occur
        end
    end
    %Only apply TDSL if it is greater than the exact solution SL
    SL(JB)=max(SL(JB),TDSL(JB));
    %================Calculate brick strains====================
    SLJB=SL(JB);
    if T<=SLJB              %No brick movement if string slack
        for JC=(1:NC)
            DSNB(:,JB)=0;
        end
    else
        Tout=(T-SLJB)/T;%Correctly proportioned movement if taut
        for JC=(1:NC)
            DSNB(JC,JB)=(SN(JC)+DSN(JC)-SNB(JC,JB))*Tout;
        end
    end
    SLout(JB)=SL(JB)/SLr(JB);
    %=======Recalculate Vecstrain from output SL================
    Vecstrain(JB) =norm(DSNB(:,1))/Time;
end
```

F

Matlab code for coordinate descent creep

```
function [SN,SS,VOLP,SNB,SLprevious,TIMEDECAYPREV,APPSNRPREV...
    ,stressout,strainout,stiffout,miscout,bricksnout...
    ,brickdsnout,debugout,stage] = Creep(SL,GGMAX,ZERO,NC...
    ,TOLBR,RLAM,RKAP,RIOT,BETA,nu,Neu,visc,m,ips,BETA2...
    ,TDtimeEnd,TDrateEnd,SN,SS,VOLP,SNB,SLprevious...
    ,TIMEDECAYPREV,APPSNRPREV,stage,Ratetype,Timestep...
    ,CreepSNR,CreepTime)
%  Hexagonal co-ordinate descent creep to either target strain
%  rate or target creep time
%  Outputs 1:7 are required for brick function
%  Outputs 8:15 are standard data output matrices
%  Output 14 is an debugging matrix of descent path
%  Inputs 1:15 are brick constants unchanged by the execution
%  of the brick code routine.
%  Inputs 16:22 are brick variables that change on each
%  execution of the brick routine.
%  Inputs 24 on are control inputs thus:
%  stage= a number indicating the test stage at end of function
%  Ratetype = Defines which strain type rate is defined in:
%      0 =Axial strain,
%      1= Shear strain
%      2=DSN(3),
%      3= Vectoral strain
%      4=Brick 1 apparent rate Neu*exp((SLout(1)-1)/visc)
%  Timestep= Step in time used during creep
%  CreepSNR= Strain rate to stop creep (strain/s), 0 to disable
%  The value SNR will be calculated based on the strain resulting
%  from the creep using the rate type as defined in Ratetype
%  CreepTime= Elapsed time at which to stop creep, 0 to disable
%Number of Bricks
NB=size(SL,2);
```

```
%Ratio of elastic shear modulus to plane strain bulk modulus
FGK=1.5*(1.0-2.0*nu)/(1.0+nu);
% Calculate proportion of material represented by each brick
SNBP=zeros(1,NB);
for J=(NB:-1:2)
    SNBP(J)=GGMAX(J-1)-GGMAX(J);
end
SNBP(1)=1-GGMAX(1);
%==================Default Properties ======================
On=1;                   %Rate effects must be on
Time=Timestep;          %Time is defined by time step
SNR=10000;              %Set SNR high initially
row=0;                  %Initial data row is 0
rupture=0;              %Set rupture as off
stageclock=0;           %Stage clock at start
Initbarring=0;          %Barring to first point of test hexagon
stressmag=zeros(6,1);   %Preassigned for speed
Repeatpoints=zeros(6,1);%Preassigned for speed
%==============Determine Creep termination type================
if CreepTime==0 && CreepSNR==0;
    error('matlab:CreepBadTerm',...
    'Both rate and time termination turn off in creep stage')
end
if CreepTime==0
    CreepTime=1E15;     %make creep time too high to be reached
end
%==========Control parameters for co-ordinate descent ==========
Strainstepstart=min(SL);   %Initial magnitude of strain change
Stresstol=0.0000001;       %Tolerance for magnitude of stress
Straintol=3;               %Tolerance for convergence
ruptureto1=0.02/180*pi();  %Tolerance for rupture =0.02 degrees
stage=stage+1;             %Update stage
%==================Preallocate for speed=======================
MaxExpectedRows=1e5;            %number of row to preallocate
stressout(MaxExpectedRows,6)=0;
strainout(MaxExpectedRows,8)=0;
stiffout(MaxExpectedRows,2)=0;
miscout(MaxExpectedRows,4+NB)=0;
bricksnout(MaxExpectedRows,NB,2)=0;
brickdsnout(MaxExpectedRows,NB,2)=0;
creeppathx{MaxExpectedRows,10}=0;
creeppathy{MaxExpectedRows,10}=0;
creeppathz{MaxExpectedRows,10}=0;
%==============Coordinate descent creep ======================
while abs(SNR)>CreepSNR && rupture<10 && stageclock<CreepTime
    rupture=0;          %Reset rupture counting
    rupturestrain=0;
```

```
%-----------------Store start parameters-------------------
TIMEDECAYPREVkeep=TIMEDECAYPREV;
APPSNRPREVkeep=APPSNRPREV;
SLpreviouskeep=SLprevious;
%----------------Initial stress relaxation----------------
DSN=[0,0,0,0,0,0];
%-----------------------Brick Routine---------------------
[DSS,~,DSNB,~,~,~,~,~,~,~,~]=bricksrdBiTDmax(Neu,visc,m,...
    SLprevious,SS,SN,ZERO,SNB,VOLP,NC,DSN,NB,SL,SNBP,...
    TOLBR,RLAM,RKAP,RIOT,BETA,FGK,ips,BETA2,On,Time,...
    TIMEDECAYPREV,APPSNRPREV,TDtimeEnd,TDrateEnd);
%stress magnitude at the moment is that at 0 strain.
stressincveccurr=sqrt(DSS(1)^2+DSS(3)^2);
%-------Parameters stored so as to exist for creep solve----
DSNBprev=DSNB;  %Previous brick strain
DSNstart=DSN;   %Strain increment vector
%-Load counters and initial conditions for each iteration
point=1;        %Set as first point on creep path
path=1;         %Set as first path
row=row+1;      %Increase row for data storage
Strainstep=Strainstepstart;%Initial length of strain steps

%-------Data output for path start when point = 1----------
%Fist point in output matrix used so point -1 code works
%correctly when finding repeats. The data is mostly NaN so
%no repeat is found but the row exists. Column 1 is the
%start point for the really first point (point=2) stored as
%an edge point to be found when point=3.
creeppathx{row,path}(point,1:9)=[DSNstart(1,1),NaN(1,6),...
    DSNB(1,1),DSNB(1,NB)];
creeppathy{row,path}(point,1:9)=[DSNstart(1,3),NaN(1,6),...
    DSNB(3,1),DSNB(3,NB)];
creeppathz{row,path}(point,1:7)=[stressincveccurr,NaN(1,6)];

%=====Find best strain path by coordinate descent method===
%while the stress increment magnitude is greater than the
%tolerance.
while stressincveccurr>Stresstol && Strainstep> Straintol*...
        max(eps(DSNstart(1)),eps(DSNstart(3))) && rupture<10;
    point=point+1; %Increase point count for path
    %---------------build up test matrix -----------------
    DSNtest(1,:)=DSNstart+Strainstep*[sind(Initbarring+0)...
        ,0,cosd(Initbarring+0),0,0,0];     %0
    DSNtest(2,:)=DSNstart+Strainstep*[sind(Initbarring+60)...
        ,0,cosd(Initbarring+60),0,0,0];   %60
    DSNtest(3,:)=DSNstart+Strainstep*[sind(Initbarring+120)...
        ,0,cosd(Initbarring+120),0,0,0]; %120
```

```
DSNtest(4,:)=DSNstart+Strainstep*[sind(Initbarring+180)...
    ,0,cosd(Initbarring+180),0,0,0]; %180
DSNtest(5,:)=DSNstart+Strainstep*[sind(Initbarring+240)...
    ,0,cosd(Initbarring+240),0,0,0]; %240
DSNtest(6,:)=DSNstart+Strainstep*[sind(Initbarring+300)...
    ,0,cosd(Initbarring+300),0,0,0]; %300
%--------------Find repeated points--------------------
for a=1:6 %Check each of the current test points
    repeatpoints=abs(DSNtest(a,1)-creeppathx{row,path}...
        (1:point-1,1:6))<3*eps(DSNtest(a,1))& ...
        abs(DSNtest(a,3)-creeppathy{row,path}...
        (1:point-1,1:6))<3*eps(DSNtest(a,1)) ;
    %get stress magnitude for repeated points
    stressmag(a,1)=sum(sum(repeatpoints.*...
        creeppathz{row,path}(1:point-1,1:6)));
    Repeatpoints(a,1)=sum(sum(repeatpoints));
end
%----Calculate stress magnitude for each strain path---
for a=1:6                   %Loop each step and run brick
    if Repeatpoints(a)==0
        %------------Load start parameters -------------
        TIMEDECAYPREV=TIMEDECAYPREVkeep;
        APPSNRPREV=APPSNRPREVkeep;
        SLprevious=SLpreviouskeep;
        DSN=DSNtest(a,:);   %Load the strain vector
        %----------------Brick Routine----------------
        [DSS,~,DSNB,~,~,~,~,~,~,~,~]=bricksrdBiTDmax...
            (Neu,visc,m,SLprevious,SS,SN,ZERO,SNB,...
            VOLP,NC,DSN,NB,SL,SNBP,TOLBR,RLAM,RKAP,...
            RIOT,BETA,FGK,ips,BETA2,On,...
            Time,TIMEDECAYPREV,APPSNRPREV,...
            TDtimeEnd,TDrateEnd);
        %stress magnitude stored for each direction
        stressmag(a)=sqrt(DSS(1)^2+DSS(3)^2);
        DSNBbest{a}=DSNB; %store DSNB for each path
    else
        DSNtest(a,:)=nan;
    end
end
%--------------Store stres path data -----------------
creeppathx{row,path}(point,1:9)=[DSNtest(:,1)',...
    DSNstart(1),DSNB(1,1),DSNB(1,NB)];
creeppathy{row,path}(point,1:9)=[DSNtest(:,3)',...
    DSNstart(3),DSNB(3,1),DSNB(3,NB)];
creeppathz{row,path}(point,1:7)=[stressmag',...
    stressincveccurr];
%Find the direction with lowest stress magnitude
```

```
[stressincvec,I] = min(stressmag); %value and index
if stressincvec<stressincveccurr;
    %Store new current stress increment vector magnitude
    stressincveccurr=stressincvec;
    %Reassign the starting point as the end lowest path
    DSNstart=DSNtest(I,:);
    %Extract DSNB for selected strain path
    DSNB=DSNBbest{I};
else %Reduce the strain step if all options go up.
    Strainstep=Strainstep/5;
end

%===============Rupture detection=====================
%Change in DSNB since last iteration
DDSNB=DSNB-DSNBprev;
%Calculate orientation of each brick
DDSNBtheta=atan(abs(DDSNB(1,:))./abs(DDSNB(3,:)));
%A strain change with an orientation below tolerance
if DDSNBtheta(1,1:NB)<rupturetol & sum(sum(abs(DDSNB)))>0
    rupture=rupture+1; %increase rupture count
    %Sum of brick 1 strain 3 occurring during rupture
    rupturestrain=rupturestrain+DDSNB(3,1);
    if rupture==10 && abs(rupturestrain)<Strainstepstart
        rupture=rupture-1; %Lower if strain not enough
    end
else
    rupture=0; %Reset rupture to zero if not failed
    rupturestrain=0; %Zero rupture strain
end
%--Store DSNB that occurred on the optimum strain path-
DSNBprev=DSNB;

%====Strain convergence but stress too high============
%===============New random path start ================
%If the strain step is low enough to terminate and the
%stress is to high and the number of paths attempted is
%less than 10
if (Strainstep<Straintol* max(eps(DSNstart(1)),...
    eps(DSNstart(3))) && stressincveccurr>Stresstol...
    && path<10) || (size(creeppathx{row,path},1)>5000 ...
    && path<10);
    %Initial strain step set as strain to solution
    Strainstepstart=sqrt(sum(DSNstart.^2));
    %Reset strain step to initial length
    Strainstep=Strainstepstart;
    randTheta=2*pi()*rand;      %random direction
    randMag=10*Strainstep*rand; %random magnitude
```

```
        %path taken from current solution point DSNstart
        DSNstart= DSNstart+[randMag*cos(randTheta)...
            ,0,randMag*sin(randTheta),0,0,0];
        DSN=DSNstart;
        %-------------Load start parameters ---------------
        TIMEDECAYPREV=TIMEDECAYPREVkeep;
        APPSNRPREV=APPSNRPREVkeep;
        SLprevious=SLpreviouskeep;
        %---------------Brick Routine----------------------
        [DSS,~,DSNB,~,~,~,~,~,~,~,~]=bricksrdBiTDmax...
            (Neu,visc,m,SLprevious,SS,SN,ZERO,SNB,VOLP,...
            NC,DSN,NB,SL,SNBP,TOLBR,RLAM,RKAP,RIOT,BETA,...
            FGK,ips,BETA2,On,Time,TIMEDECAYPREV,...
            APPSNRPREV,TDtimeEnd,TDrateEnd);
        %Stress magnitude at start of new path.
        stressincveccurr=sqrt(DSS(1)^2+DSS(3)^2);
        %Set previous brick strain at starting value
        DSNBprev =DSNB;
        %-------------Path and point adjust---------------
        path=path+1;        %increase path count
        point=1;            %set as first point of new path
        %-----Data output for path start when point = 1-----
        creeppathx{row,path}(point,1:9)=[DSNstart(1,1),...
            NaN(1,6),DSNB(1,1),DSNB(1,NB)];
        creeppathy{row,path}(point,1:9)=[DSNstart(1,3),...
            NaN(1,6),DSNB(3,1),DSNB(3,NB)];
        creeppathz{row,path}(point,1:7)=[stressincveccurr,...
            NaN(1,6)];

    end

    %=====Fails to converge on solution after 10 paths======
    %Extract best solution from the 10 paths that ran.
    if (Strainstep<Straintol* max(eps(DSNstart(1)),...
        eps(DSNstart(3))) && stressincveccurr>Stresstol...
        && path==10) || (size(creeppathx{row,path},1)>5000 ...
        && path==10)
        endstress=zeros(1,10);
        for a=1:10
            %Create a vector of stress at end of each path
            endstress(a)=creeppathz{row,a}(end,7);
        end
        [stressincveccurr,I]=min(endstress);
        %Reassign DSNstart based on extracted values
        DSNstart=[creeppathx{row,I}(end,7),0,...
            creeppathy{row,I}(end,7),0,0,0];
    end
```

```
end
%===============After solution found=======================
%Initial strain step set as strain to solution /2
Strainstepstart=sqrt(sum(DSNstart.^2))/2;
%--------------Run brick with solution---------------------
DSN=DSNstart; %DSN as the last start value reached before
              %the tolerance was satisfied
%-----------------Load start parameters --------------------
TIMEDECAYPREV=TIMEDECAYPREVkeep;
APPSNRPREV=APPSNRPREVkeep;
SLprevious=SLpreviouskeep;
%-----------------Brick Routine -------------------------
[DSS,DSNP,DSNB,~,SNT,SLout,SLprevious,~,~,TIMEDECAYPREV,...
    APPSNRPREV]=bricksrdBiTDmax(Neu,visc,m,SLprevious,SS,...
    SN,ZERO,SNB,VOLP,NC,DSN,NB,SL,SNBP,TOLBR,RLAM,RKAP,...
    RIOT,BETA,FGK,ips,BETA2,On,Time,TIMEDECAYPREV,...
    APPSNRPREV,TDtimeEnd,TDrateEnd);
%---------------Update brick parameters-------------------
SS=SS+DSS;                  %Update Stress
SN=SNT;                     %Update Strain
SNB=SNB+DSNB;               %Update brick strain
%Update current volumetric plastic strain
VOLP(1)=VOLP(1)+DSNP(1);
if  VOLP(1)>VOLP(2) %Check current against previous maximum
    %Update previous maximum volumetric plastic strain
    VOLP(2)=VOLP(1);
end
%===========Calculate strain rate ==========================
if Ratetype==0                                      %Axial
    SNR=((DSN(1)+ sqrt(3)*DSN(3))/3)/Time;
elseif Ratetype==1                                  %Shear
    SNR=(DSN(3) /sqrt(3))/Time;
elseif Ratetype==2                                  %DSN3
    SNR=(DSN(3))/Time;
elseif Ratetype==3                                  %Magnitude
    SNR=(sqrt(sum(DSN.^2)))/Time;
elseif Ratetype==4                                  %Apparent
    SNR=Neu*exp((SLout(1)-1)/visc);
else
    error('Matlab:StressRatetype','Incorrect Rate Type')
end

%====================Data Output===========================
stageclock=stageclock+Time; %add time to clock
stressout(row,:)=[SS(1),SS(2)+(sqrt(3)*SS(3)),...
    SS(1)+(2*SS(3))/sqrt(3),...
```

```
    (SS(1)+(2*SS(3))/sqrt(3))-sqrt(3)*SS(3)+SS(2),...
    DSS(1),DSS(2)+(sqrt(3)*DSS(3))];
    %[p, q, Axial,Radial,p change, q change]
strainout(row,:)=[SN(1),SN(3)/sqrt(3),...
    (SN(1)+ sqrt(3)*SN(3))/3,(2*SN(1)-sqrt(3)*SN(3))/6,...
    DSN(1),DSN(3)/sqrt(3),DSNP(1),DSNP(3) /sqrt(3)];
%[Volumetric, Triaxial shear, Axial, Radial, Volumetric
%change, Shear change, Plastic change volumetric, Plastic
%change shear]
stiffout(row,:)=[DSS(1)/DSN(1),...
    (DSS(2)+(sqrt(3)*DSS(3)) /(DSN(3)/sqrt(3)))/3];
%[Bulk,Shear]
miscout(row,:)=[stage,SNR*360000,Time,stageclock,SLout];
%[Stage,strain rate, time step, stage time,
% normalised string length]
bricksnout(row,:,1)=SNB(1,:);   %Brick strains vol
brickdsnout(row,:,1)=DSNB(1,:); %Brick strain change vol
bricksnout(row,:,2)=SNB(3,:)/sqrt(3);%Brick strain shear
%Brick strain change shear
brickdsnout(row,:,2)=DSNB(3,:)/sqrt(3);

%=========================================================
% Handling of data if creep rupture is detected on this
% creep increment this saves the workspace at the rupture
% stage and loads the last complete creep stage.
if rupture>9 % ruptured
    save creeprupture.mat %Save workspace at end of rupture
    %revert parameters back to those at the end of the last
    %successful creep stage to allow plot and continuation
    %by reducing the row number the trimming routine
    %will trim the data storage matrices.
    row=row-1;
    %load output data from RESUMEARRAY
    SN=RESUMEARRAY{1};
    SS=RESUMEARRAY{2};
    VOLP=RESUMEARRAY{3};
    SNB=RESUMEARRAY{4};
    SLprevious=RESUMEARRAY{5};
    TIMEDECAYPREV=RESUMEARRAY{6};
    APPSNRPREV=RESUMEARRAY{7};
    rupture=10; %set rupture to 10 to terminate
else
    %Create a backup cell array of the parameters output at
    %the end of the increment.
    RESUMEARRAY={SN,SS,VOLP,SNB,SLprevious,TIMEDECAYPREV,...
        APPSNRPREV};
end
```

```
end
%====Trim Preallocated matrix down to actual number of rows====
stressout=stressout(1:row,:);
strainout=strainout(1:row,:);
stiffout=stiffout(1:row,:);
miscout=miscout(1:row,:);
bricksnout=bricksnout(1:row,:,:);
brickdsnout=brickdsnout(1:row,:,:);
creeppathx=creeppathx(1:row,:);
creeppathy=creeppathy(1:row,:);
creeppathz=creeppathz(1:row,:);
%================================================================
creeppaths={creeppathx,creeppathy,creeppathz};
debugout=creeppaths;
end
```